

**AERODYNAMIC FORCES INDUCED BY CONTROLLED
TRANSITORY FLOW ON A BODY OF REVOLUTION**

A Thesis
Presented to
The Academic Faculty

by

Christopher S. Rinehart

In Partial Fulfillment
of the Requirements for the Degree
Doctor of Philosophy in the
School of Mechanical Engineering

Georgia Institute of Technology
December 2011

**AERODYNAMIC FORCES INDUCED BY CONTROLLED
TRANSITORY FLOW ON A BODY OF REVOLUTION**

Approved by:

Dr. Ari Glezer, Advisor
School of Mechanical Engineering
Georgia Institute of Technology

Dr. Mark Allen
School of Electrical & Computer
Engineering
Georgia Institute of Technology

Dr. Marc Smith
School of Mechanical Engineering
Georgia Institute of Technology

Dr. James McMichael
Aerospace, Transportation, and Advanced
Systems Laboratory
Georgia Tech Research Institute

Dr. David Parekh
School of Mechanical Engineering
Georgia Institute of Technology

Date Approved: November 10, 2011

This thesis is dedicated to my parents, my brother, and my wife, whose love, support, and guidance have had much to do with shaping my life and the successes in it.

ACKNOWLEDGEMENTS

This research would not have been possible without the guidance of my advisor, Professor Ari Glezer, and the dedication of the principal investigators for the project supporting this thesis, Jim McMichael (GTRI) and Peter Plostins (USARL). I would also like to thank the other committee members, Marc Smith, David Parekh, and Mark Allen, for their considerations, feedback, and review of my work.

Much of the work described in this thesis was part of the SCORPION project, “Self-CORrecting Projectile for Infantry OperatioN”, a joint effort between the Georgia Institute of Technology and the U.S. Army Research Laboratory (ARL) with support and direction from the Defense Advanced Research Projects Agency (DARPA). The objective was to develop and explore the applicability of micro-adaptive flow control (MAFC) technology for aerodynamic steering of spinning projectiles. The success of this project, including functional flight tests, is attributed to the efforts of the entire team. I wish to thank those with whom I was directly involved, including Andre Lovas and Gordon Brown. I also wish to thank Bob Englar for the use of his Model Test Facility wind tunnel for high-speed studies in the flight model development.

The friendship and assistance of all my colleagues at the Fluid Mechanics Research Laboratory, past and present, is greatly appreciated. I would like to thank Andrew Honohan for establishing the wind tunnel used for the completion of my work, Bojan Vukasinovic and Dan Brzozowski for their meaningful input and software assistance, and John Culp for his support of so many aspects of the FMRL facility and operations. The close friendship of Bart Smith, Mark Trautman, Andrew Honohan, Tom Crittenden, Brian English, and John Culp throughout the years has been unforgettable.

TABLE OF CONTENTS

	Page
ACKNOWLEDGEMENTS	iv
LIST OF TABLES	vii
LIST OF FIGURES	viii
NOMENCLATURE	xii
SUMMARY	xv
 <u>CHAPTER</u>	
1 INTRODUCTION	1
2 LITERATURE REVIEW	3
2.1 Aerodynamic Flow Control	3
2.2 Separation Control over Bluff Bodies	10
2.3 Mergence	15
3 EXPERIMENTAL FACILITIES AND TECHNIQUES	17
3.1 Model Development	17
3.2 Actuator Calibration	21
3.3 Wind Tunnels	23
3.4 PIV Acquisition and Analysis	26
4 FLOW CONTROL ON A BODY OF REVOLUTION	30
4.1 Early Attempts with Cross-Flow Jets	30
4.2 Parametric Effects on Aerodynamic Force	33
4.3 Transitory Aerodynamic Force	40
4.4 Modification of the Actuation Waveform	51
4.5 Recessed Jet Channel	56

4.6 Comparisons to a Conventional Steady Coanda Jet	63
5 ISOLATED INTERACTION DOMAIN STUDY	66
5.1 Background	67
5.2 Actuator Characteristics	69
5.3 The Baseline Flow over the Backward-Facing Step	78
5.4 Interaction of the Synthetic Jet with the Cross Flow	89
5.5 Geometrical Effects	104
5.6 Transient Flow Response	115
5.7 Dynamics of Oscillatory Suction and Blowing	132
5.8 Spanwise Variation	141
6 CONCLUSIONS	160
APPENDIX A: COMPARISON TO STEADY BLOWING AND SUCTION	169
REFERENCES	187
VITA	191

LIST OF TABLES

	Page
Table 1: Conversion of synthetic jet strengths to equivalent steady jet strengths	170

LIST OF FIGURES

	Page
Figure 1: Axisymmetric body shape	19
Figure 2: Actuator performance	22
Figure 3: Dynamic force measurement experimental configuration	24
Figure 4: Small closed-return wind tunnel	25
Figure 5: Typical PIV experimental configuration	27
Figure 6: Smoke visualization of stacked cross-flow configuration	31
Figure 7: Normal force developed by activation of stacked cross-flow jet	32
Figure 8: PIV images showing degree of flow turning with increasing jet strength	34
Figure 9: Normal force developed for free and constrained jets	36
Figure 10: Effect of Coanda radius on the normal force	38
Figure 11: Effect of square extensions on the normal force	39
Figure 12: Transient force in response to step modulation	41
Figure 13: Transient flow response to a step modulation	44
Figure 14: Transient flow relaxation after termination of the actuation signal	45
Figure 15: Normal force in response to momentary activation	46
Figure 16: Force and flow response to a brief pulse	47
Figure 17: Comparison of flow response in azimuthal planes, $\theta = 0^\circ$ and 9°	49
Figure 18: Comparison of flow response in azimuthal planes, $\theta = 0^\circ$ and 18°	50
Figure 19: Hot wire measurements for original and modified driving signals	52
Figure 20: Impact of amplified input signal on transient flow response	54
Figure 21: Impact of actuator braking signal on transient flow relaxation	55
Figure 22: Tail geometry	56

Figure 23: Normal force developed for axisymmetric and channeled tail extensions	57
Figure 24: Variation of aerodynamic performance with control jet thrust	60
Figure 25: Flow response for axisymmetric and channeled tail extensions	62
Figure 26: Aerodynamic normal force generated by steady tangential blowing	64
Figure 27: Augmentation ratios for jets blowing over Coanda surface	65
Figure 28: Wind tunnel test section and backward-facing step configuration	67
Figure 29: Planar actuator and Coanda surface	68
Figure 30: Comparison of actuator performance	70
Figure 31: Phase-averaged PIV of a synthetic jet issuing into a quiescent medium	72
Figure 32: Time-averaged PIV of a synthetic jet issuing into a quiescent medium	74
Figure 33: Closer view of a synthetic jet issuing into a quiescent medium	76
Figure 34: Effect of upstream suction on cross-stream distributions of streamwise velocity and the RMS fluctuation of streamwise velocity	79
Figure 35: Effect of upstream suction on the flow response to actuation	82
Figure 36: Analysis of PIV data shown in Figure 35	83
Figure 37: Time-averaged baseline flow field in the absence of actuation	85
Figure 38: Analysis of PIV data shown in Figure 37	87
Figure 39: Streamwise variation of static pressure in the absence of actuation	88
Figure 40: Time-averaged flow response to actuation at four jet strengths	90
Figure 41: Analysis of PIV data shown in Figure 40	92
Figure 42: Data of Figure 41 re-plotted in terms of variation with jet strength	94
Figure 43: Time-averaged flow response to actuation when average jet speed is matched to the free stream velocity at three values	96
Figure 44: Analysis of PIV data shown in Figure 43	98
Figure 45: Time-averaged flow response to actuation at three free stream speeds	100
Figure 46: Analysis of PIV data shown in Figure 45	102

Figure 47: Streamwise variation of static pressure with and without actuation	104
Figure 48: Time-averaged flow field for three Coanda radii	106
Figure 49: Analysis of PIV data shown in Figure 48	108
Figure 50: Time-averaged flow response for three backward step heights	110
Figure 51: Analysis of PIV data shown in Figure 50	112
Figure 52: Time-averaged flow response for three orifice step heights	113
Figure 53: Analysis of PIV data shown in Figure 52	115
Figure 54: Transient flow response to the onset of actuation at $U_\infty = 30$ m/s	116
Figure 55: Analysis of PIV data shown in Figure 54	118
Figure 56: Transient flow response to the onset of actuation at $U_\infty = 20$ m/s	121
Figure 57: Transient flow response to the onset of actuation at $U_\infty = 10$ m/s	123
Figure 58: Analysis of PIV data shown in Figures 56 and 57	125
Figure 59: Transient flow response to a single cycle pulse of actuation	128
Figure 60: Analysis of PIV data shown in Figure 59	130
Figure 61: Transient flow response for conventional and inverted signal polarities	133
Figure 62: Analysis of PIV data shown in Figure 61	136
Figure 63: High-resolution PIV images of the transient flow response, $0 < t/T_{Jet} < 4$	138
Figure 64: Time-averaged flow response to actuation at nine spanwise locations	143
Figure 65: Analysis of PIV data shown in Figure 64	145
Figure 66: Spanwise distribution of time-averaged out-of-plane mass flux	147
Figure 67: Transient flow response for select spanwise locations	150
Figure 68: Analysis of PIV data shown in Figure 67	152
Figure 69: Transient flow response for $z/w = 0$ and 0.375	154
Figure 70: Transient evolution of out-of-plane mass flux	157
Figure 71: PIV images of the flow response to steady suction and blowing	171

Figure 72: Magnified images of the flow response to steady suction and blowing	173
Figure 73: Analysis of PIV data shown in Figure 71	175
Figure 74: PIV images of synthetic jet actuation versus steady blowing	176
Figure 75: Analysis of PIV data regarding synthetic jet actuation, steady blowing, and suction	178
Figure 76: Magnified PIV images of the flow response to steady blowing	179
Figure 77: Magnified PIV images of the flow response to steady suction	180
Figure 78: High-resolution PIV images of the transient flow response, $4 < t/T_{Jet} < 5$	181
Figure 79: Phase-averaged flow response to synthetic jet actuation, $Re_{Jet} = 407$	183
Figure 80: Phase-averaged flow response to synthetic jet actuation, $Re_{Jet} = 73$	184
Figure 81: Analysis of PIV data shown in Figures 79 and 80	186

NOMENCLATURE

A	Cross-sectional area of jet orifice exit plane
Au	Augmentation ratio of induced normal force over jet thrust
a_y	Lateral acceleration
b	Cross-stream width of shear layer
ΔC_D	Change in drag coefficient
C_μ	Momentum coefficient
C_p	Static pressure coefficient
D	Body diameter
E	Square-cornered extension length
f_{act}	Actuation driving frequency
f_{mod}	Actuation pulse modulation frequency
F_N	Induced normal force
F_y	Lateral force
h	Jet orifice height
H	Backward-facing step height
J	Jet thrust
J_x	Streamwise momentum flux
J_y	Cross-stream momentum flux
L	Body length
m	Body mass
\dot{m}_{net}	Out-of-plane mass flux
Q	Volumetric flow rate
R	Coanda radius

Re_D	Free stream Reynolds number based on body diameter
Re_{Jet}	Synthetic jet Reynolds number based on orifice height
Re_{Steady}	Steady jet Reynolds number based on orifice height
S	Orifice step height
St	Strouhal number based on body diameter
St_H	Strouhal number based on backward step height
t	time
T_{Jet}	Period of synthetic jet driving frequency
T_p	Duration of driving frequency pulse-train
$T_{Settling}$	Time scale of flow modification over Coanda surface
u	Streamwise velocity component
U_{Avg}	Average jet outstroke velocity normalized by outstroke period
U_{cl}	Jet centerline (peak) velocity
U_∞	Free stream velocity
U_{Jet}	Average jet outstroke velocity normalized by actuation period
U_o	Peak sinusoidal jet velocity
U_{Steady}	Steady (conventional) jet velocity
V_{RMS}	Root-mean-squared driving input voltage
w	Jet orifice width (planar actuator)
x	Streamwise distance
x_R	Flight range distance
y	Cross-stream distance
Δy	Lateral displacement
z	Spanwise distance
α	Angle of attack

β	Momentum flux vector angle
β_{Avg}	Cycle-averaged momentum flux vector angle
ϕ	Actuation frequency phase angle
γ	Velocity vector angle at $0.5 U_{\infty}$
μ	Fluid dynamic viscosity
θ	Azimuthal angle of radial plane relative to jet orifice centerline
ρ	Fluid density

SUMMARY

The aerodynamic forces and moments on an axisymmetric body of revolution are controlled in a low-speed wind tunnel by induced local flow attachment. Control is effected by an array of aft-facing synthetic jets emanating from narrow, azimuthally segmented slots embedded within an axisymmetric backward facing step. The actuation results in a localized, segmented vectoring of the separated base flow along a rear Coanda surface and induced asymmetric aerodynamic forces and moments. The observed effects are investigated in both quasi-steady and transient states, with emphasis on parametric dependence. It is shown that the magnitude of the effected forces can be substantially increased by slight variations of the Coanda surface geometry. Force and velocity measurements are used to elucidate the mechanisms by which the synthetic jets produce asymmetric aerodynamic forces and moments, demonstrating a novel method to steer axisymmetric bodies during flight.

CHAPTER 1

INTRODUCTION

The application of fluidic devices to alter the characteristics of the flow field about a body in motion has been a subject of numerous investigations since the early 1900s. While mechanical devices such as flaps have frequently been employed for flow control, often their complexity, weight penalty, and system response time may render them detrimental or even unrealistic for implementation in demanding applications. Earlier investigations have demonstrated that flow over a moving body can be altered using mechanically simple fluidic devices, with potential for similar or stronger effects than can be achieved with mechanical devices. The steering of a projectile in flight is one example where a fluidic device may prove to be beneficial because of the extremely short time scales and small length scales of such an application, as well as the simplicity, robustness, and addressability of such a device.

The focus of one of DARPA's Micro Adaptive Flow Control (MAFC) programs was to reduce the dispersion of a spinning projectile through the use of integrated small-scale fluidic actuation to control the evolution of the external large-scale flow field. An important objective of this project was to establish an effective technology approach, apply it to an actual flight prototype, and demonstrate functionality in a flight test. The present thesis describes the flow mechanisms associated with integrated fluidic actuation that leads to alteration of the global aerodynamic forces and moments on a prototypical body of revolution. Following a review of relevant prior art in Chapter 2, and a technical overview of the test model, facilities, and experimental techniques in Chapter 3, this

thesis describes the flow control aspects of this project and related technical issues in Chapter 4. Chapter 5 describes a detailed investigation of the flow mechanisms in a two-dimensional configuration, to isolate the interaction domain between the actuation jet and the cross flow. Finally, Chapter 6 summarizes the important conclusions of this investigation.

CHAPTER 2

LITERATURE REVIEW

As noted in Chapter 1, the objective of the current work is to effect aerodynamic steering forces and moments on an axisymmetric body by using small-scale fluidic actuation to control flow separation at the base of the body. Separation flow control has historically focused on ways to improve the performance of spanwise two-dimensional aerodynamic and bluff bodies (such as airfoils and cylinders), and so the literature review begins with a review of the passive and active methods to enhance or control such flows. Further, this review examines periodic forcing via oscillatory devices, which can exploit natural instabilities in the flow to yield substantial effects with minimal input. For the specific application of this work, the transient response to the onset of such periodic actuation is critical as the associated time scales can affect the utility of the actuation. Therefore, the transitory response to pulsed modulation of periodic forcing is also discussed. In addition, since projectiles are axisymmetric bluff bodies with blunt bases, relevant examples of passive and active separation flow control on such geometries are also discussed including control of flows behind backward-facing steps.

2.1 Aerodynamic Flow Control

Control of separated flows on spanwise two-dimensional bodies such as airfoils and cylinders has been achieved in various ways. The objective is typically to cause, prevent, or reattach separated flow to effect changes in the pressure distribution over the body, and hence in the aerodynamic forces. A common approach for separation delay on

external aerodynamic surfaces is the use of passive surface devices such as vortex generators (Kuchemann 1978). These devices are typically rectangular or triangular plates that are tall enough to protrude above the boundary layer, and have an angle of attack with respect to the local flow, each creating a tip vortex which enhances mixing between the free stream and slower flow within the boundary layer, thereby re-energizing the boundary layer flow and delaying separation.

Flow control can be applied “actively” by manipulation of the flow near a solid boundary. Prandtl (1904) employed steady suction via a spanwise slot to delay separation over a cylinder. Suction was applied to the wings of full scale airplanes in the 1930s where measurable changes in take-off and landing performance matched theoretical predictions (Stueper, 1943). In most cases the mechanism is simply the removal of low-momentum fluid near the surface, which re-energizes the flow near the surface and delays separation. Similarly, steady blowing from the surface can be used to add momentum to the flow rather than removing it. Steady blowing can rely on natural attachment of flow to adjacent curved or angled surfaces called the Coanda effect (Coanda, 1936).

Application of the Coanda effect for passive separation control perhaps began with the work of Lachmann in 1917 on slots formed by divided wing sections, which allowed flow to “bleed” from the bottom to the top but in doing so enhanced aerodynamic performance. Later in 1921 Baumann took this concept further by pressurizing an interior volume within the wing to eject air from a tangential slot on the suction surface of the wing (Betz, 1961). The global flow is modified by blowing a conventional, usually planar jet along a tangential rounded or slightly angled plane surface. The jet follows this surface as a result of the reduced static pressure within the jet, and with proper placement

entrains or deflects the external flow field, hence causing aerodynamic modification. The mechanism of the Coanda effect is analyzed in detail by Newman (1961).

Since the Coanda effect can lead to flow turning of ninety degrees or more relative to the original direction, as discussed by Newman (1961), it may offer significant opportunities for flow control even in regions of gross flow separation. Such a fluidic approach can have many advantages over mechanical devices in terms of weight, power consumption, and performance capabilities, and can enable the use of less conventional airfoil shapes with superior aerodynamic performance. For example, by steady tangential blowing over a rounded trailing edge on an airfoil, Englar (2000) was able to achieve lift augmentation to jet momentum flux ratios as high as 80. Englar and Jones (2003) reported that pulsed blowing configurations can lead to similar performance gains with 55-60% lower mass flow rates. However in many cases the weight, size, and energy consumption of support equipment necessary to sustain the volumetric flow rate of steady suction or blowing is prohibitive.

Time-dependent actuation approaches that couple to the instabilities of the base flow can offer a substantial reduction in the volume flow rate that is necessary for the actuation, and consequently in the mechanical energy and scale of the actuation hardware needed for implementation. Investigations of time-periodic flow control have been reported since the 1940s beginning with controlled acoustic and mechanical disturbances. Brown (1959) found it possible to influence the frequency of a vortex shedding in the wake of a two-dimensional cylinder by introducing a sound field in the test section. By varying the frequency of the sound field around the natural frequency of the wake, it was possible to control the resulting wake frequency over a range of 0.8-1.2 the natural

frequency. Koopmann (1967) explored the coherent vortex shedding caused by transverse vibration of a spanwise cylinder in a cross-flow. He observed that the vibration induced spanwise coherence of the separation points when driven at the natural shedding frequency above a specific threshold amplitude.

The control of instabilities behind two-dimensional cylinders naturally led to interest in applying the same techniques to improve the performance of streamlined airfoils. External acoustic excitation was shown by Collins and Zelenevitz (1975) to cause partial reattachment of the flow about a stalled airfoil. However the general consensus was that external excitation was impractical. Hsiao et al. (1990) applied internal acoustic forcing (emanating from within the body) to augment the performance of both an airfoil and a spanwise cylinder. Doing so yielded an increase in lift and simultaneous drag reduction over a wide range of angles of attack, and increased the stall angle. They observed that separation control was most effective when the excitation was “locked in” to the frequency of the separating shear layer instability and applied at the separation point. However throughout their experiments the sound pressure level at the slot exit was kept constant regardless of frequency and no mention was made of corresponding velocity fluctuations. In 1991 Williams et al. realized that internal acoustic forcing is primarily dependent on the velocity fluctuation level at the exit of the control slot rather than acoustic effects. Unlike earlier applications of external acoustic forcing which affected the entire flow field, they recognized that internal acoustic forcing was not a pure source of acoustic waves, because of the flow oscillations at the orifice which are considerably higher than fluid oscillations associated with an acoustic wave. They found that even when the sound pressure level of the acoustic disturbances was

small, the velocity fluctuations could be quite large. Contradicting the limited receptivity observed by Hsiao et al., they showed that the pressure distribution over the body was insensitive to frequency over a broad range when the velocity fluctuations were held constant. In a follow-up investigation, Chang et al. (1992) confirmed that at higher forcing levels the performance was relatively insensitive to excitation frequency, but still held that at lower amplitudes peak performance still correlated to locking in with the shear layer instability.

In essence this was the recognition of a new field in flow control, via the momentum injection of oscillatory blowing and suction. It also established an ongoing debate regarding the ideal forcing frequency for such flow control. Within this group two branches have emerged relating to the dimensionless forcing frequency, $St = f_{act}D/U_\infty$. One branch relies on exploiting the instability of the separating shear layer at actuation frequencies on the order of the shear layer shedding frequency, $St \sim O(1)$ (e.g. Seifert et al. 1993, Seifert and Pack 1999). However such an approach requires operation in a narrow frequency band and is accompanied by time-dependent surface pressure and force. The work of Chang et al. showed that forcing at higher amplitudes yielded effective separation control over a much broader frequency band, up to a dimensionless forcing frequency of 20. While not understood at the time, it has since been found that the mechanisms underlying such higher frequency forcing differs from those exploiting shear layer instabilities. Instead the forcing suppresses separation by an "apparent" quasi-steady modification of the flow boundary at actuation frequencies an order of magnitude above the shedding frequency, $St \sim O(10)$, hence inducing aerodynamic forces that are virtually time-invariant (e.g., Smith et al. 1998, Amitay et al. 1999, 2001 and Erk 1997).

Glezer et al. (2003) stated that such an interaction changes the local flow curvature and alters the streamwise pressure gradient, which changes the evolution of the boundary layer resulting in the partial or complete suppression of separation. In fact a comparison performed by Amitay and Glezer in 2002, showed that continuous forcing at $St = 0.95$ resulted in oscillations in circulation that were 55% of the mean, while forcing at $St = 10$ yielded a virtually time-invariant circulation. Such time-invariant virtual aero-shaping has profound implications for enhancing the aerodynamic performance of streamlined and bluff bodies.

The oscillatory suction and blowing utilized in periodic fluidic flow control is typically achieved with a cyclic membrane-driven resonant cavity and orifice system that uses the working fluid of the surrounding flow system, and therefore can transfer linear momentum to the flow system without the injection of additional mass. Such a system is often called a synthetic jet. Upon the ejection portion of every cycle a vortex pair or ring is formed at the orifice edges; downstream a turbulent jet is synthesized from the ensuing train of ejecting vortices entraining surrounding fluid. While having zero net mass flux, the jet has a positive mean velocity and therefore momentum. The properties of these jets are well documented, as by Smith and Glezer in 1998. Such a device is attractive for flow control because it eliminates much of the fluidic passages and mechanical hardware that are needed for conventional steady jets. Synthetic jets can be produced over a broad range of length and time scales, and the interaction of these scales with those of the applied flow must be considered. When applied at frequencies high enough to be decoupled from the natural flow instabilities, their interaction with a cross-flow can displace local streamlines, inducing a virtual change in the surface shape and effecting

flow changes on length scales one to two orders of magnitude larger than the characteristic scales of the jets (Honohan et al, 2000).

While oscillatory blowing and suction has been found to produce noteworthy quasi-steady aerodynamic improvements during continuous actuation, recent work has indicated that pulse-modulation of such actuation can lead to even bigger transient gains in aerodynamic performance such as lift. Such gains may be realized either continuously by repetitive pulsation or intermittently when rapid momentary control is needed, such as in the present work (Amitay and Glezer, 2002). The mechanism for such large transient gains relates directly to the shedding of large-scale vortical structures or “starting vortices” and related oscillations in circulation. Amitay et al. (1998) explored the transient response to reattachment of separated flow over an airfoil via pulse-modulated excitation. They observed the ensuing response of strong oscillations at the natural shedding frequency, and more notably that the oscillations die out much more rapidly following the transient associated with activation of the jets compared to the termination of actuation. The difference was thought to be attributed to “natural” damping in the unforced state via wall shear stress and the shedding vortical structures. Moreover, jet actuation introduces small scale motions in the boundary layer, increasing Reynolds stresses and providing additional damping.

Amitay and Glezer (2002) further studied the role of frequency in modulated forcing, in most cases for a carrier frequency corresponding to $St = 10$. Interestingly, for a duty cycle of 25%, the frequency of modulation greatly impacted the outcome. In their comparisons they used a dimensionless modulation frequency, f_{mod} , similar to Strouhal number. At $f_{mod} = 0.27$, the result was large fluctuations brought on by the transient

starting vortices, but the average effect was effectively zero. However at $f_{mod} = 1.1$, a net positive effect did occur, which was about six times greater than that of continuous actuation, but with oscillations in circulation that were 42% of the mean. Increasing f_{mod} further to 3.3 yielded a quite smooth response in average circulation that was five times greater than that of continuous actuation, at $\frac{1}{4}$ the net momentum coefficient. But by $f_{mod} = 5.0$, the circulation was again only equivalent to continuous actuation, indicating the narrow range of effectiveness. Measurements of continuous actuation at $St = 3.3$ showed similar performance to continuous actuation at $St = 10$ for the amplitude tested, confirming that the increase in performance was attributed to the modulation of the higher carrier frequency.

2.2 Separation Control over Bluff Bodies

While the objective of the present work is to generate asymmetric steering forces and moments, the majority of separation flow control on bluff bodies has been for drag reduction. The effectiveness of approaches to reduce drag is relevant as many of these methods can also be applied in an asymmetric manner and perhaps yield side forces. For axisymmetric bodies and bluff bodies in general, the pressure drag typically dominates the viscous drag because of the large wakes associated with these bodies. As such, the objective of drag reduction is base flow modification to increase the base pressure. This has predominantly been explored via either geometrical modifications or steady pneumatic sources and sinks (usually jets or suction ports).

Passive geometrical alterations have been studied at both the nose and tail segments of axisymmetric bluff bodies. Howard and Goodman (1985) explored axially

tapered tail extensions, examining the impact of the tail corner radius as well as the advantages of circumferential and longitudinal (streamwise) groove arrangements. They observed drag reductions of 30-70% with these passive geometrical techniques. Interestingly, they found the mechanism of drag reduction for circumferential grooves was the division of one large separated flow region into several smaller ones, while longitudinal grooves exhibited attached flow that influenced neighboring separated regions. Shoulder radiusing was superior to either grooving approach at higher free stream velocities, and was attributed to a local reduction of the adverse pressure gradient. Koenig and Roshko (1985) employed a stationary control disc upstream of the nose of a blunt cylindrical body. Four regimes were identified; the lowest drag occurred when the disc diameter and distance ahead of the body (gap) allowed the separating streamline from the disc to attach to the shoulder of the body. Other regimes of higher drag were found when the disc was too small or the gap was either too large or too small. In the best cases forebody drag was almost entirely eliminated, typically when the disc diameter was $\frac{3}{4}$ of the body diameter, in conjunction with an optimal gap (about $\frac{3}{8}$ of the body diameter). In this regime the disc effectively created an 'apparent' streamlined nose for the body, with far less drag than the original blunt face. Weickgenannt and Monkewitz (2000) investigated the utility of aft mounted control discs extended short distances behind blunt bases. They observed four vortex-shedding regimes related to gap width: 1) no effect when the control disc was located very near the base, 2) a region of sharp increase in vortex shedding and drag when the disc separation (gap) was increased, leading to 3) an interval of reduced shedding and drag (about 20%) as the spacing was increased further, and 4) a region where the bodies displayed independent but additive

effects when the gap was very large. The mechanism of drag reduction was observed to be the “choking” of reverse flow from the wake into the gap cavity, which reduced the cavity pressure and extent of the wake.

Induced Coanda attachment for control of the aerodynamic drag on axisymmetric bodies has been investigated via *steady*, circumferentially-uniform blowing over rounded Coanda surfaces. Freund and Mungal (1994) demonstrated that this approach can produce substantial reductions in base drag. They found that an arrangement with two cascading axisymmetric slots utilizing the same source was superior to a single slot. With sufficiently high blowing ratios (jet velocities of 2-3 times the free stream velocity) the combination of thrust and drag reduction can produce a self-propelled state, and (as expected) higher ratios can produce net thrust. At velocity ratios on the order of one, the drag reduction observed was on the order of 15%. Measurements of base pressure distribution clearly attributed this to an increase in base pressure via Coanda entrainment. Drag benefit (the reduction in drag beyond the applied thrust) of up to 30% was observed.

The Coanda effect has also been applied within the wakes of more general bluff bodies for drag reduction, recently popular in improving the efficiency of motor vehicles. While an aft-facing jet produces thrust it can also contribute to drag reduction. The key figure of merit is the ratio between the change in drag coefficient ΔC_D , and the thrust coefficient of the jet, C_μ . Englar (2001) applied steady planar Coanda jets to the rear perimeter of commercial tractor trailers and realized significant drag reduction, with a most efficient drop of 10% at $\Delta C_D/C_\mu = -6$, equivalently a 600% recovery (amplification) of the applied thrust. More typical values of interest included 44% drag reduction at $\Delta C_D/C_\mu = -1.7$. A higher, “inefficient” blowing rate ($\Delta C_D/C_\mu = -0.55$) resulted in 78%

drag reduction, achieving a drag coefficient of 0.13, one-half that of modern sports cars. Similar work by Geropp and Odenthal (2000) on a two-dimensional automobile shape also showed the ability of steady blowing via the Coanda effect to increase base pressure by 50% and reduce drag by 10% on a more streamlined bluff body, but at an inefficient $\Delta C_D/C_{\mu} = -0.3$ (jet thrust greater than the reduction in drag).

The wake behind a bluff body is defined by a separated shear flow, not unlike that of a backward-facing step. In essence, the present work focuses on controlled activation of a Coanda effect by reattaching a separated shear layer using actuation at the point of separation from the lip of a backward facing step (at the tail of an axisymmetric bluff body). Part of the present investigation focuses on an isolated planar configuration embedded into a backward-facing step. Often attractive to researchers for its well-known and well-behaved baseline flow, the key figure in many studies of backward-facing step flows is the reattachment length, which scales directly with step height and is found to occur between five and eight step heights downstream of the step depending on the experimental configuration (Eaton and Johnston, 1981). Prior investigations of periodic forcing on the separated flow downstream from a rearward facing step (e.g. Riesenthal et al., 1985, Roos and Kegelman, 1986) have demonstrated that the flow can be significantly modified using excitation that is applied either upstream or at the base of the step with a flap-like actuator. Roos and Kegelman indicated that such excitation induces coherence and produces intensified turbulence activity. While not affecting the mean velocity profiles, the induced mixing and entrainment reduced reattachment lengths. Chun and Sung (1996) explored the impact of a sinusoidally oscillating jet emanating

from exactly the top corner of a backward step [$St_H \sim O(1)$], achieving reductions in reattachment length of up to 40% and other effects similar to Roos and Kegelmann.

Sigurdson (1995) explored related work on the reattachment of separated shear flows, but over the surface of an axisymmetric blunt body downstream from its sharp leading edge. The actuation was applied through an axisymmetric slot at the leading edge from an internal speaker-driven chamber. Notable results occurred at frequencies lower than the initial Kelvin-Helmholtz frequencies of the separating shear layer, but higher than the downstream shedding frequency. Essentially it seemed that forcing at a frequency which generated vortices spaced apart by a wavelength comparable to the separation bubble height caused the most modification to the flow. Features such as the separation bubble height, reattachment length, and pressure at separation were all reduced by up to 50%, while entrainment near the leading edge was increased. A reduction in pressure drag of up to 15% was attributed to the increased entrainment which occurred near the point of separation. It was hypothesized that the greatest drag reduction results from forcing at frequencies amplified by both the Kelvin-Helmholtz (shear layer) and shedding (wake-type recirculation) instabilities. Although this work yielded noteworthy insights, by relying on instabilities in the flow to amplify the forcing this approach has limited frequency receptivity and the ensuing structures may be undesirable.

Unlike these prior examples that exploited instabilities in the shear layer, Vukasinovic et al. (2004) explored high frequency actuation an order of magnitude higher than the natural formation frequency of the shear layer. The actuation had profound effects on the evolution of both large- and small-scale motions within the shear layer by inducing an increase in small-scale dissipation and concomitant suppression of

turbulence production. Actuation led to a significant reduction in the formation of large scale structures, due to the associated transfer of kinetic energy from the large scales to the small scales, yielding a finely mixed, broad wake region rather than a discrete shear layer. Vukasinovic and Glezer (2006) explored transitory fluidic control of a turbulent shear flow and discovered unique advantages in modulation of a higher carrier frequency. The intermittent pulse train induced the shedding of a large-scale vortical structure which promoted entrainment, but also yielded a train of small high-frequency vortices that promoted direct small-scale mixing. The combination of these two effects can potentially lead to superior mixing compared continuous forcing at either the high or low frequency.

2.3 Mergence

It is evident from the discussions of periodic separation flow control and manipulation of separated shear flows that asymmetric manipulation of the separated flow at the base of the axisymmetric bluff body in the present investigation can be used to generate desired steering forces and moments. The integration of the synthetic jet actuator into the wind tunnel model suggests that such a device can be applied to a projectile in flight particularly because it operates on millisecond time scales. For the specific application of the present work, the transient response to the onset of such actuation is critical. However, the implementation of the fluidic actuator is very important to effecting a substantial change in flow separation, and it appears to be best leveraged along with the Coanda effect. Because the Coanda effect can attach an inherently separated flow to an adjacent solid surface, exploiting this phenomenon for

flow control presents a unique opportunity to induce aerodynamic side forces that result from flow turning.

In the present work, flow separation is effected around the periphery of the body just upstream of its aft end by a small rearward-facing step upstream of an azimuthal Coanda surface at the base. The step height is selected such that the base flow does not inherently reattach to the Coanda surface. The separated base flow is attached to azimuthal segments of the aft Coanda surface using individually-controlled synthetic jets having finite azimuthal extent. The turning of the outer flow into the wake region is accompanied by net lateral aerodynamic reaction forces and pitching moments. With a view toward eventual application of this technique to generate net transient steering forces on bodies of revolution, the present investigation explores the effects of Coanda radius and jet strength on the level of the reaction force normal to the free stream (lift), with specific emphasis on the transient response of the flow to momentary activation of the synthetic jet. This transient flow response produces significant transient forces from brief actuation. Using highly resolved particle imaging velocimetry (PIV) the study also explores intricate details of the spatio-temporal interactions of jet vortices with the separating shear layer at the lip of the backward facing step.

CHAPTER 3

EXPERIMENTAL FACILITIES AND TECHNIQUES

3.1 Model Development

The present work was part of a larger team effort to show the feasibility of using MAFC to generate and control aerodynamic forces and moments on a projectile in flight sufficient to generate significant lateral changes in trajectory. The purpose of the present work was to demonstrate a method to increase the precision and accuracy of a projectile. In particular, it was an attempt to show that controlled transient lateral forces could be generated by MAFC in flight. Based on the physical properties of the projectile, an estimate of the force needed to move the projectile laterally a given distance can be derived from basic physics:

$$\Delta y = \frac{1}{2} a_y t^2 = \frac{1}{2} \frac{F_y}{m} \left(\frac{x_R}{U_\infty} \right)^2 \Rightarrow F_y = 2m\Delta y \left(\frac{U_\infty}{x_R} \right)^2$$

For a typical projectile application, the desired lateral force was estimated to be approximately 0.098 N. However, to induce this lateral steering force using flow control methods requires the generation of an asymmetric flow. And so the technology used in this effort was applied over an azimuthal segment of the circumference as will be discussed later. This was made more complex by the spin stabilization of the projectile, which restricted the opportunities available to apply this lateral force to approximately

one quadrant of the rotation. Therefore to achieve the same lateral shift over the range requires quadruple the force since it is applied only 25% of the time, or 0.392 N. A primary goal of the present work was to use robust, non-intrusive flow control approaches to generate this force over a time scale of approximately 5 msec (based on a 60 Hz spin period).

Various geometrical features of the projectile are worth reviewing in consideration of flow control opportunities. The “bullet” nose of the projectile, as expected is tapered and rounded, implying a stable and streamlined flow at the front of the body. A pair of raised rings are placed along the straight length of the body (axial position varies by model), which are spaced about 10 mm apart, each 1 mm wide, and protrude above the surface about 1 mm. Known as the rotating band, the rings are the only part of the projectile that matches the rifle barrel diameter. As a mandatory feature either on the body or the complementary sabot (which separates from the body upon flight), their function is to seal the propellant gases and grip the rifling to generate projectile spin during firing. These rings certainly trip the boundary layer and cause local flow separation. While these separated flow regions present a possible opportunity for flow control, they may also present a hindrance if they are upstream of the control zone. It should be noted that these rings can be located on the sabot and hence not affect the body in flight. Perhaps the most significant feature from the standpoint of flow control is the squared tail, which provides a clear boundary for separation of flow, and the ensuing large bluff body wake behind the body.

In establishing a wind tunnel test model, facility limitations required rescaling from the original application size. While a typical application speed may be 70 m/s, the

wind tunnel maximum speed is 40 m/s. Hence to retain a self similar flow, a double scale model was utilized with test speeds of up to 35 m/s to match the application Reynolds number of 183,000 ($Re_D = \rho U_\infty D / \mu$). While much of the original geometry was retained, slight changes were made as the project progressed, to enhance flow control effectiveness.

The axisymmetric wind tunnel model (Figure 1) was constructed of modular components that were produced using stereo-lithography. The overall body was 80 mm in diameter (D), 150 mm long (L). The mid-section and nose were hollow and coupled to the tail assembly by a central shaft. This modular design offered the flexibility to exchange sections of the model, which simplified parametric studies, and more importantly initially allowed for a quick exploration of different flow control approaches.

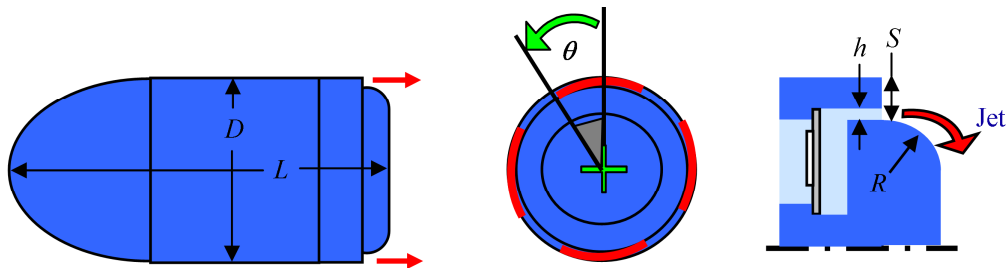


Figure 1. Axisymmetric body shape. Arrows indicate locations of synthetic jets.

In the majority of work presented, the tail assembly contained four independent, piezoelectric actuators, each with an azimuthally segmented rearward-facing orifice 0.45 mm in height (h) and 25 mm in arc length corresponding to a 38° azimuthal span ($\theta = \pm 19^\circ$). These orifices were embedded in the base of a small axisymmetric

backward-facing step. Each jet emanates rearward over an axisymmetric rounded tail extension whose surface begins tangent to the inner orifice edges and turns through ninety degrees with constant radius. The synthetic jets interact with the separating shear layer and cause, in effect, the shear layer to adhere to and follow the curved Coanda surface, quasi-steadily on the time scale of the jet (the exact spatio-temporal details are complex). In most of the present experiments, the radius of the aft tail extension (R) was 12.7 mm and the adjoining backward facing step to the circumference of the body was 1.5 mm high (S). The models depart from this configuration only for a parametric study of a particular geometric feature. The step height is shallow enough to enable local flow attachment when the control jet is activated, but high enough to prevent attachment in the absence of the jet.

In designing the flow control actuator, the spinning of the projectile was important. As noted above, periodic excitation for flow control needed to occur on a time scale that is at most a quarter of the body revolution period, or about 4 msec which on the double scale model is 16 msec. Prior work has shown that the transient response to actuation generally follows the convective time scale of the flow over the body, L/U_∞ , which for the projectile is 1.1 msec compared to 4.3 msec for the model. However another important time scale is the nominal period of the separating shear layer instabilities. Prior work discussed in the literature review has shown that to minimize oscillations in force induced by actuation, the forcing frequency should be about 3.3 times greater than the shedding frequency. Based on the Strouhal number, $St = fD/U_\infty = 0.16$, established by Roshko (1954), the shedding frequency of the model is about 70 Hz while that for the projectile is 280 Hz. In consideration of all three time scales it is

evident that the actuation frequency for the projectile should be at least 933 Hz versus 233 Hz for the model. A synthetic jet actuator was developed prior to this work with an effective performance at a driving frequency of 1 kHz, which is high enough for both the model and the projectile.

3.2 Actuator Calibration

The actuator jet was characterized in an isolated calibration chamber (free of ambient effects such as drafts, etc). The chamber houses a three-stage motor-driven traverse with various options to mount actuators to the traverse and is equipped with standard measurement equipment such as a pitot-static probe connected to a 10 torr static pressure transducer, an RTD temperature sensor, a miniature hot wire sensor (5 μm x 1 mm wire), and a constant-temperature anemometer.

The hot wire sensor is calibrated in an external calibration jet which uses compressed air and is controlled by a combination of a voltage-based pressure regulator and a needle valve. The velocity range was typically 1 to 45 m/s. The calibrator is also equipped with a circulation heater and controller to introduce temperature gradients for the determination of temperature compensation coefficients for local linearized corrections of changes in ambient temperature during later measurements. The calibrated sensor is placed at the center of the jet orifice at the exit plane and its output is sampled phase-locked to the actuation input at a rate that is nominally 50 times higher than the actuator driving frequency.

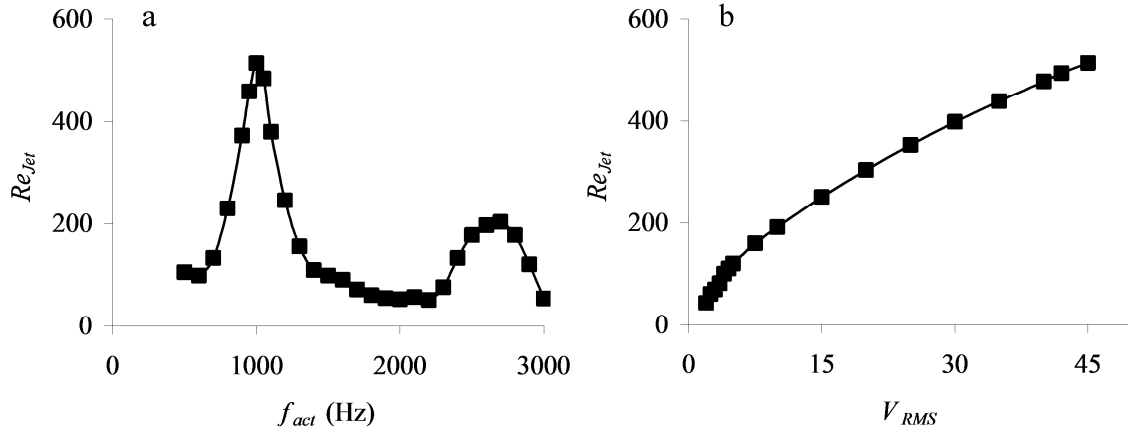


Figure 2. Actuator performance: (a) frequency response at 45 V_{RMS} and, (b) response to input voltage at $f_{act} = 1000$ Hz.

The performance of the actuator is shown in Figure 2. The jet velocity at the center of the orifice was measured over a broad range of driving signal frequencies and amplitudes using a single miniature hot wire sensor. The average output velocity over the blowing cycle U_{Jet} is normalized by the entire period T_{Jet} and the jet Reynolds number is defined as $Re_{Jet} = \rho U_{Jet} h / \mu$, where h is the orifice height (0.45 mm). It is clearly evident in Figure 2a that the primary actuator resonance occurs at 1 kHz (i.e., the resonant frequency of the diaphragm/cavity combination). A secondary resonance occurs at about 2.7 kHz. In all of the present experiments, the actuators were driven at the primary resonance of 1 kHz. Figure 2b shows the actuator response to input voltage at its primary resonant frequency. A maximum average output velocity of $U_{Jet} = 17.5$ m/s (as normalized by the entire period) equivalent to $Re_{Jet} = 500$, was measured at 45 volts rms input voltage where the peak velocity is about 55 m/s. The actuator performance is limited by the maximum voltage and displacement of the piezoelectric driver.

3.3 Wind Tunnels

Over the course of this work, three wind tunnels were utilized. Initial force measurements, and later development of the 40 mm flight test model, were conducted at the GTRI-ATAS Model Test Facility. This is a closed-return, atmospheric, low-speed wind tunnel having a maximum free stream speed of $U_\infty = 65$ m/s, with a 0.76 m tall x 1.1 m wide rectangular test section 2.3 m in length. The facility is equipped with a dual strain-gage based force balance sting developed in-house for the preliminary measurement of forces acting on the 80 mm model. The 40 mm flight test model was tested using a 12 mm diameter x 0.3 m sting mounted to a rear strut, with an integrated Kistler 9017A dynamic force sensor.

The majority of force measurement experiments, and all PIV measurements of the axisymmetric model, were conducted in the Georgia Tech FMRL low-speed open-return atmospheric wind tunnel, which has a 0.9 m square test section 3 m in length, with a contraction ratio of 9:1, capable of free stream speeds up to $U_\infty = 40$ m/s. Further details of this facility are described in the thesis by Honohan (2003). The model was supported at the center of the wind tunnel test section by a 25 mm diameter x 0.3 m sting that extended upstream from a lateral plate behind the body. The sting was integrated with a Kistler 9017A dynamic piezoelectric load cell having a range of +/- 1 kN, a sensitivity of 11 pC/N, and a frequency response of 60 kHz. The overall arrangement is shown schematically in Figure 3. The sensor output was connected to the PC-based data acquisition system through a Kistler 5010B charge amplifier, which had a resolution of 0.01 pC or about 1 mN for the sensor utilized. The force measurement system was calibrated with static weights and adjusted via the amplifier gain. The flow field near the

aft section of the model was measured in various meridional planes (through the centerline) using a TSI particle image velocimetry (PIV) system with a New Wave Research 120 mJ dual-head YAG laser. Particle seeding in the plane of view was accomplished by the injection of theatrical fog through a slotted airfoil that was placed in the tunnel plenum upstream of the test section contraction.

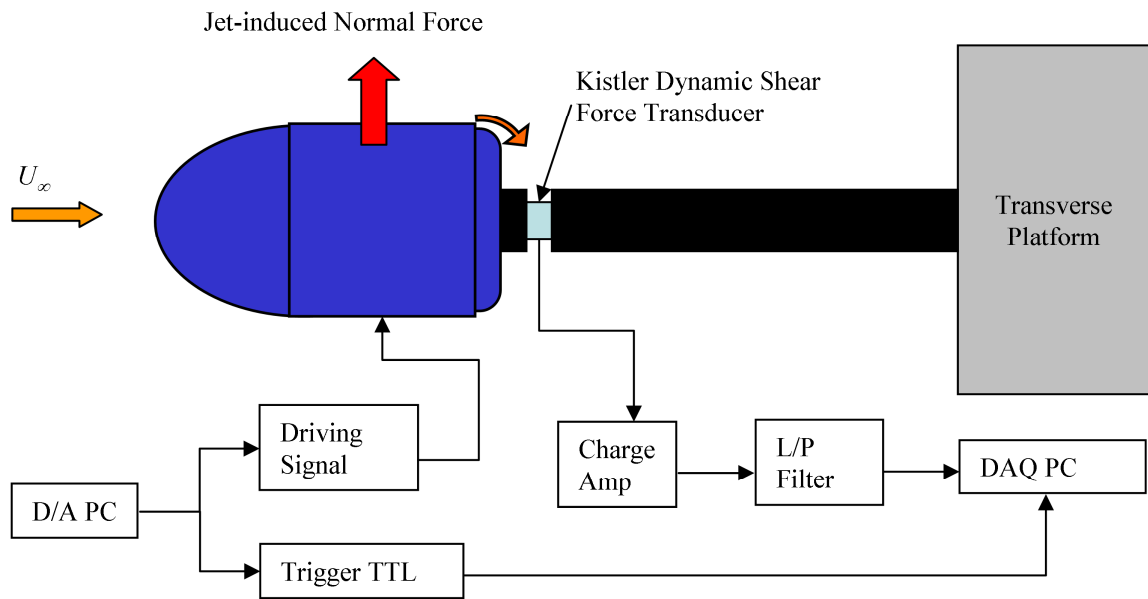


Figure 3. Dynamic force measurement experimental configuration.

For closer visual access and isolation of the tail region, later in-depth work was performed in a smaller low-speed closed return atmospheric wind tunnel, with a rectangular test section 0.25 m wide x 0.40 m high x 1.4 m in length and a contraction ratio of 9.25:1, with a maximum free stream speed of $U_\infty = 34$ m/s. The complete facility is shown in Figure 4. Although closed return, the pressure in the test section was within one torr of atmospheric pressure. The actuator for this facility was identical to those in

the axisymmetric models, but in a planar base that spanned the entire width of the tunnel (0.25 m). Further details of this configuration are discussed in Chapter 5. The temperature of the tunnel was maintained at room temperature (72° F) using a chilled water system through a 1 m square 2-row 24 tube copper heat exchanger in the flow ahead of the contraction with a three-way bypass valve controlled by a stand-alone PI temperature controller referencing the test section temperature. The tunnel was equipped with standard measurement equipment such as a pitot-static probe, a 48 port pressure switching valve system, an RTD temperature sensor, and a PC-based data acquisition system. The flow field near the aft section of the model was measured in a number of cross stream planes using a LaVision particle image velocimetry (PIV) system with a New Wave Research 50 mJ dual head YAG laser. Particle seeding in the plane of view was accomplished by the injection of theatrical fog into the return side of the blower.

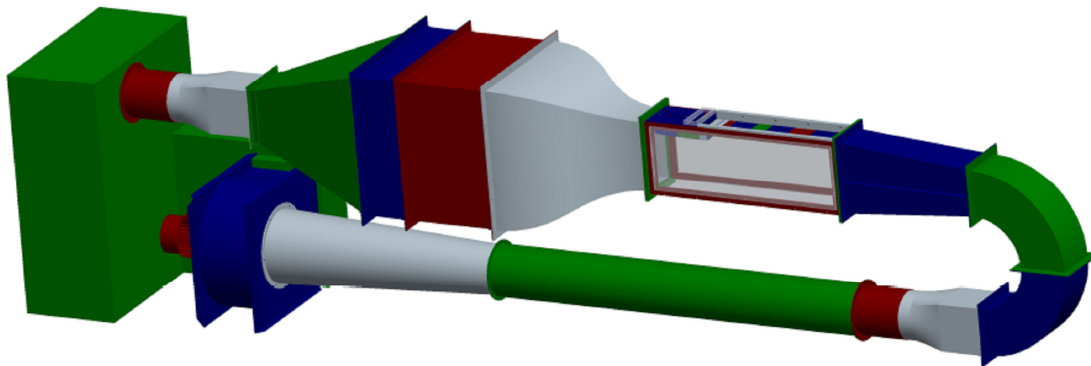


Figure 4. Small closed-return wind tunnel.

3.4 PIV Acquisition and Analysis

Particle Image Velocimetry (PIV) measurements were obtained via dedicated commercial software, using traditional two-frame FFT cross-correlation techniques (Raffel, Willert, and Kompenhans, 1998), with a Gaussian peak fit algorithm which yields sub-pixel velocity resolution. PIV images were captured using a 1008x1018 pixel Kodak MegaPlus ES 1.0, 30 Hz 8-bit CCD camera which has a high-speed electronic shutter capable of capturing image pairs within time increments as small as 600 ns under computer controlled synchronization with a dual head laser for sheet illumination at the specified interval. A typical PIV experimental configuration is shown in Figure 5. Because PIV involves the collection and analysis of many realizations, the majority of the data processing was done on an array of networked computers dedicated exclusively for this purpose.

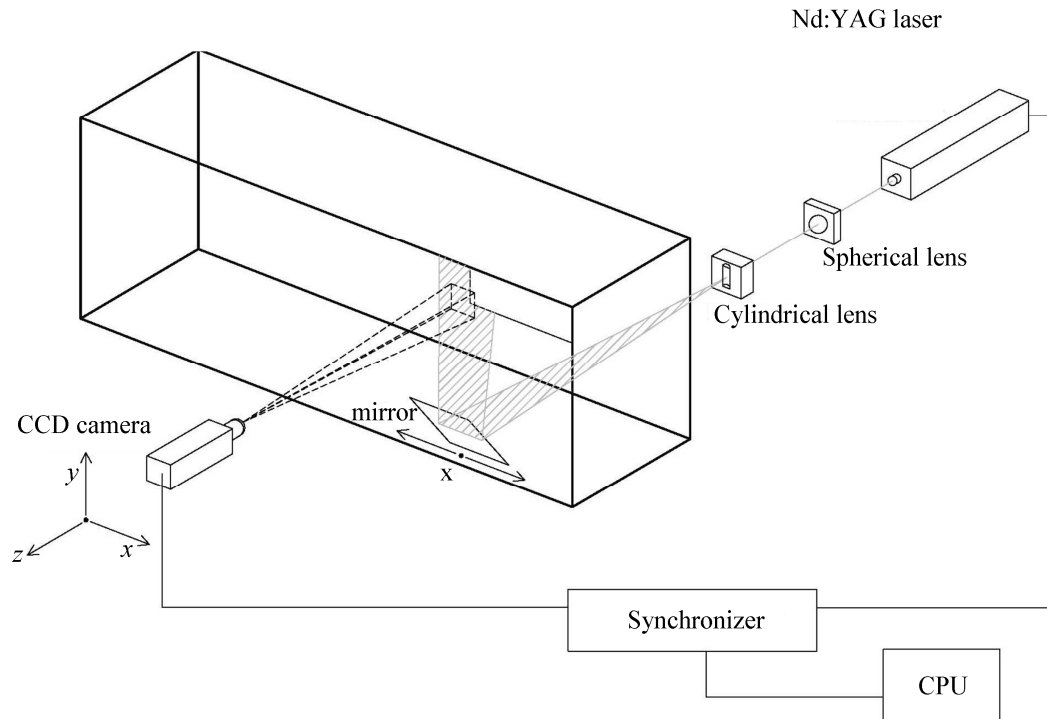


Figure 5. Typical PIV experimental configuration.

All data were collected with a traditional single orthogonal camera arrangement, limited to in-plane measurements which yield two velocity components assuming negligible time-averaged out of plane motion. The time delay between successive image pairs is typically a few microseconds. The PIV measurements are typically phase-locked to the actuator waveform and a given data set consists of a few hundred image pairs. The data is typically retained in this phase-incremented set format throughout processing, so that phase variations in properties can be observed. Before any processing occurs, background noise is first removed by subtracting the minimum set intensity of each pixel from all instances in a given set. This most significantly eliminates the influence of reflections and inactive pixels of non-zero intensity.

The surface of the body is defined from a silhouette in a reference image. Often this is done by applying a pixel intensity threshold as the surface is indicated by a line of laser light reflection. This threshold typically does not yield a single line but rather a band of pixels. This band is averaged and offset to yield a line that corresponds to the actual surface to within a few pixels. The potential inaccuracy is not very significant for two reasons; the minimum intensity subtraction removes any surface reflection that is not covered by the mask, and any valid data lost to the mask is negligible relative to the expected spatial resolution of the data, which is usually a dozen pixels or more. After being applied to the image, this mask is retained for later use after vector calculation to again be applied to the vector map.

As mentioned earlier, PIV is performed via a two-frame FFT cross-correlation technique which yields sub-pixel displacement resolution, down to 0.1 pixel displacements. The velocity vectors are validated using two algorithms. First, a maximum displacement or equivalent velocity magnitude is applied that corresponds to the maximum expected displacement of at most 1/3 of an interrogation region. Second, assuming adequate spatial resolution, a given velocity vector is related to its neighbors using a median filter based on eight neighboring vectors. The vector is validated only if it deviates from the neighbor median within a specified multiple of the RMS deviation of the neighbors, which is determined from a distribution of the RMS deviation for an over-sampled phase-averaged data set.

A custom PIV software package based in Matlab was used for higher level processing. Averaged velocity components, Reynolds stresses, and vorticity are obtained from this software for the entire field, for each phase or data set. Vorticity is computed

from the averaged data set, not individual realizations. While vorticity can be calculated via spatial differentiation in both directions, it can also be computed by localized circulation on the data grid as described by Raffel, Willert, and Kompenhans (1998). Both methods were utilized in the analysis of the data being presented, and are considered equivalent.

CHAPTER 4

FLOW CONTROL ON A BODY OF REVOLUTION

Wind-tunnel investigations were conducted to determine the aerodynamic forces induced by fluidic actuation on an axisymmetric projectile model. The effect of the actuation was assessed from direct force measurements and flow measurement using PIV. Dynamic measurements of activation, deactivation, and pulsed transient responses were explored using time-resolved force measurements and phase-locked PIV. The transient response is of interest, as previously discussed, because the rotation rate of the flight test model requires that the aerodynamic forces and moments, and hence the flow-turning process, must respond to actuation within a fraction of the revolution period (16.7 msec). Phase-locked PIV measurements were taken in radial planes on and off the centerline of the orifice to investigate the three-dimensionality of the flow turning. Conventional jets were also explored as an alternative means of generating forces for higher speed applications, and to compare with the synthetic jets.

4.1 Early Attempts with Cross-Flow Jets

An initial flow control approach was based on the earlier work of Sigurdson (1995) and Amitay et al (1999) and focused on controlled flow attachment near the leading edge of the model. The work of Sigurdson on blunt axisymmetric body drag reduction showed that leading edge separation could be reduced by actuation. Amitay et al found that on an airfoil at high angle of attack, synthetic jet cross-flows in a separated

region could be used to close the separation, drastically alter the flow, and thereby increase lift substantially.

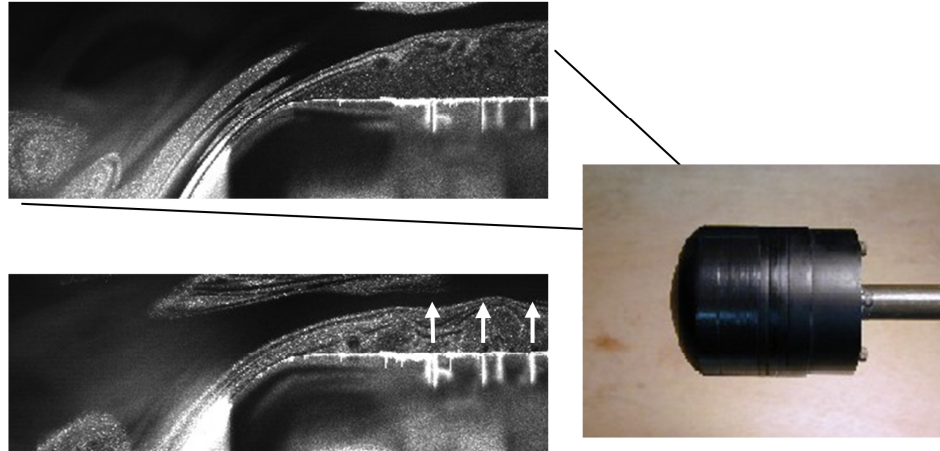


Figure 6. Smoke visualization of stacked cross-flow configuration with blunt nose, jets active in lower picture ($Re_D = 105,000$, $Re_{Jet} = 368$).

As noted in Chapter 3, typical projectiles have a pair of raised rings near the tail of the body that grip the barrel rifling and seal the propelling gases behind the projectile during launch. For the purpose of flow control, the rings were moved to the front end of the model with the idea that flow will locally separate around these rings in flight, and be controlled by a streamwise array of radially-blowing, azimuthally-slotted synthetic jets that are placed downstream of these rings. Asymmetric side forces would be produced by asymmetric actuation. Rings of varying height were explored, as were various nose shapes to alter the degree of separation. With a blunt nose in place, smoke visualization did indicate a 50% reduction in the height of the separation (as shown in Figure 6), similar to the results of Sigurdson. However, the changes in the side forces were small.

Even with the blunt nose, and with an array of four actuators operating in series, the peak force generated was less than 0.1 N, and varied significantly with angle of attack, as shown in Figure 7. Besides the complexity of the actuation, it was suggested by Army ballisticians that the blunt nose was not acceptable because of the increased drag and potential dynamic instability in flight.

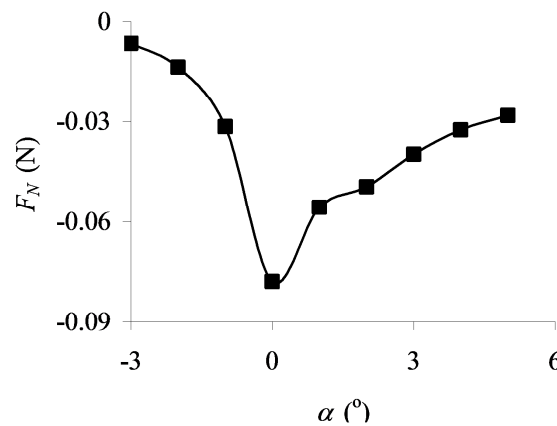


Figure 7. Normal force developed by activation of stacked cross-flow jet configuration versus angle of attack with a blunt nose ($Re_D = 188,000$, $Re_{Jet} = 368$).

Since the original body is streamlined and is not subjected to appreciable changes in angle of attack (4 degrees or less), it was believed that the degree of separation near the nose was not sufficient to cause a substantial change in the symmetry of the flow around the body and consequently in the aerodynamic forces. This reasoning led to actuation at the tail of the body, where the flow is inherently separated. As discussed in the literature review, flow control near the tail (e.g. circulation control and drag reduction such as the Coanda-based work of Englar, 2001, and Freund and Mungal, 1994) has demonstrated that the base flow can be substantially altered. Additionally, the work of Smith and

Glezer (1997) has shown that a free shear flow can be substantially vectored by an adjacent collinear synthetic jet, and suggests a similar effect may occur on the separated flow at the base of a bluff body.

The second approach was to implement an azimuthally-segmented synthetic jet issuing rearward from the back face of a step behind the main body, flowing tangentially over a Coanda tail surface. The step fixes the location of flow separation, and when one jet actuator is activated, the flow is asymmetric and results in a side force. This approach turned out to be very successful and was the basis for the bulk of the present work.

4.2 Parametric Effects on Aerodynamic Force

The effectiveness of the synthetic jet in attaching and turning the flow over the Coanda surface is illustrated in Figure 8 (the body diameter (D) is 80 mm and the radius of the Coanda surface (R) is 12.7 mm) for $Re_D = 131,000$. Figure 8a shows a silhouette of the Coanda tail region of the wind tunnel model and the direction of the normal force acting on the body when the top (in this view) control jet is activated. The jet is issuing as indicated from the upper rear behind a small step at which the Coanda tail radius begins.

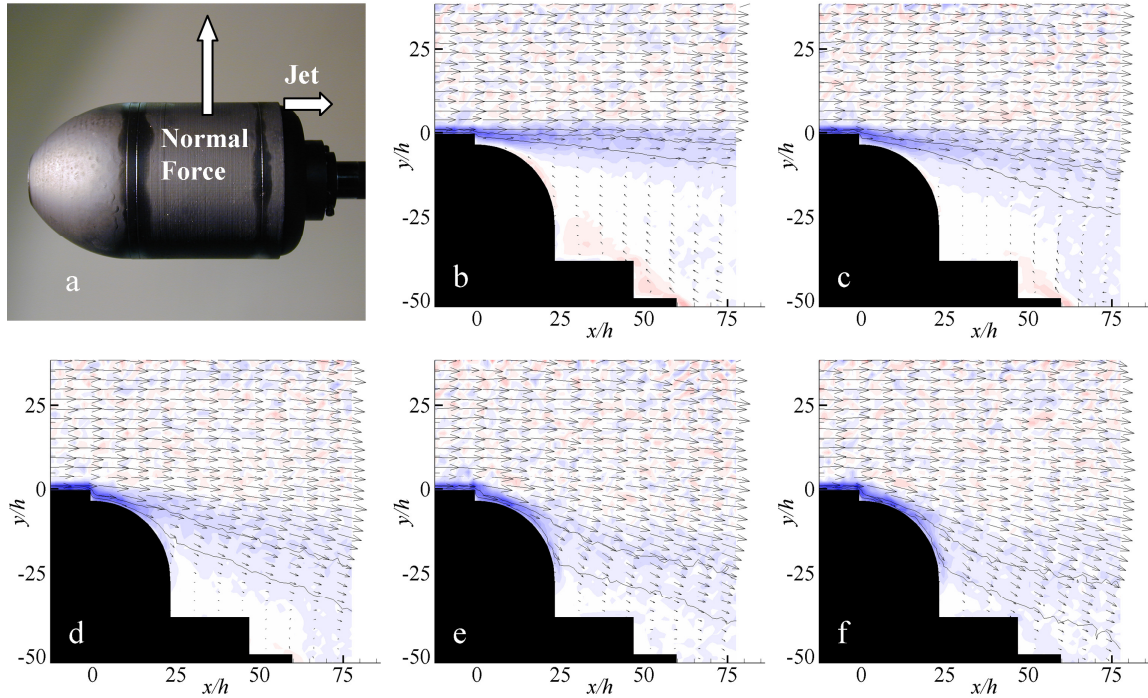



Figure 8. PIV images showing degree of flow turning with increasing jet strength, $Re_D = 131,000$: (a) model image, (b) $Re_{Jet} = 0$, (c) 146, (d) 291, (e) 437, (f) 510. Vorticity scale: $-20,000$  $20,000$ 1/s. $y/h > 25$: Vector lengths indicate 25 m/s.

Figure 8b-f presents time-averaged velocity vector fields obtained from PIV measurements (the field of view measures 50 mm on each side). These data were obtained over a range of jet speeds that correspond to control jet Reynolds numbers $Re_{Jet} = 0, 146, 291, 437,$ and 510 (the jet speed is varied by changing the actuation voltage to the piezoelectric diaphragm). Spanwise vorticity concentrations within the surface boundary layer upstream from separation and within the separated shear layer are depicted via shaded raster plots superposed on the vector plots. Additionally, contour lines of velocity magnitude are shown at 0.2 and $0.5 U_\infty$ to further illustrate the direction and spreading of the flow behind the body. In the absence of actuation (Figure 8b), the flow over the Coanda surface is completely separated. As a result of the interaction

between the actuation jet and the cross flow, a low-pressure region forms near the jet actuator (as confirmed by Honohan, 2003), the free stream begins to turn around the surface, and the separation line moves farther downstream. The degree of turning increases with jet momentum flux, with the flow near the surface turns through the full ninety degree extent of the Coanda radius at higher jet strengths. The velocity magnitude contour lines show that initially at $Re_{Jet} = 146$ the flow vectors but does not attach to the Coanda surface. With increasing jet strength the flow attaches to the surface and then follows the radius to an increasing extent. As this occurs more of the upstream flow is brought downward into the area behind the body, effectively eliminating the wake by $Re_{Jet} = 510$.

Since the actuator orifice has a finite azimuthal extent, and is adjacent to inactive regions, it is expected that the effect of the actuation is not azimuthally uniform. To explore the extent of the actuator's interaction with neighboring flow regions, small streamwise bounding fences were placed along the azimuthal orifice edges to extend the low pressure domain induced along the jet's orifice. The results in Figure 9a and b show significant increase in force at jet strengths and higher free-stream speeds when the fences are present. In the original unbounded configuration, the variation of force with jet strength (Figure 9a) is quite linear for $Re_{Jet} > 50$, however the data suggest the sensitivity of the induced normal force to jet strength for $Re_{Jet} < 50$ is nominally about three times larger. This higher sensitivity at low voltages appears to be associated with the flow attaching behind the step, which is the mechanism that initiates vectoring of the separated shear flow. While there is great sensitivity to this mechanism, the relationship between jet strength and induced force suggests that this mechanism is not abrupt but

rather occurs progressively with increasing jet strength. It is thought that during this progression the separated shear flow is increasingly entrained by the jet and that this effect is maximized once the jet is strong enough to bring the flow down to the surface behind the jet orifice. Once this occurs, the remaining force generation is attributed to the degree of flow turning as the flow along the surface increasingly follows the Coanda radius with increasing jet strength, as previously illustrated in Figure 8. The addition of fences creates a very different, gradual effect which increases in sensitivity with jet strength, and results in a greater induced force for $Re_{Jet} > 350$. This indicates that edge effects are significantly suppressed and that the jet speed is more uniform along the orifice span.

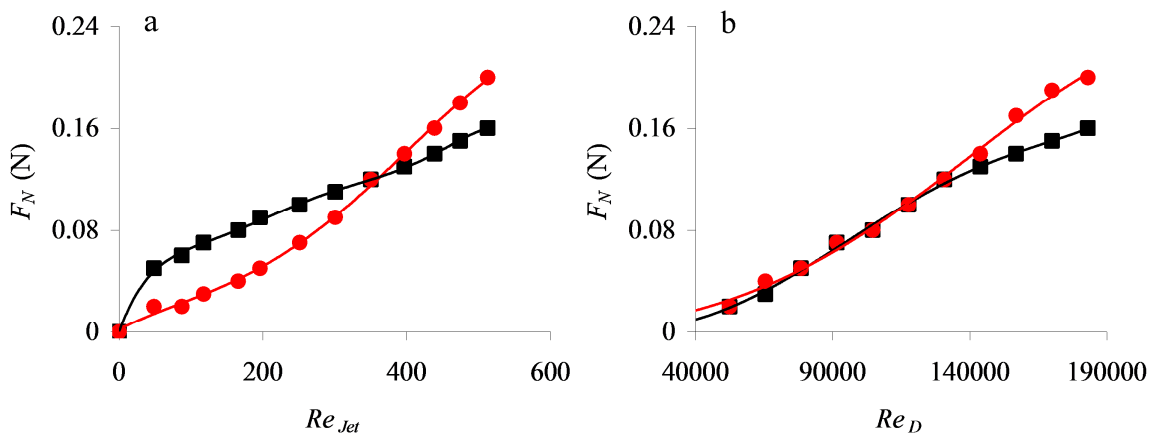


Figure 9. Normal force developed for free and constrained jets. (a) Force vs. jet strength, ($Re_D = 183,000$), and (b) Force vs. free stream speed, ($Re_{Jet} = 510$).

■ Free jet, ● Constrained

The variation of force with free stream speed at fixed jet strength (Figure 9b) indicates a well-behaved, almost linear relationship even in the unbounded configuration.

Prior work by Smith and Glezer (1997) on the vectoring of a free shear flow with an adjacent collinear synthetic jet confirmed that for a given jet strength the local surface pressure decreases almost linearly with increasing free stream speed, which supports the observed relationship. At higher speeds the fences extend performance and linearize the relationship to free stream speed.

The explanation of the differences brought on by the fences is thought to be two-fold. The increase in performance at higher strengths and speeds is surely due to an increased azimuthal uniformity in flow turning. However the drop in performance at lower strengths is somewhat puzzling. It is conjectured that in the absence of the fences, the jet has a narrower spanwise extent and may give rise to a streamwise counter-rotating vortex pair that enables stronger flow attachment downstream of the jet orifice. This effect probably saturates at higher jet speeds. The effect of the geometry near the jet orifice edges is explored further in a later section.

A parametric study was conducted to determine the effect of the Coanda radius R on the force levels generated by actuation. Configurations tested were a sharp corner (defined as $R/h = 0$), and $R/h = 7.1, 14.1, 21.2, 35.3, 42.3, 49.4$. Figure 10a and b show the variation of the (dimensional) force with Re_D (for $Re_{Jet} = 480$, where the minimum Re_D tested is 52,000), and with Re_{Jet} (for $Re_D = 183,000$), respectively for each of the Coanda radii. It is remarkable that some degree of flow turning and an aerodynamic force are achieved even in the absence of a Coanda surface, suggesting that the basic mechanism, namely the creation of a low pressure domain near the aft end of the body, is created simply by the interaction of the synthetic jet with the free stream. It is known from earlier work by Smith and Glezer (2002) and Honohan (2003) that a low pressure

region forms in the interaction domain of a synthetic jet in a cross flow, supporting this hypothesis.

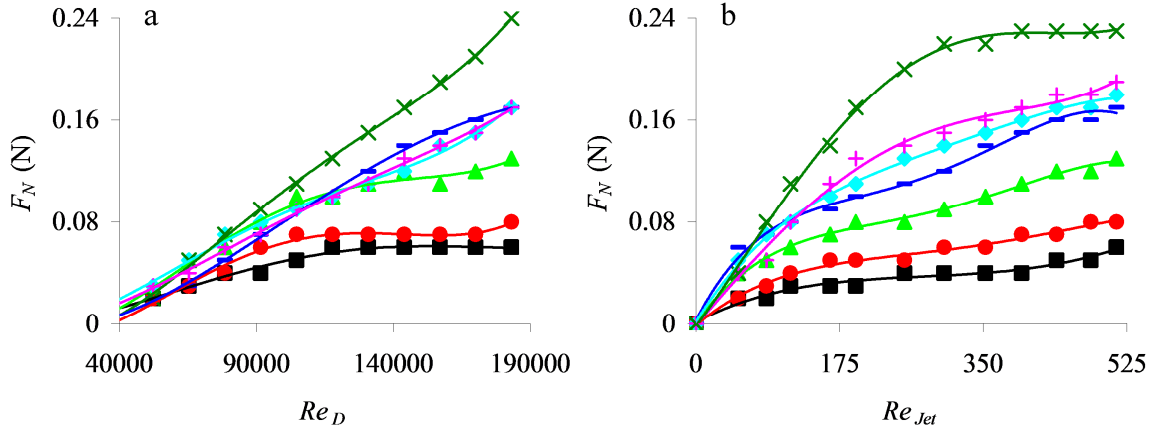


Figure 10. Effect of Coanda radius on the normal force, (a) variation with free stream speed, ($Re_{Jet} = 480$), and (b) variation with jet strength, ($Re_D = 183,000$). $R/h = \blacksquare 0$ (sharp corner), $\bullet 7.1$, $\blacktriangle 14.1$, $\blacksquare 21.2$, $\blacklozenge 35.3$, $\blackplus 42.3$, $\blacktimes 49.4$

The data in Figure 10 show that for a given level of Re_D (Figure 10a) or Re_{Jet} (Figure 10b), the normal force increases with R (at least over the range tested here), ostensibly due to the increased surface area. Furthermore, for $R/h < 20$ in Figure 10a (i.e., fixed Re_{Jet}), the rate of increase of the normal force decreases with increasing Re_D . However, this effect diminishes with increasing R such that for the largest radius tested here ($R/h = 49.4$), the normal force varies almost linearly with Re_D . On the other hand, when Re_D is fixed and the strength of the control jet is varied (Figure 10b), it is shown that the effectiveness of the jet saturates beyond a given jet strength. The data further indicate that the jet strength at which saturation occurs increases with R . As might be

anticipated, smaller surface curvature hastens this saturation because of the larger adverse streamwise pressure gradient associated with the smaller radius.

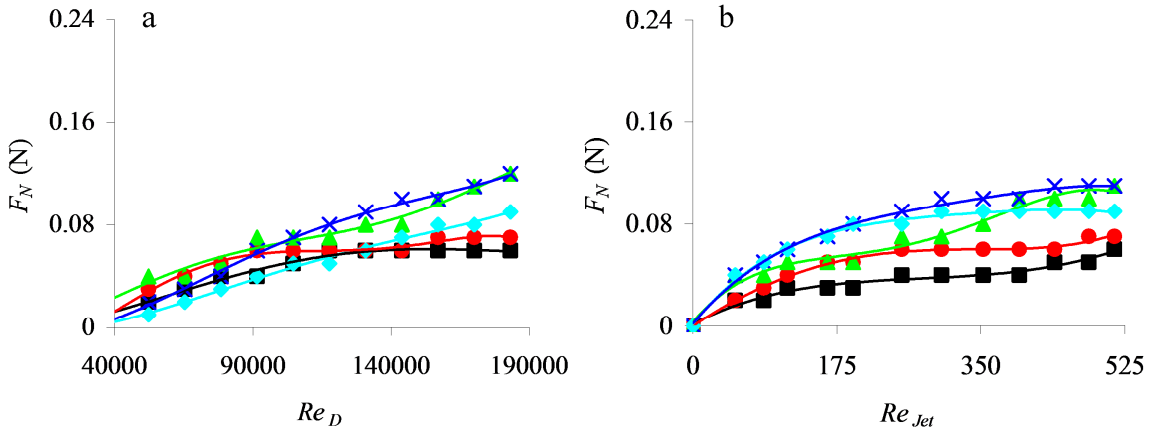


Figure 11. Effect of square extensions on the normal force, (a) variation with free stream speed, ($Re_{Jet} = 480$), and (b) variation with jet strength, ($Re_D = 183,000$). $E/h = \blacksquare 0$ (sharp corner), $\bullet 3.5$, $\blacktriangle 7.1$, $\times 10.6$, $\blacklozenge 14.1$

Since a measurable force was obtained even without a Coanda tail extension, the impact of sharp-edged tail extensions was also explored. With the step height and actuator slot geometry held constant as before, the length of the extension E along which the jet ejected tangentially was varied (Figure 11). While the forces generated are smaller than in the presence of Coanda tail extensions, the trends are noteworthy. In general, the rate of change of the induced force slightly decreases with increasing free stream speed and jet strength. The induced force increases with extension length up to $E/h = 10.6$ as might be expected, because the extension increases the ability of the separating flow to reattach, and the normal projected area increases with extension length. It is noteworthy that the trend for the longest extension shown here ($E/h = 14.1$)

is different. At a fixed jet strength, for $Re_D < 130,000$ the induced force is lower than in the absence of an extension and ultimately only exceeds the force produced by the $E/h = 3.5$ extension for $Re_D > 160,000$. At a fixed free stream the variation with jet strength is similar to that of the $E/h = 10.6$ extension, but levels off and even slightly diminishes for $Re_{Jet} > 300$. It appears that the low pressure region formed next to the surface of the extension is somewhat enhanced for extensions up to approximately $E/h = 10$. This low pressure region results in vectoring of the near wake flow and in induced force. Longer extensions increase the distance to the wake and their effectiveness diminishes.

4.3 Transitory Aerodynamic Force

Given the dynamic nature of the application as previously discussed, it was desirable to assess the aerodynamic response to transient actuation as might be effected by pulse- or step-modulation of the actuator's driving signal. Pulsed actuation control input might be useful when it is desired to use the induced aerodynamic forces to provide an impulse of prescribed magnitude and/or duration. In earlier work on the control of flow separation on two-dimensional bluff bodies and stalled airfoils, Amitay and Glezer (2001) demonstrated that the transient effects that are associated with the onset and termination of the actuation can lead to the generation of large momentary aerodynamic forces. The magnitude of these forces is typically larger than the steady forces, which are associated with the suppression of separation or partial flow reattachment. In fact, in a later work, Amitay and Glezer (2002) showed that the characteristic time constants that are associated with these forces are such that they can be retriggered time-periodically to

achieve larger time-averaged lift than is attainable with conventional time-harmonic actuation.

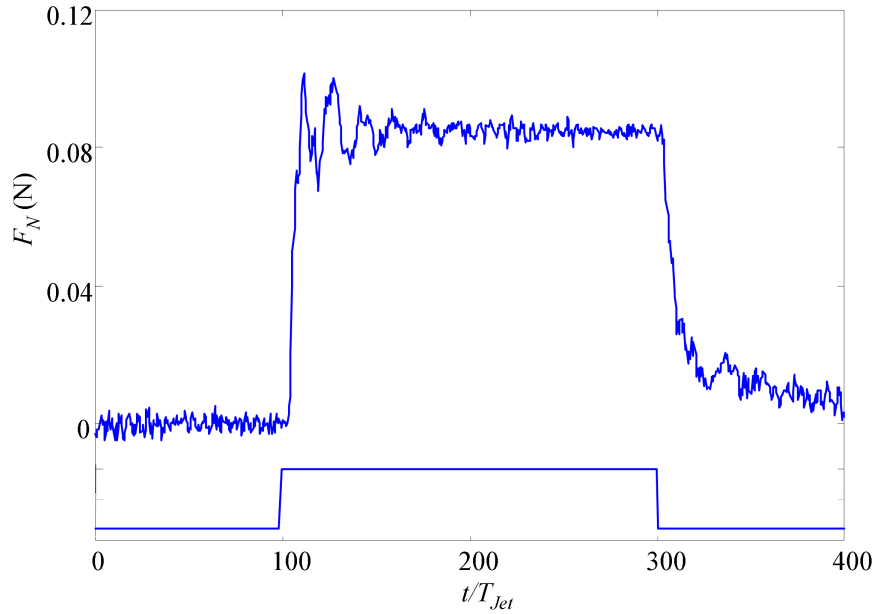


Figure 12. Transient force in response to step modulation (bottom trace) of the jet actuation waveform, ($Re_D = 131,000$, $Re_{Jet} = 480$, $T_p/T_{Jet} = 200$).

The dynamic force response of the present axisymmetric body to pulse-modulated actuation is shown in Figure 12. These measurements were complicated by the response of the force transducer to the actuation frequency. The data shown in Figure 12 were filtered to remove the actuation frequency through a novel technique in which force records measured phase-locked to the actuation waveform at consecutive phase increments were averaged to achieve a box-car filter effect. The driving frequency was 1 kHz (the resonant frequency of the synthetic jet actuator), and the forcing period, T_{Jet} , is therefore 1 msec. When the jet actuator is activated, the characteristic rise time of the

normal force to the level that is associated with continuous actuation is commensurate with the time it takes the flow about the body to adjust to the modification in the shape of the surface as a result of the displacement of the free stream by the interaction domain with the control jet. This time scale is clearly connected with the convective time scale of the flow, calculated as the ratio of the characteristic dimension of the body (length) over the speed of the free stream. The convective time scale in the present measurements ($U_\infty = 25$ m/s) is about 6 msec, which is in agreement with the rise time in Figure 12. In fact, the force overshoots and undergoes several oscillations at a frequency that is close to the shedding frequency of the body (70 Hz), which decay within 5-6 cycles. However, it must be borne in mind that these force measurements were taken phase-locked to the top-hat modulation waveform of the actuation and therefore the decay may be attributed to loss of coherence of the shed vortical structures within the wake relative to the actuation waveform. The characteristic fall time following the termination of the control input is approximately 20 msec, notably longer than the rise time. This may be due to viscous effects during the release of vorticity accumulated downstream of the jet during actuation, a phenomenon similar to the mechanism of airfoil dynamic stall delay.

The structure of the near-wake velocity field during the application of step-modulated actuation is shown in Figure 13a-f. The phase-averaged vector plots shown in the cross-stream plane were obtained from PIV measurements taken phase-locked to the modulating waveform using incremental delays. ($Re_D = 131,000$ and $Re_{Jet} = 480$.)

The vector plot in Figure 13a is of the time averaged velocity field before the onset of the actuation. Shaded raster plots of the spanwise vorticity are superposed on the vector plots. The structure of the natural wake is evident, with a large recirculation zone

that scales with the body diameter. Figure 13b shows the first vortical structure that is produced by jet actuator at 1.5 msec after the onset of the actuation, which is advected downstream by the free stream and can be followed in successive images. The next image (Figure 13c) was taken 2.5 msec after the actuation onset and shows the second vortical structure moving along the Coanda surface. The flow begins to turn strongly in Figure 13c and d where the inflow to the wake becomes evident. At the same time, the circulation formed in the natural wake is divided by the inflow of the higher velocity upstream fluid. The majority of this circulation becomes separated from the body by Figure 13e and is advected downstream as the structure of the near wake adjusts to the local flow attachment on the Coanda surface. This may be thought of as a precursor to the turning of the flow into the wake region, which is almost complete by Figure 13f, approximately six actuation cycles (one convective time scale) following the actuation onset.

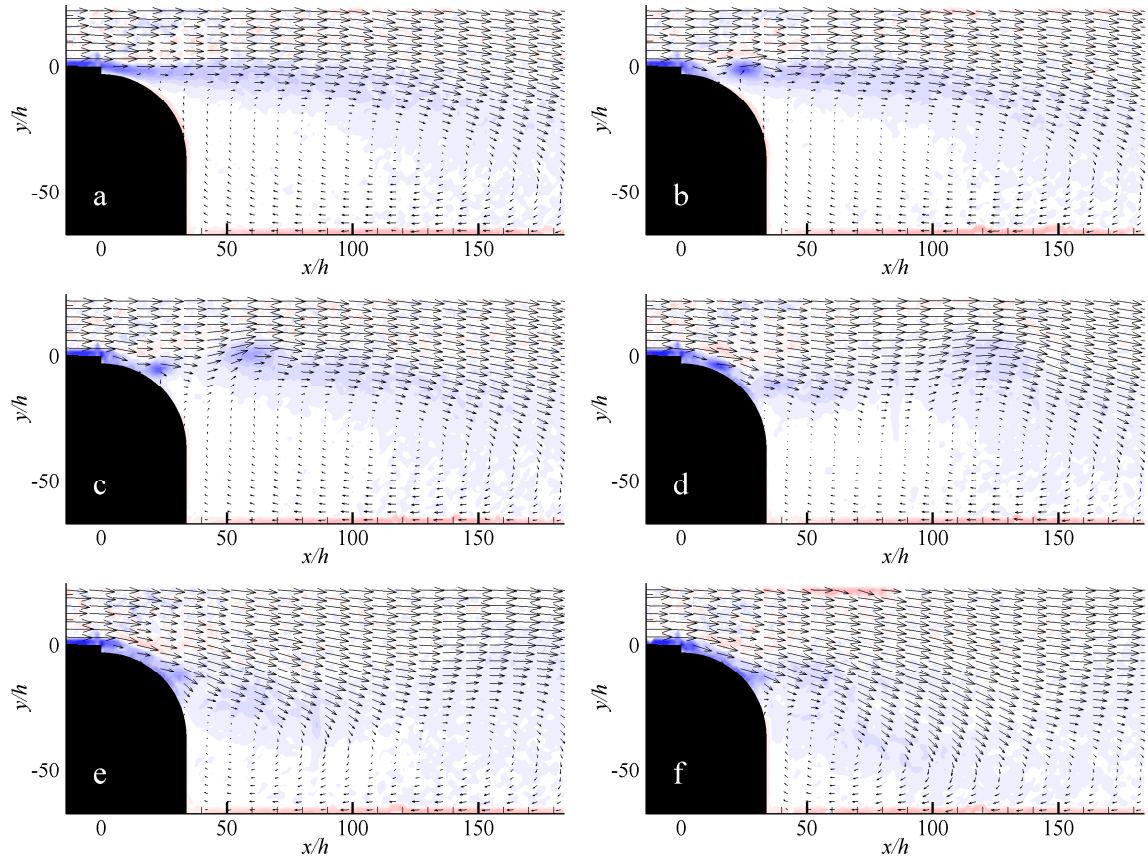



Figure 13. *Transient flow response to a step modulation of the synthetic jet actuation signal, ($Re_D = 131,000$, $Re_{Jet} = 480$): (a) $t/T_{Jet} = 0$, (b) 1.5, (c) 2.5, (d) 4.0, (e) 5.5, (f) 6.5. Vorticity scale: $-20,000$  $20,000$ 1/s. $y/h > 20$: Vector lengths indicate 25 m/s.*

The flow response following the termination of the actuation is shown in Figure 14a-f. Figure 14a and b still exhibit the advection of vortical structures that is probably the result of the resonance decay of the diaphragm motion after the termination of the driving signal. It is remarkable that while the shear layer at the edge of the step is completely detached from the Coanda surface by Figure 14c (3.75 msec following the termination of the actuation), the flow in the near wake downstream is still turned towards the centerline of the body. This suggests that the aerodynamic force on the body does not completely decay and may be related to the prolonged relaxation time observed

in the dynamic force measurements in Figure 12. Still, much like the activation, within a convective time scale of about 6 msec the response is essentially complete, as shown in Figure 14e. Even before two convective time scales have passed, the flow appears to have reached a fully separated state, as in Figure 14f.

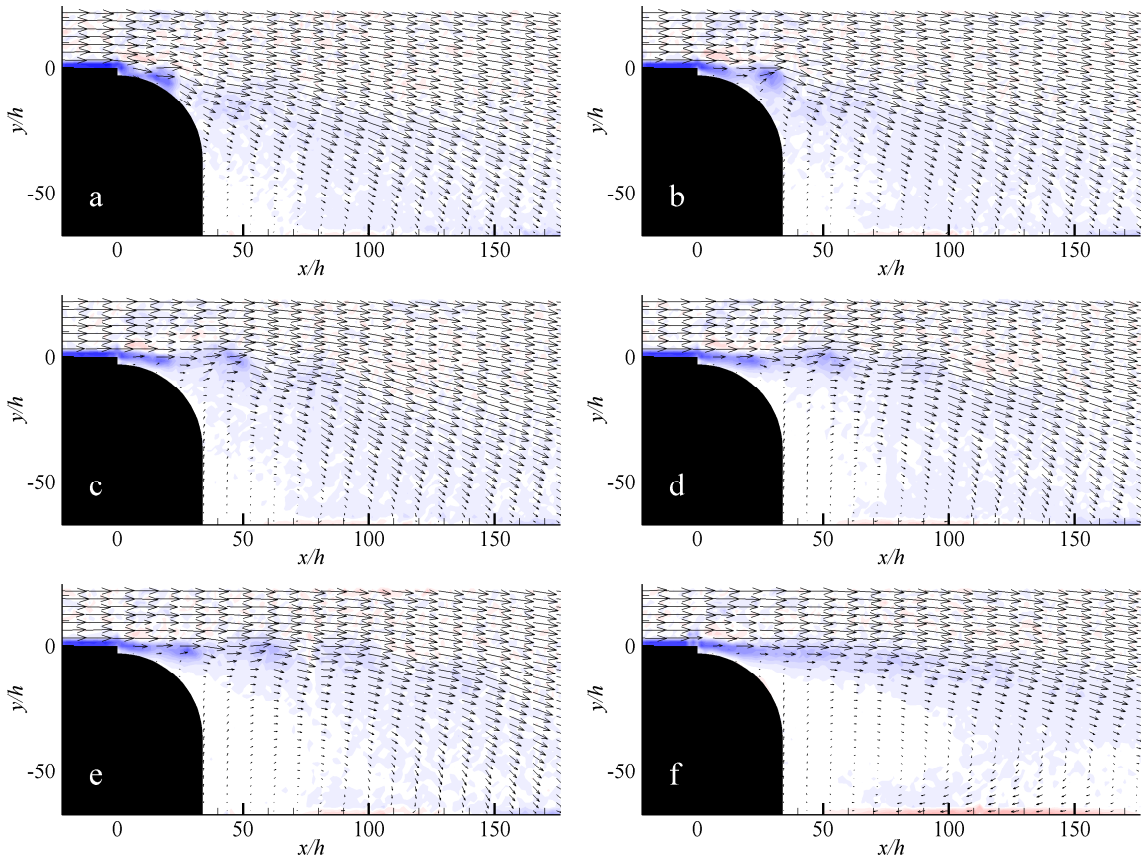



Figure 14. Transient flow relaxation after termination of the actuation signal, ($Re_D = 131,000$, $Re_{Jet} = 480$): (a) $t/T_{Jet} = 0$, (b) 2.25, (c) 3.75, (d) 5.0, (e) 6.25, (f) 10. Vorticity scale: -20,000  20,000 1/s. $y/h > 20$: Vector lengths indicate 25 m/s.

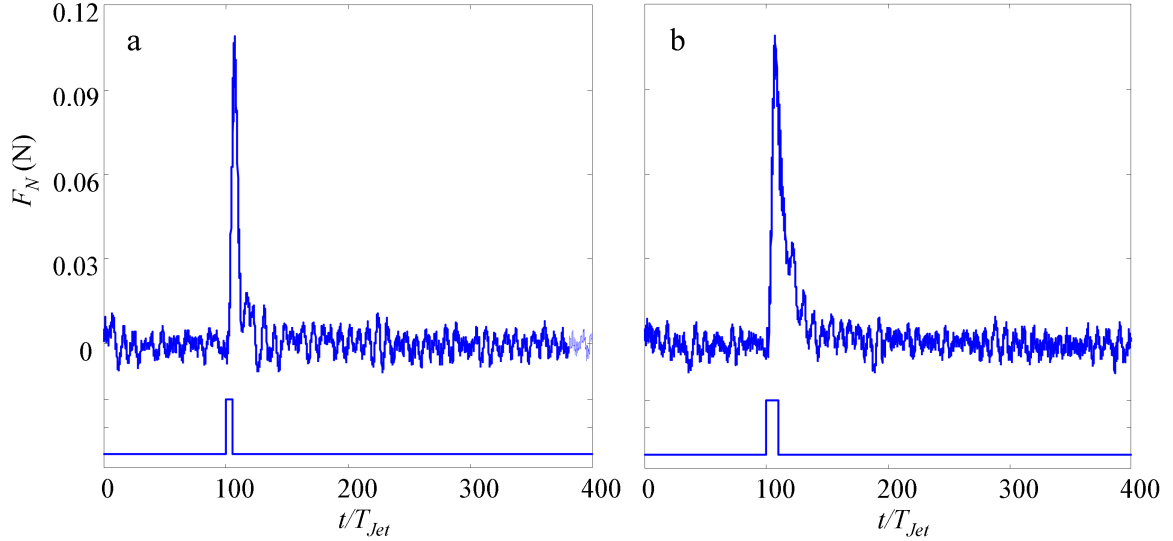


Figure 15. Normal force in response to momentary activation of the synthetic jet, modulation waveform shown at bottom, ($Re_D = 131,000$, $Re_{Jet} = 480$): (a) $T_p/T_{jet} = 5$, (b) $T_p/T_{jet} = 10$.

As evident in Figure 12, the normal force rises to its peak value within about 5 actuation cycles. The dependence of the rise time on the duration of brief pulse-modulation waveform was investigated in a series of experiments in which the duration of the modulation pulse was varied. Figure 15a and b show the force resulting from pulsed actuation with periods of 5 and 10 msec that correspond respectively to 5 and 10 oscillation cycles of the actuator diaphragm (1 kHz). In both cases the peak force is larger than the quasi-steady force that is obtained with continuous time-periodic actuation in agreement with the observation of Amitay and Glezer (2002). When the actuation period is increased (Figure 15b), the impulse of the aerodynamic force increases while its peak remains unchanged; this suggests that it might be possible to achieve a required impulse by integrating the effect of a series of discrete pulses. However the time needed

for relaxation between pulses to generate the next peak may limit the repetition rate as this force is related to the onset vortex discussed in connection with Figure 13.

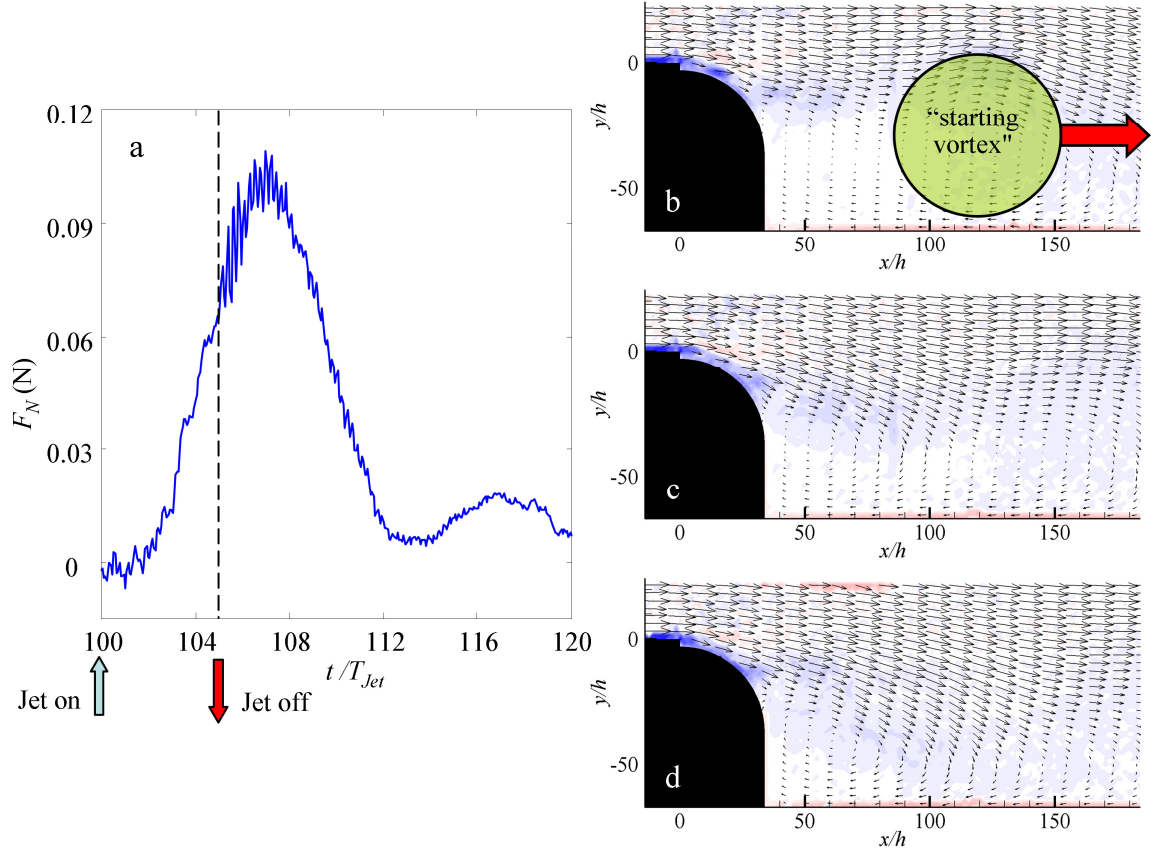



Figure 16. Force and flow response to a brief pulse activation of the synthetic jet, ($T_p/T_{jet} = 5$, $Re_D = 131,000$, $Re_{Jet} = 480$): (a) dynamic force, (b) phase-locked PIV images in the near wake at $t/T_{jet} = 4.0$, (c) 5.5, (d) 6.5. Vorticity scale: -20,000  20,000 1/s. $y/h > 20$: Vector lengths indicate 25 m/s.

Figure 16a shows the time trace of the force engendered by a 5 msec pulse (plotted using an expanded time scale). This plot clearly shows that the induced aerodynamic force continues to rise following the termination of the pulsed actuation. The rise time to the peak value is nominally 7 msec which is very close to the convective

time scale of the flow over the body. The vector plots in Figure 16b-d on the right (Figure 13d, e, and f repeated for convenience) suggest that the continued rise time is connected with the formation and advection of the large scale “starting vortex” into the wake, and indicate that the continued rise of the aerodynamic force following the termination of the actuation results from global vorticity dynamics. It is not surprising then that doubling the pulse duration as in Figure 15b, does not lead to an increase in the peak force. Once enough high-momentum free stream fluid is vectored into the wake as a result of the collapse of the separated flow, the response continues without further input but cannot be sustained beyond the advection of the vorticity from the separated flow domain. The ability to achieve a pulsed force following the termination of actuation is noteworthy.

The PIV measurements presented up to Figure 16 have been on the orifice centerline. However, as implied by the actuation performance associated with the bounding fences earlier, the effect of actuation is not azimuthally uniform (i.e. along the span of the orifice). To obtain better insight into details of the flow turning, PIV measurements were taken in azimuthal planes (remaining through the axis of the body) near the orifice edge and halfway between the edge and centerline. These data show significant spanwise variations not just in the flow turning but also in the transient development. The field of view is 25 mm square, $Re_D = 131,000$, and $Re_{Jet} = 480$. The angle θ is defined as the azimuthal rotation of the measurement plane about the body axis from the orifice centerline ($\theta = 0^\circ$). Recall that the orifice spans 38° or $\theta = \pm 19^\circ$.

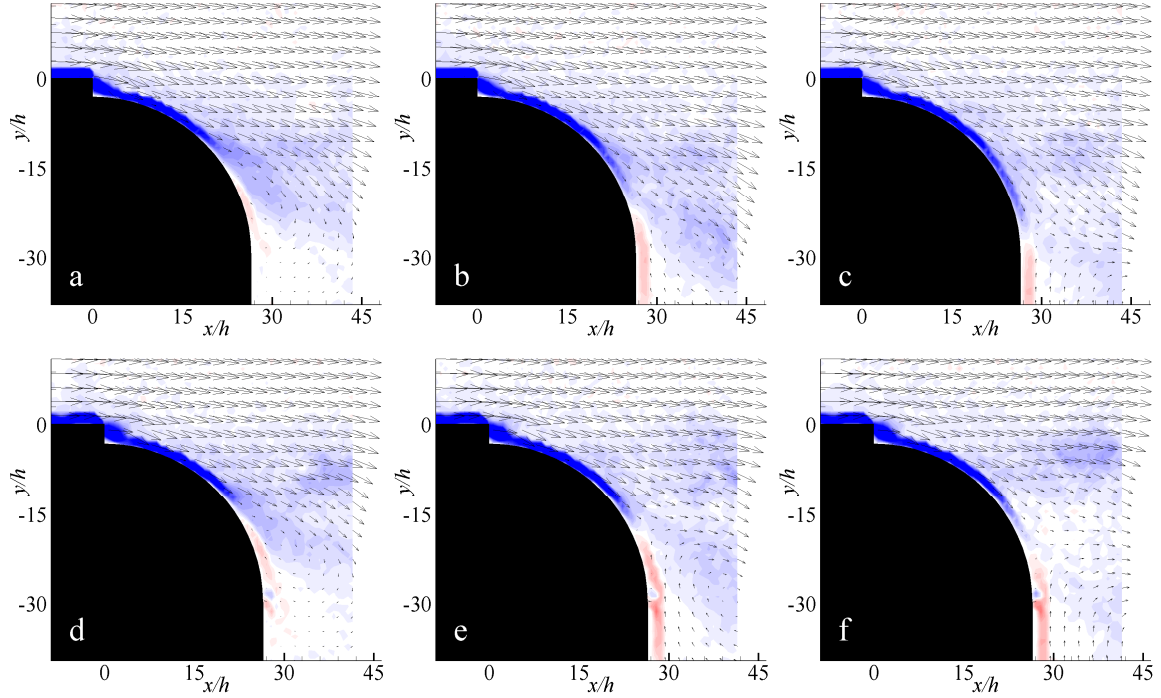


Figure 17. Comparison of flow response in azimuthal planes during activation, ($Re_D = 131,000$, $Re_{Jet} = 480$). Centerline (top row, $\theta = 0^\circ$): (a) $t/T_{Jet} = 4.00$, (b) 5.00 , (c) 6.00 , and halfway to orifice edge (bottom row, $\theta = 9^\circ$): (d) 4.00 , (e) 5.00 , (f) 6.00 . Vorticity scale: $-20,000$ $20,000$ 1/s. $y/h > 10$: Vector lengths indicate 25 m/s.

Figure 17a-f compares the flow on the centerline ($\theta = 0^\circ$) and in a radial plane halfway between the orifice edge and centerline ($\theta = 9^\circ$). At $t/T_{Jet} = 4.0$ (i.e 4 actuation cycles), the flow in both views (Figure 17a and d) is essentially identical. But surprisingly beyond this point the flow in the plane $\theta = 9^\circ$ actually begins to recede from its bending into the wake simultaneously while the centerline flow continues to bend further into the wake. The flow in Figure 17f stops vectoring halfway (45°) around the Coanda radius compared to vectoring around the entire 90° of the radius on the centerline in Figure 17c. This difference appears to be sustained under steady actuation. A similar behavior is observed in Figure 18a-f in the plane $\theta = 18^\circ$ through the orifice edge. The

flow at $t/T_{Jet} = 3.0$ (Figure 18d) is very similar to the flow in the center plane (Figure 18a), but thereafter recedes from the wake and attachment to the Coanda surface ceases by $t/T_{Jet} = 5.0$ (Figure 18f). It appears that while initially the flow turning is two-dimensional (up to $t/T_{Jet} \approx 3$), the attachment to the Coanda surface weakens as a result of three-dimensional (edge) effects such that the flow near the edge of the orifice appears to return almost to an unforced separated shear layer. As shown in Figure 17 halfway between the orifice edge and centerline the flow is almost two dimensional up to $t/T_{Jet} = 4$, suggesting a 1 msec (or 1 jet period) delay between the planes $\theta = 9^\circ$ and 18° which is indicative of the migration of the edge effects towards the center plane.

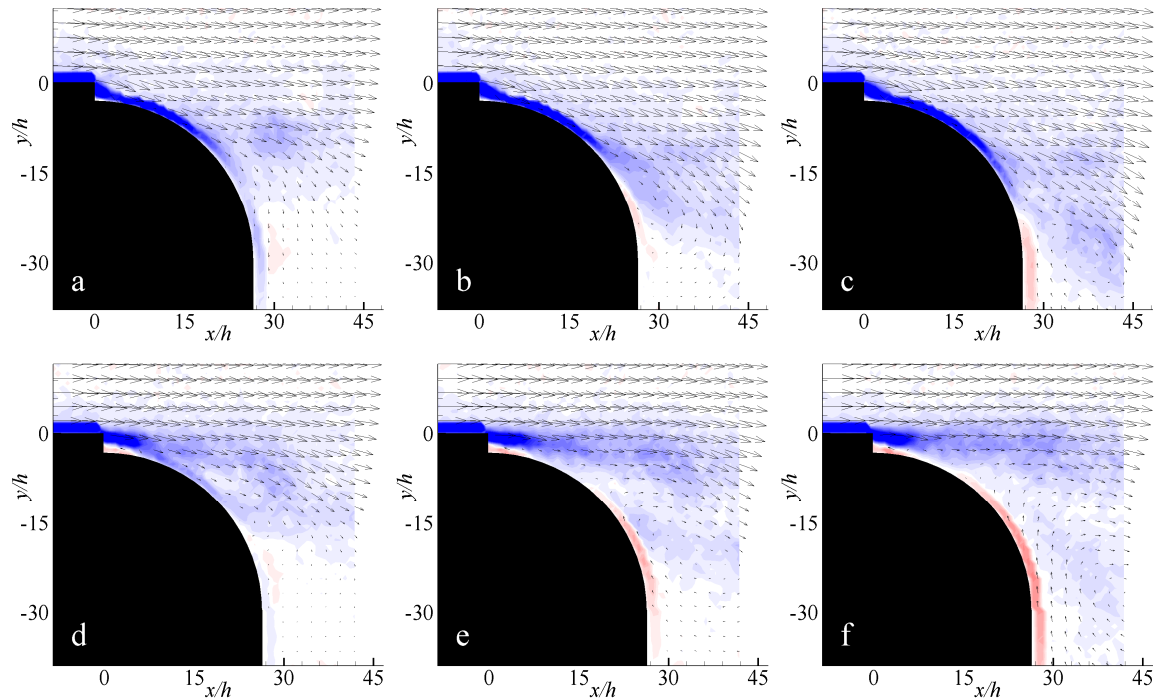



Figure 18. Comparison of flow response in azimuthal planes during activation, ($Re_D = 131,000$, $Re_{Jet} = 480$). Centerline (top row, $\theta = 0^\circ$): (a) $t/T_{Jet} = 3.00$, (b) 4.00 , (c) 5.00 , and orifice edge (bottom row, $\theta = 18^\circ$): (d) 3.00 , (e) 4.00 , (f) 5.00 . Vorticity scale: $-20,000$  $20,000$ 1/s. $y/h > 10$: Vector lengths indicate 25 m/s.

These three-dimensional effects are hard to capture using 2-D PIV. Clearly the close field of view does not capture the overall state of the flow, and from earlier measurements it is known that at least one convective time scale, about 6 msec, is needed for the response to stabilize. It is conjectured that the initial receptivity of the flow off of the centerline to vectoring is likely due to the transient dynamics associated with the collapse of the separated flow domain. While the initial influx of high-momentum fluid that is associated with this separation collapse is capable of overcoming adverse streamwise pressure gradients, it appears that as the flow response stabilizes, a spanwise pressure gradient develops near the edge of the jet, which leads to reduced spanwise effectiveness. These effects are discussed further in a later section.

4.4 Modification of the Actuation Waveform

Isolated hot wire measurements in the jet actuator orifice indicate that peak velocity is achieved within about three cycles following the onset of actuation. It was also observed that the jet continues to form following the termination of actuation, with 2-3 cycles of significant jet velocity, and over 10 msec of measurable actuator output. This lagging response of the jet actuator to both activation and deactivation clearly affects the response time of the aerodynamic forces. It was considered that the response time of the actuator, and ensuing aerodynamic response, could be reduced through modification of the input driving signal.

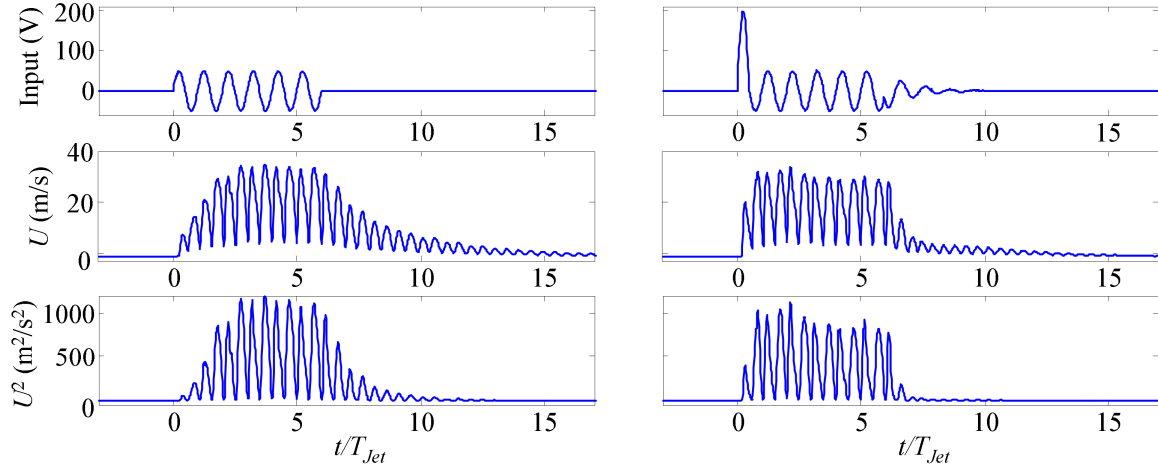


Figure 19. Hot wire measurements of orifice velocity in response to original (left) and modified (right) driving signals, $Re_{Jet} = 480$.

Figure 19 shows the input signal and corresponding hot wire output for the original (left) and modified (right) driving signals. Through trial and error it was found that amplifying the first half-cycle of the sinusoidal input signal was most effective in decreasing rise time, from three actuation cycles to one-half. Using a gain of four relative to the base signal, the piezoelectric diaphragm is forced from its resting state to a higher initial displacement, already near its steady resonant condition and therefore reducing the time to reach maximum displacement (and maximum jet velocity). This high voltage is permissible upon start-up, but would cause disc failure if sustained as mechanical limits would be exceeded. An inverted, phase-shifted, exponentially decaying braking signal minimized actuator ringing, and left little more than one-half of a cycle of notable jet velocity beyond deactivation. The phase-shift, while difficult to predict precisely, allows the driving signal to precede the motion of the disc in this dynamic setting, applying a force in the opposing direction to slow the disc. The exponential decay allows this braking to be applied at an appropriate magnitude to match

the natural decay of the disc motion without causing opposing motion. Therefore with this approach, actuator rise and fall responses were both decreased from three cycles to one-half, a significant improvement of 2.5 msec for each.

Of course, the motivation for the modified input signal was to reduce flow turning response times. PIV measurements on the orifice centerline, shown in Figure 20a-f, indicate significant differences. Within one-half cycle ($t/T_{Jet} = 0.5$) the difference is evident; flow attaches behind the step and the separating shear layer is already pinched off when the modified actuation waveform is used (Figure 20d) while both features are essentially absent in the original waveform (Figure 20a). The response to the modified waveform is much more rapid, with flow vectoring onto the Coanda radius by $t/T_{Jet} = 0.75$ (Figure 20e). It takes another full cycle ($t/T_{Jet} = 1.5$) for the original waveform to exhibit similar features (Figure 20b). This one cycle lag continues, as seen comparing the modified waveform at $t/T_{Jet} = 1.25$ (Figure 20f) to the original waveform at $t/T_{Jet} = 2.25$ (Figure 20c); the flow around the Coanda surface is similar but the starting vortex of the modified waveform has much more definition than that of the original waveform and an upward flow is clearly visible underneath that is not present in the original waveform. While the convective time scale does not change, it is conjectured that this accelerated response combined with the stronger, more coherent vortical structures probably cause a higher peak force. Regrettably, dynamic force measurements were not obtained during this study.

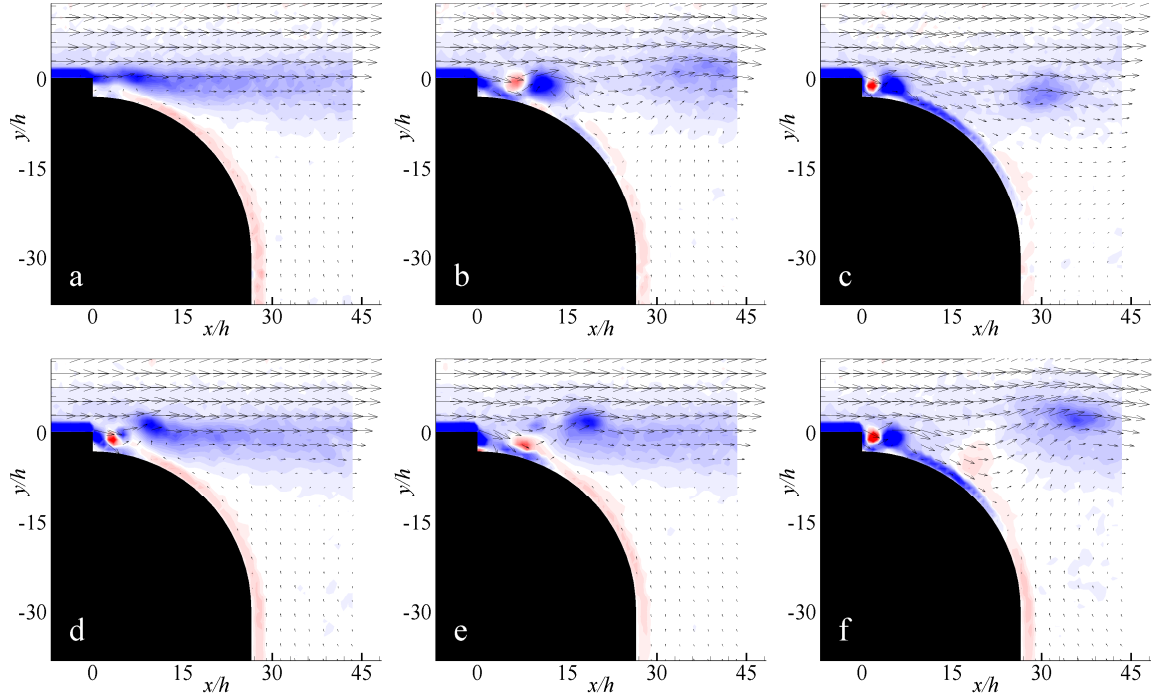


Figure 20. Impact of amplified input signal on transient flow response, ($Re_D = 131,000$, $Re_{Jet} = 480$). Standard sine wave (top row): (a) $t/T_{Jet} = 0.50$, (b) 1.50, (c) 2.25, and modified waveform (bottom row): (d) $t/T_{Jet} = 0.50$, (e) 0.75, (f) 1.25. Vorticity scale: $-20,000$ $20,000$ 1/s. $y/h > 10$: Vector lengths indicate 25 m/s.

PIV measurements of deactivation (Figure 21a-f) show similar improvements in response with the modified waveform. Data is shown for a six-cycle actuation driving signal pulse, terminating at $t/T_{Jet} = 6.00$. The sequence begins at $t/T_{Jet} = 7.50$ for the original waveform in Figure 21a, and at $t/T_{Jet} = 7.00$ for the modified waveform in Figure 21d. Timing of the figures was chosen such that each pair of images exhibits a similar extent of flow vectoring in the wake in terms of the distribution of vector angle and magnitude. The timing of the two waveforms in the first pair (Figure 21a and d) were separated by 0.5 msec and the other two pairs were separated by 1 msec each. In terms of flow turning and wake character, these images illustrate that it generally takes an extra 1 msec (equivalently the period of an additional actuation cycle) for the original waveform

to achieve the same state as the modified waveform. Beyond this, vorticity of the forming shear layer for the modified waveform is more coherent and concentrated than that of the original waveform even 1 msec later, as shown in Figure 21b and e. While the convective time scale does not change, the apparent accelerated restoration of the shear layer with the modified waveform also appears to accelerate the wake restoration as shown in Figure 21c and f, which likely reduces oscillations in force as well.

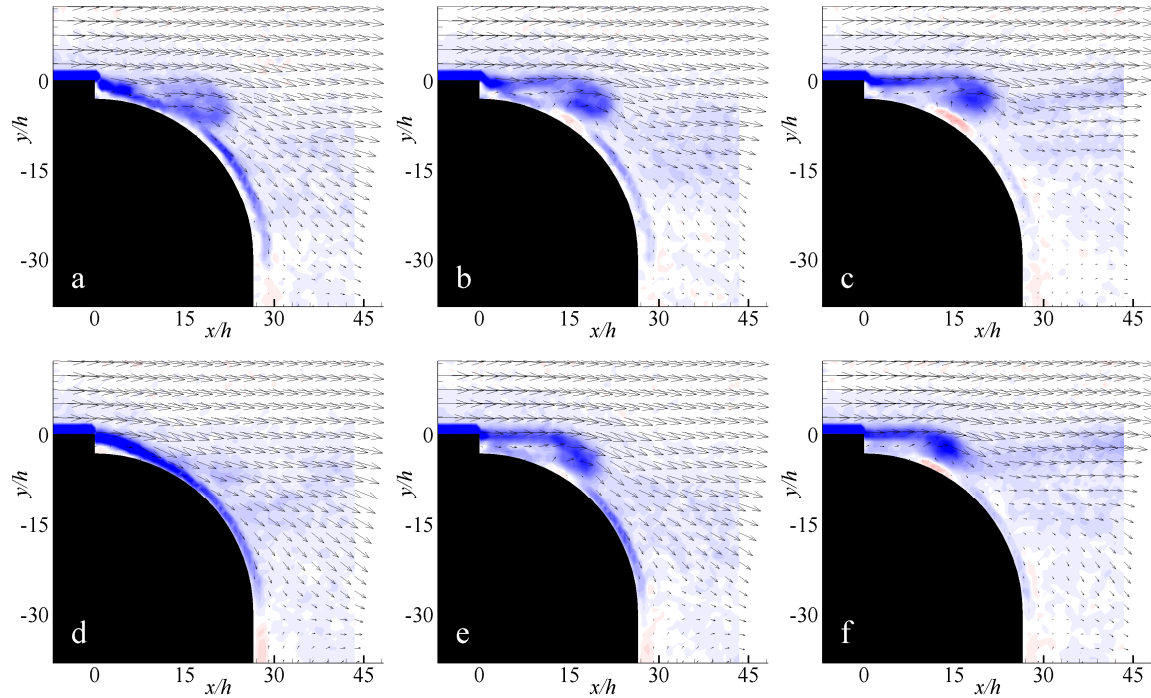



Figure 21. Impact of actuator braking signal on transient flow relaxation, ($Re_D = 131,000$, $Re_{Jet} = 480$, $T_p/T_{Jet} = 6$). Standard sine wave (top row): (a) $t/T_{Jet} = 7.50$, (b) 8.50, (c) 9.50, and phase-shifted, damped braking signal (bottom row): (d) 7.00, (e) 7.50, (f) 8.50. Vorticity scale: -20,000  20,000 1/s. $y/h > 10$: Vector lengths indicate 25 m/s.

4.5 Recessed Jet Channel

As noted in section 4.2, spanwise constraint of the jet improves its interaction with the crossflow by constraining spanwise entrainment along the jet edges, thereby increasing the induced low-pressure domain. The effect of the spanwise variation in the low pressure domain is apparent by the reduced degree of vectoring of the oncoming flow in off-center planes as confirmed by PIV measurements in section 4.3. With this in mind, slight geometric alterations were explored to improve the induced pressure near the spanwise edges of the jet.

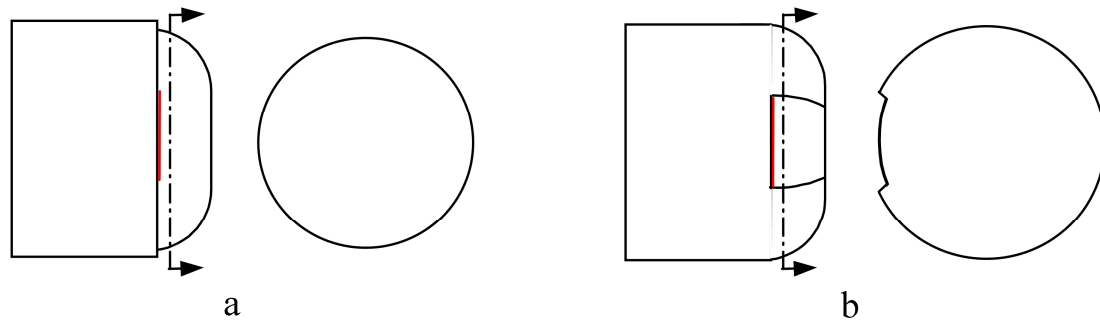


Figure 22. Tail geometry: (a) Axisymmetric and (b) Channeled tail extensions.

Unlike the original configuration with an axisymmetric 1.5 mm backward-facing step adjoining the Coanda radius (Figure 22a), in the altered configuration the actuator step is confined to the azimuthal span of the orifice, while the remainder of the tail has no step, creating a 1.5 mm depression that forms a channel-like trough which retains the original Coanda surface, over which the actuator jet operates (Figure 22b). This trough effectively isolates the jet and reduces azimuthal entrainment along the orifice. The effectiveness of this approach is compared to the original configuration while retaining

the same actuator base and forebody. First the jet strength is maintained at $Re_{Jet} = 500$ while the free stream speed is varied. As shown in Figure 23a, the force generated with the axisymmetric tail reaches a maximum force of 0.169 N at $Re_D = 196,000$ while the channeled configuration reaches a maximum force of 0.463 N, almost three times that of the axisymmetric tail at the same Re_D . At first look the axisymmetric tail appears at this scale to follow a linear relationship with Re_D , but upon closer inspection both curves closely follow a quadratic relationship that simply scales up with the channeled tail, as shown via the fitted lines on the plot.

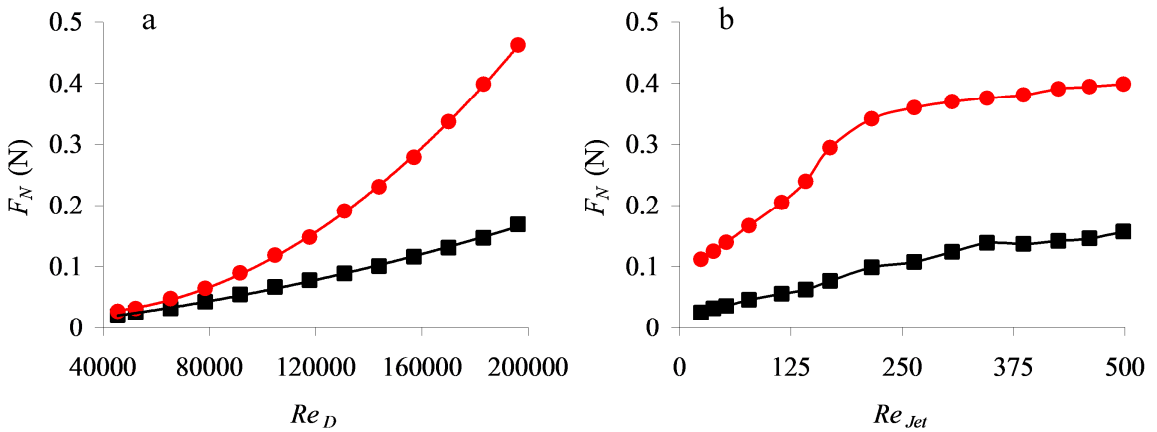


Figure 23. Normal force developed for axisymmetric and channeled tail extensions: (a) Force vs. free stream speed, $Re_{Jet} = 496$, (b) Force vs. jet strength, $Re_D = 183,000$.

■ Axisymmetric tail, ● Channeled tail

Larger differences in performance between the two configurations are observed when the jet strength is varied (Figure 23b). At a fixed Re_D (183,000), the induced force varies almost linearly with Re_{Jet} for the axisymmetric configuration. However, in the presence of the channel the variation of the induced force with jet strength exhibits two

regimes. For $Re_{Jet} < 215$ the force developed increases at a rate generally three times greater than that of the axisymmetric configuration, while for $Re_{Jet} > 215$ the force increases at a rate similar to the axisymmetric configuration but at a higher level. The maximum force of 0.399 N is 2.5 times that of the axisymmetric configuration at the same jet strength. These results are quite surprising compared to the earlier work with bounding fences, which offered at most a 25% increase in performance and in fact reduced the sensitivity to jet strength at lower levels. It is evident that the blockage of spanwise entrainment does not influence the primary limitation of the effect despite the limitation being related to edge effects. While the channel geometry is less intrusive than the fences, its features help to generate a much greater effect and offer insight into the resistance caused by edge effects. Through further analysis and PIV these issues will be explored.

More can be inferred from the data plotted in Figure 23b when it is re-plotted in terms of the thrust of the actuation jet, as shown in Figure 24. Assuming a uniform velocity distribution and sinusoidal velocity fluctuation (approximately valid for the purpose of comparison), the average control jet thrust (J) is calculated by integrating the momentum flux passing through the orifice over an actuator cycle period:

$$J = \frac{1}{T_{Jet}} \int_0^{T_{Jet}} \rho A U_o^2 \sin^2(2\pi * f_{act} t) dt = \frac{\rho A U_o^2}{2} = \frac{\pi^2 \rho A U_{Jet}^2}{2}$$

Where the average outstroke velocity (U_{Jet}) occurring over the period $T_{Jet}/2$ is normalized by the entire period of actuation (T_{Jet}) and related to peak velocity of the sinusoidal waveform (U_o) by:

$$U_{Jet} = \frac{1}{T_{Jet}} \int_0^{T_{Jet}/2} U_o \sin(2\pi * f_{act} t) dt = \frac{U_o}{\pi}$$

Shown first in terms of normal force (Figure 24a) and then in terms of augmentation ratio Au (Figure 24b), this further illustrates the improved performance of the channeled configuration. The augmentation ratio (Au) is defined as the ratio of the measured normal force over the applied control jet thrust, which indicates the effective amplification of the thrust via the induced aerodynamic effect. The linear trends of Figure 24b indicate a power law relationship between Au and J for either configuration, with a near-constant offset between them. It is noteworthy that at the lowest jet strength tested ($Re_{Jet} = 24$) $Au = 2500$ for the channeled configuration, compared to $Au = 550$ with the axisymmetric. At maximum jet strength ($Re_{Jet} = 500$), Au for the two configurations is 20 and 8 respectively.

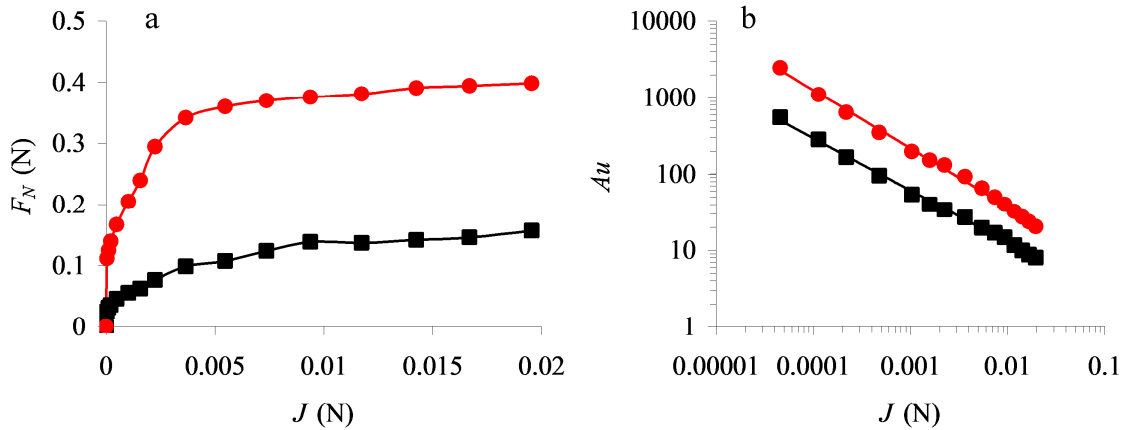


Figure 24. Variation of aerodynamic performance with control jet thrust, ($Re_D = 183,000$): (a) normal force, and (b) augmentation ratio.

■ Axisymmetric tail, ● Channeled tail

Some of the effects of the channeled configuration are demonstrated in PIV measurements (Figure 25), at three radial planes, $\theta = 0^\circ, 9^\circ,$ and 18° . The images in the top row are of the original axisymmetric configuration, and those in the bottom row are of the channeled configuration. Note that in off-center planes, laser light reflecting off the side wall of the channel saturated the image in the area projected by the side wall into the measurement plane, making that area immeasurable. As such, the silhouette of the Coanda radius shown in the images is higher for those cases, however the flow over the actual Coanda surface within the channel is not resolved and therefore the vorticity calculations show falsely elevated gradients along the Coanda surface. Beyond the surface, the balance of the measurements still indicates the great difference between the configurations.

The measurements on the orifice centerline (Figure 25 left column) show that the vectoring of the wake is rather similar in the absence and presence of the channel above

and behind the Coanda radius. However within the domain adjacent to where the Coanda radius ends (at the bottom of the field of view), the channeled configuration (Figure 25d) exhibits a stronger extension of vectoring into this region. In the measurement plane at $\theta = 9^\circ$ (halfway between the orifice centerline and edge, Figure 25 middle column), the channeled configuration (Figure 25e) again exhibits similar extended vectoring into the lower field of view, as opposed to the slight upward flow of recirculation observed in the same region of the axisymmetric configuration (Figure 25b). While in the absence of the channel the flow appears to detach from the Coanda surface and cease vectoring halfway around the Coanda radius, the presence of the channel results in vectoring around the entire Coanda radius and beyond. In fact the flow in this view for the channeled configuration appears quite similar to that of the axisymmetric configuration on the centerline. This enhancement in vectoring is a clear indication of the reason for improved aerodynamic performance. Near the spanwise edge of the orifice ($\theta = 18^\circ$, Figure 25 right column) the flow in the absence of the channel is completely separated while the presence of the channel still results in considerable vectoring up to halfway around the Coanda radius, similar to the axisymmetric configuration at $\theta = 9^\circ$. PIV data was also acquired in radial planes beyond the azimuthal edge of the channel, and no significant flow attachment or vectoring was observed, suggesting the enhanced performance is attributed only to the effects within the orifice span.

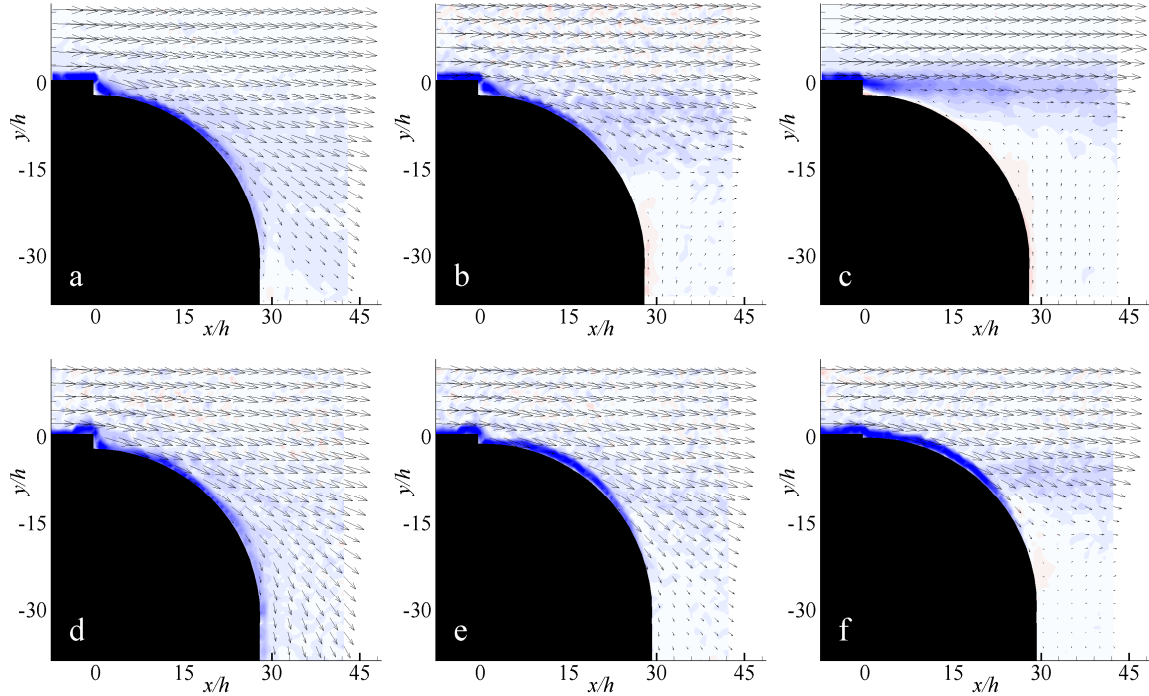



Figure 25. Comparison of flow response to steady actuation for axisymmetric (top row), and channeled (bottom row) tail extensions, ($Re_D = 131,000$, $Re_{Jet} = 496$): (a & d) centerline ($\theta = 0^\circ$), (b & e) halfway to orifice edge ($\theta = 9^\circ$), and (c & f) orifice edge ($\theta = 18^\circ$). Vorticity scale: $-30,000$  $30,000$ 1/s. $y/h > 10$: Vector lengths indicate 25 m/s.

It appears that the primary effect of the channel sidewalls is to restrict spanwise, azimuthal entrainment. This restriction may also cause larger streamwise suction which may explain the enhanced vectoring even on the jet centerline. However, the bounding fences discussed in section 4.2 should have accomplished a similar effect but did not. Upon examination it is apparent that these fences were not sealed tightly at the Coanda surface, and therefore did not block spanwise entrainment. Furthermore the substantial protrusion of the fences into the cross flow (six times taller than the channeled walls), may have restricted entrainment from the outer stream. In addition, the absence of backward step and associated local separation adjacent to the channel may change the

location of separation there, and therefore the effectiveness of the jet. Finally, the channel sidewalls, which lie in radial planes, contract the wall jet azimuthally towards the axis of the body, accelerating the jet as it follows the Coanda surface and thereby sustaining its momentum and further entrainment of the outer flow. (In contrast, the bounding fences were parallel.)

4.6 Comparisons to a Conventional Steady Coanda Jet

As discussed in Chapter 2, the Coanda effect was established through the use of steady blowing tangential to an adjacent curved surface. While the advantages provided by the synthetic jet actuator in terms of low energy and zero net mass flux remain clear, it is constructive to compare to the performance with steady blowing. With this in mind an aluminum tail assembly externally similar to the original stereolithographed synthetic jet tail was designed to accommodate a conventional steady jet driven by an external air supply. The same sting-mounted forebody and tail geometry was retained. Compressed air was routed through tubing along the transverse plate and support sting into the rear of the body, and the flow was controlled by a remote solenoid valve. The thrust level was determined by measuring the volume flow rate of air passing through the tubing using an inline flow meter. The orifice geometry of the jet was identical to that of the synthetic jet model and the result was a steady conventional jet flowing tangential to the Coanda surface.

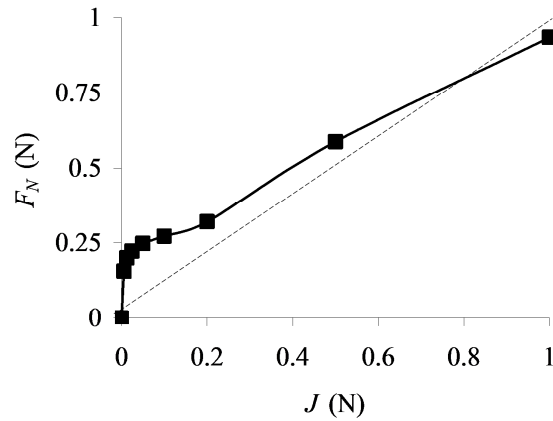


Figure 26. Aerodynamic normal force generated by steady tangential blowing over Coanda tail surface, $Re_D = 183,000$.

Figure 26 shows variation of the resultant aerodynamic normal force generated with control jet thrust J . The dashed line indicates an augmentation ratio equal to one. These data show that for $J < 0.8$ N, the aerodynamic force is higher than the applied jet thrust, with the greatest sensitivity at the lowest thrust levels measured. In particular, at the lowest thrust level measured ($J = 0.006$ N) the augmentation ratio Au is 25. However, at $J = 1$ N, Au is less than 1, indicating that the induced aerodynamic normal force is less than the applied thrust. Coanda surfaces of smaller and larger radii were also explored with similar results where augmentation at low thrust levels increases with radius. Similar to synthetic jets, tangential blowing is most effective at low thrust levels (cf. Figure 24a). In fact the variation of Au with J for both the synthetic and conventional jets (Figure 27) shows that $Au \sim J^{-0.7}$ over five decades indicating that for this geometry the amplification is independent of the jet type. Moreover, in the range of overlapping thrust levels, the difference in performance is below 10%.

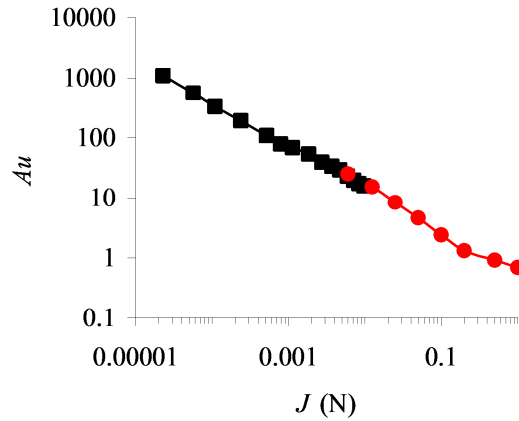


Figure 27. Augmentation ratios for jets blowing over Coanda surface, $Re_D = 183,000$.
 ■ Synthetic jet, ● Steady jet

In association with earlier PIV measurements (e.g. Figure 8) these data suggest that regardless of jet type the efficiency of augmentation goes against the degree of induced flow turning, which is related to jet velocity. While complete saturation is not evident within the range explored here, the degree of flow turning and induced aerodynamic force continue to increase with jet strength but at a decaying rate. On this basis it is conjectured that for a given thrust level the azimuthal span of the jet should be maximized to achieve the greatest effect (within geometrical limitations). For equivalent thrust, a narrower jet of higher velocity would have stronger flow turning and therefore a smaller Au than a wider jet of less velocity. While the wider jet would exhibit a lesser degree of induced flow turning, this would occur over a larger area and with a greater Au that would result in greater induced aerodynamic force.

CHAPTER 5

ISOLATED INTERACTION DOMAIN STUDY

The prior chapter described the generation of steering forces on an axisymmetric body using synthetic jet actuation. The effects of several actuation parameters were investigated including geometrical and input signal modifications, with characterization of the transient response and spanwise variation of the flow vectoring. Perhaps one of the most noteworthy observations regarding the mechanism of the flow turning was the continued rise in normal force following the cessation of a burst of a few (five) actuation cycles. Corresponding PIV measurements indicated that the actuation burst resulted in a larger scale flow response which continued momentarily following termination, and then weakened and ended on the local convective time scale. This illustrated that the transient response is at least partially inertial, and that force generation is associated with the global flow vectoring, even in the absence of actuation.

The objective of the present chapter is to further investigate the mechanics of flow vectoring on a simplified, two-dimensional model that isolates the interaction domain between the jet and the cross flow, eliminating coupling to the scale of the body. The actuator performance is first established and compared to that of the axisymmetric model, and studied in further detail. The experimental configuration is also studied, including upstream boundary layer properties and the impact of various geometrical parameters on the baseline and flow response to actuation. The time-averaged and transient flow response to actuation is then studied in detail at various velocity ratios, on the jet orifice center plane and across the span of the test section.

5.1 Background

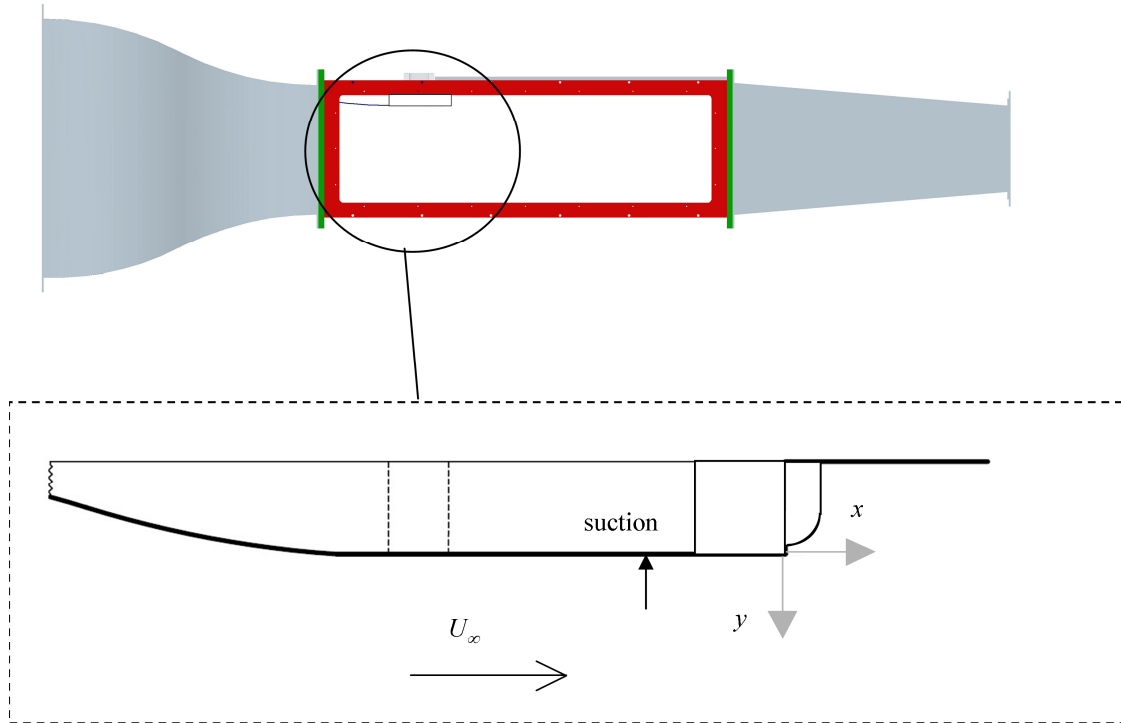


Figure 28. Wind tunnel test section and backward-facing step configuration.

The detailed experiments were conducted in a small wind tunnel with improved optical access (cf. Chapter 3). The closed return atmospheric wind tunnel had a rectangular test section that was 0.25 m wide, 0.40 m high, and 1.4 m long, with free stream speeds up to $U_\infty = 34$ m/s (Figure 28). The forward portion of the ceiling of the test section contained a false floor 50 mm below the original surface, formed by a curved tapering plate starting in the contraction. The false floor ended with an abrupt backward-facing step, where flow vectoring was accomplished. This 50 mm tall step was placed 0.23 m downstream from the end of the contraction and spanned the entire width of the

test section. A spanwise suction slot measuring 230 x 1.5 mm was incorporated in the false floor approximately 100 mm upstream of the backward-facing step, to remove the incoming turbulent boundary layer. Suction was applied by a simple 50 mm diameter return pipe that returned this portion of the flow back to the inlet of the blower, shunting approximately 20 cfm at full speed or 0.35% of the flow volume entering the test section. The suction could be throttled via a valve but was found to work best when the valve was fully open for the given configuration. While the experimental configuration was embedded into the ceiling, all presentations and discussions throughout this chapter are in reference to an inverted view as if the ceiling were actually the floor, to be consistent with the investigation of the axisymmetric model.

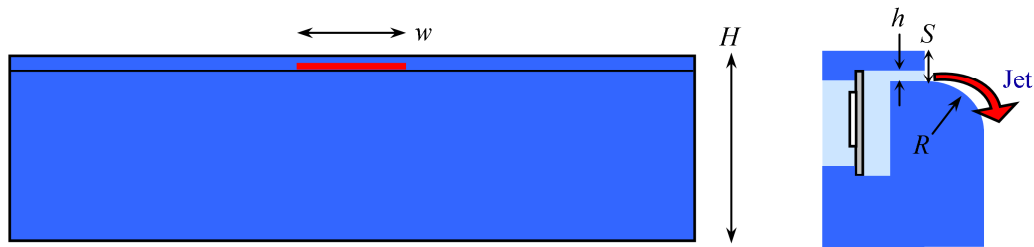


Figure 29. Planar actuator and Coanda surface.

A single actuator identical to those of the axisymmetric model was integrated within the base of the step which spanned the entire width of the test section (0.25 m), as shown in Figure 29. The orifice height (h) was 0.45 mm and its spanwise extent (w) was 25 mm centered symmetrically about the step's centerline. The orifice was integrated into the base of a 1.5 mm high backward facing step (referred to as the orifice step height S) as on the axisymmetric body, and its bottom side was tangential to a rounded

interchangeable Coanda surface extension (of radius R), as can be seen in the image to the right in Figure 29. The assembly formed a 50 mm high backward-facing step (H) as described above. This model represents a two-dimensional variant of the aft end of the axisymmetric model. The planar geometry eliminates the complexity associated with the flow over the axisymmetric body (effectively introducing an “infinite” body radius), isolating the interaction domain between the jet and the cross flow from the circulation and length scale associated with the axisymmetric body.

5.2 Actuator Characteristics

Given the intention of drawing parallels between the flow response to actuation in the planar and axisymmetric configurations, it is important to begin by comparing actuator performance. Hotwire measurements of the velocity at the actuator’s orifice indicate that while the jet performance in the two configurations is similar, there are some differences. In terms of frequency response, the planar actuator has a slightly narrower band around 1 kHz, with slightly lower amplitude (Figure 30a). However the magnitude of spectral components over much of the frequency band presented is double to triple that of the axisymmetric actuator, with a broader and higher secondary peak about 2600 Hz. Additionally, the variation of the planar jet speed with input voltage at 1 kHz reveals about 30% reduction over the majority of the measured range (Figure 30b). These differences do not affect the ability to compare the results between the two test platforms, since the primary peak occurs at essentially the same frequency and since the differences in flow vectoring are known from earlier PIV measurements to be minor for $Re_{jet} > 400$. One apparent advantage of the planar configuration is the higher secondary spectral

velocity peak, which may enable the study of flow response to a higher forcing frequency around 2600 Hz, where the jet speed is only 25% lower than at the primary peak. There are two possible reasons for these differences in performance: actuator construction and the volume of the external cavity on the opposite side of the piezoelectric disc. The actuator base is made of aluminum, compared to the stereolithographed epoxy of the axisymmetric model, and the base is thicker, both of which make the structure more rigid. Additionally, the volume bounding the external side of the piezoelectric disc is about 18 times smaller for the planer jet than the axisymmetric jet, but this is still 18 times larger than the volume of the actuator chamber (which is the same in both designs). For all experiments in this chapter, the actuation frequency is 1 kHz unless noted.

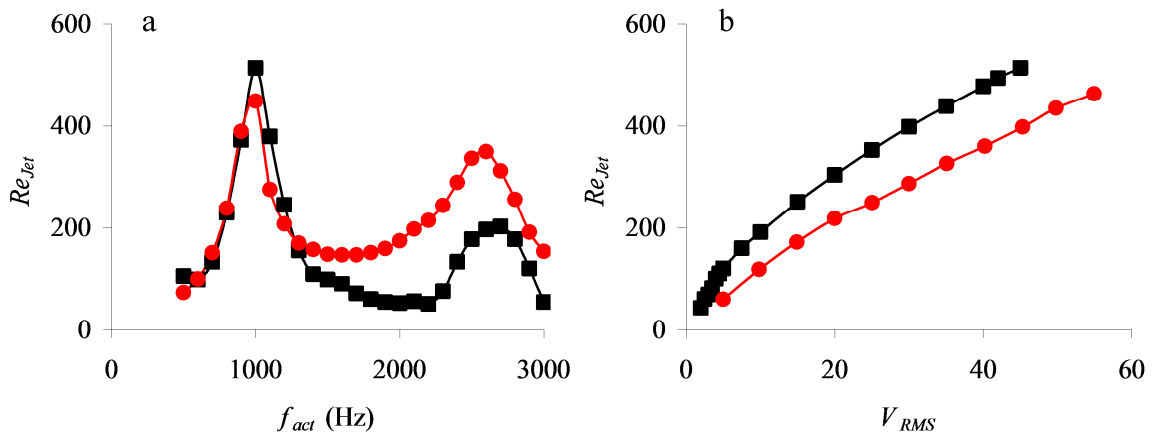


Figure 30. Comparison of actuator performance: (a) frequency response at $45 V_{RMS}$, (b) variation with input voltage at $f_{act} = 1$ kHz.
 ■ Axisymmetric actuator, ● Planar actuator

Prior to the investigation of the interaction with the cross flow, it is useful to characterize the effect of actuation in the presence of the flow surfaces but in the absence

of a cross flow. High resolution phase-averaged PIV measurements shown in Figure 31 indicate the size and trajectory of the individual vortices ejected during a single actuation cycle for $Re_{Jet} = 407$. The sequence of images begins at the onset of the suction stroke (first half of the actuation cycle), $0 < \phi < 180^\circ$. The vortex ejected during the prior blowing stroke is evident immediately downstream of the orifice at $\phi = 0^\circ$ (Figure 31a). As the cycle progresses between $\phi = 0^\circ$ and 120° (Figure 31a-d), the earlier vortex is advected along the Coanda surface while its core remains at a nominally fixed distance above the surface. It is also noteworthy that its distance from the orifice increases slowly compared to the speed of ejection, ostensibly as a result of the concomitant actuator suction. (The core moves at about 5 m/s between $\phi = 0^\circ$ and 120° compared to neighboring jet velocities exceeding 30 m/s). The velocity vectors indicate that during this progression the flow around the vortex core slows as it diffuses, and throughout there is a stagnant region to the upper right (downstream) of the field of view that suggests the downstream flow (beyond the vortex) exits the interaction domain without recirculation. Concurrently the upstream flow appears to be entrained from the region above and to the left of the vortex, intertwined with the adjoining suction flow into the orifice (discussed below); there is even a clear dividing line (moving slowly downstream as the cycle progresses from $\phi = 40^\circ$ to 180°) evident between the flow feeding into the orifice and flow being entrained synergistically by the downstream vortex. While up to about $\phi = 120^\circ$ there is an induced upstream flow (to the left and above the vortex core), the magnitude of the induced reverse flow (above the vortex) diminishes by $\phi = 180^\circ$ (Figure 31e) while the streamwise flow between the core and the surface intensifies. This trend continues to $\phi = 220^\circ$ (Figure 31f) where the induced reverse flow above the core is

immeasurable as the core moves away from the orifice (and the surface). It is remarkable that even though the vorticity concentration within the core seems to diminish because of spreading, the induced velocity between the core and the surface is still significant even as the next vortex is being ejected at $\phi = 260^\circ$ (Figure 31g).

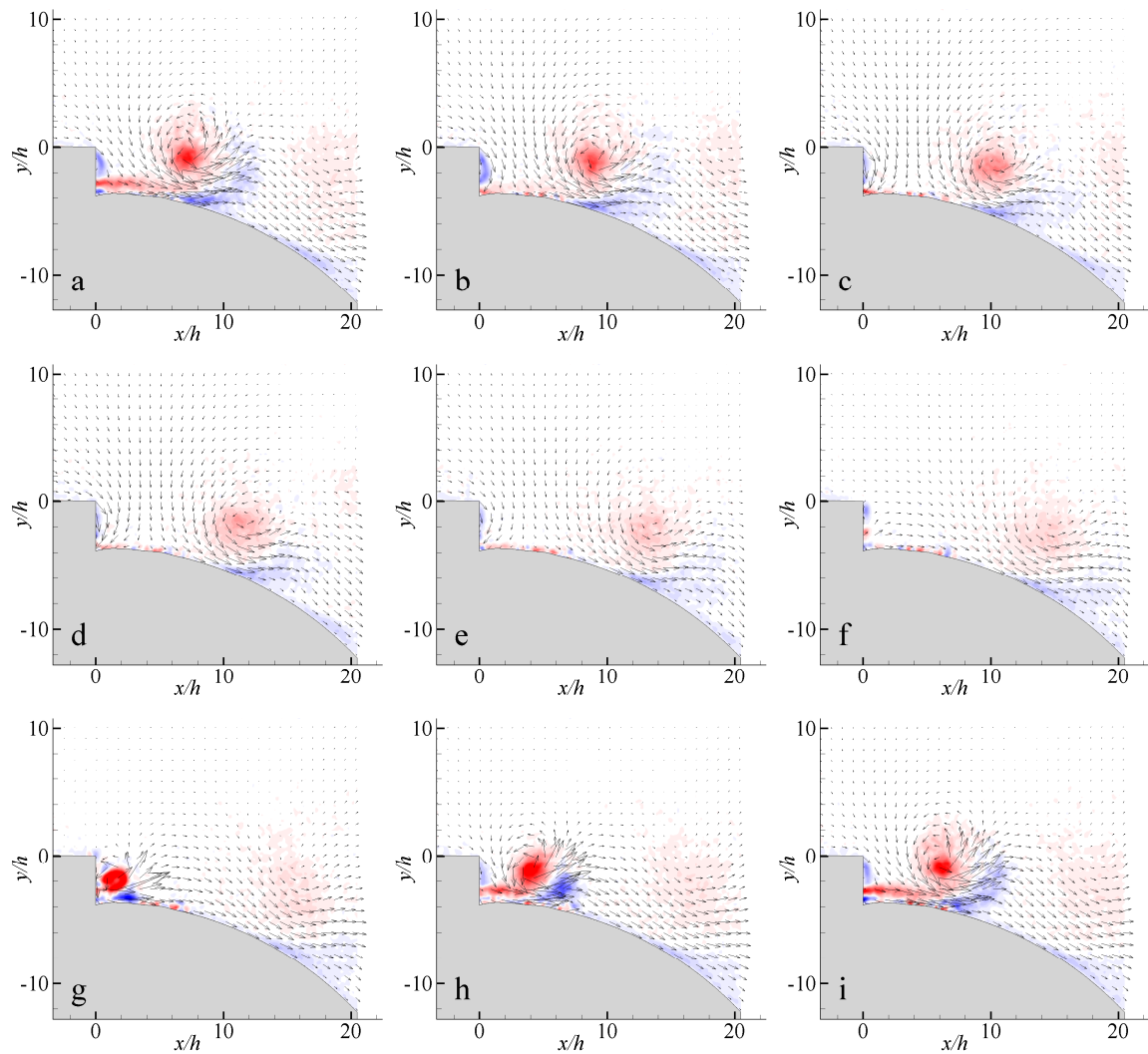


Figure 31. Phase-averaged PIV images in the cross-stream (x - y) plane at center-span of a synthetic jet issuing into a quiescent medium, $Re_{Jet} = 407$. (a) $\phi = 0^\circ$, (b) 40° , (c) 80° , (d) 120° , (e) 180° , (f) 220° , (g) 260° , (h) 300° , (i) 340° .

Vorticity scale: $-100,000$  $100,000$ 1/s. Vector length $\rightarrow = 30$ m/s.

The suction flow occurs along the orifice edge and the region directly above it with peak suction occurring at $\phi = 90^\circ$ as might be expected. It is noteworthy that at least in this center-span plane, the predominant source of the fluid flowing into the actuator is from above and upstream of the orifice edge, not along the Coanda surface. In fact, during the later stages of suction ($80 < \phi < 180^\circ$, Figure 31c-e), there is a clear dividing streamline that ends with a stagnation point between the suction and vortex flows approximately one orifice step height downstream along the Coanda surface, where the flow upstream of the division is directed toward the orifice while the flow downstream is induced by the prior vortex. As the blowing phase begins at $\phi = 180^\circ$ (Figure 31e), there is a small lag in the expected outward response at the orifice as a low level of suction remains apparent. From this point the prior vortex appears to move horizontally, with increasing separation from the surface as the flow spreads underneath it. A newly ejected vortex is apparent by $\phi = 260^\circ$ (Figure 31g), whose core diameter expands to almost twice the orifice step height by $\phi = 340^\circ$ (Figure 31i). This expansion is accompanied by induced entrainment of flow from above in a manner similar to the suction earlier in the cycle. The entrainment continues as the vortex simultaneously moves downstream with the early stages of the next suction stroke, until the division in the flow between the orifice and vortex becomes evident again around $\phi = 80^\circ$ (Figure 31c) during the next suction stroke.

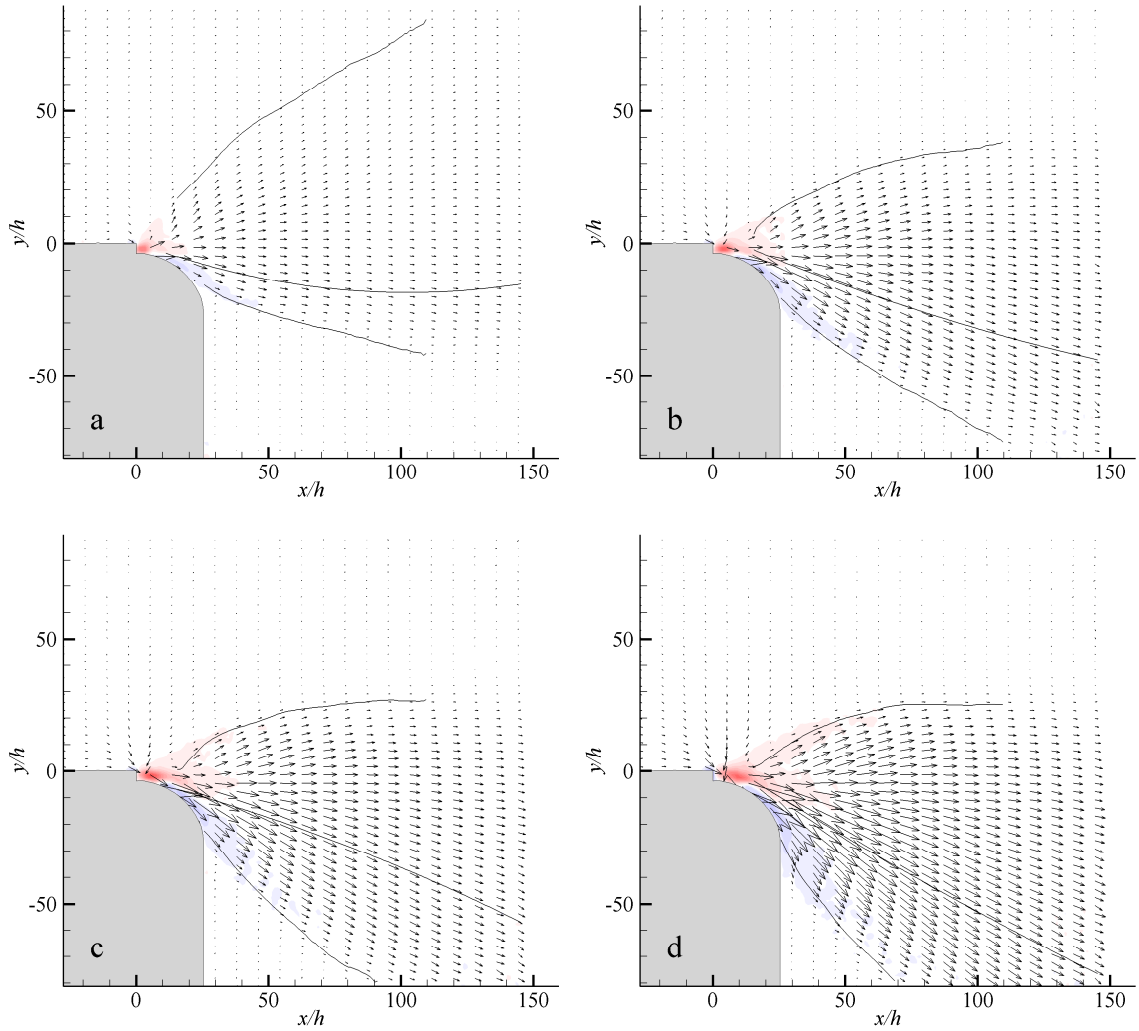



Figure 32. Time-averaged PIV images at center-span of a synthetic jet issuing into a quiescent medium. The contour lines show the streamwise variation of the cross-stream elevations of the jet's centerline velocity U_{cl} and of jet speeds (on both sides of the centerline) that are $0.2 U_{cl}$. (a) $Re_{Jet} = 145$, (b) 218, (c) 291, (d) 407. Vorticity scale: $-10,000$  $10,000$ 1/s. Vector length $\rightarrow = 3.5$ m/s.

It is also useful to consider the time-averaged jet structure for various jet strengths, as shown in Figure 32. For clarity, lines are overlaid on the vector plots to indicate the centerline of the jet as defined by the peak velocity at each streamwise position, as well as the cross-stream elevations where the velocity magnitude is 20% of

the peak velocity thereby marking the width of the jet. At $Re_{Jet} = 145$ (Figure 32a), the jet flow can be detected over most of the field of view, even on the far right of the image at $x/h = 145$. While the jet centerline is slightly below the orifice, the flow spreads much farther on the upper side away from the surface, reaching to the top of the field of view. This asymmetric spreading is probably associated with asymmetric entrainment. The jet initially expands along the Coanda surface, but appears to separate from it after turning through 45 degrees of the Coanda radius curvature. After separating from the surface, the vectoring of the flow along the lower boundary initially decreases and then remains constant over the remainder of the range plotted. The flow along the centerline is also vectored slightly downward initially, but then becomes parallel to the x axis by $x/h = 100$. As jet strength is increased to $Re_{Jet} = 218$ (Figure 32b), flow adherence to the Coanda surface increases, with the centerline of the jet now achieving a downward angle of about 20° below the x-axis throughout most of the range (tapering off a few degrees slowly after $x/h = 80$), with greater spreading of the jet into the domain downstream of the backward facing step. Much of the jet flow above the centerline is also vectored downward, however this segment of the jet spreads faster in the cross-stream direction and its upper bound is still angled upward throughout the measurement domain. Increasing to $Re_{Jet} = 291$ (Figure 32c) further enhances the downward vectoring, with the centerline angle increasing slightly with downstream distance but remaining about 20° below the x-axis, while the upper bound levels off within the range plotted. Finally, at $Re_{Jet} = 407$ (Figure 32d) the centerline vectoring angle increases to about 30° below the x-axis, tapering off a few degrees for $x/h > 110$. The jet appears to follow the entire Coanda surface curvature but separates near its downstream end, and the flow segment

below the centerline continues to move downward. The upper bound is vectored upward initially, but levels off by $x/h = 75$.

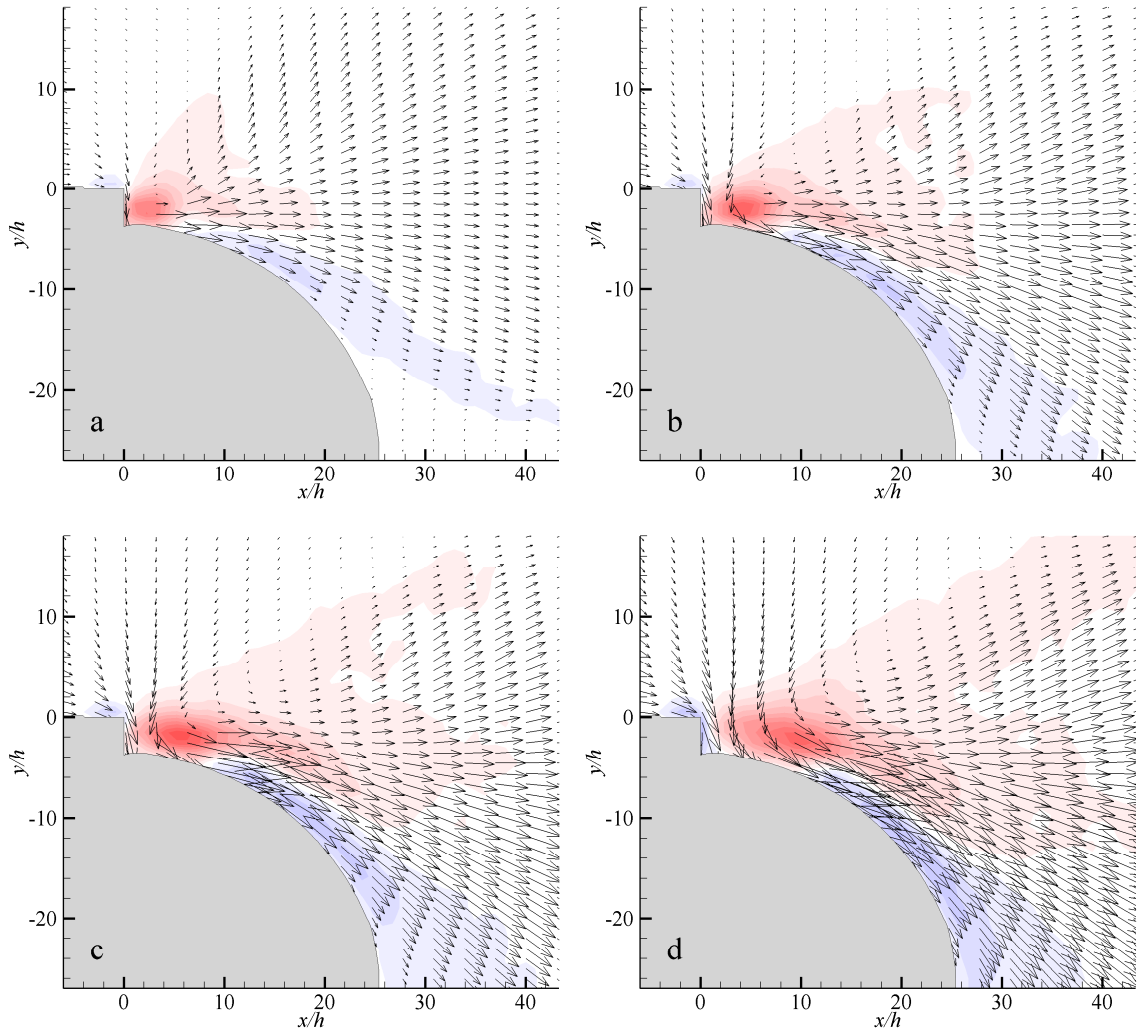
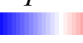


Figure 33. Closer view of time-averaged cross-stream flow field at center-span of a synthetic jet issuing into a quiescent medium. (a) $Re_{Jet} = 145$, (b) 218, (c) 291, (d) 407. Vorticity scale: $-10,000$  $10,000$ 1/s. Vector length $\rightarrow = 2.5$ m/s.

A close-up view of the time-averaged flow field is shown in Figure 33. The entrainment of upstream ambient fluid toward the orifice is visible directly above the

orifice edge for all jet strengths, as discussed in connection with Figure 31. In fact, a time-averaged reverse flow (upstream) is evident within the downward flow above the orifice, most notably for $Re_{Jet} = 291$ and 407 between $6 < x/h < 12$. The time-averaged vorticity concentrations are clearly evident, with red counter-clockwise concentrations immediately adjacent to the orifice, and blue clockwise concentrations spreading downstream adjacent to the Coanda surface, both of which intensify and expand with jet strength. The boundary formed between these two concentrations and extending along the upper edge of the blue concentrations defines the centerline of the jet as illustrated in Figure 32. Perhaps the most striking feature of the close-up view is the rapid, extensive cross-stream spreading of the upper edge of the jet; this actuator configuration does not produce a wall jet that simply follows the curved surface as is normally observed in two-dimensional jets over Coanda surfaces (e.g. Newman 1961). It is conjectured that this difference is attributed to the strong entrainment from above and the upward deflection of the induced flow by the discrete vortex structures issuing with each jet cycle as seen during the later stages of the blowing stroke in Figure 31. These structures generate a locally recirculating flow that vectors a portion of the induced flow upward on the downstream side which may be central to the observed upward cross-stream spreading. The difference in cross-stream spreading above and below the jet centerline may also be attributed to interaction of the jet with the floor surface below the backward facing step.

5.3 The Baseline Flow over the Backward-Facing Step

Prior to the investigation of the jet interaction with the cross flow, the baseline flow over the surface of the step is first established and characterized in some detail. In preliminary experiments the boundary layer thickness and turbulence intensity upstream of the jet orifice was found to influence the interaction between the jet and the cross flow, particularly if the boundary layer thickness scales with the jet interaction domain. As mentioned in Section 5.1, the present facility is equipped with a suction slot 100 mm upstream of the interaction domain ($\sim x/h = -222$), along the false floor which extends to the upper corner of the orifice edge. The small portion of the flow which is removed (0.35%) is returned back to the inlet of the tunnel blower, bypassing the test section. This suction feature allows for the modification or removal of the boundary layer, allowing for the development of a thinner boundary layer in the 100 mm range leading to the interaction domain.

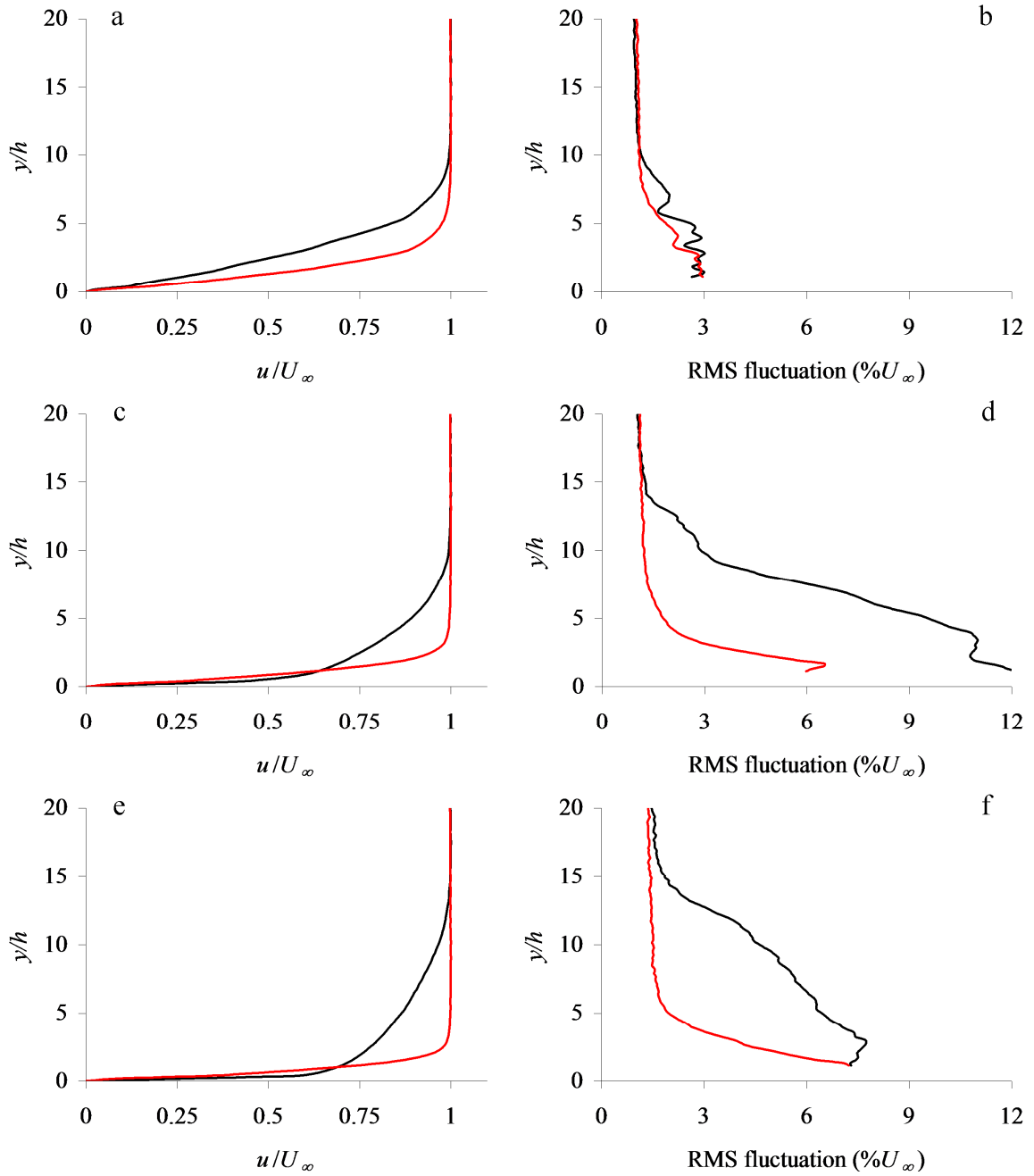


Figure 34. Effect of upstream suction on cross-stream distributions of streamwise velocity and the RMS fluctuation of streamwise velocity: (a & b) $U_\infty = 10$ m/s, (c & d) 20 m/s, and (e & f) 30 m/s. (—) Baseline without suction and (—) with suction

Shown in Figure 34 are cross-stream distributions of streamwise velocity profiles at $U_\infty = 10, 20,$ and 30 m/s (Figure 34a, c, and e, respectively), and the corresponding RMS fluctuations of the streamwise velocity (Figure 34b, d, and f), with and without suction, at $x/h = -50$ (immediately upstream of the orifice edge) in the absence of actuation. As is clearly evident from distributions of the streamwise velocity, the suction substantially changes the thickness of the boundary layer at the three free stream speeds. In the presence of suction, the boundary layer is substantially (up to three times) thinner with strong cross-stream gradients. The largest changes occur at $U_\infty = 30$ m/s where the displacement thickness (normalized by h) is reduced from 1.89 to 0.91 with suction, and the momentum thickness (normalized by h) is reduced from 1.29 to 0.33. Even more noteworthy are the changes in RMS fluctuations of the streamwise velocity. It should first be noted that the RMS fluctuations appear to converge to constant values by $y/h = 20$ indicating the turbulence level within the free stream, which over the velocity range studied vary from 1.03 to 1.35%, and are almost independent of suction for $y/h > 15$. At $U_\infty = 10$ m/s (Figure 34b), the effect of suction on the RMS fluctuations is minimal, essentially smoothing the fluctuations for $y/h < 10$. At $U_\infty = 20$ m/s (Figure 34d), the effect of suction is substantial and the flow reaches the free stream level by $y/h = 8$. Further, the magnitude of the peak fluctuation level in the presence of suction is reduced by about half and the cross-stream elevation is closer to the surface. At $U_\infty = 30$ m/s (Figure 34f), the baseline fluctuations are notably smaller than at $U_\infty = 20$ m/s for $y/h < 8$, suggesting that perhaps the flow was transitioning to turbulence around $U_\infty = 20$ m/s. However, as these measurements were only 75 mm downstream from the suction slot, the flow by this position only reaches $\frac{3}{4}$ of the minimum critical flat-plate Reynolds number

(2×10^5) even at $U_\infty = 30$ m/s. More likely this reduction in baseline fluctuations is thought to be related to the performance of the tunnel blower and lack of true upstream plenum prior to the contraction, which perhaps stabilizes to form a plenum-like performance only under higher loads. At this velocity the peak measured fluctuation magnitude is not significantly altered by suction, but the position is again much closer to the surface, and the fluctuation distribution is greatly improved over the measured range. It should be noted that while velocity measurements are plotted for $y/h < 1$, RMS fluctuations are limited by the spatial resolution of the PIV measurements near the surface as they are sensitive to errors filtered by the averaging of velocity measurements.

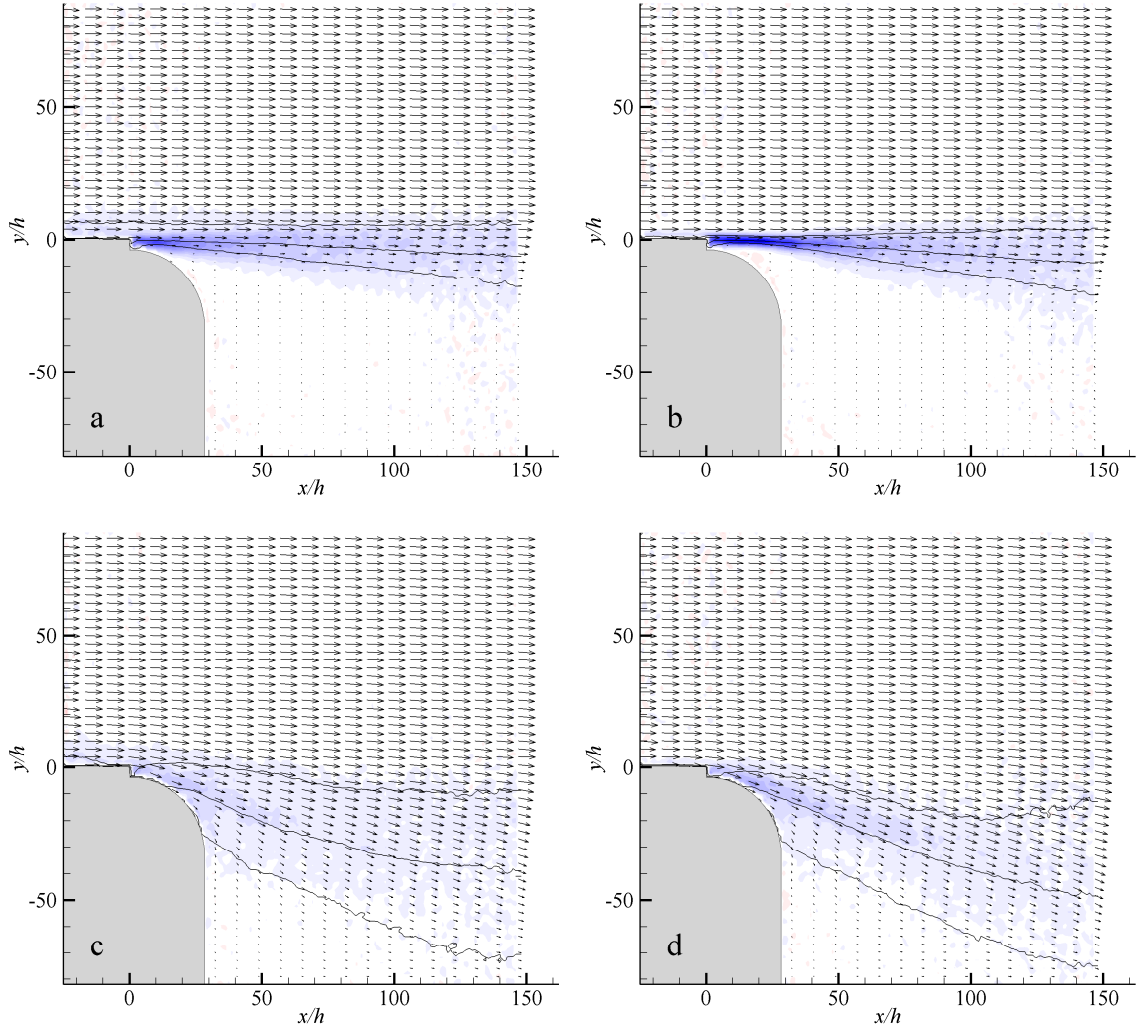



Figure 35. The effect of upstream suction on the interaction of the synthetic jet with the cross flow at $U_\infty = 30$ m/s: (a) baseline flow without suction, (b) baseline flow with suction, (c) response to actuation without suction, (d) response to actuation with suction. Line contours indicate velocity magnitudes of 0.2, 0.5, and 0.9 U_∞ . Vorticity scale: -20,000  20,000 1/s. $y/h > 50$: Vector lengths indicate 30 m/s.

The effects of suction on the interaction domain between the jet and cross flow are shown in Figure 35 (at $U_\infty = 30$ m/s) including the baseline flow (Figure 35a, b), and (as a prelude to Section 5.4) with the interaction between the synthetic jet and the cross flow (Figure 35c, d). Contour lines overlaid on the vector plots indicate velocity

magnitudes at levels of 0.2, 0.5, and 0.9 U_∞ . For the baseline flow (Figure 35a, b), it appears that the suction results in a reduction in the cross-stream spreading of the shear layer that forms downstream of the backward step with higher vorticity concentration, as would be expected given the thinner upstream boundary layer. However, farther downstream ($x/h > 75$) there is little difference between the shear layers in the absence and presence of suction. The flow response to synthetic jet actuation (Figure 35c, d) has a slightly more visible and lasting receptivity to upstream suction. Certainly even in the absence of suction, the actuation results in significant flow attachment to the Coanda surface (Figure 35c). However the addition of suction diminishes the cross-stream width of the layer without reducing the degree of vectoring as the low speed sides of the shear layer are almost identical (Figure 35c, d).

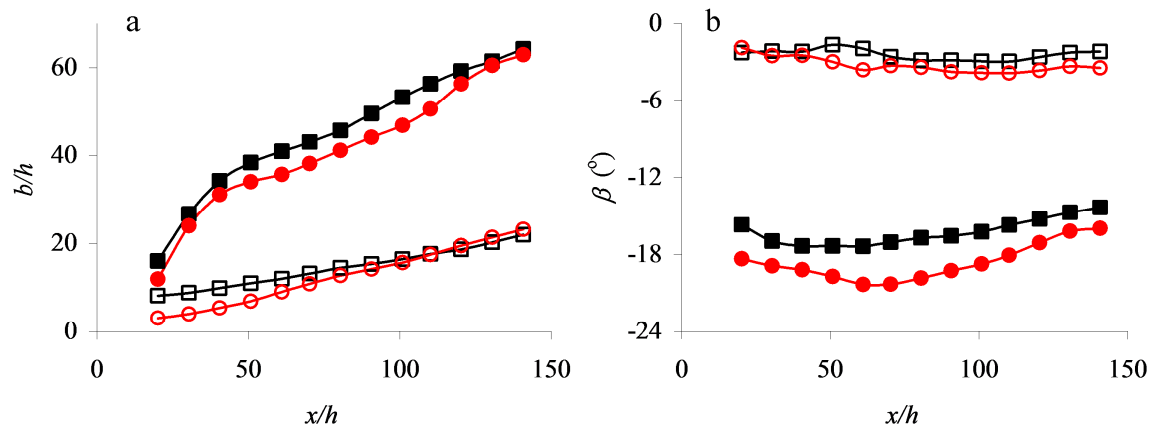


Figure 36. Analysis of PIV data shown in Figure 35 regarding effect of upstream suction on the interaction of the synthetic jet with the cross flow at $U_\infty = 30$ m/s: Streamwise variations of (a) the shear layer's cross-stream width and (b) the angle of the momentum flux vector calculated between cross-stream elevations of 0.2 and 0.9 U_∞ . \square Baseline flow without suction, \circ Baseline flow with suction, \blacksquare Actuated flow without suction, \bullet Actuated flow with suction

These differences are better quantified by considering the streamwise variations of the shear layer's cross-stream width between cross-stream elevations of velocities in the band between 0.2 and 0.9 U_∞ , and the angle of the momentum flux vector calculated between the same elevations. As expected, the layer widths in Figure 36a correspond well to the observations of the PIV (Figure 35). In the absence of actuation the shear layer grows linearly streamwise but the growth rate with suction is higher and while closer to the step suction results in a narrower layer, for $x/h > 120$ the width of the layer with suction slightly exceeds the width in the absence of suction. In the presence of actuation, the cross-stream spreading of the layer is considerably higher and exhibits two roughly linear domains. For $x/h < 50$ the growth rate is significantly higher (almost double) than for $x/h > 50$. As noted in connection with Figure 35c and d, suction results in a somewhat narrower layer for $x/h < 120$. Figure 36b shows that suction has little effect on the baseline flow, with a slight increase in downward vectoring of typically one degree. However in the presence of actuation, suction clearly increases flow vectoring throughout the field of view by two or three degrees. This effect is not surprising since the thinner boundary layer results in interaction of the jet with higher momentum fluid. The suction leads to enhanced vectoring by up to four degrees around $x/h = 70$ which diminishes somewhat with streamwise distance thereafter. Given the great improvements in flow quality and only slight changes in flow response, the rest of the present experiments were conducted with the application of upstream suction.

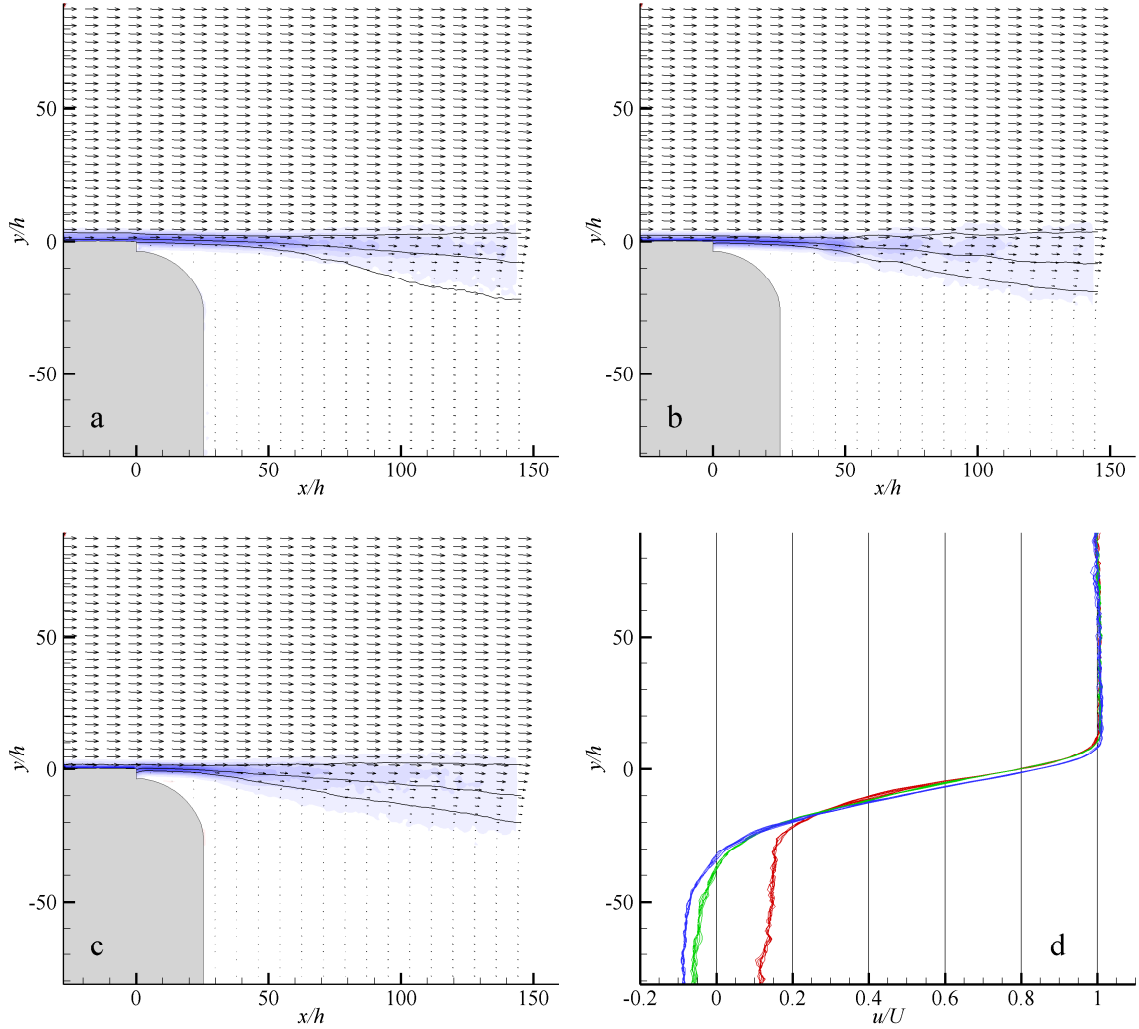


Figure 37. Time-averaged baseline flow field in the absence of actuation: (a) $U_\infty = 10$, (b) 20, and (c) 30 m/s. Line contours indicate 0.2, 0.5, and 0.9 U_∞ . Vorticity scale: -20,000 20,000 1/s. $y/h > 50$: Vector lengths indicate U_∞ . (d) Individual cross-stream distributions of streamwise velocity at $x/h = 140$: (—) $U_\infty = 10$, (—) 20, and (—) 30 m/s.

The baseline flow field is further characterized using PIV in the presence of suction. Images of the baseline flow (with suction, without jet actuation) are shown in Figure 37 for $U_\infty =$ (a) 10, (b) 20, and (c) 30 m/s. In each of these figures the velocity components are normalized by the corresponding free stream speed for comparison.

While the effects of the back-facing step on the upstream flow ($x/h < 20$) are minimal, there is a noticeable change in the low-speed edge of the shear layer for $x/h > 40$, which spreads slightly with increasing free stream speed (denoted more by the vorticity than the $0.2 U_\infty$ contour line), and begins spreading earlier (farther upstream) with increasing free stream speed. To further illustrate this, normalized cross-stream velocity profiles at $x/h = 140$ are shown in Figure 37d. These profiles clearly show that the width of the shear layer increases with a low-speed transition (in du/dy) that becomes more gradual with increasing free stream speed. However these profiles overlap almost identically over the majority of the shear layers' widths. The profiles also show differences in the wake flow on the low speed side of the shear layers, in magnitude and direction. At $U_\infty = 10$ m/s, the transition to wake flow from the shear layer is abrupt and the wake below has a streamwise velocity component near $0.15 U_\infty$. At $U_\infty = 20$ m/s the transition from shear layer to wake is much more gradual, and in fact the velocity reverses direction for $y/h < -40$. At $U_\infty = 30$ m/s the shear layer is still larger, and the transition to wake is smooth, converging to a near-constant reverse flow with a magnitude of about $0.08 U_\infty$, part of the greater recirculation expected behind a backward-facing step.

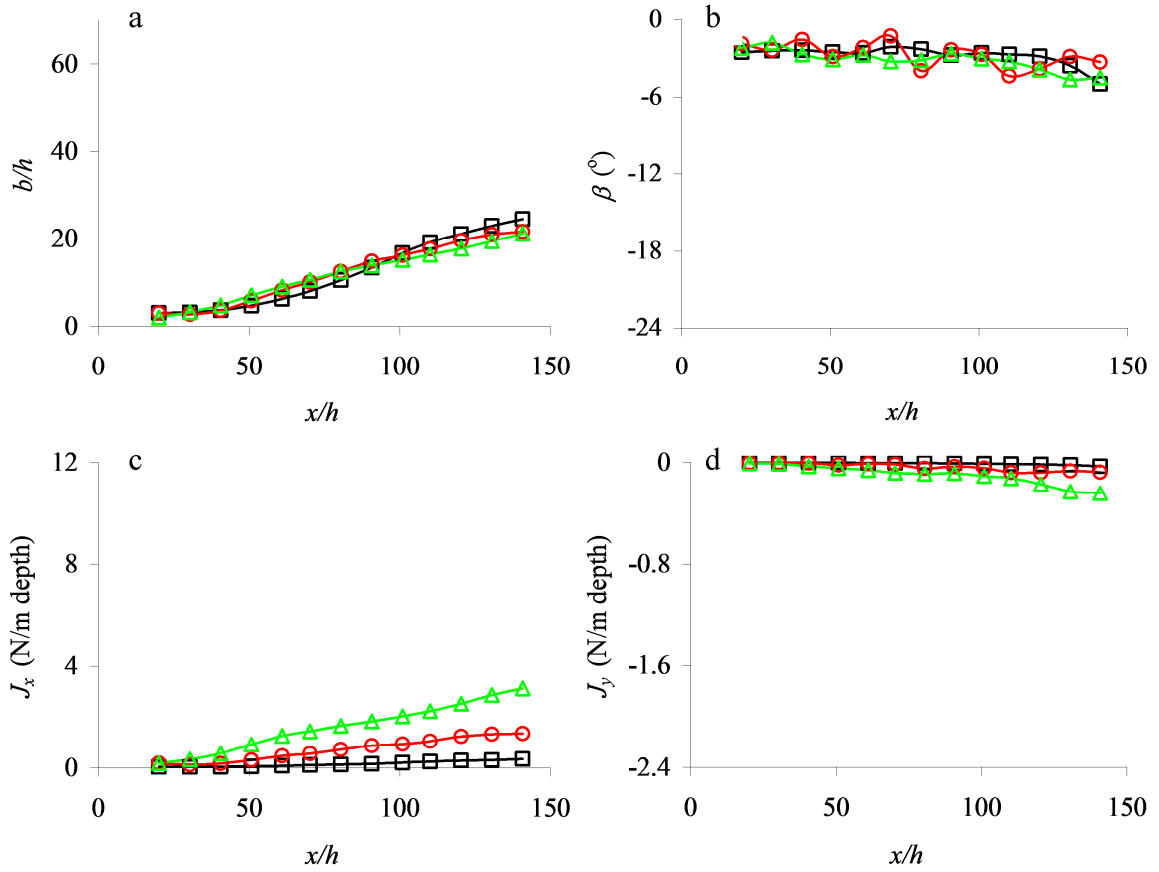


Figure 38. Analysis of PIV data shown in Figure 37 regarding the baseline flow at three free stream speeds: Streamwise variations of (a) the shear layer's cross-stream width, (b) the angle of the momentum flux vector, (c) the streamwise component of momentum flux, and (d) the cross-stream component of momentum flux calculated between cross-stream elevations of 0.2 and $0.9 U_\infty$. $U_\infty = \square 10, \circ 20, \triangle 30$ m/s

For completeness, these baseline PIV measurements were further analyzed by considering the streamwise variations of the shear layer's cross-stream width between cross-stream elevations of 0.2 and $0.9 U_\infty$, and the components and angle of the momentum flux vector calculated between the same elevations. The analysis is shown in Figure 38. The vertical scales were chosen to be comparable to those of experiments with actuation (discussed in later sections) for direct comparison and reference. In terms

of layer width and momentum flux vector angle, the three free stream speeds show almost identical behavior. Not surprisingly the streamwise momentum flux increases with U_∞ , as well as x/h (as the shear layer entrains fluid from the free stream). There is a small increase in cross stream momentum flux certainly for $U_\infty = 30$ m/s, likely also attributed to the entrainment of free stream fluid combined with the expected reattachment of the flow further downstream.

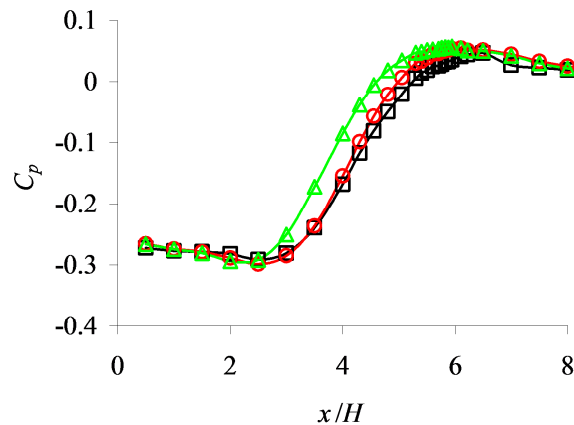


Figure 39. Streamwise variation of the static pressure along the test section floor in the absence of actuation: $U_\infty = \square$ 10, \circ 20, \triangle 30 m/s

To further characterize the global flow field (beyond the field of view of the PIV measurements), streamwise distributions of the static pressure coefficient C_p (normalized by the free stream dynamic pressure) were measured on the test section floor downstream of the step for the three free stream speeds as shown in Figure 39. These measurements indicate the presence of a recirculation domain downstream of the step within $x/H < 2.5$ where pressure is nearly invariant, followed by a recovery to reattachment via an adverse

pressure gradient through $x/H = 6$ where reattachment occurs, followed by the natural favorable pressure gradient in the test section. As shown by earlier investigators (e.g. Eaton and Johnston, 1981) the flow downstream of a backward facing step typically attaches within approximately five to seven step heights downstream of the step. These data show that the increase in free stream speed leads to an upstream migration of the attachment point by an increment of $0.5 x/H$, and a small increase in the magnitude of the adverse pressure gradient. The transition through the adverse pressure gradient occurs noticeably farther upstream for $U_\infty = 30$ m/s, likely where entrainment into the shear layer is strongest.

5.4 Interaction of the Synthetic Jet with the Cross Flow

It was shown in Section 4.2 that for a given free stream speed, the vectoring of the flow over the Coanda surface is proportional to jet strength. The present study considers not only the dependence of flow vectoring on this variation in jet strength, but also the effects of matched ratios of jet and free stream speeds and the variation of free stream speed for a given jet strength. The effects of variation in jet strength for a fixed free stream speed is shown in Figure 40, using time-averaged PIV data obtained in a plane through the centerline of the jet orifice, at $U_\infty = 30$ m/s. (The baseline flow without actuation is shown in Figure 37c.) The corresponding plots in Figure 41, show the normalized cross-stream width of the flow between the contours 0.2 and $0.9 U_\infty$ as well as the momentum flux vector components and angle between the same contours. Baseline data is also plotted for comparison.

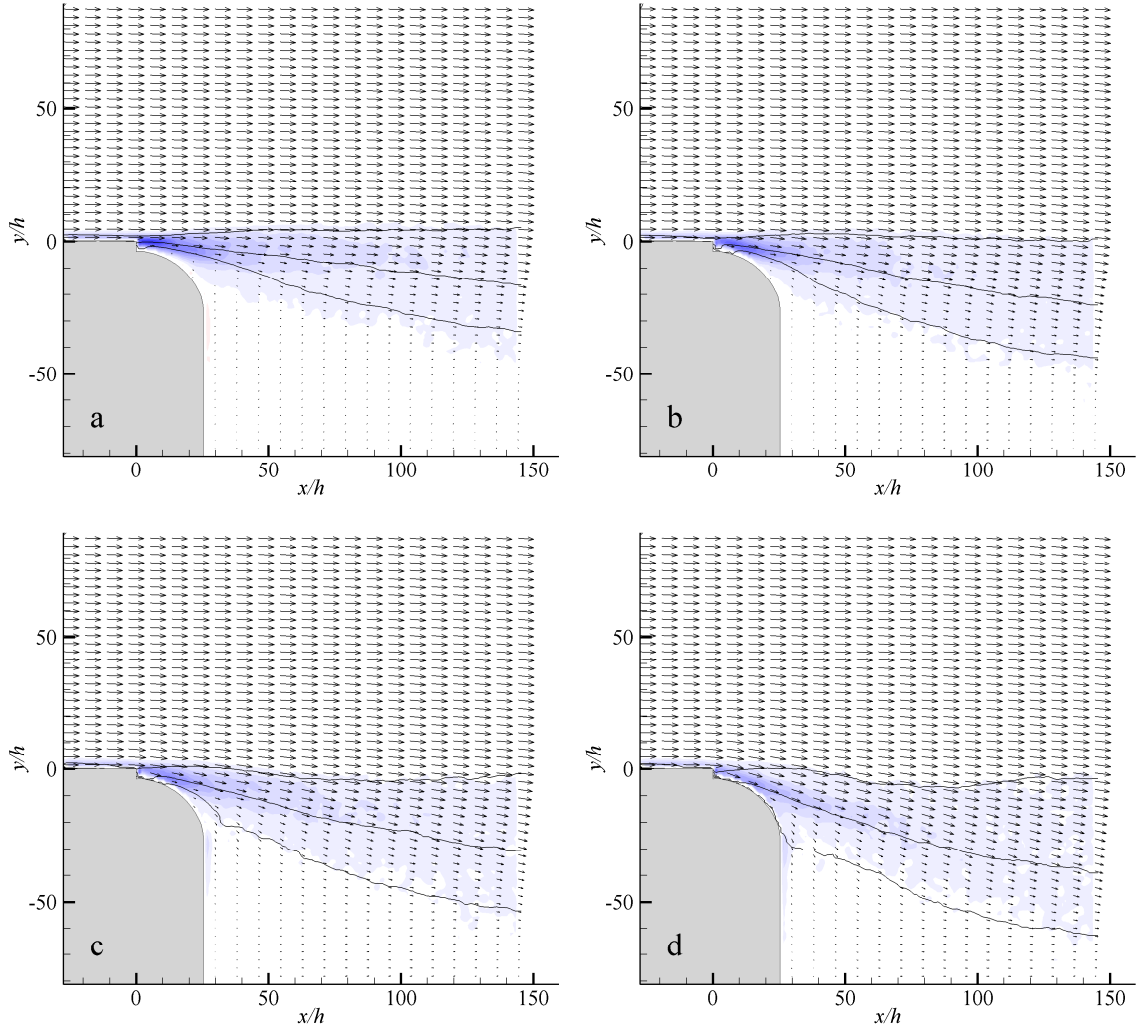



Figure 40. PIV images of the time-averaged flow field response to actuation at four jet strengths while $U_\infty = 30$ m/s: (a) $Re_{Jet} = 145$, (b) 218, (c) 291, (d) 407. Line contours indicate 0.2 , 0.5 , and $0.9 U_\infty$. Vorticity scale: $-20,000$  $20,000$ 1/s. $y/h > 50$: Vector lengths indicate 30 m/s.

As discussed earlier in connection with Figure 37, in the absence of actuation the flow separates at the upper corner of the orifice edge, forming a shear layer over the wake behind the step whose width grows linearly as shown in Figure 41a. Within the presented field of view (spanning $x/H = 1.6$) the unforced flow vectors 2-4 degrees below the x-axis, as shown in Figure 41b. In the presence of slight actuation at $Re_{Jet} = 145$, the flow

in Figure 40a appears to maintain separation at the upper corner of the orifice edge, but the corresponding plots in Figure 41 show significant streamwise effects. For example the shear layer width is greater than the baseline by a b/h increment of about 10 over most of the range. In measurements without a cross flow (Figures 32 and 33), this case ($Re_{Jet} = 145$) exhibited a relatively wide range of influence despite its low strength, but did not particularly cause downward vectoring beyond the area adjacent to the Coanda surface ($x/h < 30$). That localized effect is evident here in the presence of a cross flow in Figure 41b as shown by the sharp decline of momentum flux vector angle down to -6 degrees by $x/h = 40$, where after the vector angle holds almost constant. Incrementing to $Re_{Jet} = 218$, Figure 40b, the flow vectoring intensifies but it still does not appear to attach to the Coanda surface. The shear layer is wider and vectors further downward across the view, as also indicated in Figure 41, and small changes in the velocity field are evident across much of the wake downstream of the step. A similar trend continues as the jet strength is increased to $Re_{Jet} = 291$ (Figure 40c), and some attachment to the Coanda surface begins to occur. By $Re_{Jet} = 407$, the flow is fully attached to the Coanda surface and the shear layer is substantially wider, as reflected most notably by the $0.2 U_\infty$ contour adhering to the Coanda surface throughout the full 90 degree span of the radius, and its ensuing lower streamwise path. These results are in good agreement with the measurements in the absence of a cross flow (Figure 32), except that attachment to the Coanda surface occurs farther upstream in the absence of the cross flow, since the jet actuation alters the momentum of the cross flow near the surface.

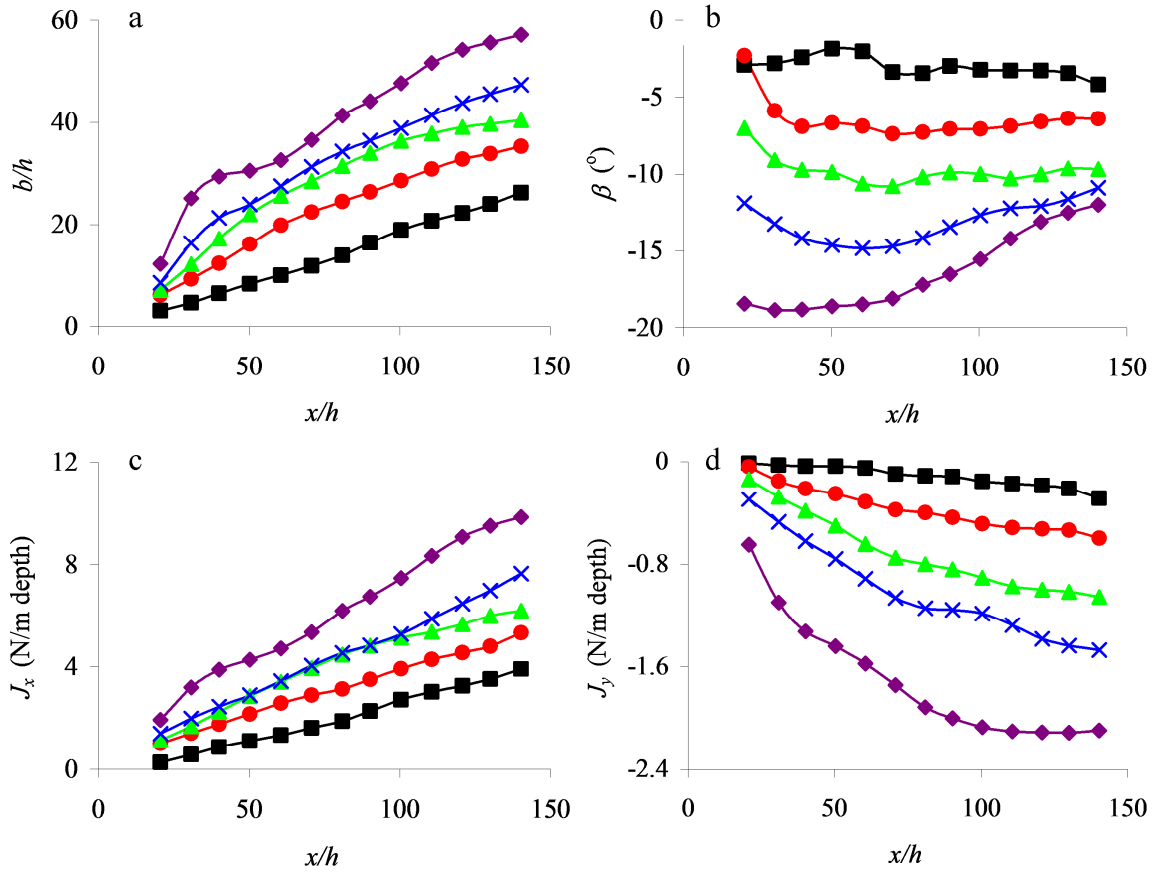


Figure 41. Analysis of PIV data shown in Figure 40 regarding the flow response to actuation at four jet strengths while $U_\infty = 30$ m/s: Streamwise variations of (a) the shear layer's cross-stream width, (b) the angle of the momentum flux vector, (c) streamwise momentum flux, and (d) cross-stream momentum flux calculated between cross-stream elevations of 0.2 and $0.9 U_\infty$. $Re_{Jet} = \blacksquare 0$ (baseline), $\bullet 145$, $\blacktriangle 218$, $\times 291$, $\blacklozenge 407$

In terms of overall trends, the plots in Figure 41 show quite clearly that whether speaking of shear layer width or momentum flux, at a fixed free stream speed the effect of increasing jet strength is incremental improvements in performance across the field of view. The streamwise variation of layer width and momentum flux is mostly linear beyond the interaction domain of the jet with the cross flow ($x/h > 50$). The increment in layer width and streamwise momentum flux between $Re_{Jet} = 218$ and 291 is less than that

of $Re_{Jet} = 145$ and 218 , suggesting a shift in the flow vectoring mechanism at higher strengths likely related to the Coanda surface attachment noted above. Also, for $Re_{Jet} > 218$, the flux vector angle increases with downstream distance, and occurs earlier with increasing jet strength, suggesting a limit on the downstream reach of the jet-induced effect; for $Re_{Jet} = 406$, the vector angle rises from -19 degrees at $x/h = 40$ to -12 degrees at $x/h = 140$. As such a volume of the free stream is entrained into the shear layer by the actuation it is not surprising that the streamwise momentum flux of the band between 0.2 and $0.9 U_\infty$ increases with jet strength and streamwise distance. However despite evidence elsewhere of saturation at higher jet strengths, the cross-stream momentum flux for $Re_{Jet} = 407$ occurs with great increment over lower strengths, and only stabilizes for $x/h > 110$. The data of Figure 41 were also plotted in terms of Re_{Jet} at a few streamwise positions, in Figure 42. These data show that the shear layer width and streamwise momentum flux increase linearly with Re_{Jet} , while the rate of change of cross-stream momentum flux increases with Re_{Jet} . The sensitivity of momentum flux vector angle to Re_{Jet} decreases slightly with streamwise distance, certainly for $Re_{Jet} > 250$.

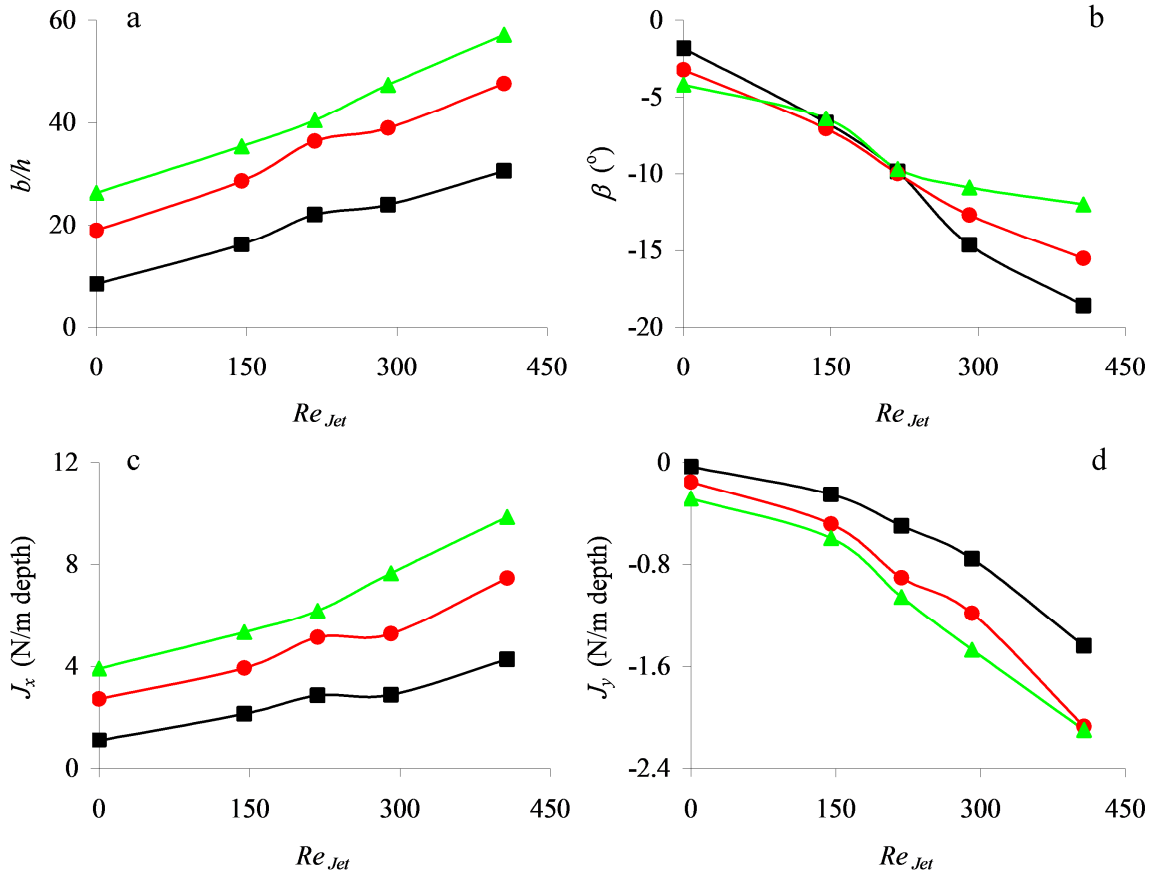


Figure 42. Data of Figure 41 re-plotted in terms of variation with jet strength at three streamwise positions: $x/h = \blacksquare 50, \bullet 100, \blacktriangle 140$

The effect of actuation at jet speed (averaged outstroke velocity normalized only by the blowing period $T_{Jet}/2$, or equivalently $U_{Avg} = 2*U_{Jet}$) matched to the free stream at $U_\infty = 10, 20, \text{ and } 30 \text{ m/s}$ is shown in Figure 43. All three cases are at the same dimensionless momentum coefficient, C_{μ} , a parameter often discussed in flow control that as shown here can result in different flow responses even at the same setting. In the figures the velocity vector magnitude of each data set has been normalized by the corresponding free stream speed to facilitate direct comparison of the PIV vector plots at the different speeds. When $U_\infty = U_{Avg} = 10 \text{ m/s}$ ($Re_{Jet} = 145$, Figure 43a), as might be

expected from the prior discussion related to Figure 40, the actuation does not exhibit much effect. In fact the integral quantities in Figure 44 show a very weak response primarily indicated by changes in momentum flux vector angle within the jet interaction domain $x/h < 50$. As was established in earlier measurements without a cross flow (Figure 32), the evolution of the jet at $Re_{Jet} = 145$ is very different from the other two velocities explored ($Re_{Jet} = 291$ and 407), with little attachment to the Coanda surface and only slight vectoring. In comparison to the baseline measurement at this free stream (Figure 37a), it is clearly evident that the effect caused by actuation at this low level disappears by $x/h = 140$, despite minor attachment to the Coanda surface as reflected by the $0.2 U_\infty$ contour. Unlike the other two (stronger) velocities explored, this jet strength ($Re_{Jet} = 145$) has a greater streamwise effect at $U_\infty = 30$ m/s (Figure 40a) for $x/h > 50$ in terms layer width and vectoring angle, ostensibly aided by the momentum of the cross flow. For $x/h < 50$ the weaker cross flow allows the jet to follow the majority of the Coanda surface as reflected by the $0.2 U_\infty$ contour, thereby causing a wider layer width and stronger vectoring until $x/h = 50$ where the momentum of the entrained cross flow begins to dominate the response with a weaker effect than at $U_\infty = 30$ m/s.

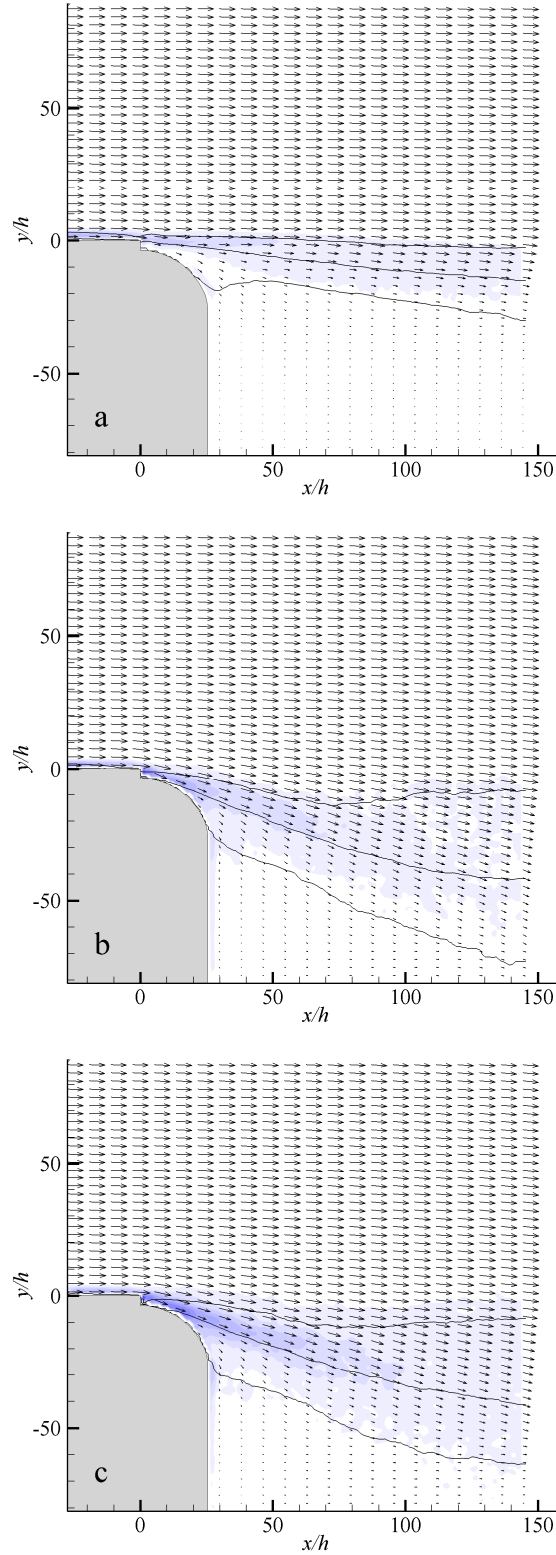



Figure 43. PIV images of the time-averaged flow field response to actuation when average jet speed is matched to the free stream velocity at three values: (a) $U_\infty = U_{Avg} = 10$, (b) 20, (c) 30 m/s. Line contours indicate 0.2, 0.5, and 0.9 U_∞ . Vorticity scale: -20,000  20,000 1/s. $y/h > 50$: Vector lengths indicate U_∞ .

When $U_\infty = U_{Avg} = 20$ m/s ($Re_{Jet} = 291$, Figure 43b), the (normalized) flow field and contours of velocity magnitude indicate more changes in the flow than for $Re_{Jet} = 291$ at $U_\infty = 30$ m/s (Figure 40c), with the shear layer (as delineated by the contours) approximately 50% wider near $x/h = 150$. The evolution of the shear layer appears almost identical to that of $U_\infty = U_{Avg} = 30$ m/s ($Re_{Jet} = 407$, Figure 43c), except for subdued vorticity within the interaction domain and shear layer for $x/h < 50$, and a slightly deeper reach of vectoring at $U_\infty = U_{Avg} = 20$ m/s (by y/h increment of 10) as indicated by the $0.2 U_\infty$ contour which reaches $y/h = 75$ near $x/h = 140$. These observations are further supported by Figure 44 where shear layer width and momentum flux vector angle are similar for those two speeds, with vector angles up to three degrees greater for $U_\infty = U_{Avg} = 20$ m/s. Not surprisingly however the momentum flux components are substantially larger for $U_\infty = U_{Avg} = 30$ m/s (given the greater momentum of both the cross flow and jet – the data analysis was not normalized like the vector plots). Note that as discussed in Section 5.2 in the absence of a cross flow (Figure 32), the flow fields for $Re_{Jet} = 291$ and 407 are similar, with $Re_{Jet} = 407$ having a centerline vectoring angle that is approximately ten degrees greater. This opposes the greater effect seen with the cross flow at $Re_{Jet} = 291$ ($U_\infty = U_{Avg} = 20$ m/s), and together with the greater momentum flux components of $U_\infty = U_{Avg} = 30$ m/s, this suggests the flow vectoring effect is a balance between the cross flow momentum and the vectoring ability of the jet (which is related to jet strength), relating back to the observations for $U_\infty = U_{Avg} = 10$ m/s ($Re_{Jet} = 145$) as well.

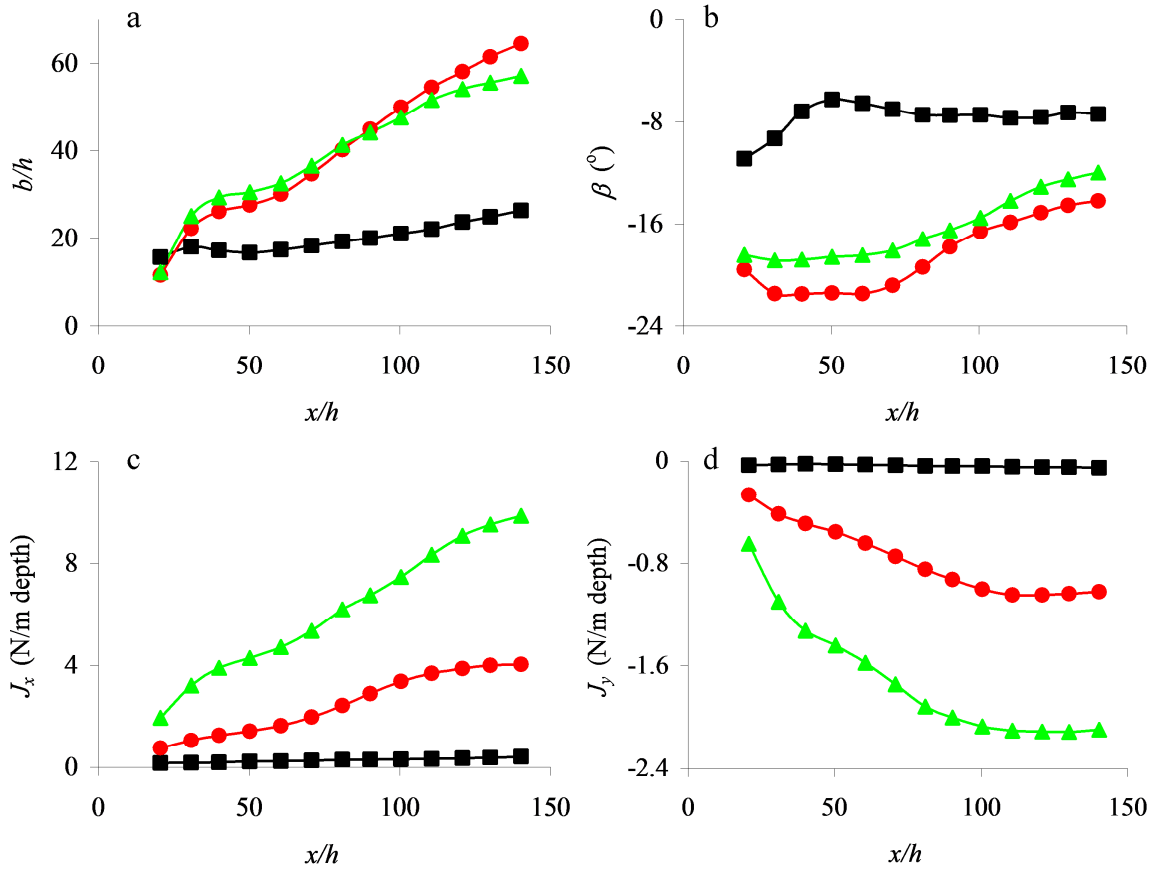


Figure 44. Analysis of PIV data shown in Figure 43 regarding the flow response to actuation for average jet speed matched to the free stream velocity at three values: Streamwise variations of (a) the shear layer’s cross-stream width, (b) the angle of the momentum flux vector, (c) streamwise momentum flux, and (d) cross-stream momentum flux calculated between cross-stream elevations of 0.2 and 0.9 U_∞ . $U_\infty = U_{Avg} = \blacksquare$ 10, \bullet 20, \blacktriangle 30 m/s

Given the studies of flow response at various jet strengths (for a fixed free stream speed) and at matched velocity ratios, it is natural to extend the discussion to fixed jet strength at various free stream speeds. The jet strength was set at $Re_{Jet} = 407$ and $U_\infty = 10, 20, \text{ and } 30 \text{ m/s}$ respectively. The data, normalized by the respective free stream speed, are shown in Figure 45. It is evident that for fixed jet strength, the degree of initial flow vectoring ($x/h < 50$) decreases with increasing U_∞ , suggesting again that the free

stream momentum offers increasing resistance to the entrainment of the actuator. However as shown in Chapter 4 (e.g. Figure 23), induced force increases with U_∞ , implying that even while the degree of vectoring may decrease with U_∞ , it is more than offset by the increasing momentum of the entrained cross flow. Note that the $0.2 U_\infty$ contours are truncated at the lower free stream speeds as they cross the bottom edge of the field of view prior to the downstream edge of the image; as the data processing shown in Figure 46 is based on the band between 0.2 and $0.9 U_\infty$, the data for $U_\infty = 10$ m/s is not shown for $x/h > 75$, and the data for $U_\infty = 20$ m/s is not shown for $x/h > 120$. Still the difference in variation of momentum flux vector angle with free stream speed is substantial for $x/h < 50$. The angle for $U_\infty = 10$ m/s at $x/h = 20$, -40 degrees, is double that of $U_\infty = 30$. It is interesting that all three cases (in so far as their respective data is shown) display trends indicating convergence to a similar angle, about $\beta = -15$ degrees by $x/h = 140$.

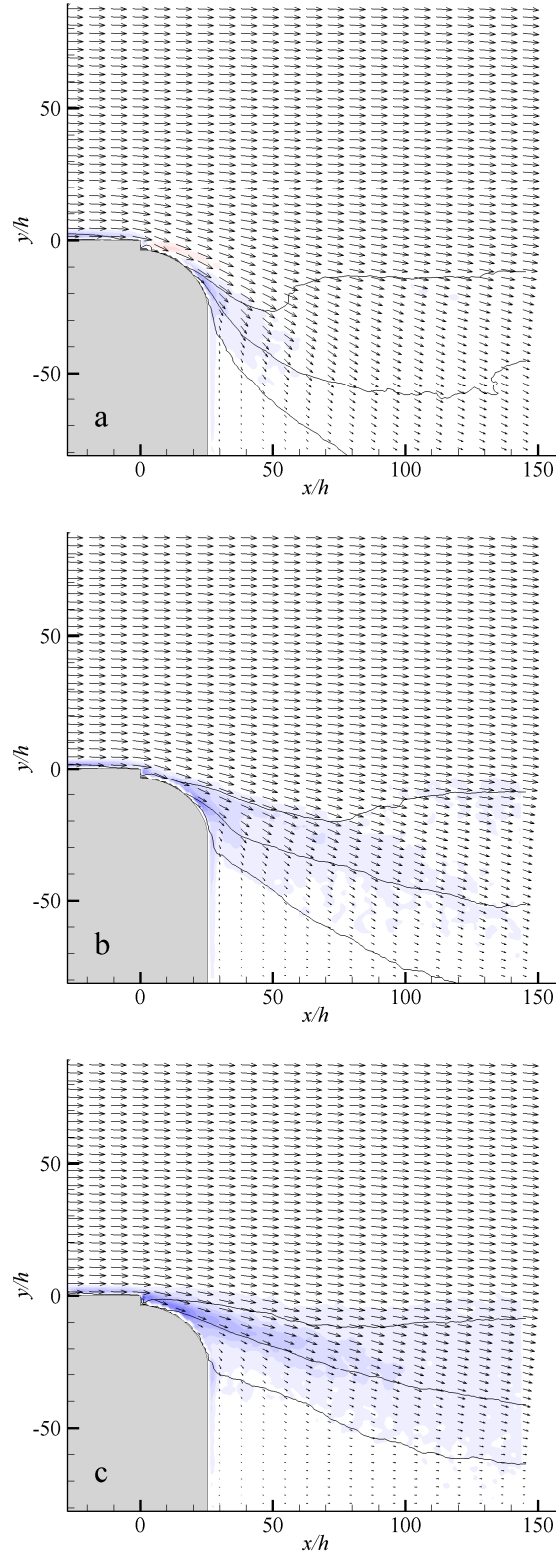


Figure 45. PIV images of the time-averaged flow field response to actuation at three free stream speeds while $Re_{Jet} = 407$: (a) $U_\infty = 10$ m/s, (b) 20 m/s, (c) 30 m/s. Line contours indicate 0.2, 0.5, and 0.9 U_∞ .

Vorticity scale: -20,000  20,000 1/s. $y/h > 50$: Vector lengths indicate U_∞ .

For further consideration, the velocity vector angle for the contour at $0.5 U_\infty$ (defined as γ) is plotted in Figure 46e. While only based on a point measurement rather than a cross-stream integration of a larger set, further insight into the streamwise vectoring behavior is revealed as this vector angle is not affected by the truncation of the $0.2 U_\infty$ contours. As suggested by β and further supported by γ , the vector angles for the three free stream speeds converge to a similar value by $x/h = 140$, to about -20 degrees. This convergence suggests the limited extent of the jet interaction domain and the transition to global flow defined by the greater configuration for $x/h > 100$. However the width of the shear layer, based on the PIV, clearly remains affected by actuation beyond the field of view. For $U_\infty = 10$ m/s it is interesting to observe in the PIV image (Figure 45a) that only a small domain adjacent to the Coanda surface about $x/h = 20$ where the mean velocity is 20% higher than U_∞ despite $U_{Avg} = 3 U_\infty$, indicating how quickly the strength of the jet is subdued by the cross flow. The flow response at $U_\infty = 10$ m/s likely shows the potential for improvement at $U_\infty = 30$ m/s if it were possible to further increase the jet strength.

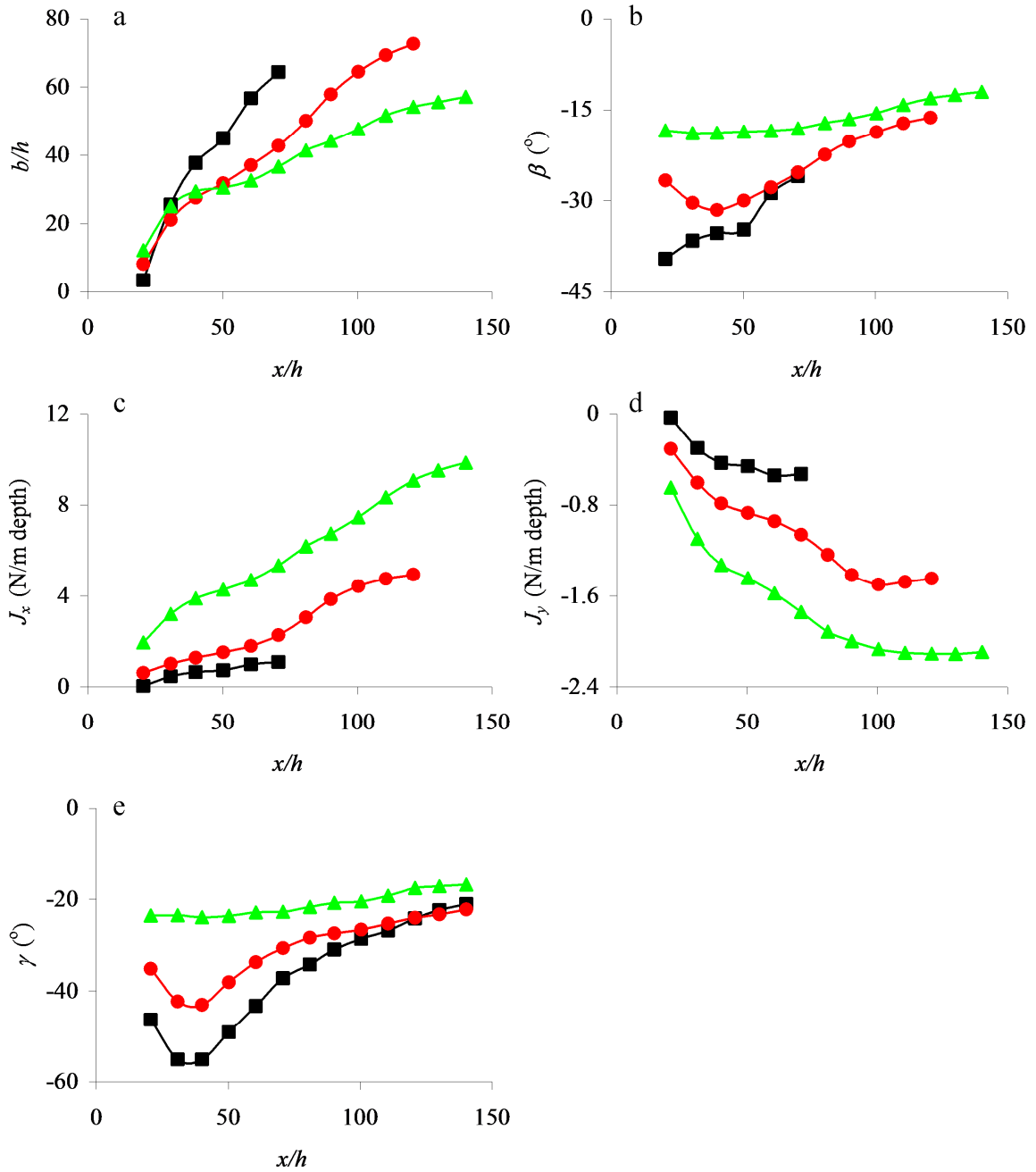


Figure 46. Analysis of PIV data shown in Figure 45 regarding the flow response to actuation at three free stream speeds while $Re_{Jet} = 407$: Streamwise variations of (a) the shear layer's cross-stream width, (b) the angle of the momentum flux vector, (c) streamwise momentum flux, and (d) cross-stream momentum flux calculated between cross-stream elevations of 0.2 and $0.9 U_\infty$, and (e) velocity vector angle at $0.5 U_\infty$. $U_\infty = \blacksquare 10, \bullet 20, \blacktriangle 30$ m/s

As the PIV measurements were limited to the immediate interaction domain, it is constructive to characterize the effects of actuation on the global flow field via the pressure distribution on the floor surface downstream of the step, at the three free stream speeds studied as shown in Figure 47 (which also includes the baseline measurements). It is remarkable that in the presence of actuation ($Re_{Jet} = 407$) the pressure distributions on the flat surface collapse, and the reattachment length (approximate location of peak pressure where the adverse gradients vanish) shortens slightly from $x/H = 6$ to about $x/H = 5.75$ for all three U_∞ . The pressure rise during actuation begins at about $x/H = 1$ compared to $x/H = 2$ to 3 for the baseline cases, with a streamwise rate of rise $dC_p/d(x/H) = 0.117$ which is lower than the corresponding rate for the baseline at $U_\infty = 10$ m/s. This indicates that the actuation alters the size of the separation bubble and the outer flow about it. However, even though the flow in the near field is significantly different (cf. Figure 45), the global scale of the bubble appears to be independent of U_∞ as for all three free stream speeds the reattachment length is shortened by only $0.25 H$ in the presence of actuation. And while there must be actuation threshold in terms of jet strength, the global effect clearly saturates even as the degree of local flow vectoring and attachment to the Coanda surface is still being affected. As the force measurements in Chapter 4 (e.g. Figure 23) showed induced force on the body increasing with U_∞ for a similar range of local flow vectoring, it is evident that induced force on the Coanda surface relates to the local effect independent of global saturation.

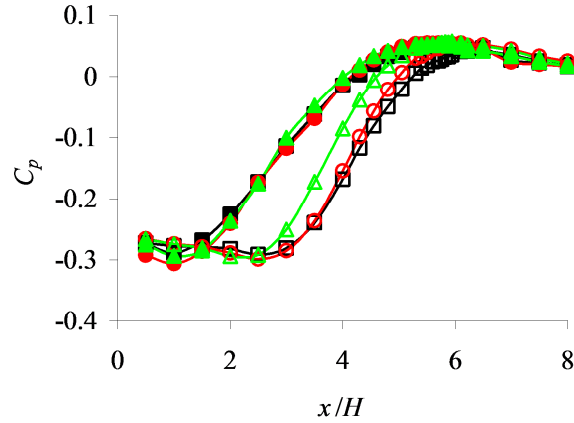


Figure 47. Streamwise variation of static pressure along the test section floor for three free stream speeds, with and without actuation. In the absence of actuation: $U_\infty = \square$, \circ , and \triangle 10, 20, and 30 m/s. With actuation ($Re_{Jet} = 407$): $U_\infty = \blacksquare$, \bullet , \blacktriangle 10, 20, 30 m/s.

5.5 Geometrical Effects

The experimental configuration of this isolated backward step configuration was rather arbitrarily duplicated from the axisymmetric body, and so it is worthwhile to consider the impact of various geometrical parameters including the radius of the Coanda surface (R), the overall step height (H), and orifice step height (S). The work on the axisymmetric model (Section 4.2) showed that the magnitude of induced force increases with Coanda radius R . However PIV measurements were not done and so it is not clear whether this was due to a change in flow vectoring or the variation in normal projected surface area over which the pressure acts. While direct force measurements are not possible here, presuming a similar effect the present configuration offers further insight through PIV. For this study, three Coanda radii were selected, corresponding to $R/h = 14.1$, 28.2, and 42.3. ($R/h = 28.2$ is the baseline radius, as was the case in the axisymmetric work.) The results are presented in Figure 48 and include PIV vector plots

of the baseline flow along with the response to actuation for each radius. The most noticeable difference between the radii appears to be the extent of attachment to the Coanda surface upon actuation, which increases with radius (at a diminishing rate) as indicated by the $0.2 U_\infty$ contours. Related to this, the shear layer width immediately downstream of the surface appears to increase with radius; however if shear layer widths are compared at the same streamwise (x/h) positions, even above the Coanda surface it becomes evident they are independent of radius. In fact if the other radii are overlaid on a given frame, the point of separation of the lower contour from the surface is predicted quite well, independent of radius. This suggests the variation in induced force is due to the change in surface area over which the pressure acts, rather than changes in flow response with radius.

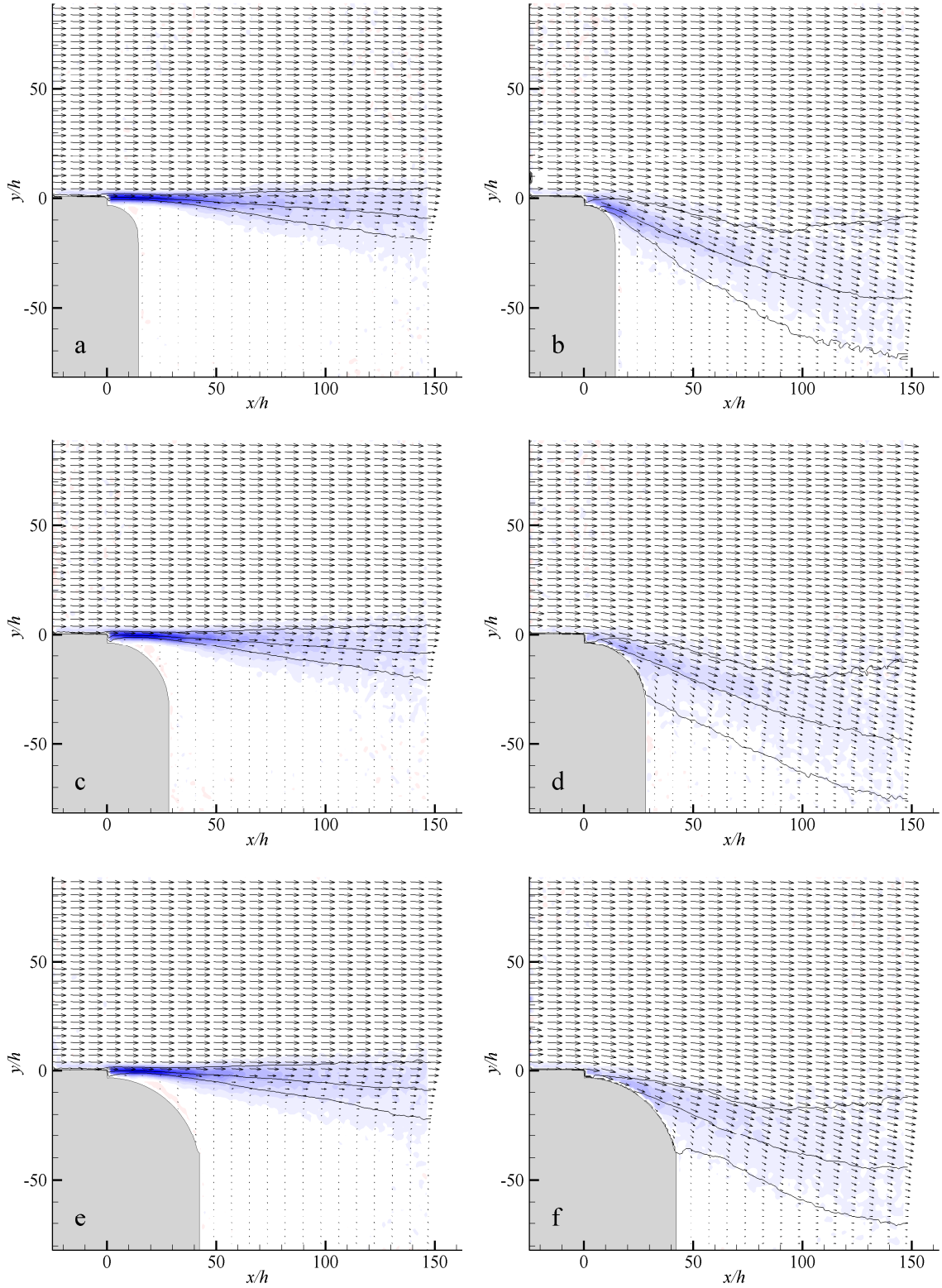
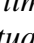


Figure 48. PIV images of the time-averaged flow field for three Coanda radii while $U_\infty = 30$ m/s, in the absence of actuation (left column) and with actuation (right column, $Re_{Jet} = 407$): (a & b) $R/h = 14.1$, (c & d) 28.2, and (e & f) 42.3. Vorticity scale: -20,000  20,000 1/s. $y/h > 50$: Vector lengths indicate 30 m/s.

The associated data analysis, in Figure 49 confirms the lack of influence of radius on the baseline flow, with only minor and inconsistent variations versus radius in the presence of actuation (in terms of streamwise variation in layer width and momentum flux vector angle). Interestingly for $R/h = 42.3$, there is a decrease in shear layer width and flux vector angle during actuation for $60 < x/h < 100$ suggesting a more concentrated induced vectoring effect. This at first appears to be a favorable effect but upon further consideration of the PIV is likely attributed to “blockage” by a physical obstruction. One possibility is the floor below. The $0.2 U_\infty$ contour makes a complete ninety degree turn along the surface (to a deeper cross stream position than the smaller radii), and then just after separation it kicks upward by a y/h increment of about five before returning to a downward path for $x/h > 50$, roughly parallel to that of $R/h = 28.2$ but at a higher cross stream position. This suggests the vectoring could continue if not for the presence of the wall below as it appears an adverse pressure gradient is opposing the vectoring on the lower side; this will be explored further later in this section by changing the floor height.

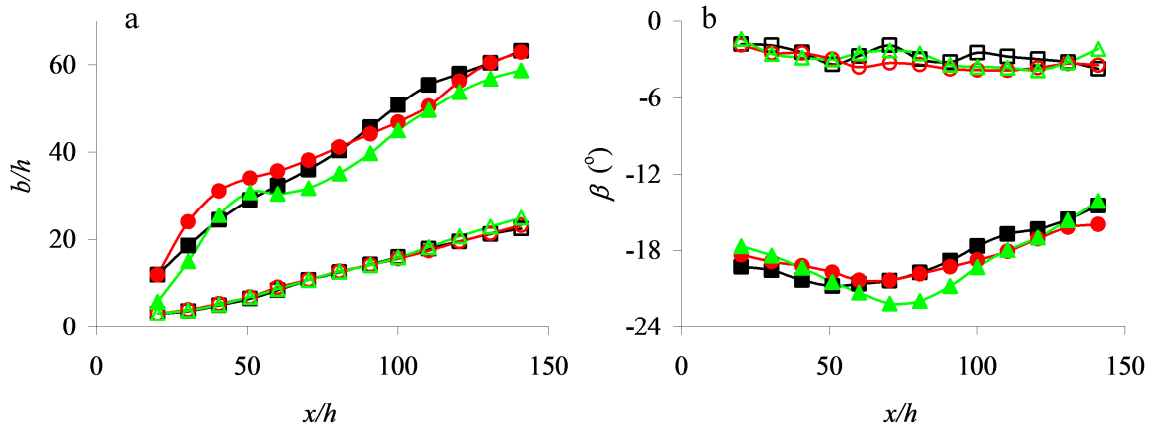


Figure 49. Analysis of PIV data shown in Figure 48 regarding the impact of Coanda radius on the flow response while $U_\infty = 30$ m/s: Streamwise variations of (a) the shear layer's cross-stream width and (b) the angle of the momentum flux vector calculated between cross-stream elevations of 0.2 and $0.9 U_\infty$.
 In the absence of actuation: $R/h = \square$ 14.1, \circ 28.2, \triangle 42.3
 With actuation ($Re_{Jet} = 407$): $R/h = \blacksquare$ 14.1, \bullet 28.2, \blacktriangle 42.3

However the flow vectoring performance at lower U_∞ (Figure 45a & b) suggests the floor height is not the problem as in those cases the flow vectored much deeper despite the same floor position. It is rather conjectured that the larger radius ($R/h = 42.3$) is blocking the flow vectoring response as could be observed by overlaying the larger radius onto the flow response for $R/h = 28.2$ (Figure 48d), where that geometry would cover the $0.2 U_\infty$ contour and much flow above until $x/h = 40$. In that way it limits the extent to which the outer flow can vector downward until the Coanda surface radius drops out of the way, as the outer flow tends to vector linearly (clearly from $0.5 U_\infty$ contour upward). Conversely overlaying the geometry of $R/h = 28.2$ onto the flow response for $R/h = 14.1$ does not interfere with its $0.2 U_\infty$ contour. The idea of blockage seems counter-intuitive in consideration of the Coanda effect, however it has already

been shown that the jet is limited in its vectoring ability as it is opposed by the momentum of the free stream, and further in Section 4.2 it was shown that the jet can vector the cross flow even without a Coanda extension, suggesting a natural path for the vectored flow (linear for the most part) susceptible to being impeded by oversized extensions. Interestingly the concentrated layer of vectored flow caused by the blockage of the larger radius strengthens vectoring for a short distance ($50 < x/h < 75$) even as the vector angles of the smaller radii are rising. However by $x/h = 75$ the effect reverses and the vector angle of $R/h = 42.3$ rises to meet that of the other radii by $x/h = 120$. Overall this blockage effect is relatively inconsequential over the range explored, and flow vectoring performance is not substantially dependent upon selection of Coanda radius R .

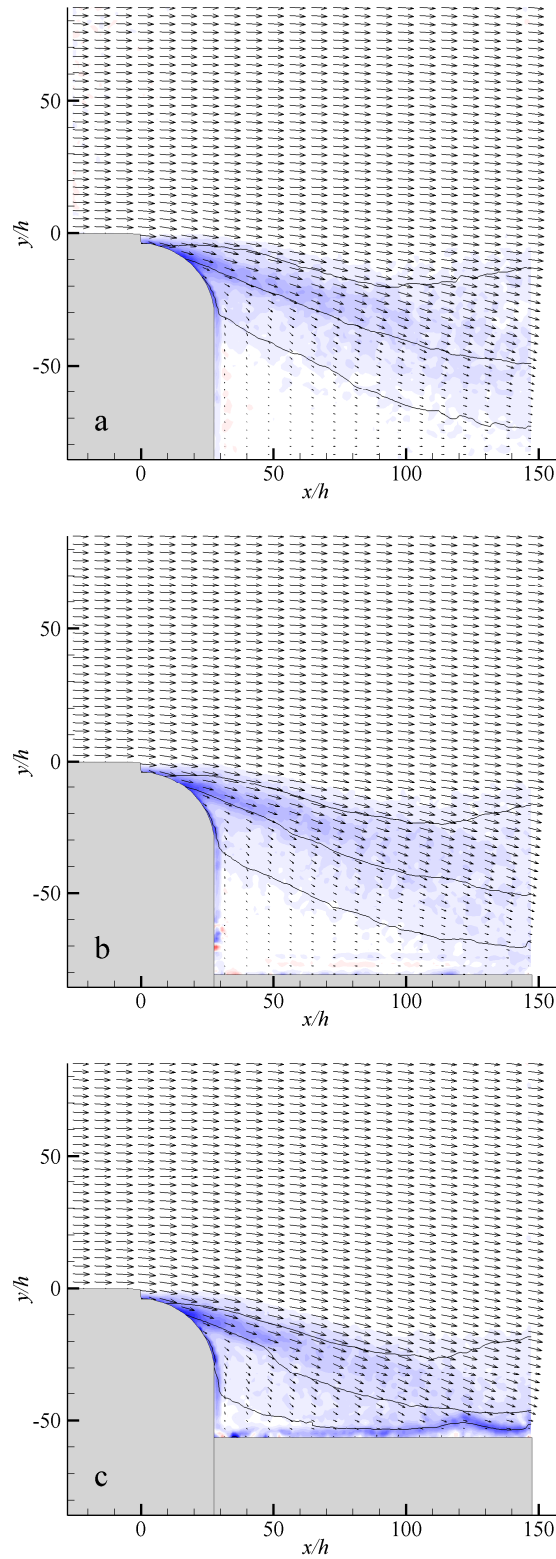
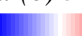


Figure 50. PIV images of the time-averaged flow response to actuation for three backward step heights while $Re_{Jet} = 407$ and $U_\infty = 30$ m/s: (a) $H/h = 111$, (b) 82, and (c) 56. Line contours indicate 0.2, 0.5, and 0.9 U_∞ . Vorticity scale: -20,000  20,000 1/s. $y/h > 50$: Vector lengths indicate 30 m/s.

In relation to Figure 47 discussed earlier, streamwise distributions of static surface pressure downstream of the step indicate that the magnitude of flow vectoring due to actuation appears to be relatively decoupled from the global flow as is evidenced by the fact that the point of reattachment is relatively unchanged. As this length depends strongly on the overall step height H , it is instructive to consider the effect of changing this height. This effect is demonstrated by using a “false floor” downstream of the step, spanning the width of the test section, with a streamwise length of at least six step heights to ensure attachment. In comparison to the baseline step height of $H/h = 111$, step heights of $H/h = 82$ and 56 were explored. The results shown in Figure 50 indicate that the floor clearly obstructs the vectored flow by $H/h = 56$. Despite clear impingement of the flow onto the false floor near $x/h = 50$, the flow vectoring appears to remain essentially the same across all three step heights. Figure 51 indicates that the flow vectoring (in terms of angle) is greater for $H/h = 82$ by a few degrees compared to the baseline $H/h = 111$, but similar in overall behavior in terms of layer width and vector angle. The vector angle of $H/h = 56$ is greater by up to six degrees prior to impingement near $x/h = 50$, with a shear layer width similar to the others to that point. This suggests that as long as the vectored flow does not impinge on the horizontal surface, the response is relatively independent of step height. Further this would suggest that the overall step height should be of a scale that is multiple times larger than the interaction domain as defined by orifice step height, Coanda radius, etc. to avoid interaction with the lower surface.

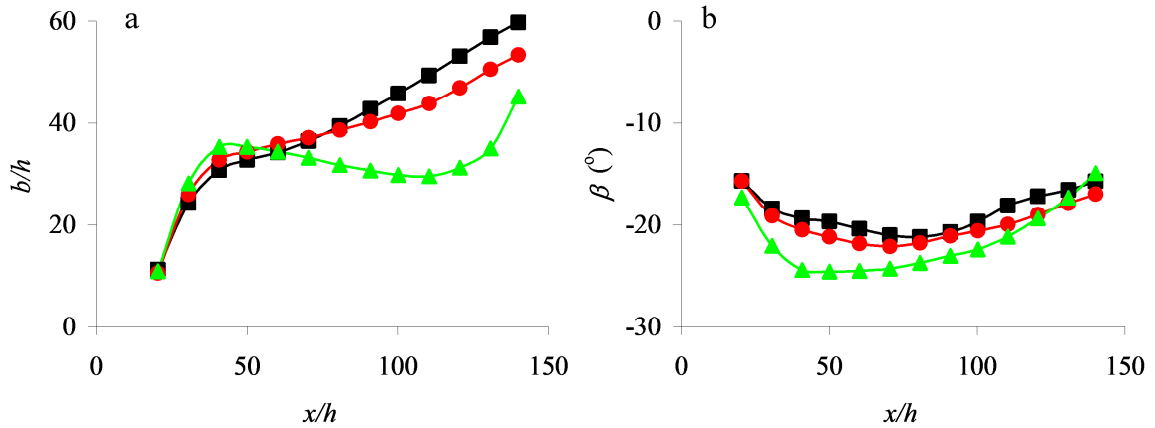


Figure 51. Analysis of PIV data shown in Figure 50 regarding the impact of backward step height on the flow response to actuation while $Re_{Jet} = 407$ and $U_\infty = 30$ m/s: Streamwise variations of (a) the shear layer's cross-stream width and (b) the angle of the momentum flux vector calculated between cross-stream elevations of 0.2 and $0.9 U_\infty$. $H/h = \blacksquare 111, \bullet 82, \blacktriangle 56$

The orifice step height (S) is also considered to be relevant as this feature is clearly within the interaction domain of the actuator. Due to limitations of the configuration, it was varied by simply adding thin covers over the upstream surface between the suction slot (100 mm upstream) and the orifice edge, spanning the width of the test section. In addition to the baseline orifice step height ($S/h = 3.3$), $S/h = 6.7$ and 10 were tested and the results are shown in Figure 52. It is clear that the orifice step height has a crucial effect on the flow vectoring. Doubling the orifice step height to $S/h = 6.7$ substantially reduces the effect and tripling the orifice step height to $S/h = 10$ virtually isolates the jet from vectoring the flow; however the shear layer is still widened by the actuation as reflected by the contour lines. From this it is evident that the distance between the cross flow and the orifice (and Coanda surface below) is very important in determining the flow response.

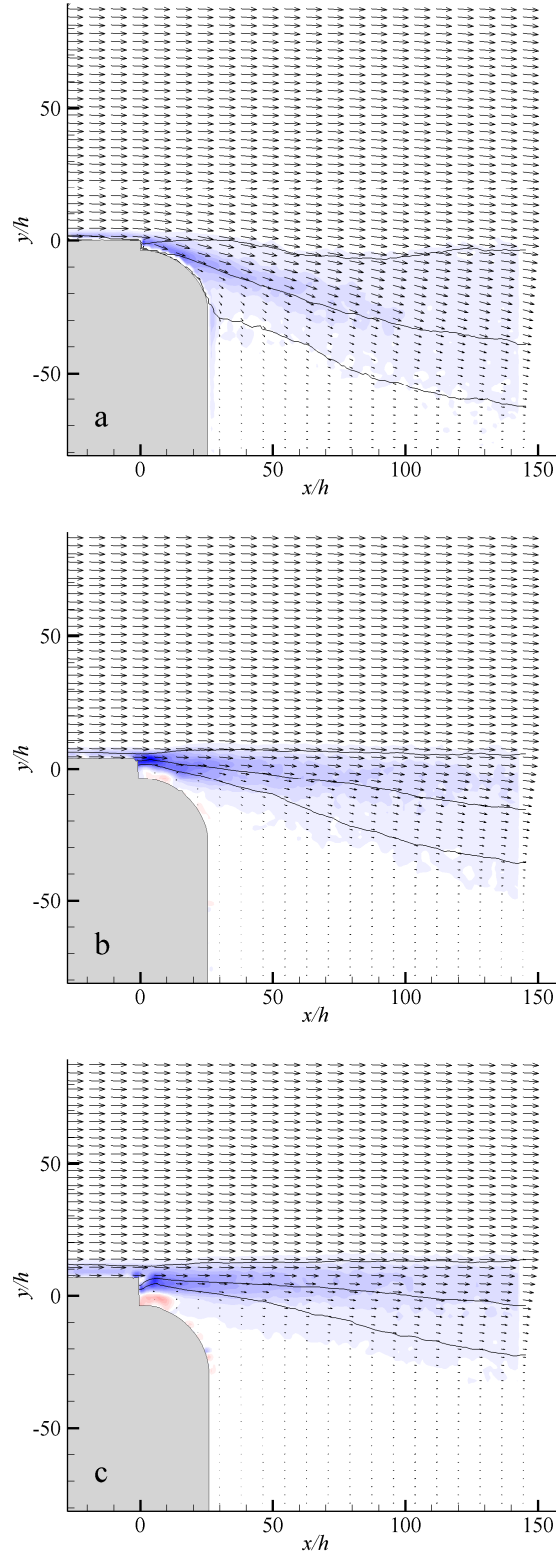



Figure 52. PIV images of the time-averaged flow response to actuation for three orifice step heights while $Re_{Jet} = 407$ and $U_\infty = 30$ m/s: (a) $S/h = 3.3$, (b) 6.7 , and (c) 10 . Line contours indicate 0.2 , 0.5 , and $0.9 U_\infty$. Vorticity scale: $-20,000$  $20,000$ 1/s. $y/h > 50$: Vector lengths indicate 30 m/s.

Figure 53 further illustrates these differences, with drastic reductions in vector angle for the higher orifice step heights over the entire field. The baseline without actuation ($S/h = 3.3$) is also included for reference. As observed earlier in the phase-averaged measurements of the actuator in the absence of a cross flow (Figure 31), the counter-rotating vortices ejected during each blowing stroke initially scale with orifice step height (S), and double in size upon advection along the Coanda surface. As discussed by Smith and Glezer (1998) and others, this scaling is related to the height of the orifice and other specific actuator properties (such as actuator chamber volume, forcing displacement and frequency, etc) rather than orifice step height. Coincidentally in this configuration however the scale of these structures being similar in size to the (baseline) orifice step height offers ideal interaction with the adjacent cross flow. As the orifice step height is raised, obviously these structures have less interaction with the cross flow and even more, the jet suction loses its ability to entrain the cross flow; upon tripling the baseline orifice step height the jet essentially has no interaction with the cross flow. Notably however the (mean) reduced local pressure caused by actuation (as discussed in Chapter 4) still has an effect on the cross flow as shown in Figure 53 for $S/h = 10$, widening the shear layer across the range (greater than the baseline by a b/h increment of about 7) and causing (somewhat irregular) increase in flow vectoring of a few degrees compared to baseline.

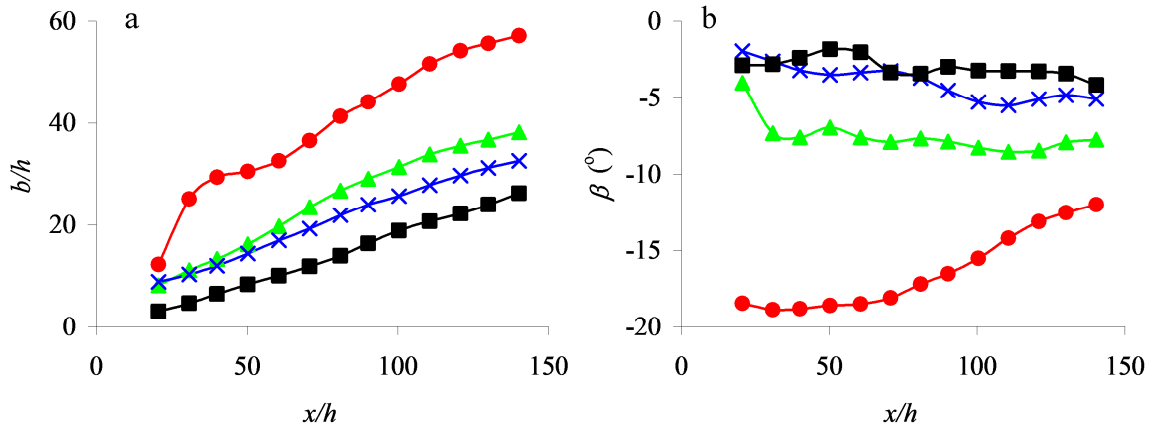


Figure 53. Analysis of PIV data shown in Figure 52 regarding the impact of orifice step height on the flow response to actuation while $Re_{Jet} = 407$ and $U_\infty = 30$ m/s: Streamwise variations of (a) the shear layer's cross-stream width and (b) the angle of the momentum flux vector calculated between cross-stream elevations of 0.2 and $0.9 U_\infty$. $S/h = \blacksquare$ 3.3 (baseline without actuation), \bullet 3.3, \blacktriangle 6.7, \times 10

5.6 Transient Flow Response

As discussed in Chapter 4, the transient response to the onset of actuation for the axisymmetric model is thought to scale with the characteristic convective time scale (based on body length). However, the isolation of the interaction domain in the present configuration removes this global time scale and is expected to accentuate the effects of the local time scale. To study the effect of time scales in this configuration, the flow response was measured at three free stream speeds ($U_\infty = 10, 20,$ and 30 m/s), at fixed jet strength of $Re_{Jet} = 407$. Phase-locked measurements of pulse-modulated actuation at 1 kHz were acquired at incremented trigger delays relative to the 10 Hz modulation waveform where each phase point included 300 realizations. The input signal is configured to produce the blowing stroke on the first half of the cycle, and suction on the second half.

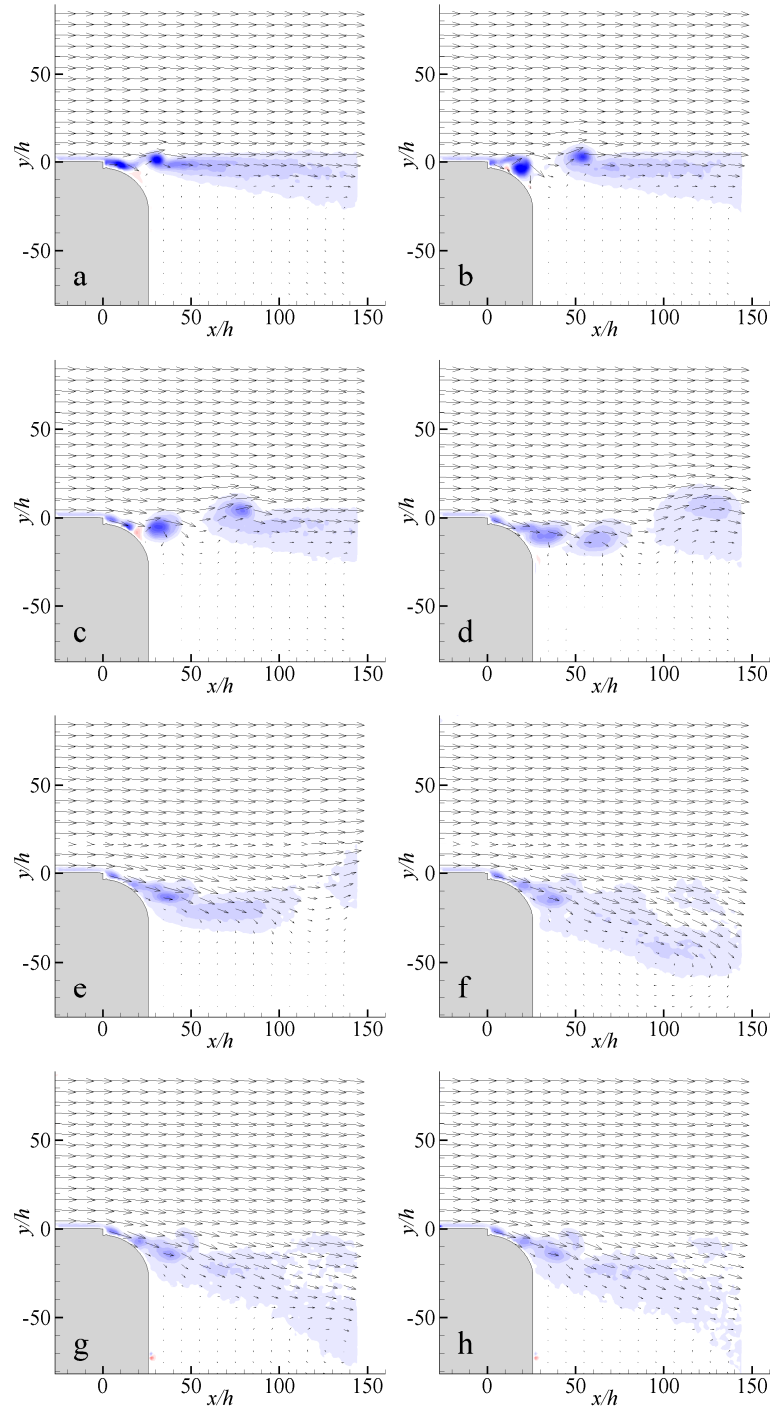



Figure 54. PIV images of the phase-averaged transient flow response to the onset of actuation while $Re_{Jet} = 407$ and $U_\infty = 30$ m/s: (a) $t/T_{Jet} = 1.0$, (b) 1.5, (c) 2.0, (d) 3.0, (e) 4.0, (f) 6.0, (g) 8.0, (h) 10.0. Vorticity scale: $-20,000$  $20,000$ 1/s. $y/h > 50$: Vector lengths indicate 30 m/s.

PIV images at key phase points for $U_\infty = 30$ m/s are shown in Figure 54. It is evident that the transient flow structures are similar to those of the flow downstream of the axisymmetric body under the similar conditions (cf. Figure 13). After one actuation cycle (Figure 54a) the (shear layer) vortex sheet breaks into a starting vortex that begins to form at $x/h = 30$, which is advected downstream. Meanwhile the surface vorticity layer upstream is ingested into the actuator during the suction stroke. At $t/T_{Jet} = 1.5$ (Figure 54b), the second blowing stroke is complete, forming another vortex adjacent to the Coanda surface at $x/h = 20$ via the ejection of vorticity accumulated during the suction stroke, in effect modulating the upstream boundary layer vorticity through actuation. By $t/T_{Jet} = 2.0$ (Figure 54c) this second vortex begins to move downstream while upstream flow begins to tilt downward behind the orifice edge, already attached through 30° of the Coanda surface. Further, the starting vortex is now centered about $x/h = 75$ and rolled upward into the free stream, disconnected from the tilted upstream vorticity layer. At $t/T_{Jet} = 3.0$ (Figure 54d) the vectoring is more pronounced as the free stream begins to deflect toward the wake downstream of the Coanda surface. The starting vortex now centered about $x/h = 130$ is approximately double its diameter at $t/T_{Jet} = 2.0$. After four cycles (Figure 54e) the starting vortex is out of the field of view and the vectored outer flow continues to be deflected into the wake. By $t/T_{Jet} = 6.0$ (Figure 54f) the vectoring of the flow appears to stabilize, with a low level recirculation evident in the wake. It is remarkable that for $t/T_{Jet} > 4$ the shedding of large-scale vortices subsides and the coherence of successive vortices within the shear layer is significantly reduced; the layer is continuous by $t/T_{Jet} = 8$ (Figure 54g). Based on these data it is concluded that for $U_\infty = 30$ m/s the primary flow vectoring response occurs within $10 T_{Jet}$.

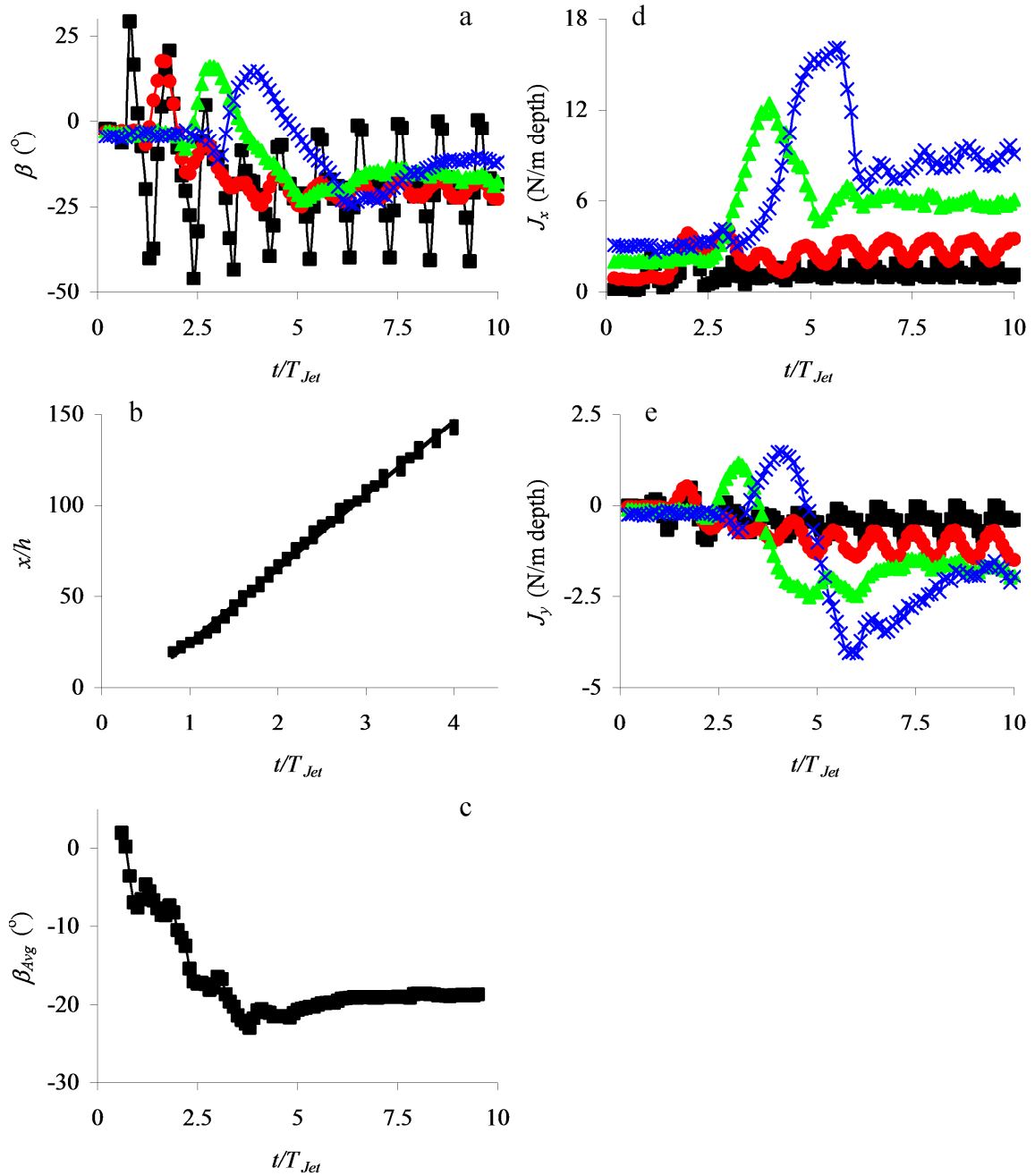


Figure 55. Analysis of PIV data shown in Figure 54 regarding the transient flow response to the onset of actuation while $Re_{Jet} = 407$ and $U_\infty = 30$ m/s: Temporal variations of (a) the angle of the momentum flux vector at four streamwise positions, (b) the trajectory of the peak momentum flux vector angle (c) the cycle-averaged momentum flux vector angle at $x/h = 20$, (d) streamwise momentum flux, and (e) cross-stream momentum flux, calculated between cross-stream elevations of 0.2 and 0.9 U_∞ . $x/h = \blacksquare$ 20, \bullet 50, \blacktriangle 100, \times 140 (for a, d, & e)

The cross-stream phase-averaged momentum flux was computed for $0.2 U_\infty < u < 0.9 U_\infty$ at select streamwise positions for each time increment recorded relative to actuation. Figure 55a shows the phase-locked temporal variation of the momentum flux vector angle (β) at four streamwise stations: $x/h = 20, 50, 100,$ and 140 . Adjacent to the surface, at $x/h = 20$, β is highly oscillatory throughout the duration of the data record and varies initially between 30° and -50° , but then oscillates at nearly constant amplitude (between 0° and -40°) for $t/T_{Jet} > 7$. The amplitude of the oscillations diminishes significantly at $x/h = 50$ (varying by 10° for $t/T_{Jet} > 7$), and at $x/h = 100$ and 140 it shows a single hump followed by a slight rise that levels off by $t/T_{Jet} > 7$ after the vectoring of the outer flow is complete. This hump is associated with the formation and advection of the starting vortex in Figure 54. The trajectory of the starting vortex may be assessed from the position of the peak angle of β at each time increment as shown in Figure 55b. It is remarkable that the streamwise position of this peak varies almost linearly with time indicating that the streamwise speed of the vortex is nearly constant ($0.6 U_\infty$). To further clarify the transient response near the surface, the temporal variation of β at $x/h = 20$ was smoothed by cycle-averaging (in a rolling manner) over one actuator period, defined as β_{Avg} , as shown in Figure 55c. This averaged response reaches its lowest value, -23 degrees, near $t/T_{Jet} = 4$, and thereafter rises up to stabilize at -19 degrees. In fact the response can be characterized by a settling time $T_{settling}$ by projecting the asymptotic (average) vector angle that the flow converges toward (near the end of the measurements) back to its intersection with a linear fit to the rapid decay, which in this case yields $T_{settling} = 3.0 T_{Jet}$. This is an indicator of the time scale of the flow modification above the Coanda surface at $x/h = 20$, particularly related to the vectoring of the outer flow rather

than the attachment of jet along the surface as this measure is based on the band of data between $0.2 U_\infty < u < 0.9 U_\infty$. Time traces of the streamwise and cross-stream components of the momentum flux are shown in Figure 55d and e respectively. For both components the oscillations near the Coanda surface ($x/h < 50$) are small compared to the changes farther downstream. For $x/h = 100$ and 140 there are significant temporal changes during the passage of the starting vortex. A substantial peak in streamwise momentum flux (at $t/T_{Jet} = 4.0$ and 5.5 for $x/h = 100$ and 140 respectively) indicates significant streamwise acceleration of the flow as the vortex passes that settles to about half of the peak level for $t/T_{Jet} > 7$. However the changes in cross-stream momentum flux take longer to subside and at $x/h = 140$ the starting vortex is still strong enough to induce a strong cross-stream change that continues to $t/T_{Jet} = 10$.

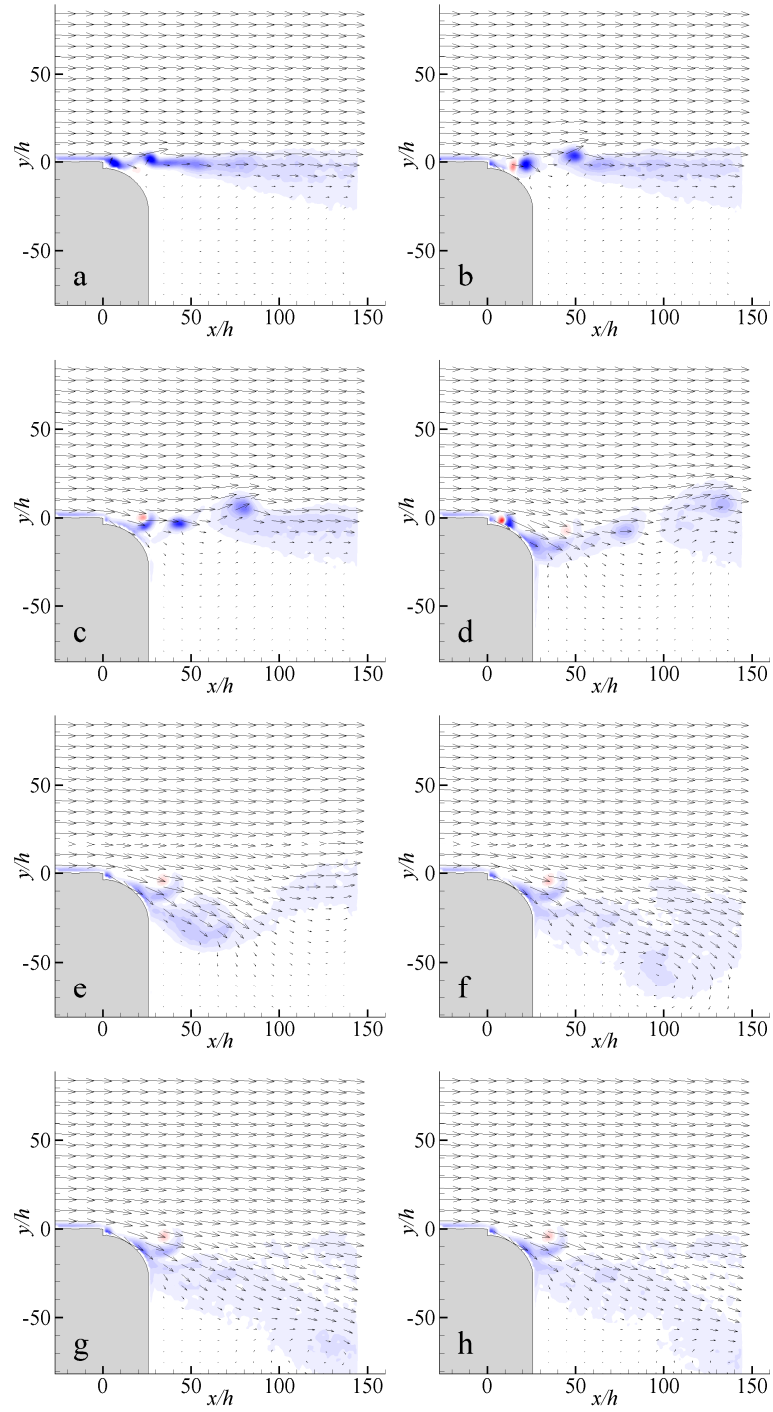



Figure 56. PIV images of the phase-averaged transient flow response to the onset of actuation while $Re_{Jet} = 407$ and $U_\infty = 20$ m/s: (a) $t/T_{Jet} = 1.25$, (b) 2.00, (c) 2.90, (d) 4.40, (e) 6.05, (f) 9.05, (g) 12.05, (h) 15.05. Vorticity scale: -15,000  15,000 1/s. $y/h > 50$: Vector lengths indicate 20 m/s.

Figures 56 and 57 show the corresponding transient flow response to the onset of actuation for $U_\infty = 20$ and 10 m/s, respectively. These PIV images show that the starting vortex and satellite vortical structures are advected considerably slower (compared to the images in Figure 54) as might be expected based on the reduced free stream speeds. The primary flow vectoring responses appear to occur by $15 T_{Jet}$ for $U_\infty = 20$ m/s and $30 T_{Jet}$ for $U_\infty = 10$ m/s. At these speeds while Re_{Jet} remains at 407, the corresponding dimensionless momentum coefficients (C_μ) of the actuation increase significantly (by 2.25 and 9 respectively), which as discussed earlier in the study of time-averaged measurements results in stronger flow vectoring (cf. Figure 45). However attachment of the jet along the surface of the Coanda radius occurs on an apparent fixed time scale, as evident from inspection of the figures (and frames in between) along with higher resolution plots of the same data (not shown). Perhaps driven by jet strength but surprisingly independent of cross stream velocity, attachment to the radius appears to begin about $t/T_{Jet} = 1.5$ and continue through $t/T_{Jet} = 3.5$ whereby flow is attached along the full extent of the Coanda surface. After this time, vectoring of the cross stream above strengthens the flow along the surface as it proceeds in the global transient response, but does not change the radial extent of attachment. It is not clear how variation in driving frequency may change this response time, but it is surely related to jet strength.

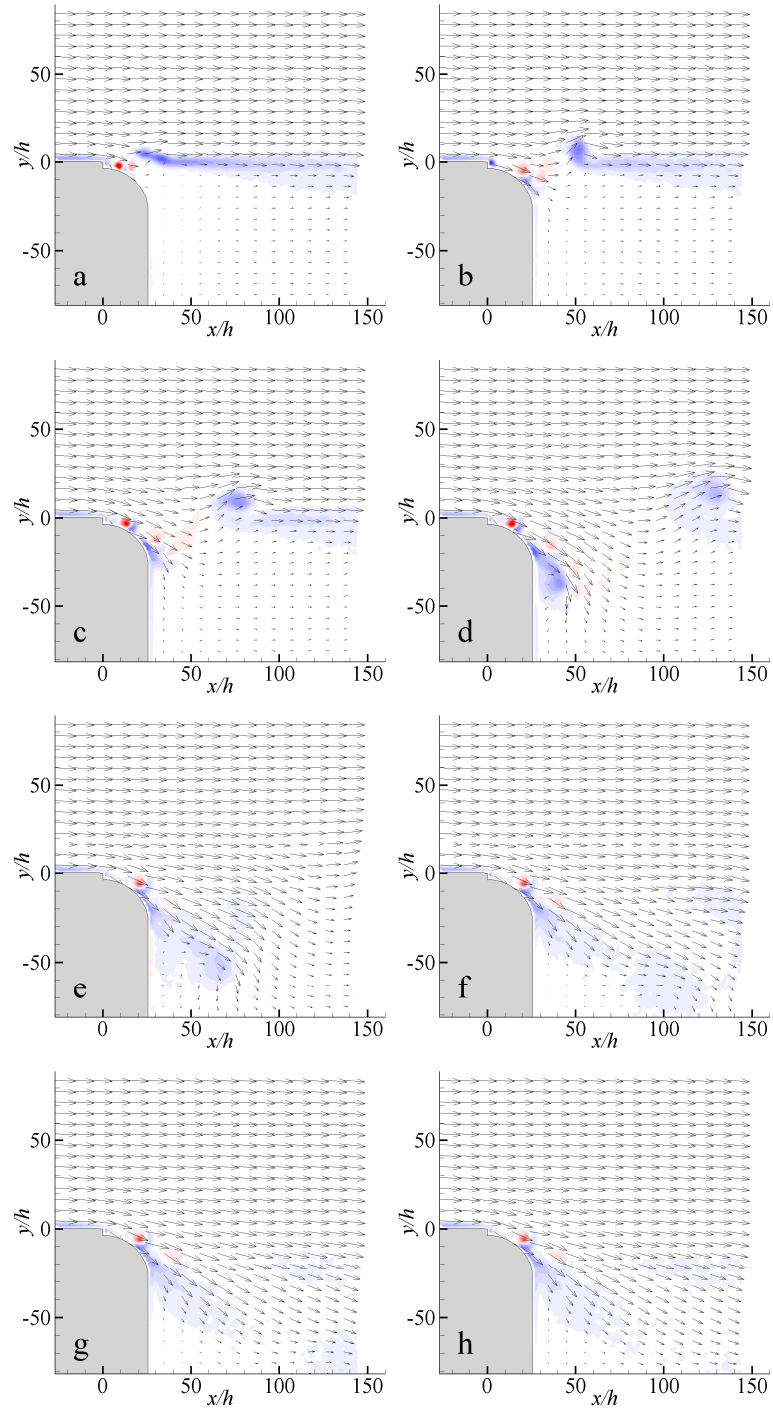



Figure 57. PIV images of the phase-averaged transient flow response to the onset of actuation while $Re_{Jet} = 407$ and $U_\infty = 10$ m/s: (a) $t/T_{Jet} = 2.7$, (b) 4.2, (c) 5.7, (d) 8.7, (e) 12.0, (f) 18.0, (g) 24.0, (h) 30.0. Vorticity scale: $-10,000$  $10,000$ 1/s. $y/h > 50$: Vector lengths indicate 10 m/s.

Figure 58a and d show the temporal variation of the momentum flux vector angle (β) at four streamwise stations ($x/h = 20, 50, 100,$ and 140) for $U_\infty = 20$ and 10 m/s, respectively. The behavior of both quite similar to that seen at $U_\infty = 30$ (Figure 55a) except that the trends converge to greater vectoring angles as expected in correlation with the increase in C_μ . Also related to this, the spread between the converging angles at each streamwise station increases with C_μ , most notably between $50 < x/h < 100$, which suggests that increases in C_μ have the most effect near the surface, as is evident from the PIV images as well. The trajectory of the starting vortices for $U_\infty = 20$ and 10 m/s are shown in Figure 58b and e, respectively, and found to both be linear and moving near $0.6 U_\infty$ similar to that found for $U_\infty = 30$. Figure 58c and f show the variation of β for each respective U_∞ at $x/h = 20$ after smoothing by cycle-averaging (in a rolling manner) over one actuator period (defined as β_{Avg}), similar to that shown in Figures 55e but again reflecting greater vectoring angles in association with increasing C_μ . $T_{setling}$, a time scale of the flow modification above the Coanda surface at $x/h = 20$ defined by projecting the asymptotic β_{Avg} that the flow converges toward, back to its intersection with a linear fit of the rapid decay. For $U_\infty = 10$ m/s, $T_{setling} = 7.2 T_{Jet}$, and for $U_\infty = 20$ m/s, $T_{setling} = 4.2 T_{Jet}$, compared to $T_{setling} = 3.0 T_{Jet}$ for $U_\infty = 30$ m/s. While are only estimates, these values suggest that the response near the surface does not scale directly but rather accelerates somewhat with decreasing U_∞ (and implicitly with increasing C_μ), perhaps related to the fixed time scale of the flow attachment to the Coanda surface of about $3.5 T_{Jet}$ at the studied jet strength ($Re_{Jet} = 407$). Still, it is reasonable to say that the time response of the global flow modification in general scales directly with U_∞ .

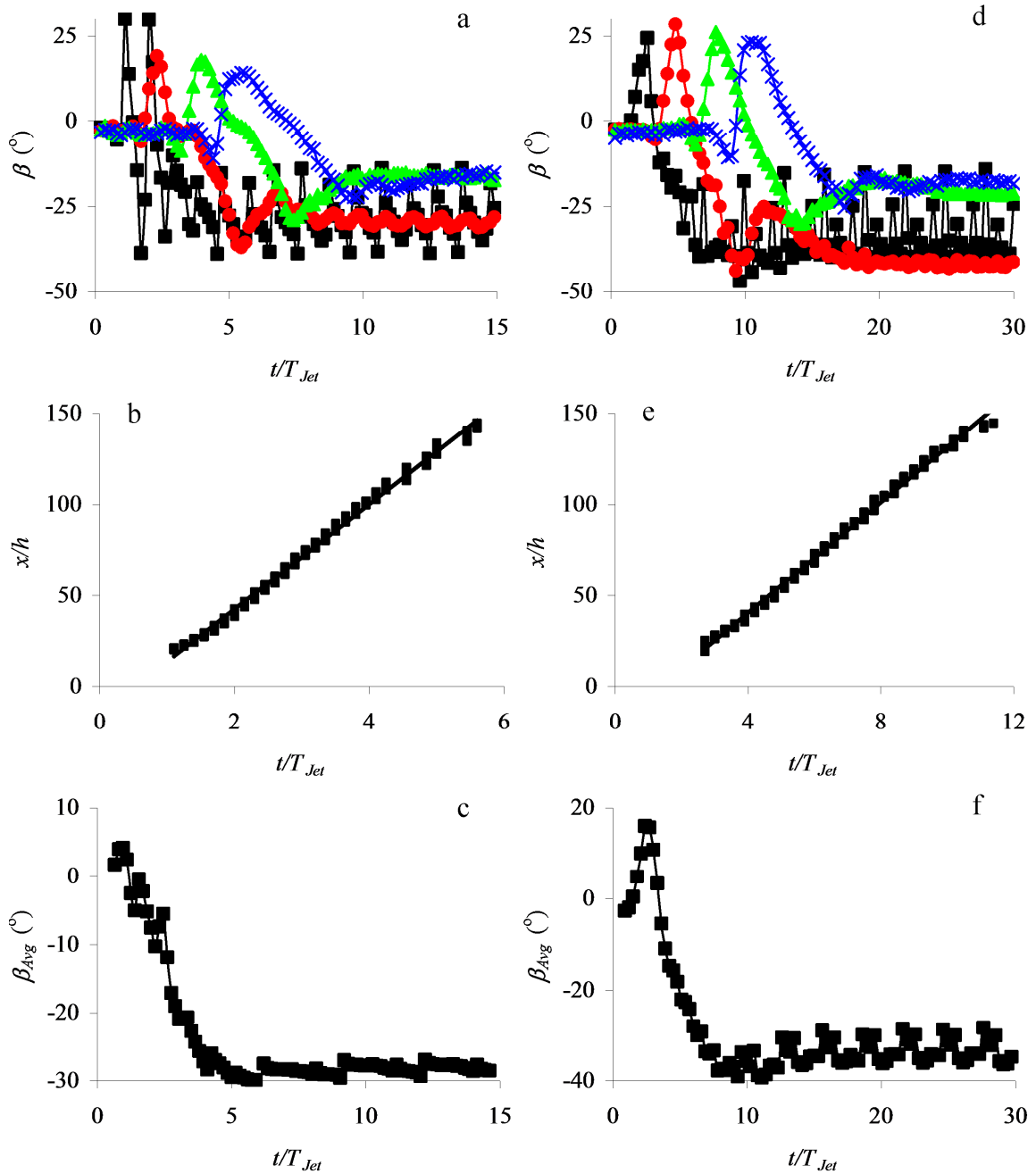


Figure 58. Analysis of PIV data shown in Figures 56 and 57 regarding the transient flow response to the onset of actuation while $Re_{Jet} = 407$ and $U_\infty = 20$ m/s (left column) and 10 m/s (right column): Temporal variations of (a & d) the angle of the momentum flux vector (at $x/h = \blacksquare$ 20, \bullet 50, \blacktriangle 100, \times 140), (b & e) the trajectory of the peak momentum flux vector angle, and (c & f) the cycle-averaged momentum flux vector angle at $x/h = 20$, calculated between cross-stream elevations of 0.2 and $0.9 U_\infty$.

The PIV images together with the plots of temporal variation of β for the three U_∞ suggest the primary transient response scales with the duration of the measurements (10 msec for $U_\infty = 30$, 15 msec for $U_\infty = 20$, and 30 msec for $U_\infty = 10$) which is also the convective time scale of the length of the recirculation domain (6 H). The floor pressure measurements showed that actuation alters the pressure distribution in the region of rising pressure prior to attachment (cf. Figure 47), so it is clear that actuation influences the entire region of recirculation even though it does not have a significant impact on the streamwise length of the recirculating flow domain (as the point of reattachment remains about $x/H = 6$ independent of actuation and U_∞). And so it is not surprising that the duration of the flow vectoring response is related to the scale of the global flow, namely the recirculation zone, whose length is known to scale with the overall height of the backward-facing step. By the time fluid in the free stream has traveled from the orifice edge at the moment of actuation to the point of reattachment to the floor six step heights downstream, the flow has essentially stabilized into the vectored state. (Assuming constant velocity of $0.6 U_\infty$ the starting vortex is still formally within the interaction domain at this time but likely centered near $y/h = 0$, isolated well above the recirculating flow domain.) Looking back at the axisymmetric work (cf. Section 4.3), it appears that the time scale of the flow response was not related to the body length but rather the streamwise length of the time-averaged wake behind the body, which coincidentally is about the same length. For a free-standing body the wake length is driven by body diameter, however in those experiments the model was held by a sting which in essence caused an axisymmetric backward-facing step flow that scaled with the step height

(difference between body and sting radii) of about 25 mm, causing a streamwise wake length of about 150 mm, also the length of the body.

Earlier dynamic force measurements on the axisymmetric body (cf. Section 4.3) appeared to indicate that the cessation of actuation prior to the completion of the transient response still allowed the response to proceed, indicating that perhaps the duration of actuation can be less than the time scale of the region it affects. Clearly this is due to the mechanism set in motion during the actuation. However as indicated in the exploration of a modified driving signal to sharpen the response of the actuator in Section 4.4, without a braking function ringing exists due to the physical inertia of the piezo disc, which extends actuator output for a few cycles after the input signal removal. So without a sharp actuator response, it is likely that shortening the duration by a few cycles has little impact, but certainly the majority of the expected duration must be present to generate the effect. Using a single cycle input without a braking function, an experiment was conducted to observe the response to an expectedly short duration of actuation. Based on earlier hotwire measurements, perhaps two weaker but meaningful cycles are expected to occur after the single active cycle, but at $U_\infty = 30$ m/s the expected duration of the transient response is 10 cycles as discussed earlier. Therefore the duration of this actuation should be too short to generate a substantial response.

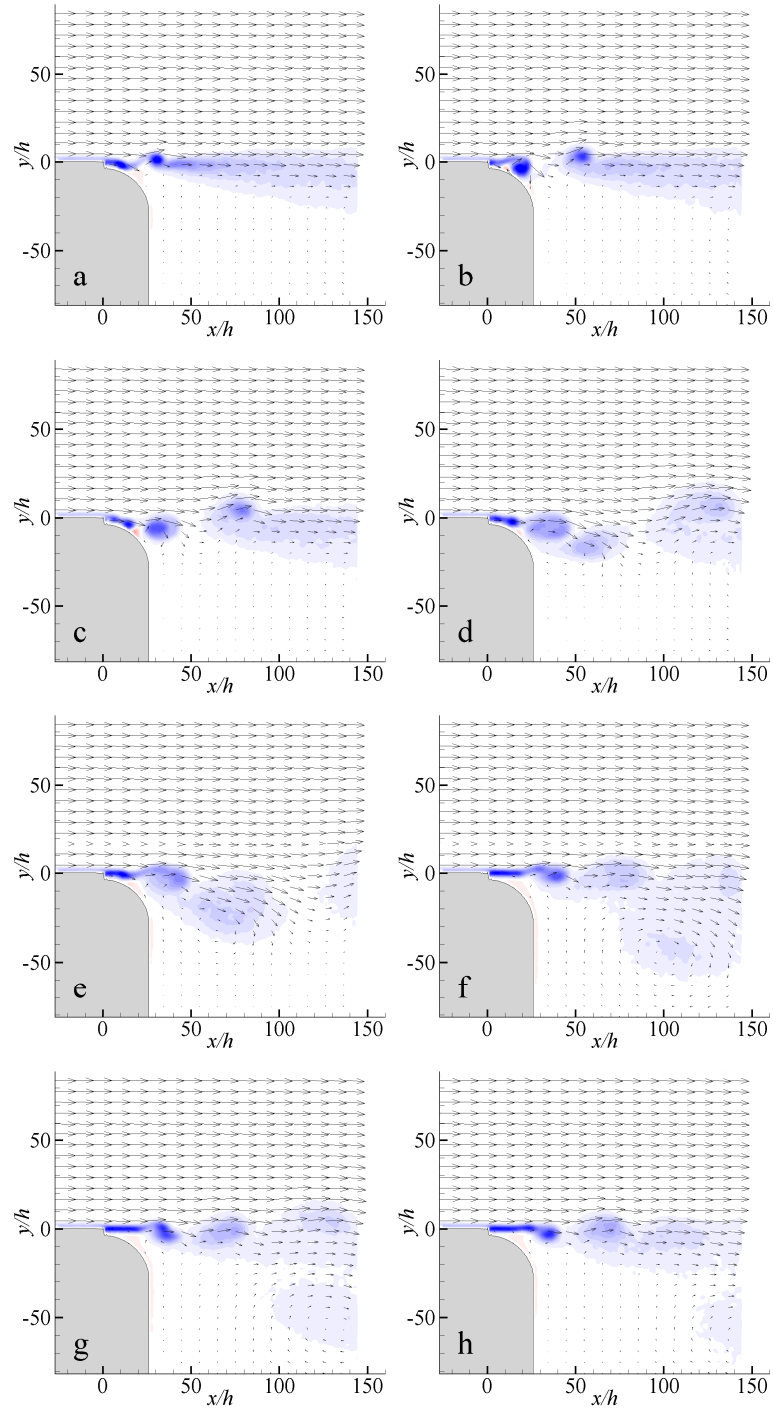



Figure 59. PIV images of the phase-averaged transient flow response to a single cycle pulse of actuation (ending at $t/T_{Jet} = 1.0$) while $Re_{Jet} = 407$ and $U_{\infty} = 30$ m/s: (a) $t/T_{Jet} = 1.0$, (b) 1.5, (c) 2.0, (d) 3.0, (e) 4.0, (f) 6.0, (g) 8.0, (h) 10.0. Vorticity scale: -20,000  20,000 1/s. $y/h > 50$: Vector lengths indicate 30 m/s.

The PIV measurements of the flow response to a single actuation cycle are shown in Figure 59. It is remarkable that even though the actuation is terminated at $t/T_{Jet} = 1$, the response of the flow is identical to the step modulated actuation up to approximately $t/T_{Jet} = 3$ (cf. Figure 54a-d). In fact, as shown in Figures 59d and e up to $t/T_{Jet} \approx 4$, single pulse actuation results in stronger vectoring (in the region of $50 < x/h < 100$) than for the step modulated flow. In studying the sequence further it becomes evident that this stronger vectoring is actually the precursor of a larger clockwise vortex that subsequently forms behind the body, which does not appear in the same sequence of the step modulated response. This recirculation is the beginning of the restoration of the baseline wake, occurring rather quickly once actuation is removed, and starting from the second vortex formed by the suction of the first cycle (and released by a low level of blowing from actuator inertia during a smaller second stroke as seen at $t/T_{Jet} = 1.5$). As the flow begins to recover from the transient, ($t/T_{Jet} > 4$) this larger clockwise vortex forms (in Figure 59e centered about $x/h = 65$, $y/h = -30$) on the low speed of the shear layer and grows in size to span the entire field of view behind the body as its center is slowly advected downstream to $x/h = 135$, $y/h = -55$ by $t/T_{Jet} = 8$ (Figure 59g). The center of the vortex moves out of view by $t/T_{Jet} = 10$ (Figure 59h) and the flow begins to resemble the baseline but with some small coherent structures in the shear layer, attributed to the low level ringing of the actuator that continues for a few cycles as discussed in Section 4.4.

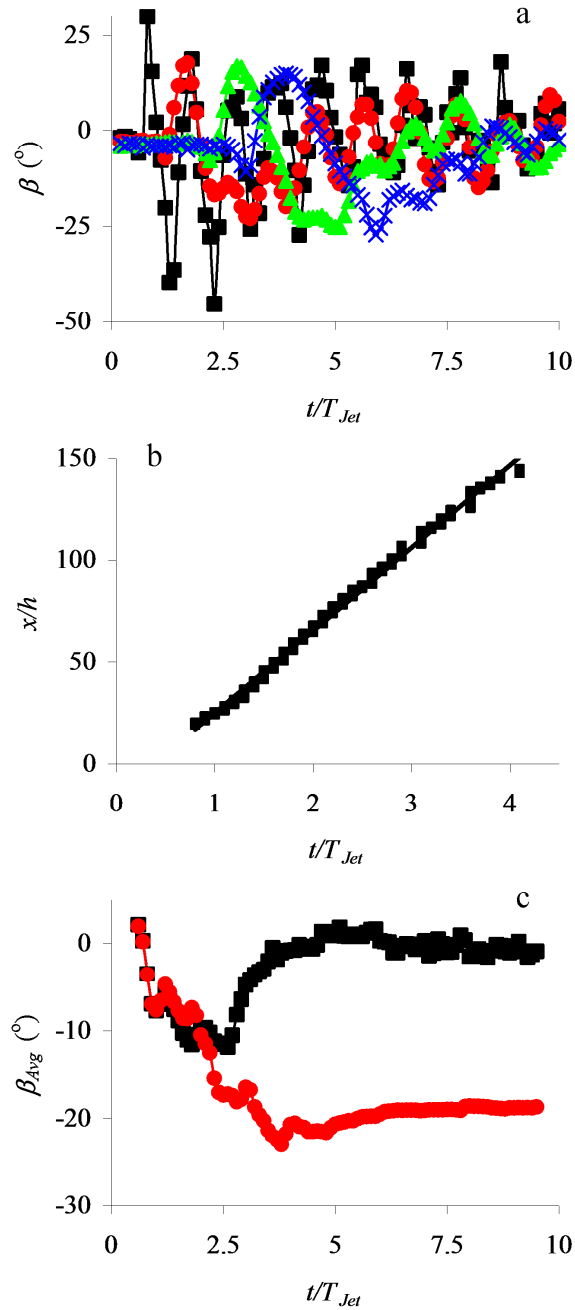


Figure 60. Analysis of PIV data shown in Figure 59 regarding the transient flow response to a single cycle pulse of actuation (ending at $t/T_{Jet} = 1.0$) while $Re_{Jet} = 407$ and $U_\infty = 30$ m/s: Temporal variations of (a) the angle of the momentum flux vector (at $x/h = \blacksquare 20, \bullet 50, \blacktriangle 100, \times 140$), (b) the trajectory of the peak momentum flux vector angle, and (c) the cycle-averaged momentum flux vector angle at $x/h = 20$ (for \blacksquare step modulation, and \bullet single cycle pulse), calculated between cross-stream elevations of 0.2 and $0.9 U_\infty$.

Further analysis of the single pulse data is shown in Figure 60. Similar plots for the step modulated response can be found in Figure 55 for direct comparison. Initially the behavior of the single pulse flux vector angle is similar to that of step modulation, up to $t/T_{Jet} = 2.5$ in agreement with the PIV images. From there however the oscillations in flux vector angle (most clearly seen in traces shown for $x/h = 20$ and 50) for the single pulse follow a rising trend as the flow recovers to the baseline condition, approaching a mean flux vector angle of about zero. For example, at $x/h = 20$ large oscillations are present throughout the 10 cycles of time plotted as in the case of sustained actuation, but after following an initial mean decline, the oscillations begin to rise at $t/T_{Jet} = 2.5$ and by $t/T_{Jet} = 6$ are actually oscillating about a mean positive angle of perhaps 5 degrees. The behavior at $x/h = 50$ is similar, but appears to drop down to a slightly negative mean value by $t/T_{Jet} = 8$. At $x/h = 100$ the sustained case exhibits a relatively smooth behavior that converges to about -20 degree; the single pulse case drops down to -25 degrees by $t/T_{Jet} = 5$, but then quickly rises to zero by $t/T_{Jet} = 7$, and thereafter oscillates about zero effectively. Similar behavior occurs at $x/h = 140$, on a slower time scale. Perhaps not surprisingly, plots of the streamwise trajectory of the first angular peak (Figure 60b) are absolutely identical for both cases, suggesting that even one pulse is capable of initiating the wake flow response mechanism, but it is clear from the other observations that more pulses are needed to complete the response to near-sustained levels. In particular, Figure 60c overlays the temporal variation of β_{Avg} at $x/h = 20$ (smoothed by cycle-averaging over one actuator period) for the single pulse and step modulated input. The averaged response for the single pulse barely reaches -10 degrees by $t/T_{Jet} = 2$, and thereafter rises

quickly to near zero by $t/T_{Jet} = 5$, compared to the step modulation which continues a downward trend to -23 degrees near $t/T_{Jet} = 4$ followed by stabilization about -19 degrees.

5.7 Dynamics of Oscillatory Suction and Blowing

As noted earlier, all measurements of the transient response to this point have been with the signal polarity set to produce a blowing stroke over the first half of each cycle, $0 < \phi < 180^\circ$ (hereafter referred to as the conventional signal polarity). As this was rather arbitrary, it is instructive to assess the role of the suction stroke by inverting the polarity of the input signal and comparing the results over the first few cycles of the transient response. By simply shifting the phase of the input signal by 180 degrees, the suction occurs first (hereafter referred to as inverted signal polarity). While this change clearly has no impact on continuous actuation, it may be important for the transient response.

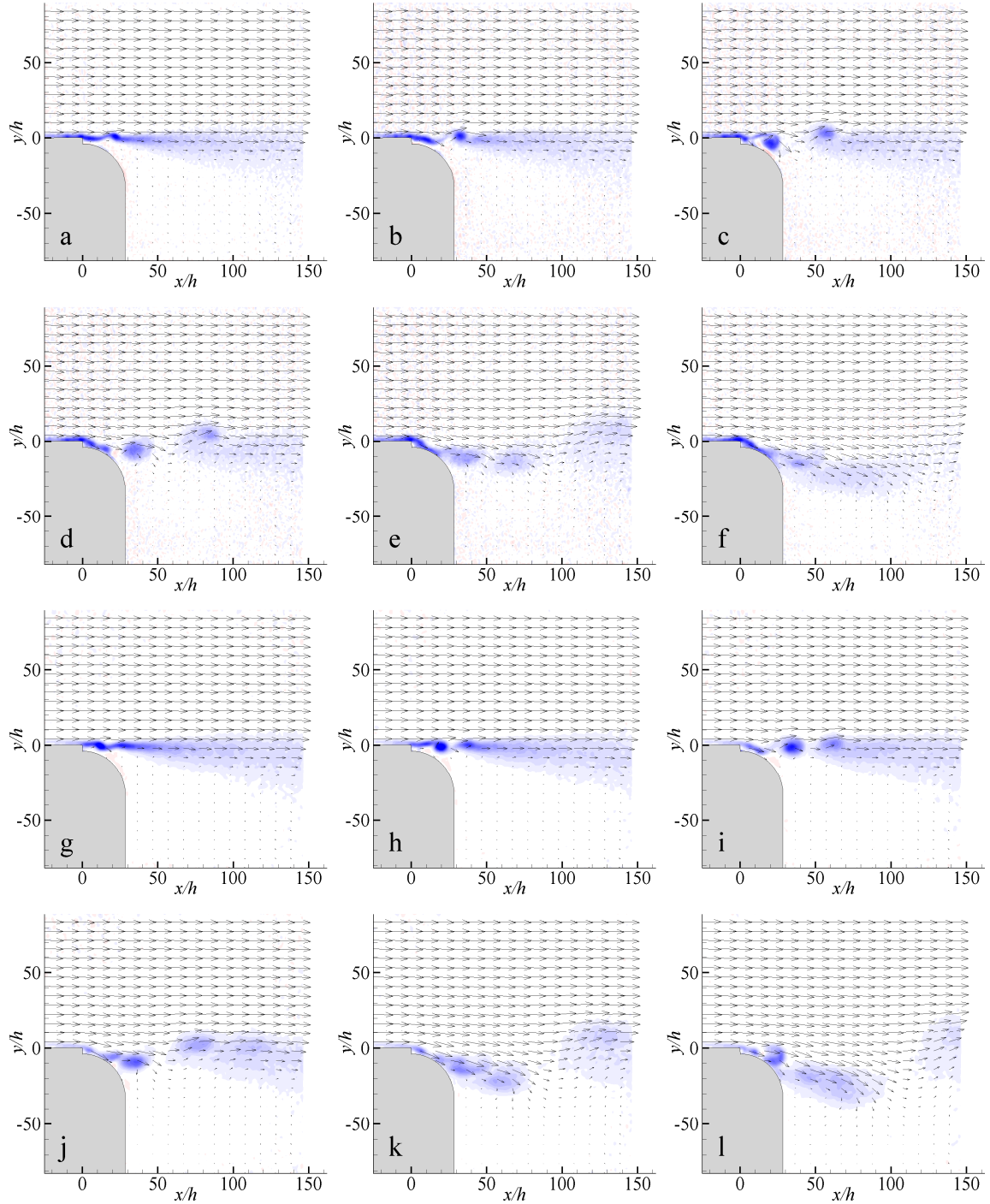


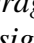
Figure 61. PIV images of the phase-averaged transient flow response to the onset of actuation for conventional and inverted signal polarities while $Re_{Jet} = 407$ and $U_\infty = 30$ m/s. Conventional polarity (blowing first): (a) $t/T_{Jet} = 0.75$, (b) 1.0, (c) 1.5, (d) 2.0, (e) 3.0, (f) 4.0. Inverted polarity (suction first): (g) $t/T_{Jet} = 0.75$, (h) 1.0, (i) 1.5, (j) 2.5, (k) 3.5, (l) 4.5. Vorticity scale: $-20,000$  $20,000$ 1/s. $y/h > 50$: Vector lengths indicate 30 m/s.

Figure 61 shows the flow response for both conventional and inverted signal polarities ($Re_{Jet} = 407$, $U_\infty = 30$ m/s) and demonstrates subtle differences between them. At $t/T_{Jet} = 0.75$ a coherent structure (from which the starting vortex forms) is apparent in both but there is an obvious difference in flow angle between expulsion and suction. For the conventional signal, the wave in the shear layer is upward, towards the free stream. With the inverted signal, the wave is downward, toward the Coanda surface, and the core of the structure is upstream by an x/h increment of about 10 compared to the conventional signal. Advancing to $t/T_{Jet} = 1.0$ further amplifies this observation. By $t/T_{Jet} = 1.5$ the starting vortex is evident and appears to be at a similar streamwise position in both cases, about $x/h = 60$. With conventional polarity the starting vortex contains the vortex ejected by the first blowing stroke, however for inverted polarity the vortex of the first blowing stroke is further upstream at $x/h = 35$, distinct from the starting vortex. This suggests the actuator suction induces the severing of the shear layer, “seeding” the formation of the starting vortex. Even more, with the inverted signal the vortex from the first blowing stroke trails the starting vortex downstream, and in doing so consolidates with it, causing its center to shift upstream such that the response becomes delayed by a $0.5 T_{Jet}$ time increment as can be seen by comparing Figure 61d (conventional signal at $t/T_{Jet} = 2.0$) to Figure 61j (inverted signal at $t/T_{Jet} = 2.5$). Comparing the flow for the inverted signal at $t/T_{Jet} = 3.5$ (Figure 61k) to that of the conventional signal at $t/T_{Jet} = 3.0$ (Figure 61e), the flows are again very similar except that the inverted case exhibits more downward vectoring along with a stronger upwash downstream of it. Viewing both cases at $t/T_{Jet} = 4.0$ (Figure 61f and l), the flows including the vectored region are very similar, except that the downstream upwash remains clearly in view for the inverted case. It becomes

apparent that the response for the inverted signal is about one half cycle slower than for the conventional signal, as a result of the starting vortex melding with the vortex generated by the first blowing stroke trailing behind it. This actually causes a stronger downward flow vectoring during some portions of the flow response, along with a delayed upwash of the downstream flow which follows the starting vortex. This could imply that the inverted signal (applying suction first) offers a stronger transient response in terms of force generated, however with an apparent time delay of $0.5 T_{Jet}$.

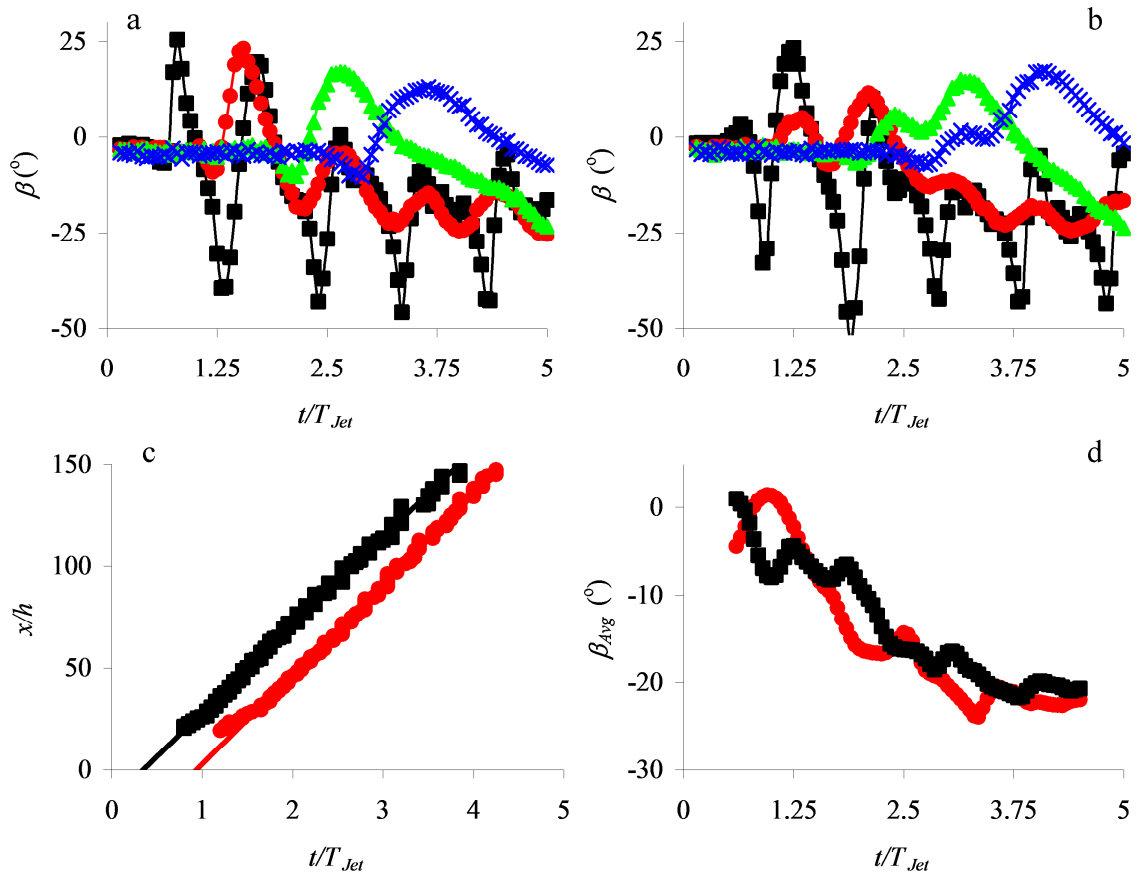


Figure 62. Analysis of PIV data shown in Figure 61 regarding the transient flow response to the onset of actuation for conventional and inverted signal polarities while $Re_{Jet} = 407$ and $U_\infty = 30$ m/s: Temporal variations of the momentum flux vector angle for (a) conventional and (b) inverted polarity (at $x/h = \blacksquare 20, \bullet 50, \blacktriangle 100, \times 140$), and related plots of (c) the trajectory of the peak momentum flux vector angle and (d) the cycle-averaged momentum flux vector angle at $x/h = 20$, calculated between cross-stream elevations of 0.2 and $0.9 U_\infty$. \blacksquare conventional, \bullet inverted polarity

Analysis of the PIV data presented in Figure 62 further supports the observed differences. In the plots of momentum flux angle versus time, the response to the inverted signal (Figure 62a) clearly has initial low-level positive angular (local) peaks followed by secondary positive absolute peaks of at least twice the magnitude of the first, at all plotted streamwise positions. These secondary peaks are of similar magnitude to

those of the conventional signal response (Figure 62b) at most streamwise positions, except at $x/h = 50$ where the inverted signal response shows smaller magnitude that seems attributable to the first-stroke blowing vortex trailing the starting vortex as a separate structure through that position. Most interesting are overlaid plots of the streamwise trajectory of the absolute angular peak shown in Figure 62c. The speed of the start up vortices for both cases is quite constant and nearly the same, and the temporal offset between them is consistent, calculated on the basis of a linear fit to be an increment of $0.591 T_{Jet}$, essentially the half-cycle offset created by the inverted signal polarity, further confirming that signal polarity has a significant effect on the transient response. Also of note are the overlaid plots of β_{Avg} versus time shown in Figure 62d, which of course begin 180 degrees out of phase, and retain an out-of-synch behavior even as the mean angle drops by 20 degrees. Interestingly, despite observations of lagging in response the inverted signal reaches the lowest mean angle plotted, about -25 degrees at about $t/T_{Jet} = 3.25$, before rising up to converge toward the same mean angle as the conventional signal, about -22 degrees. This behavior is likely attributed to the stronger vectoring seen in the related PIV images. It however suggests that the transient response over the Coanda surface is not delayed by the inverted polarity, as opposed to the delay seen in the wake. It is not clear then how the induced force may be affected, although the force response seen with the axisymmetric model (cf. Figure 16) seemed to scale with the wake response.

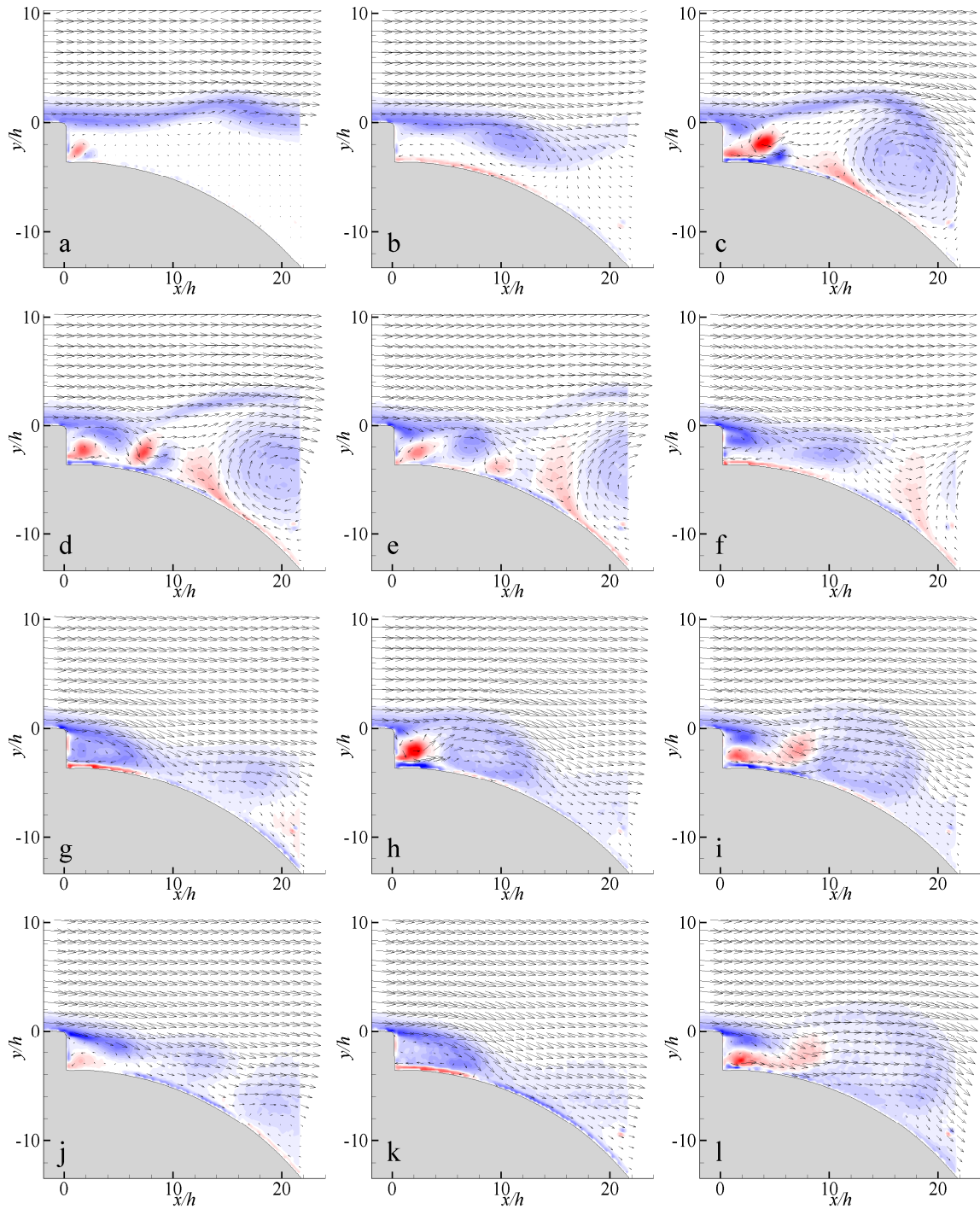



Figure 63. High-resolution PIV images of the phase-averaged transient flow response to the onset of actuation while $Re_{Jet} = 407$ and $U_\infty = 30$ m/s: (a) $t/T_{Jet} = 0.625$, (b) 1.000, (c) 1.375, (d) 1.500, (e) 1.625, (f) 1.750, (g) 2.000, (h) 2.250, (i) 2.375, (j) 2.625, (k) 3.000, (l) 3.375. Vorticity scale: $-100,000$  $100,000$ 1/s. $y/h > 9$: Vector lengths indicate 30 m/s.

To shed some light on the details of the flow near the orifice and the ensuing Coanda surface, high resolution PIV data was acquired on the orifice centerline at the onset of activation in $0.025 T_{Jet}$ increments, corresponding to nine degree cycle resolution. The actuation signal was pulse modulated to include five consecutive actuation cycles with the conventional polarity of blowing first ($U_\infty = 30$ m/s, $Re_{Jet} = 407$). A few key images during the onset of actuation are shown in Figure 63. Since the actuator starts from rest at a central position, the first blowing stroke is weak compared to later strokes (cf. Section 4.4). However a small vortex pair is evident at $t/T_{Jet} = 0.625$ (Figure 63a) which has already influenced the separating shear layer in the form of a traveling wave. The first suction stroke, completed by $t/T_{Jet} = 1.000$ (Figure 63b), ingests the original vortex pair, and pulls the separating shear layer downward close to the Coanda surface. The separating shear layer vorticity associated with the wave begins to roll up, and as the second blowing stroke begins, this vortex structure is pushed downstream by the second ejecting vortex pair to begin forming a large start-up vortex (cf. Figure 54 for larger view), as shown at $t/T_{Jet} = 1.375$ (Figure 63c). However, by the end of this second blowing stroke, $t/T_{Jet} = 1.500$ (Figure 63d), this ejecting vortex pair is still being held close to the Coanda surface by the newly formed shear layer roll-up occurring just upstream of the jet-ejected pair. By being held close, the pair dissipates in place near the Coanda surface as the second suction stroke begins, as shown at $t/T_{Jet} = 1.625$ (Figure 63e). The second roll up is so intense, and so near the Coanda surface that the reversed (counter clockwise) vortex of the pair ejected from the jet orifice is actually severed into two segments by it, as first seen at $t/T_{Jet} = 1.500$. The upstream segment of this vorticity is ingested by the jet during the subsequent suction stroke, last seen at t/T_{Jet}

= 1.625 adjacent to the jet orifice. The suction also initiates a third roll up of the separating shear layer while the second roll up is advected downstream as visible at $t/T_{Jet} = 1.750$ (Figure 63f), near the end of the second suction stroke.

The process of repeatedly concentrating and advecting the separating shear layer vorticity continues through subsequent cycles of the actuator diaphragm as shown in the details of the next 1.5 cycles. At the end of the second suction stroke, $t/T_{Jet} = 2.000$ (Figure 63g), a large vortex is located in the corner region of the backstep and promotes attachment of the outer free-stream flow to the Coanda surface. The third ejection stroke is even more powerful than the second, and the ejected vortex pair can be seen at $t/T_{Jet} = 2.250$ (Figure 63h). It has enough energy to penetrate through the attaching outer flow and move away from the Coanda surface, taking the previously rolled up shear layer along with it. However, by $t/T_{Jet} = 2.375$ (Figure 63i), the reverse vorticity is again sheared in half by the shear layer above. As before the portion downstream is quickly diffused while the portion near the orifice is re-ingested during the ensuing suction stroke, as can be seen at $t/T_{Jet} = 2.625$ (Figure 63j). The outer flow is again drawn downward by the suction and promotes further attachment of the outer flow to the Coanda surface. By the end of this third suction stroke, $t/T_{Jet} = 3.000$ (Figure 63k), a strong recirculation again exists behind the step, and the outer flow is drawn further into contact with the Coanda surface. While not shown much further as it becomes repetitious, this process of attachment grows cycle by cycle until a steady state is reached at about the end of the fifth cycle (in the extent of this field of view). As was shown in Figure 16 (Section 4.3), force generation on the axisymmetric model reaches its peak within 5 actuation cycles, supporting this observation. At $t/T_{Jet} = 3.375$ (Figure 63l), the

forth vortex pair from the jet is seen penetrating through the attached flow region and leaving the backstep region, except again, for a portion of the reversed vorticity that is sheared off and drawn back toward the orifice for subsequent re-ingestion.

In summary, the detailed vortex interactions are complex, but in essence the repeated suction cycles encourage attachment behind the orifice step, gathering the upstream boundary layer vorticity as it enters the region. The blowing strokes help to effectively “dispose” of this gathered vorticity, apparently at a frequency that conveniently performs the disposal before the trapped vortex grows beyond the influence of the suction. Further the blowing stroke adds momentum to the flow along the Coanda surface and together with the trapped vorticity that it advects, vectors the flow downward behind the Coanda surface.

5.8 Spanwise Variation

In the present investigation the synthetic jet orifice has a finite width (25 mm wide orifice in a 250 mm wide base), and therefore 3-D effects are significant as noted in connection with the axisymmetric model (cf. Chapter 4). The planar configuration enables investigation in discrete orthogonal planes (rather than meridional planes through the model’s axis). For PIV measurements in parallel cross-stream planes the PIV camera and the transmitting optics were traversed in the spanwise direction in unison to retain the same spatial resolution and avoid camera lens adjustments. The laser sheet was aligned such that spanwise movement of the optics did not change the orthogonality of the sheet relative to the test section. Because of symmetry, data were only collected between center span and the wall opposite to the camera. Data within the expected interaction

domain, up to 25 mm (1 z/w increment) from the center span (the orifice half width, $w/2$, is +/- 12.7 mm, with its spanwise edge located by definition at $z/w = 0.5$), was collected in 3.2 mm or 0.125 z/w increments, while data over the remainder of the span was collected in 6.4 mm or 0.25 z/w increments, yielding 23 planes of view. All 23 planes were used in analysis but only select representative views are shown in the presented PIV images. (In these experiments $Re_{Jet} = 407$ and $U_\infty = 30$ m/s.)

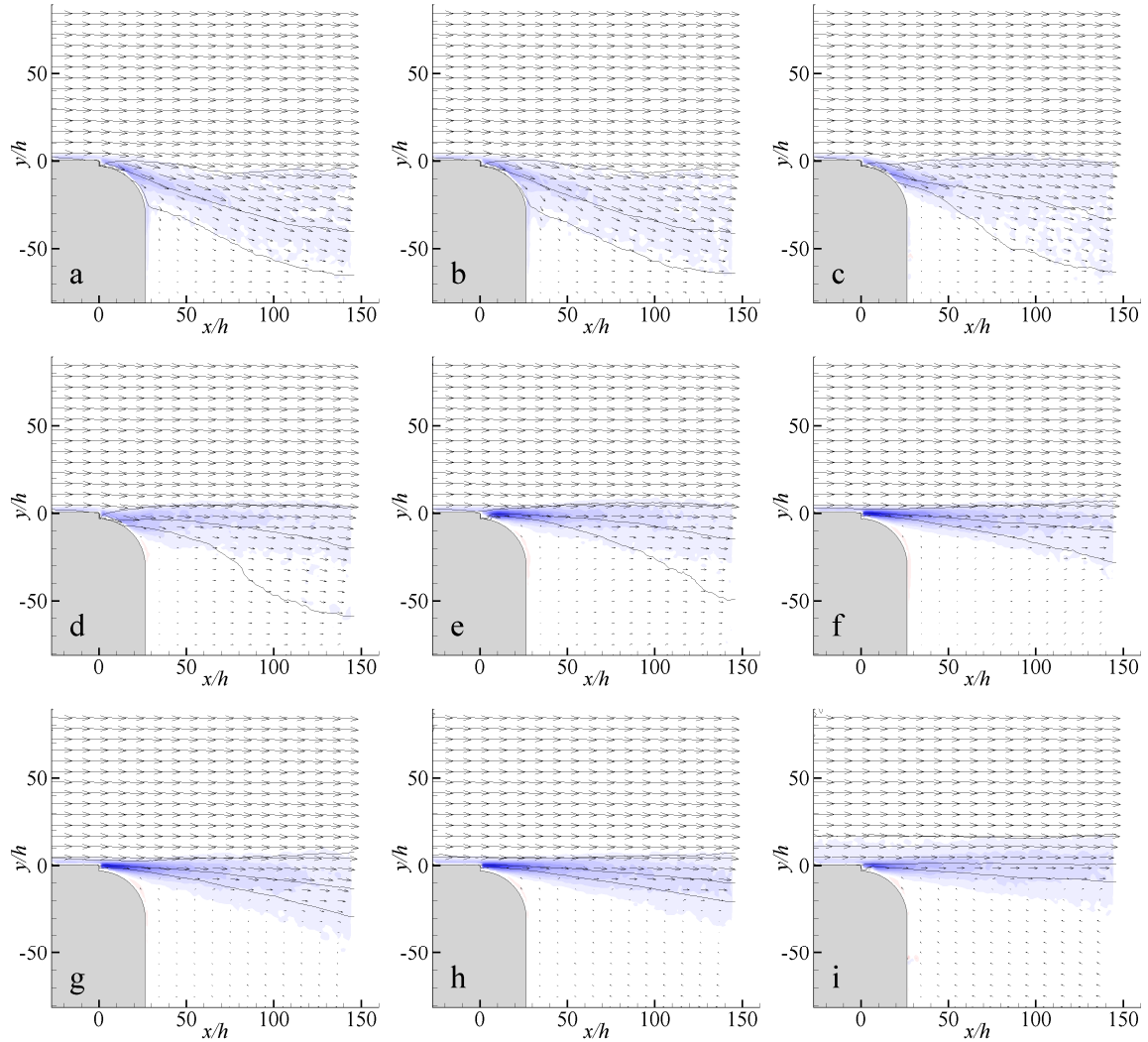


Figure 64. PIV images of the time-averaged flow response to actuation at nine spanwise locations while $Re_{Jet} = 407$ and $U_\infty = 30$ m/s: (a) $z/w = 0$, (b) 0.125, (c) 0.250, (d) 0.375, (e) 0.50, (f) 1.00, (g) 2.00, (h) 3.00, (i) 4.00. Line contours indicate 0.2, 0.5, and 0.9 U_∞ . Vorticity scale: -20,000 20,000 1/s. $y/h > 50$: Vector lengths indicate 30 m/s.

Figure 64 shows the time-averaged flow response in several cross stream planes. These data clearly indicate that the effect of the vectoring diminishes past $z/w = 0.25$ (Figure 64c) although the actuation still results in cross stream spreading of the separating shear layer towards the low-speed stream through $z/w = 0.5$ (at the spanwise edge of the orifice) indicating increased entrainment from the low speed side.

Surprisingly, the vectoring at $z/w = 0.125$ appears slightly stronger than that of the centerline, most notably adjacent to the Coanda surface and likely due to variations in jet velocity across the orifice. It is noteworthy that these findings are similar to the earlier observations with the axisymmetric model (cf. Figure 25). For $z/w > 1$ (Figure 64f), the effect of the actuation is negligible. The effects of the test section side walls become apparent at $z/w = 3$ and 4 (Figure 64h and i) where the shear layer gets thinner owing to wall effects (the test section wall is at $z/w = 5.0$).

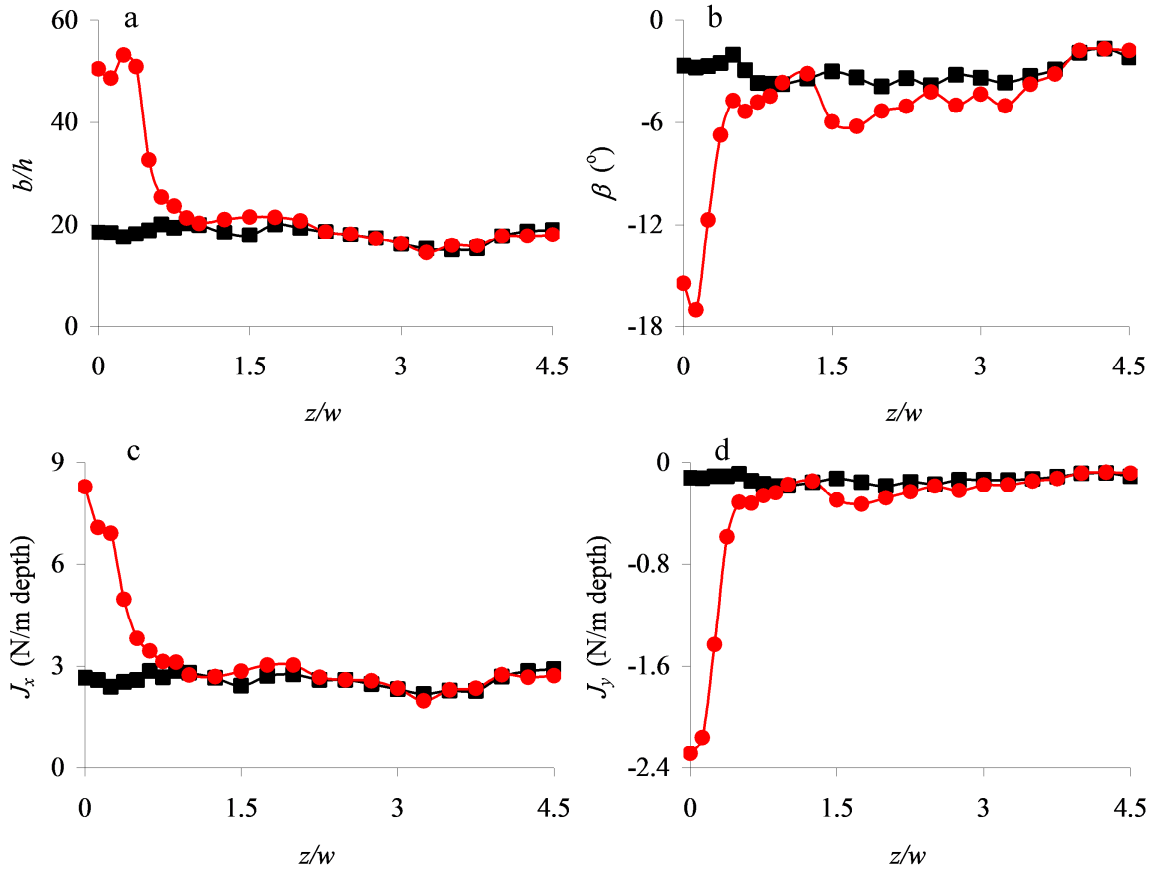


Figure 65. Analysis of PIV data shown in Figure 64 (among other intermediate locations) regarding the flow response to actuation across the test section span while $U_\infty = 30$ m/s: Spanwise variations of (a) the shear layer's cross-stream width, (b) the angle of the momentum flux vector, (c) streamwise momentum flux, and (d) cross-stream momentum flux calculated between cross-stream elevations of 0.2 and $0.9 U_\infty$ at $x/h = 100$. ■ Baseline in the absence of actuation, and ● with actuation ($Re_{Jet} = 407$).

Figure 65 shows spanwise distributions of shear layer width (a), and momentum flux vector angle (b) and its components (c and d) for the time-averaged flow response, computed from the cross stream PIV measurements at $x/h = 100$ in the absence and presence of jet actuation between elevations of 0.2 and $0.9 U_\infty$ similar to PIV analysis elsewhere in this chapter. These data show that for $z/w > 1$ the flow is hardly affected by actuation, in support of the PIV images. In fact the actuation primarily affects the flow

within $z/w < 0.5$, with transitional effects (heading quickly to baseline level) apparent between $0.5 < z/w < 1$. Small differences are also evident for $1.5 < z/w < 2.5$, especially in terms of momentum flux vector angle (up to 3° difference). Note also that the vector angle at $z/w = 0.125$ is about two degrees stronger than on the centerline, in support of the observation for the PIV images. These data show that the baseline flow (without actuation) also varies somewhat across the span. Both cases show the same rise in flux vector angle for $z/w > 4$, related to sidewall effects.

To further analyze three-dimensionality of the flow, the effects of the spanwise velocity component (not captured by the two-dimensional PIV measurements) were characterized by considering conservation of mass within a closed control volume. Since the flow is incompressible and time-averaged, the analysis accounts only for fluxes across the control surfaces. In the absence of spanwise velocity measurements the imbalances of mass fluxes based on the streamwise and cross stream components are used to assess the magnitude of the spanwise (out of plane) flow. In particular, the spanwise variation of the out-of-plane flow allows for further assessment of the effects of the actuator. The control volume quite simply is the extent of the field of view of the PIV images (along with the actuator surfaces as further interior boundaries), and each spanwise position is treated independently in essentially a two dimensional manner. The mass fluxes across the boundaries of a given measurement plane are calculated and summed, and the deviation of the in-plane calculation from zero reveals the net out-of-plane mass flux (on a per unit depth basis). While these values may not be definitive in an absolute sense, they do allow for a relative comparison across the test section for this field of view, which can reveal the degree and extent of cross-span flow in the interaction

domain. Even more, as the distribution of this net flux can be known across the entire span, the integration of this data should equate to zero as in accounting for the entire control volume mass must be conserved. This serves as a good cross-check of the calculations in a global sense, but a small amount of error could be expected as the measurements are samples at discrete locations (taken progressively over the span of an hour or more of time) and a small amount of interpolation is required near the test section side walls.

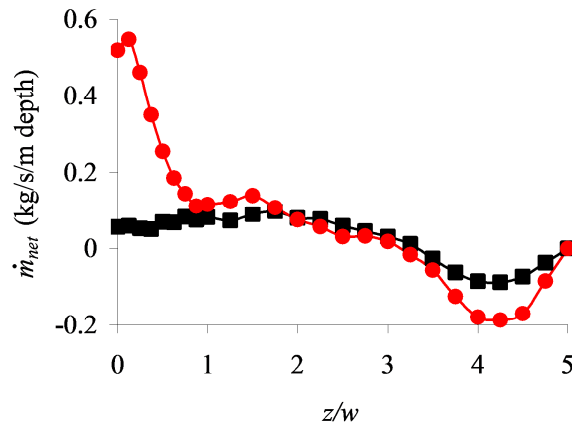


Figure 66. Spanwise distribution of out-of-plane mass flux calculated from time-averaged PIV data obtained at 23 spanwise locations while $U_\infty = 30$ m/s. ■ Baseline in the absence of actuation, and ● with actuation ($Re_{Jet} = 407$).

The distributions of net cross-stream mass flux for the baseline and continuous actuation cases are shown in Figure 66. By the convention of this calculation, a negative value indicates mass loss (out-flux) while a positive value indicates mass gain (in-flux) on a given plane. In correlation with the momentum flux analysis, there is a spanwise variation in mass flux even for the baseline without actuation. The most prominent

feature of the baseline distribution is the deficit centered about $z/w = 4.25$ and spanning about $0.75 z/w$ in either direction. As observed in the PIV images, the flow in this area is affected by corner vortices and other side wall effects. The mass flux is positive for $z/w < 3.25$ and follows a smooth shallow curve, indicating that the mass outflux from the outward deficit is softly absorbed across the remaining interior span. Spanwise integration of this distribution yields an error value of 0.0032 kg/s , 1.7% of the incoming flow in this control volume, a reasonable error for these measurements.

A comparison of the baseline distribution to that of the continuous actuation shows differences across the span. A deficit near the side wall similar to that of the baseline is also evident in the actuated case, which is more pronounced (about twice the magnitude) but with the same spanwise extent. Both cases reach a net flux of zero at about $z/w = 3.25$. The trend between the cases is similar for $2.0 < z/w < 3.0$, with influx doubled for the actuated case in $1.0 < z/w < 2.0$. But the most obvious feature is the large influx of mass in the region of $0 < z/w < 1.0$, peaking at $z/w = 0.125$ with influx ten times greater than the baseline. Obviously this is due to the flow vectoring caused by actuation, which entrains flow not only from the free stream above, but from the neighboring side regions. Keep in mind that these spanwise distributions reflect the net mass flux through the control volume defined by each plane, which is the difference between the mass flux flowing through the right and left planes of each control volume (imagining the plane of measure is a control volume of an infinitesimal spanwise width), and does not indicate the outright mass flux flowing through each control volume. While the net flux in the region of $1.0 < z/w < 3.0$ is nearly zero, it is understood that the mass being lost in the region of $3.0 < z/w < 5.0$ is being transported through the intermediate region with little

net contribution, to be utilized by the region of the actuator. In this way it becomes clear that actuation influences the entire span of the test section despite only causing flow vectoring over a small central segment of the span. Spanwise integration of the actuated distribution yields an error value of .0065 kg/s, 3.5% of the incoming flow in this view.

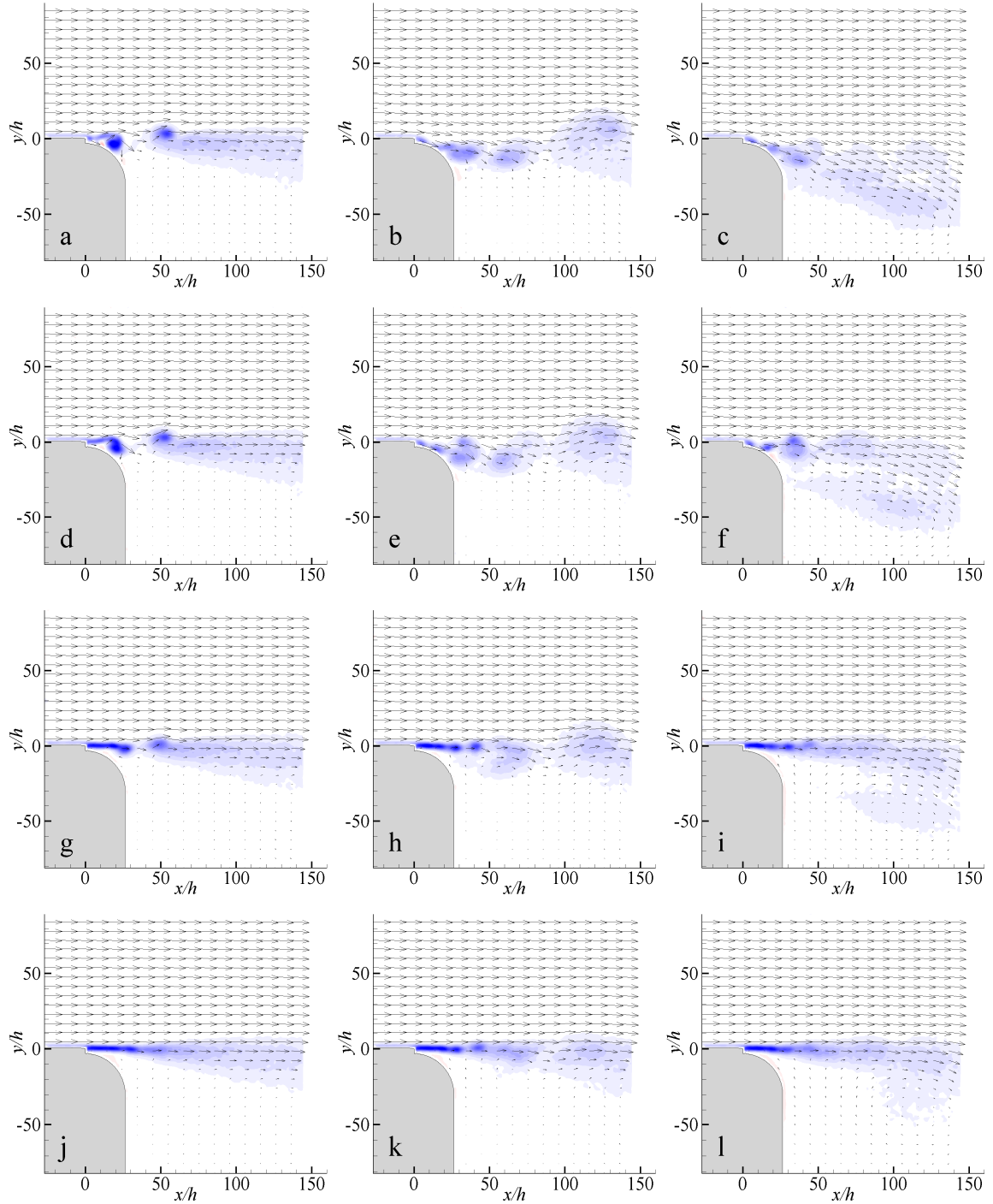


Figure 67. PIV images of the phase-averaged transient flow response to the onset of actuation for select spanwise locations at $t/T_{\text{Jet}} = 1.5$ (left column), 3.0 (center column), and 4.5 (right column) while $Re_{\text{Jet}} = 407$ and $U_{\infty} = 30$ m/s: (a, b, & c) $z/w = 0$, (d, e, & f) 0.375 , (g, h, & i) 0.625 , (j, k, & l) 0.875 . Vorticity scale: $-20,000$ $20,000$ 1/s. $y/h > 50$: Vector lengths indicate 30 m/s.

The spanwise evolution of the flow during the transient response to the onset of actuation was also recorded over the same 23 planes of view across the span ($Re_{Jet} = 407$, $U_\infty = 30$ m/s) over 10 actuation cycles. The variation of the flow across the central span is shown in Figure 67 during $t/T_{Jet} = 1.5, 3$, and 6 , each at $z/w = 0, 0.375, 0.625$, and 0.875 . At $t/T_{Jet} = 1.5$ (Figure 67, left column) coherent vortical structures are evident through $z/w = 0.625$ and comprise the starting vortex (located about $x/h = 50$) and the vortex formed by the second blowing stroke (adjacent to the Coanda surface). Both vortices appear to weaken with spanwise distance from the centerline which may be attributed to variations in jet output along the span of the orifice, and the limited reach of the jet (beyond the span of the orifice) against increasing influence from adjacent unforced flow. By $z/w = 0.875$ the flow appears unforced. At $t/T_{Jet} = 3$ (Figure 67, center column) the spanwise effects of the actuation extend to $z/w = 0.875$ (faintly) although the attachment to the Coanda surface subsides between $0.375 < z/w < 0.625$. Finally, at $t/T_{Jet} = 6$ (Figure 67, right column), the flow appears to be nominally vectored through $z/w = 0.375$ and beyond this domain the effect of the actuation is manifested by the formation of a recirculation domain on the low speed side that extends through $z/w = 0.875$. Overall, it appears that the transient response grows in span with time and streamwise distance, while simultaneously narrowing in effect at the Coanda surface as previously observed on the axisymmetric body (cf. Figures 17 and 18).

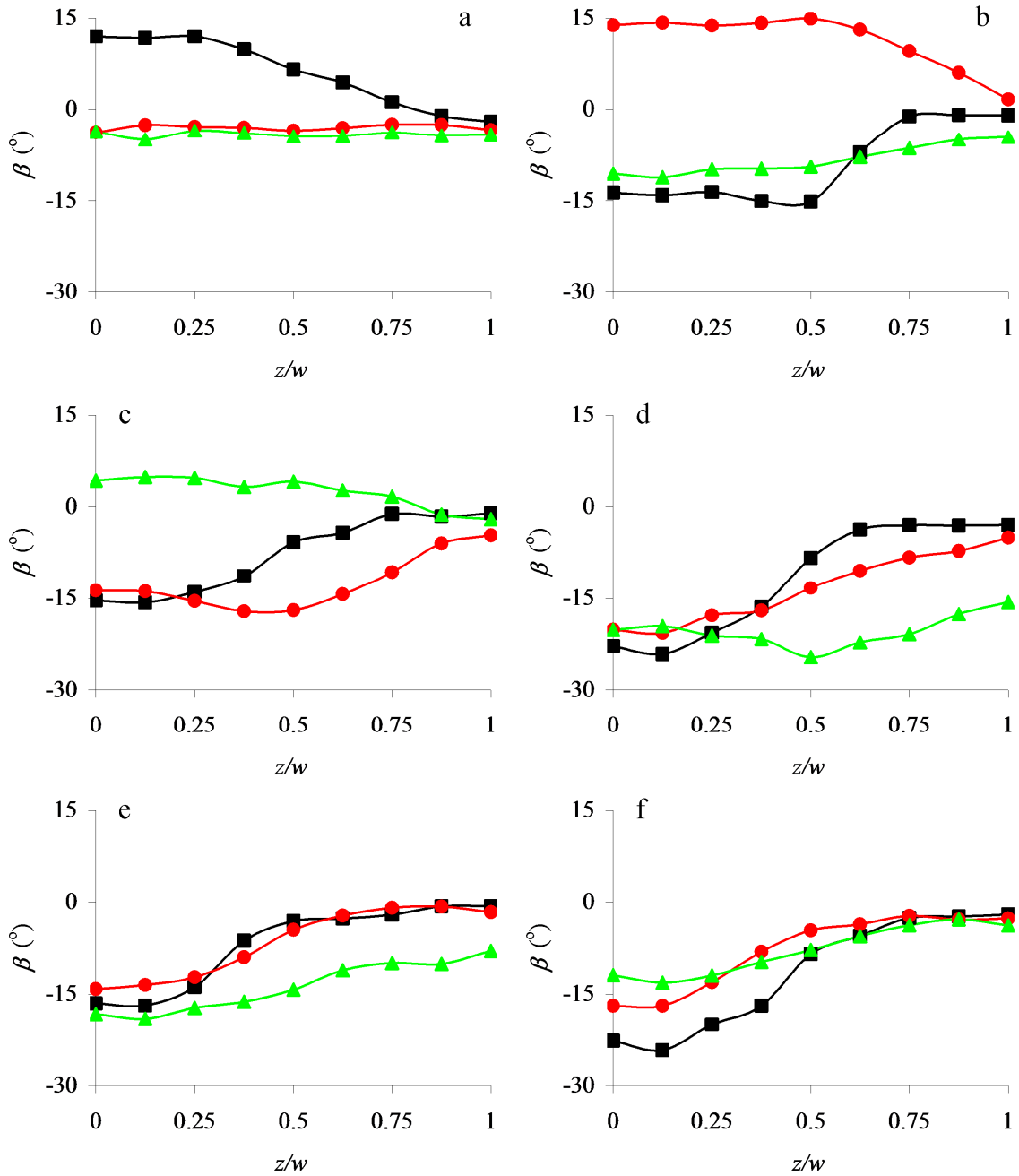


Figure 68. Analysis of PIV data shown in Figure 67 (among other temporal and spatial increments) regarding the transient flow response to the onset of actuation while $Re_{jet} = 407$ and $U_\infty = 30$ m/s: Spanwise variations of the angle of the momentum flux vector calculated between cross-stream elevations of 0.2 and $0.9 U_\infty$ at three streamwise locations for (a) $t/T_{jet} = 1.5$, (b) 3.0 , (c) 4.5 , (d) 6.0 , (e) 7.5 , (f) 9.0 . $x/h = \blacksquare 50, \bullet 100, \blacktriangle 140$

Figure 68 shows the spanwise variation of the momentum flux vector angle calculated from the PIV data between elevations of 0.2 and 0.9 U_∞ at $x/h = 50, 100,$ and 140 for $t/T_{Jet} = 1.5$ (a), 3 (b), 4.5 (c), 6 (d), 7.5 (e), and 9 (f). At $t/T_{Jet} = 1.5$ there is measurable response only at $x/h = 50$, with positive (upward) angles of up to 12 degrees near the centerline in association with the starting vortex as it moves downstream. At $t/T_{Jet} = 3.0$ these upward angles are measured at $x/h = 100$ up to $z/w = 0.75$ while the flow at $x/h = 50$ now vectors downward from -15° at the centerline, decreasing through the spanwise edge of the orifice at $z/w = 0.5$ and thereafter relaxes to 0. From $t/T_{Jet} > 4.5$ the spanwise variations of angle at $x/h = 50$ remain reasonably similar while the downstream distributions continues to vary until ultimately all three distributions are nominally similar at $t/T_{Jet} = 9$ showing some vectoring for $z/w < 0.5$ but almost none in the outboard spanwise segment. However up to $t/T_{Jet} = 7.5$ it should be noted that the response to actuation causes a measurable response across the field of view to $z/w = 1$, twice the width of the orifice.

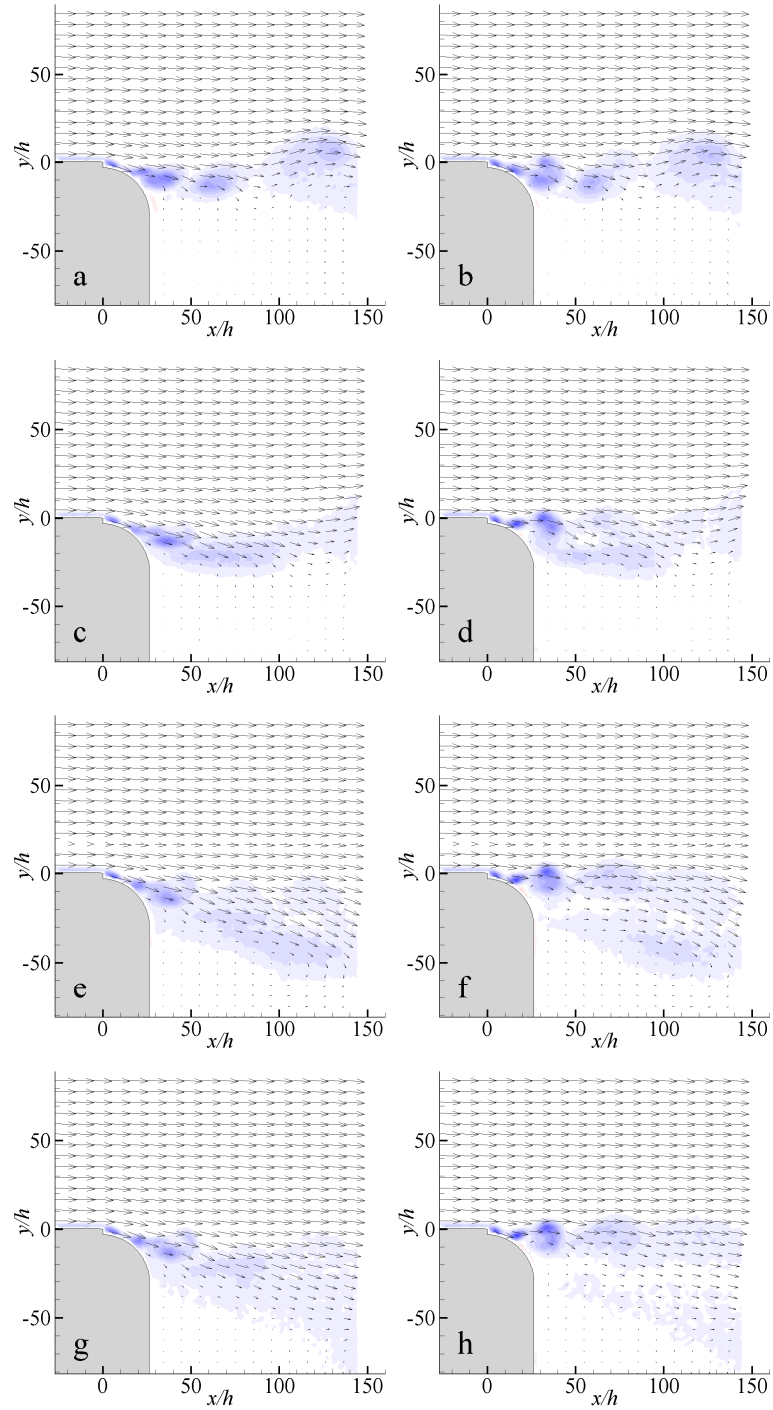



Figure 69. PIV images of the phase-averaged transient flow response to the onset of actuation for $z/w = 0$ (left column) and 0.375 (right column) while $Re_{Jet} = 407$ and $U_\infty = 30$ m/s: (a & b) $t/T_{Jet} = 3.0$, (c & d) 4.0 , (e & f) 6.0 , and (g & h) 10.0 . Vorticity scale: $-20,000$  $20,000$ 1/s. $y/h > 50$: Vector lengths indicate 30 m/s.

It can be concluded from this spanwise study of the transient response that attachment of flow to the Coanda surface is the key to sustained flow vectoring regardless of spanwise position. However despite absence of attachment to the surface in more distant planes, vectoring of flow into the wake will occur there in the short term during the transient response. A consistent feature across the observed planes is the large recirculation zone present at $t/T_{Jet} = 6$ (cf. Figure 67). The vectoring into the wake, on any plane studied here, is greatest at approximately $t/T_{Jet} = 6$ in association with this recirculation zone (cf. Figure 68). The amount of recession from the condition achieved at this time varies greatly with position as noted. But the evolution up to this time is much more similar across a wider span, indicating this is a turning point in the mechanism. A comparison of the flow at $z/w = 0.375$ against that of the centerline ($z/w = 0$) is perhaps the best example to study, shown in Figure 69 at select points in time. The response at $z/w = 0.375$ has been pivotal throughout this discussion because the flow attaches to the surface behind the orifice but does not follow the radius, however minimal vectoring effect occurs. While the jet at $z/w = 0.375$ is not capable of following the Coanda surface to the same extent as at the centerline (whether due to local jet velocity or external effects), for the first few cycles that is not important. Essentially for $t/T_{Jet} < 3$ the mechanism primarily involves the formation of the starting vortex and attachment to the surface behind the orifice. The vectoring into the wake really only begins after $t/T_{Jet} = 3$, and for vectoring to occur immediately adjacent to the surface the flow must follow the Coanda surface, and the variation in ability of the flow to remain attached to the Coanda surface is what causes the much greater variation in the end result. However between $4 < t/T_{Jet} < 6$ another effect occurs, which causes transient vectoring into the

wake farther downstream; when the starting vortex rolls up it is not only collecting the baseline shear layer but absorbing and exposing the previously stable baseline recirculation that defined the original wake. In the void left behind the vectoring begins, and while the starting vortex is still clearing out the baseline remnants farther downstream, the newly vectored flow drives a new recirculation to form due to the shearing with the quiescent flow in the area below that was previously a part of the original baseline recirculation. The void left behind by the starting vortex is redefined by the vectoring. The scale of the new recirculation relates directly to the starting vortex as it quite simply fills the void left as the starting vortex moves downstream. It appears to reach somewhat of a critical mass at about $t/T_{Jet} = 6$, with a scale of about one step height (H), as the recirculation builds up inertia energized by the vectoring above. Even far from the centerline this energized recirculation helps to draw vectored flow downward at its downstream end, accentuating the vectoring effect even where the vectoring is otherwise minimal. From this point as the starting vortex moves downstream the recirculation grows to the scale of the original structure (about $6*H$ as indicated by earlier floor pressure measurements) and in doing so no longer aids the flow vectoring, which occurs on a much shorter length scale of approximately one step height H , as seen by $t/T_{Jet} = 10$. Recall however that unlike the recirculation, the vectoring effect is not related to the step height, as previously identified; it is coincidentally a good scale to apply with this configuration. Simply as could be expected, the vectoring effect is maximized when the recirculation is of the same scale, as occurs at $t/T_{Jet} = 6$.

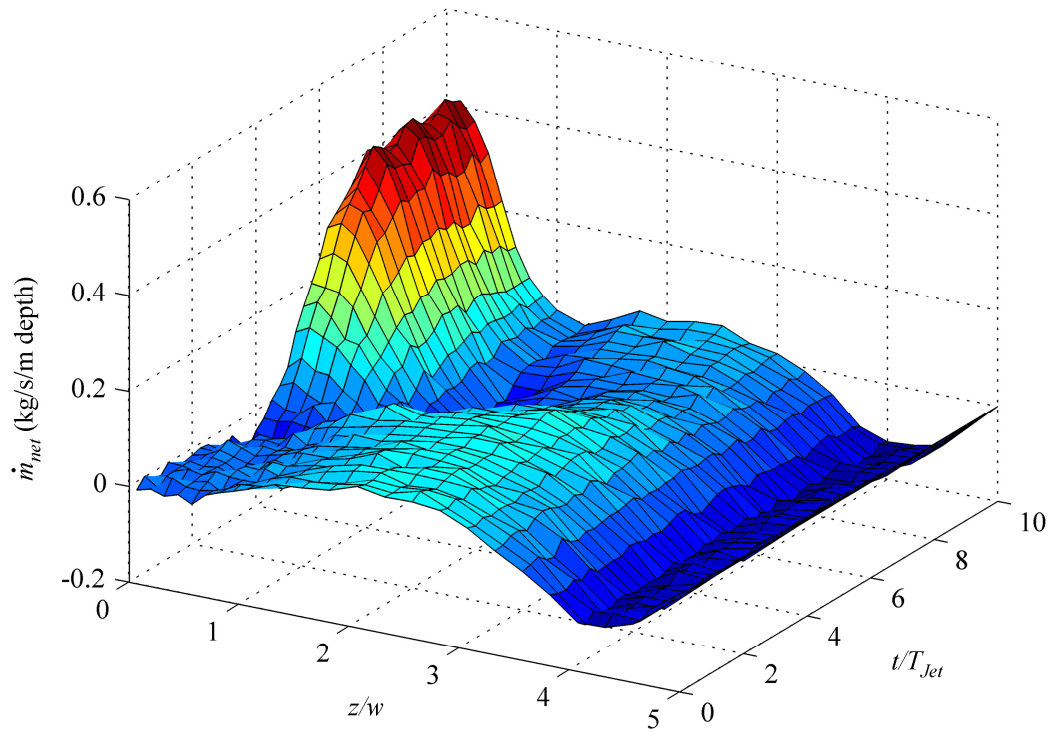


Figure 70. Three-dimensional mapping of the transient evolution of out-of-plane mass flux in response to the onset of actuation, across the span of the test section.

The transient evolution of the spanwise distribution of mass flux is depicted in a three-dimensional map in Figure 70. For the first three actuation cycles the spanwise distribution of mass flux remains relatively flat and constant, near the baseline level previously discussed in relation to time-averaged measurements shown in Figure 66. The sustained gutter-like trough near the outer edge (around $z/w = 4$) is related to wall effects and has little impact on the effect of interest. The transient response to actuation is characterized by the appearance of a strong peak at the centerline for $t/T_{Jet} > 4$ which grows in magnitude and span to extend beyond the spanwise edge of the actuator by $t/T_{Jet} = 7$ and is commensurate with the vectoring of the flow near center span. The spanwise

distribution of mass flux appears to stabilize by $t/T_{Jet} = 8$ and remains about constant thereafter. The most striking feature of this map is the relatively narrow transition from the baseline to the actuated condition. The core of the shift in the distribution occurs near center span, essentially between $3 < t/T_{Jet} < 7$. A diagonal depression is formed along the base where the large influx to the center begins just before $t/T_{Jet} = 4$, where surprisingly a drop in the mass flux (i.e. an outflux) occurs between $0 < z/w < 1$. The depression spans $1 < z/w < 3$ by $t/T_{Jet} = 7$, indicating that as the influx commences the location of the local deficit rolls outward in time and spreads until the effects of the deficit are distributed across the span, as is seen in the lower surface elevations in the area behind (after) the depression. As in the continuous cases, each distribution was integrated across the span at each point in time to confirm the conservation of mass, with small but reasonable errors ($< 5\%$).

The data presented here show that the transient response affects the entire span of the test section. Mass is entrained from across the span to produce the flow vectoring effect that is observable to some degree up to twice the width of the orifice. The limited spanwise uniformity during the early stages of the transient response ($t/T_{Jet} < 3$) is apparently not so much connected to the Coanda radius but simply attachment to the tangential portion of the Coanda surface behind the orifice which weaker areas of the jet are similarly capable (despite not being able to follow the Coanda radius). Interestingly, during these early stages the spanwise distribution of mass flux is essentially invariant, suggesting only local effects. Attachment along a greater portion of the Coanda radius is the key to sustained flow vectoring, which only occurs over approximately the central half of the actuator, for $t/T_{Jet} > 3$. The drastic changes in mass flux that occur between 3

$< t/T_{Jet} < 7$ appear to be associated with the starting vortex that is advected downstream and the ensuing vectoring into the wake near the center of the span. However during this time a recirculation which forms just upstream of the starting vortex conjoins with weaker actuation effects near the outer edges of the orifice to generate a transient vectoring into the extended wake, which has a maximum effect at about $t/T_{Jet} = 6$ and then vanishes once the recirculation on the low speed side grows to alter the wake in the presence of actuation. During this time, between $7 < t/T_{Jet} < 10$, mass becomes entrained from the outer regions of the span and the overall response stabilizes, in keeping with the convective time scale associated with the length of the baseline recirculation in the wake.

CHAPTER 6

CONCLUSIONS

The effectiveness of fluidic-based aerodynamic flow control for the generation of significant normal forces on a body of revolution in flight was demonstrated in extensive wind tunnel experiments. Actuation was effected by an azimuthal array of rearward-facing synthetic jets integrated into the aft segment of the model's tail section along with a toroidal aft control (Coanda) surface. The azimuthally-segmented control jets issued tangential to the Coanda surface from high aspect ratio orifice slots.

The flow over the tail section was normally separated and formed a nominally axisymmetric wake. Activation of one of the jets led to local attachment of the separated flow to the adjacent Coanda surface and consequently caused local turning of the free stream toward the center of the near wake and induced aerodynamic reaction force on the body. Time-averaged velocity measurements using PIV over a range of control jet strengths showed that as a result of the interaction between the jet and the cross flow a low-pressure region forms near the actuator, the cross flow turns around the surface, and the separation moves farther downstream. The degree of turning increases with jet Reynolds number (and momentum coefficient). The rate of change of the normal force that is effected by the flow turning over the Coanda surface varied with jet strength, and in the presence of small streamwise fences at the azimuthal edges of the jet that regulate entrainment of ambient air, the variation of the normal force with actuation voltage was almost linear over the entire range of actuation input. It is remarkable that some degree of flow turning and an aerodynamic force were achieved even in the absence of a Coanda

surface, suggesting that the basic mechanism namely the creation of a low pressure domain near the aft end of the body may be created simply by the interaction of the synthetic jet with the free stream. The measurements also showed that for given flow or control jet strength, the normal force increases with the radius of the Coanda surface.

The aerodynamic response of the platform to transient actuation was assessed using pulse- or step-modulation of the actuation waveform. The characteristic rise time of the normal force to the level that is associated with continuous actuation was commensurate with the convective time scale of the flow (in fact, the force overshoots and undergoes several oscillations at a frequency that is close to the shedding frequency of the body). The characteristic fall time following the termination of the actuation is typically longer than the rise time and is associated with the separation of the flow from the Coanda surface. It was also shown that when the actuation pulse is shorter than the convective time scale, the induced aerodynamic force continues to rise following the termination of the pulsed actuation on the order of the convective time scale in connection with the shedding of a starting vortex induced by activation of the control jet. The present results also suggest that there is coupling between the jet activation and the intrinsic dynamics of the wake region. Measurements in radial planes at various azimuthal positions away from the centerline indicate significant variation in the flow turning over the azimuthal span of the orifice. More notably, and likely attributable to transient force peaks, these azimuthal variations are more apparent when the actuation is quasi-steady than during transient operation following jet start-up. The evolution of flow turning during the first few cycles appears azimuthally uniform, after which the flow away from the centerline recedes, to the extent that separation reappears near the orifice

edge during continuous actuation. Elevation of neighboring tail surfaces through the use of a channeled geometry improves flow turning over the orifice span and consequently improves the aerodynamic performance.

Comparison of the aerodynamic performance of synthetic and conventional (steady) control jets indicated that the global effects of the actuation are quite similar in that the augmentation ratio (Au) of the aerodynamic force to the thrust of the actuation jet J varies like $Au \sim J^{-0.7}$ over five decades regardless of whether the actuation jet is synthetic or steady. This also indicates that the augmentation is most significant when the thrust of the actuation jet is low. Therefore, the ability to amplify thrust via tangential blowing over the Coanda tail surface appears related more to the limits of potential to induce aerodynamic force via flow turning rather than the choice of forcing method. However, a self-contained synthetic jet actuation system is very appealing for systems in which an external air supply is not available.

To further understand the flow mechanics of the interaction of a synthetic jet with the cross flow, a simplified planar model which isolated the interaction domain of the flow turning was investigated. The increase in flow vectoring with jet strength at a fixed cross flow speed matched the results observed earlier for the axisymmetric model. While in the absence of the cross flow the jet readily attaches to the Coanda surface, the interaction with the cross flow delays attachment, requiring about twice the jet strength to achieve a similar result. A comparison of matched (cross flow to jet) velocity ratios over a range of free stream speeds suggested that once attachment to the Coanda surface is established, the vectoring angle may only depend on this velocity ratio. For a given jet strength, the vectoring was found to decrease with increasing cross flow speed,

suggesting that the vectoring capability is defined by the geometry and the resistance of the cross flow (as may be measured by its increased momentum) limits the effectiveness of the actuator.

The effects of geometrical parameters such as Coanda radius, floor height, and orifice step height were also considered. Within the range of parameters studied only the orifice step height was found to cause changes in the sustained flow vectoring, because of its direct effect on the interaction domain of the actuator. The vortical structures which eject from the actuator (whose scales are defined by the orifice height) must be able to interact with the cross flow, and therefore the orifice edge should only be a few width multiples taller than the orifice height.

Pressure measurements on the horizontal wall downstream of the backward facing step showed that the flow reattached approximately 5 to 6 step heights downstream of the step. It is noteworthy that the distribution of wall pressure changed only slightly in the presence of actuation, indicating the isolation of the interaction of the actuation with the cross flow over the Coanda surface. However the length scale of the wake was found to directly influence the transient response to the onset of actuation. Through a study of the transient response at various cross flow speeds (with fixed jet strength) it was found that the time scale of the response depends on to the convective speed of the cross flow and the length scale of the wake. The stabilization of the flow to the newly vectored state naturally involves a recreation of the wake in this state, which requires at least one convective time scale, and is known from pressure measurement to remain similar in size despite the local vectoring.

The evolution of the flow over the Coanda surface following transitory actuation was found to be characterized by two time scales. First, for the given actuation jet Reynolds number (Re_{Jet}) and a Coanda surface, the characteristic time for flow attachment along the surface appeared to be on the order of three jet cycles, independent of the cross flow speed. Another relevant time scale is a “global” time scale $T_{settling}$ that is associated with the settling of the transitory modifications of the flow over the Coanda surface (as measured at $x/h = 20$). The present investigation has shown that the settling time $T_{settling}$ decreases with increasing tunnel speed ($7.2 T_{Jet}$, $4.2 T_{Jet}$, and $3.0 T_{Jet}$ at $U_\infty = 10, 20, \text{ and } 30 \text{ m/s}$, respectively), and are probably affected by the presence of the recirculating domain downstream of the step even though the actuation does not have a significant impact on the streamwise length of the recirculating flow domain which scales with the height of the step.

A study of the reversal of the order of suction and blowing at the onset of transitory actuation (by changing the polarity of the piezoelectric disc) revealed slight differences in the transient flow response, related to the linkage between the oscillating suction and blowing of the synthetic jet actuator. The present experiments demonstrated that to maximize the transient response the blowing stroke should occur first, otherwise the starting vortex which forms following the first suction stroke is held back by the ensuing blowing stroke, as these two combine during advection downstream. This results in a delay of half an actuation cycle in the transient evolution of the wake. High-resolution PIV measurements of the jet interaction domain revealed additional details of the coupling between the actuator’s suction and blowing strokes. The suction essentially accumulates vorticity from the upstream boundary layer that is shed from the corner

above the orifice edge. New, counter-rotating vortex pairs are formed and ejected time-periodically. The coupled suction and ejection lead to the formation of a low-pressure domain and results in turning of the cross flow to the Coanda surface while also entraining free stream cross flow fluid.

A detailed investigation of spanwise variation in the flow response to actuation was conducted using PIV at spanwise increments along the span of the test section with emphasis on balance of mass flux. Time-averaged measurements during continuous actuation indicated that the vectoring effect is stronger over the central half of the actuator orifice as expected from earlier axisymmetric measurements. However spanwise distributions of momentum flux vector angle suggest flow vectoring effects (of a few degrees) exist up to three times the width of the orifice. The spanwise distribution of net out-of-plane mass flux showed that the effects of the vectored flow are felt over the entire width of the test section, with flow entrained from the domain near the tunnel walls towards the vectored flow near center span even though the test section is ten times wider than the jet orifice.

The spanwise effects of the response to transitory actuation revealed nominally two-dimensional response over the extent of the orifice up to $t/T_{Jet} = 3$ following the onset of actuation. However for $t/T_{Jet} > 3$ the three-dimensionality of the jet flow becomes evident, leading to recession of the cross flow vectoring near the orifice edges ($z/w > 0.375$). The onset of a low-level recirculation domain (adjacent to the actuator in intermediate stages, clearly seen at $t/T_{Jet} = 6$) temporarily enhances the vectoring of flow into the wake even far from the centerline, as measured by the momentum flux vector angle. This recirculation domain is initiated by the departure of the original starting

vortex and stretches in length during the remaining transient response until the new vectored state is reached. Temporal and spanwise variations of the out-of-plane flow revealed that the largest changes in the field of view occurred during the intermediate stages of the transient response ($3 < t/T_{Jet} < 7$) that is associated with the passing of the starting vortex and the ensuing vectoring of the cross flow. During this time it was evident that make up flow needed to support the vectoring started close to center span and later in the transient response spread outboard towards the walls of the test section.

In summarizing this work, several key observations are worth noting. The flow vectoring is a balance between the momentum of the cross flow and forces that are induced near the flow boundary by enhanced entrainment near the Coanda surface upon jet actuation. The interaction of the actuation jet with the cross flow is afforded by an orifice step height similar in scale to the vortices that form the jet, enabling their interaction with the cross flow. For a given cross flow speed, the vectoring is affected by the control jet strength and the characteristic scale of the Coanda surface, although large Coanda radii appear to cause blockage of flow vectoring which suggests a relationship between Coanda radius and orifice step height. The vectoring saturates once the cross flow becomes fully attached to the Coanda surface and appears to be entrainment-limited. Within geometrical limitations, the induced aerodynamic force increases with the spanwise extent of the actuation jet as thrust sensitivity to saturation is reduced in combination with an increase in affected surface area. A comparison between the vectoring effects of synthetic and steady actuation jets over the Coanda surface revealed a power law relation of augmentation to thrust over several orders of magnitude regardless of the specific nature of the actuation jet, suggesting that the vectoring is dominated by

entrainment of the cross flow and simply requires an adjacent perturbation to cause attachment and vectoring. It is noteworthy that the augmentation is largest at low thrust levels (less than 0.001 N) where the synthetic jet is most effective.

The present investigation employed a finite-span actuation jet and demonstrated that flow vectoring occurs over the central half of the orifice span. The diminution of the vectoring near the outer edges of the jet can be attributed to edge effects as a result of the spanwise variation in the jet strength, and lateral (azimuthal) entrainment of the (separated) cross flow which reduces the low pressure domain downstream of the jet orifice. It was shown that these azimuthal entrainment effects can be significantly mitigated by using elevated streamwise sidewalls to form an open “channel” along the edges of the actuation jet, restricting this lateral entrainment and thereby increasing the entrainment-induced streamwise suction which enhances vectoring even downstream of the jet centerline. In addition, the use of a recessed channel and the absence of a backward-facing step beyond the azimuthal edge of the jet may delay separation there, and therefore enhance the effectiveness of the jet. Furthermore the channel sidewalls, which lie in radial planes on an axisymmetric model, contract the wall jet azimuthally and accelerate the flow as it follows the Coanda surface, thereby sustaining its momentum and further entrainment of the outer cross flow.

Synthetic jet actuation (unlike steady jets) lends itself to transitory actuation and momentary application of aerodynamic steering forces. The transitory flow response scales with the characteristic streamwise length of the near wake, which is affected by the local flow dynamics in the presence of actuation. The initial transient evolution of the flow attachment immediately downstream of the jet appears to be affected by jet strength

and its interaction with the adjacent to the Coanda surface. For effective pulsed operation of the jet (using amplitude modulation), the pulse duration has to be long enough to cause local cross flow vectoring over the Coanda surface. Actuation with a single pulse has demonstrated that while the starting vortex that is associated with the onset of flow attachment commences within one actuation cycle, significant flow vectoring and aerodynamic force requires several actuation cycles. It is interesting to note that the transient effect along the span of the jet is more pronounced than the quasi-steady effect associated with continuous actuation indicating that the spanwise edge effects occur over longer time scales. In fact, the spanwise starting vortex extends farther along the span than the ensuing flow vectoring. Measurements of spanwise volume flux indicate that the effects of the actuation are felt well beyond the spanwise edges of the jet (up to five orifice jet widths), indicating that it might be possible to augment vectoring effects by exploiting the interactions of spanwise-segmented actuation jets.

Finally, it is noted that the findings of this research played an important role in the realization of DARPA's SCORPION (Self CORrecting Projectile for Infantry OperatioN) program that focused on the development of the synthetic jet based micro-adaptive flow control (MAFC) technology for aerodynamic steering of spinning projectiles in collaboration between Georgia Tech and ARL's Weapons and Materials Research Directorate. In the SCORPION platform, lateral aerodynamic forces were generated by the interaction of a single synthetic jet actuator over a tail Coanda surface for one quarter of every spin revolution. Following full system design, g-hardening, and integration, successful flight tests were conducted and demonstrated the effectiveness of the present MAFC approach for generating significant lateral movement of a projectile in flight.

APPENDIX A

COMPARISON TO STEADY BLOWING AND SUCTION

Through the discussion of inverting the order of suction and blowing, and the high resolution study of the vortex interactions adjacent to the orifice (cf. Section 5.7), the roles of the alternating suction and blowing appear evident. It appears that the oscillation leads to shedding of upstream boundary layer vorticity that is accumulated during the suction stroke, and the blowing stroke is necessary to inject the impulse that triggers flow vectoring. However, historically the Coanda effect was established through the use of steady blowing, and flow control has often been applied via steady suction as well, as discussed in the literature review (Chapter 2). While the advantages provided by the synthetic jet actuator in terms of low energy and zero net mass flux remain clear, it seems that the present discussion would not be complete without an examination of steady suction and steady blowing. With this in mind the planar actuator (cf. Section 5.1) was designed to also accommodate steady blowing and suction upon removal of the piezo disc. Through the use of conventional pneumatic controls and flow meters, it is easy to generate and control precise flow to or from the actuator chamber. While the configuration does not allow for an accurate study of the onset of either approach, the continuous time-averaged response can be observed.

The calculation of average thrust (J) for the synthetic jet is described in Section 4.5. The jet strength for the continuous jets is characterized in terms of its Reynolds number based on orifice height, $Re_{steady} = \rho U_{steady} h / \mu$, and the average velocity is

determined from the measured volume flow rate. The following table is useful in organizing the settings to be studied in this experiment:

Table 1. Conversion of synthetic jet strengths to equivalent steady jet strengths

Re_{Jet}	U_{Jet} (m/s)	J (N)	U_{steady} (m/s)	Q (L/min)	Re_{steady}
145	5.0	0.0017	11.1	7.5	323
218	7.5	0.0038	16.7	11.3	484
291	10.0	0.0067	22.2	15.0	645
407	14.0	0.0131	31.1	21.1	904

The four settings shown in the Table 1 originate from the synthetic jet data used in the time-averaged experiments in Chapter 5 (cf. Figure 40). For the conventional jets the air supply was regulated using a needle valve, and the volume flow rate was measured with a digital flow meter. In the suction experiments, a fluidic-driven venturi vacuum device was used along with the flow meter at the inlet of the vacuum port.

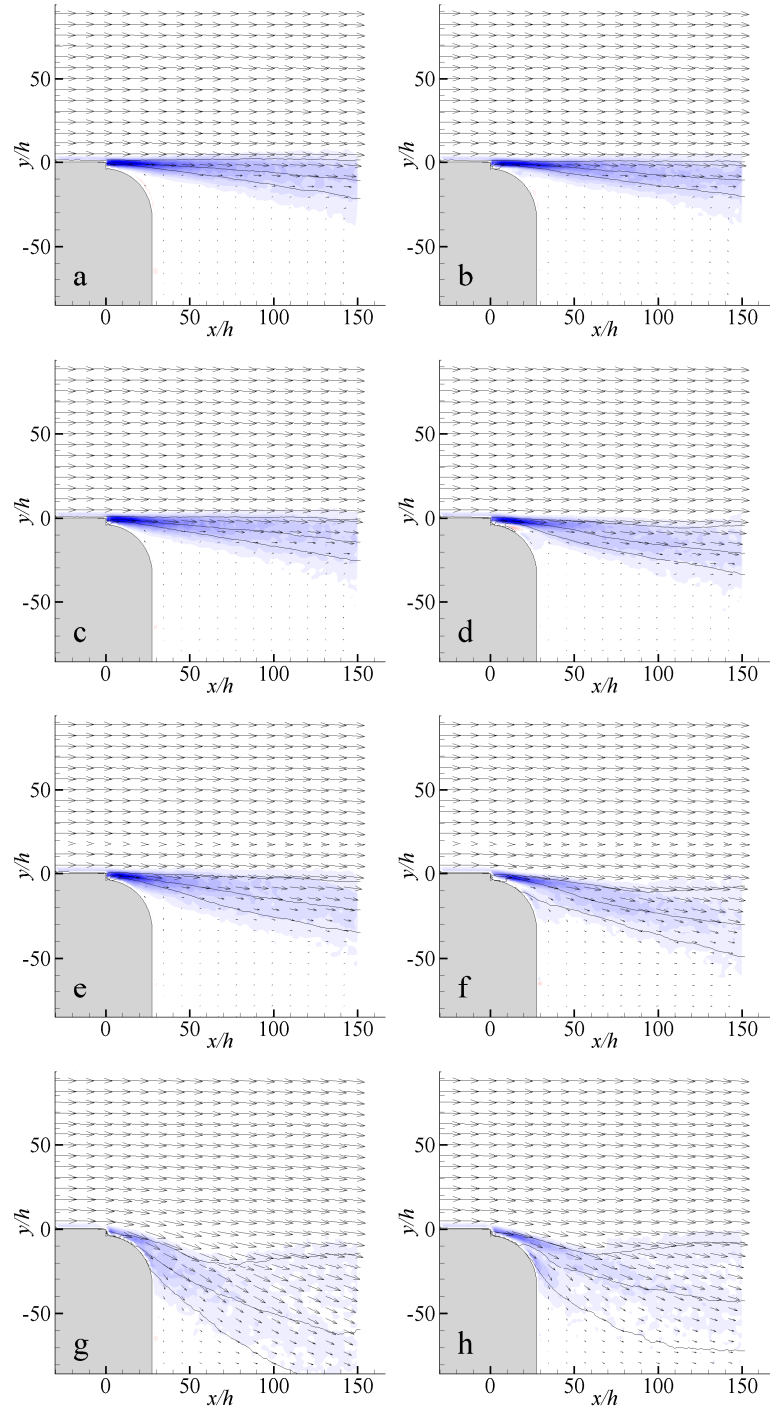



Figure 71. PIV images of the time-averaged flow field response to steady suction (left column) and steady blowing (right column) while $U_\infty = 30$ m/s: (a & b) $Re_{Steady} = 323$, (c & d) 484, (e & f) 645, and (g & h) 904. Line contours indicate 0.2, 0.5, and 0.9 U_∞ . Vorticity scale: -15,000  15,000 1/s. $y/h > 50$: Vector lengths indicate 30 m/s.

The measurements of steady suction and blowing are shown in Figure 71. It is immediately evident that both approaches have a similar effect on the flow, and a similar dependence of flow vectoring on jet strength. Once substantial vectoring is achieved, such as at $Re_{steady} = 904$, the suction exhibits slightly stronger vectoring into the wake near the right side of the field of view ($x/h > 90$), as indicated by the contour lines. Magnified images of $Re_{steady} = 904$ for both suction and blowing, shown in Figure 72, clarify this difference. At this strength, the velocity within the orifice is equal to the free stream speed. In steady blowing (right image) the jet exits the orifice underneath the separating shear layer that forms from the upper corner of the orifice edge (lack of seeding in air supply obscures initial measurement). The jet entrains flow from the shear layer, but the volume flow rate is insufficient. As the jet spreads along the Coanda surface, a velocity deficit is evident relative to the free stream across the entire field of view. It appears that because of this deficit, the jet is unable to entrain sufficient high-momentum fluid from the free stream and the vorticity clearly indicates that the shear layer and local free stream follow a vectored line across the view while the Coanda surface curves downward, causing the jet to spread, lose momentum, and become isolated from the free stream. Conversely the steady suction entrains the upstream boundary layer and causes it to attach to the Coanda surface, filling in this void with free stream fluid. Some of the lower velocity fluid from the boundary layer still appears to move downstream along the Coanda surface, and a slight deficit exists as the flow expands while following the radius, but the shear layer certainly appears to follow the surface more closely, and the free stream is effectively more engaged in the flow attachment. Because of this, the flow for the suction case is more efficient about vectoring into the

wake further downstream. And so it appears that a slight advantage can be given to suction by the nature of its mechanism.

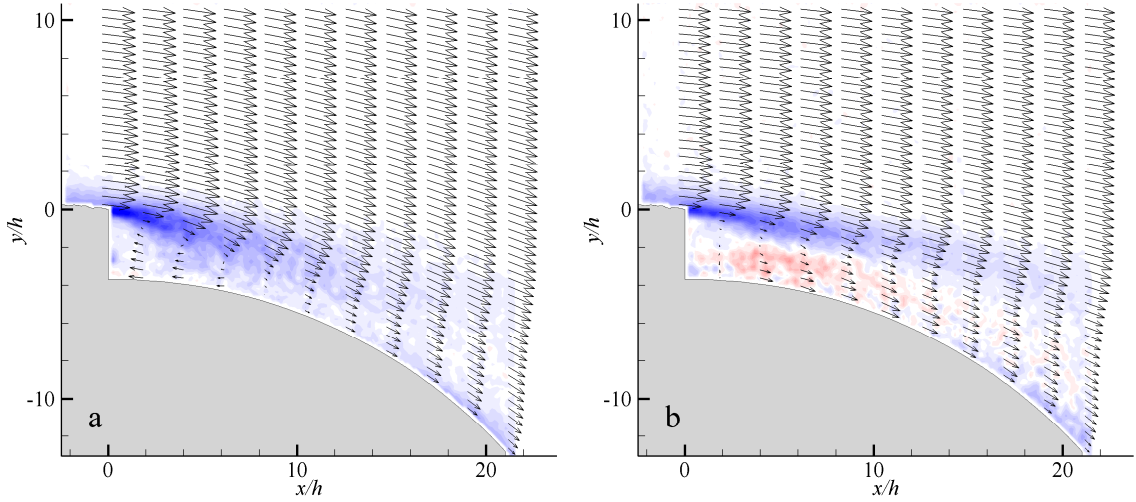


Figure 72. Magnified PIV images of the time-averaged flow field response to (a) steady suction and (b) steady blowing while $U_\infty = 30$ m/s and $Re_{Steady} = 904$. Vorticity scale: $-100,000$ $100,000$ 1/s. $y/h > 10$: Vector lengths indicate 30 m/s.

To further characterize these differences, analysis of the PIV measurements in Figure 73 shows the normalized width of the flow in the contour band between 0.2 and $0.9 U_\infty$, along with the momentum flux vector components and angle calculated for the same band of data. To simplify the comparisons between suction and blowing on these plots, a polarity convention was assigned such that suction results in negative jet strength while blowing results in positive jet strength. Overall, the results are surprisingly symmetric about zero despite the opposing directions of jet orifice flow, in support of the general similarities in the large-view PIV of Figure 71. Both approaches cause the shear layer to expand about four times wider than the baseline, with a substantial effect on

momentum flux vector angle. All four plots essentially support the same conclusion, that blowing causes a measurable effect at lower strength, certainly by $Re_{steady} = 400$, compared to suction not causing similar effects until $Re_{steady} = -650$. However, once the effect occurs under suction, the result in terms of momentum flux components and angle is certainly stronger than blowing for a given strength, by about 30%. The greater final result for suction is understood to be attributed to the direct entrainment of the free stream onto the Coanda surface. The reasons for the difference in initial response and related sensitivity will be explored further.

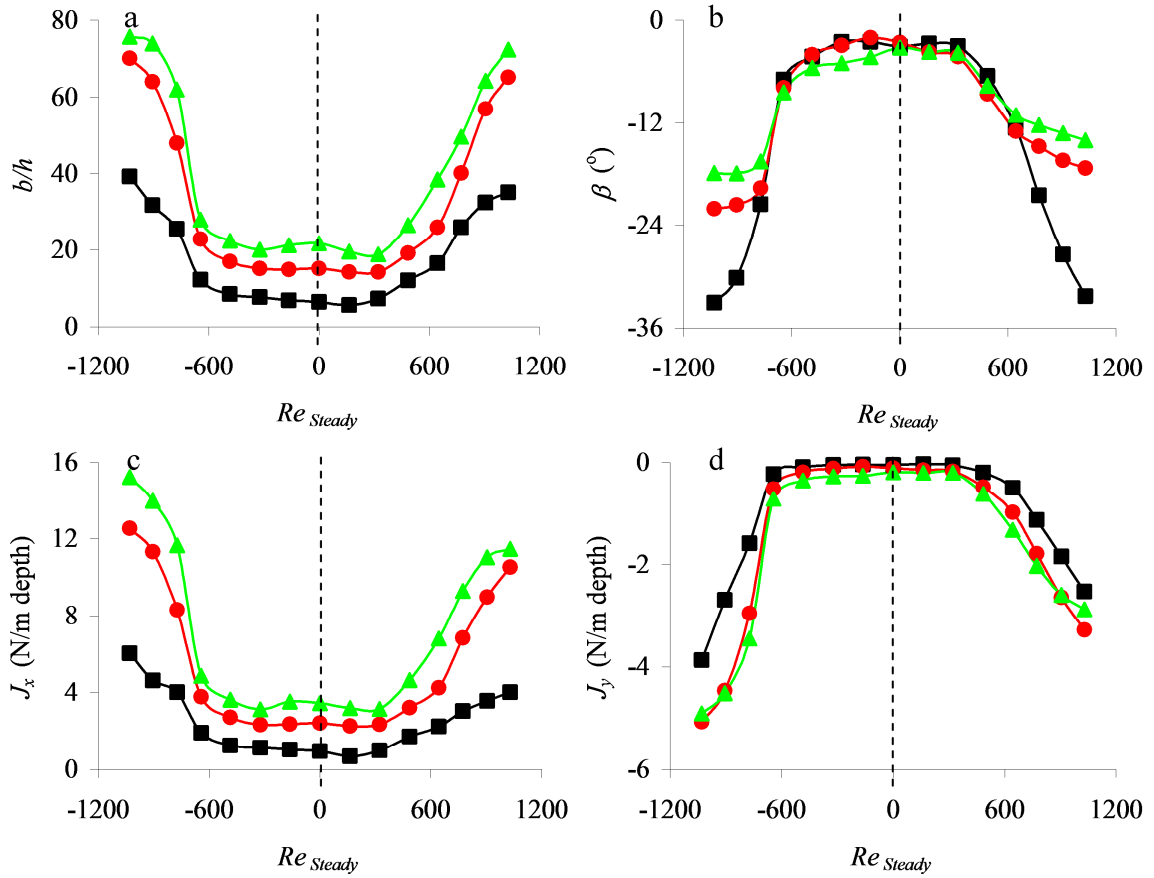


Figure 73. Analysis of PIV data shown in Figure 71 (among other intermediate jet strengths) regarding the flow response to steady suction and blowing while $U_\infty = 30$ (negative values of Re_{Steady} indicate suction): Streamwise variations of (a) the shear layer's cross-stream width, (b) the angle of the momentum flux vector, (c) streamwise momentum flux, and (d) cross-stream momentum flux calculated between cross-stream elevations of 0.2 and $0.9 U_\infty$ at three streamwise locations. $x/h = \blacksquare 50, \bullet 100, \blacktriangle 140$

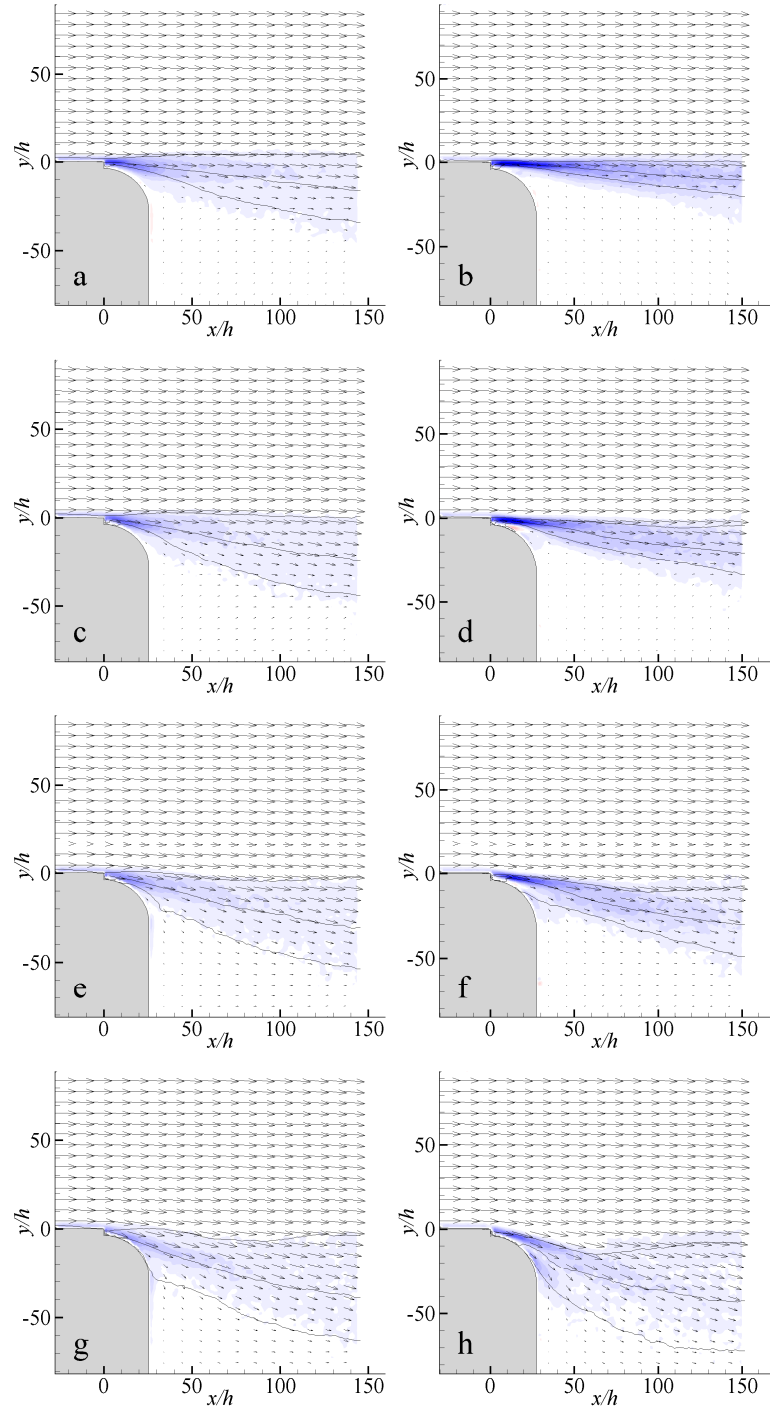



Figure 74. PIV images of the time-averaged flow field response to synthetic jet actuation (left column) versus steady blowing (right column) while $U_\infty = 30$ m/s: (a & b) $J = 0.0017$ N ($Re_{Jet} = 145$, $Re_{Steady} = 323$), (c & d) $J = 0.0038$ N ($Re_{Jet} = 218$, $Re_{Steady} = 484$), (e & f) $J = 0.0067$ N ($Re_{Jet} = 291$, $Re_{Steady} = 645$), and (g & h) $J = 0.0131$ N ($Re_{Jet} = 407$, $Re_{Steady} = 904$). Line contours indicate 0.2 , 0.5 , and $0.9 U_\infty$. Vorticity scale: $-20,000$  $20,000$ 1/s. $y/h > 50$: Vector lengths indicate 30 m/s.

For comparison to the synthetic jet, time-averaged measurements (previously shown in Figure 40) are placed along side the steady blowing measurements in Figure 74. Whereas at lower forcing levels the steady blowing and suction were identical, there are substantial differences compared to the synthetic jet. At $Re_{steady} = 323$, compared to an equivalent $Re_{Jet} = 145$ for the synthetic jet, the vectoring into the wake is far deeper for the synthetic jet. Analysis shown in Figure 75 helps to further quantify these differences, with steady suction also included, all shown at $x/h = 100$ and plotted in terms of jet thrust for direct comparison. In general it is evident that the synthetic jet exhibits superior performance for $J > 0.01$ but thereafter is worse than either steady approach. For the synthetic jet up to $J = 0.005$ the shear layer width is twice that of either steady approach, which follow each other quite closely over the presented range. However in terms of momentum flux vector angle, the synthetic jet follows the behavior of steady blowing quite closely. The momentum flux components are less revealing, other than showing that steady suction causes a great deal of cross-stream momentum flux for $J > 0.01$, effectively twice that of steady blowing.

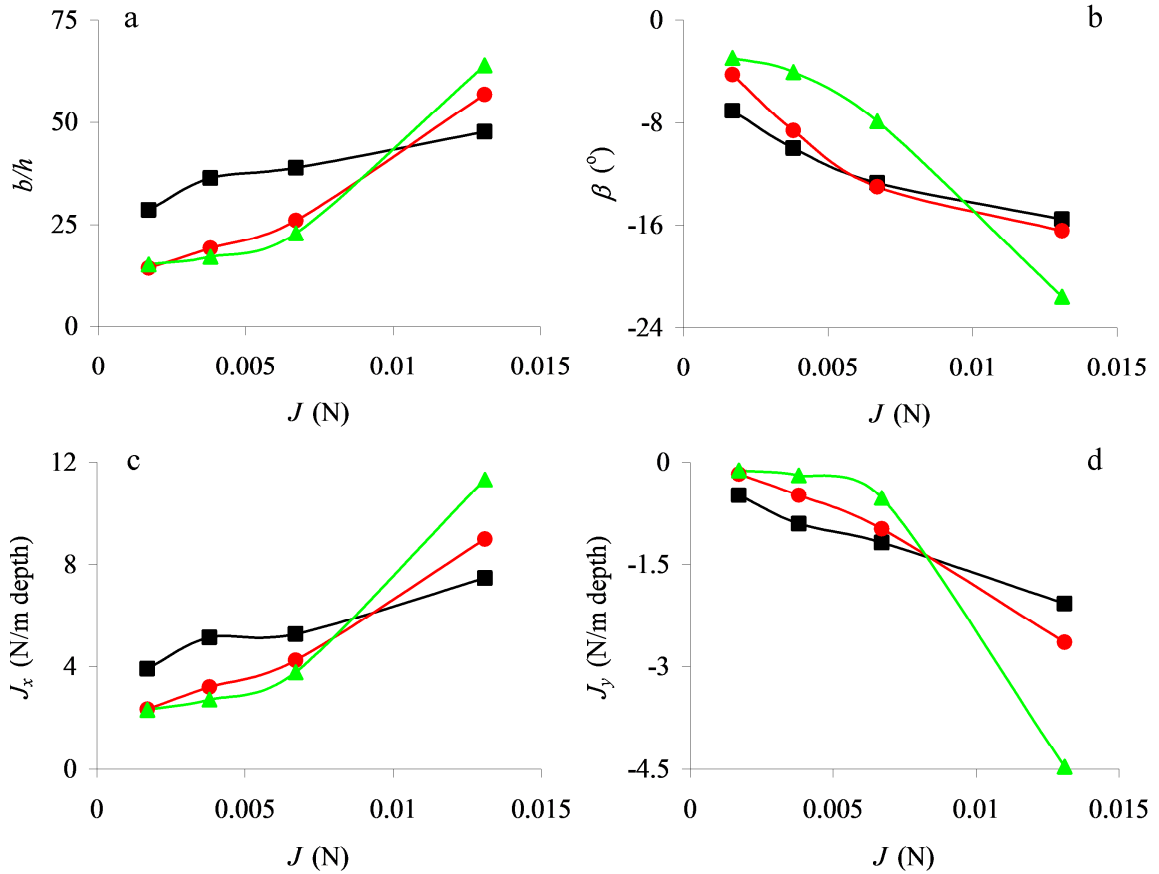


Figure 75. Analysis of time-averaged PIV data regarding the flow response to synthetic jet actuation, steady blowing, and suction while $U_\infty = 30$: Performance versus jet strength for (a) the shear layer's cross-stream width, (b) the angle of the momentum flux vector, (c) streamwise momentum flux, and (d) cross-stream momentum flux calculated between cross-stream elevations of 0.2 and $0.9 U_\infty$ at $x/h = 100$. ■ synthetic jet, ● steady blowing, and ▲ steady suction

Further insight is again revealed by higher resolution images, in Figure 76 of the blowing case for various jet strengths. An additional lower strength of $Re_{steady} = 161$, comparable to an equivalent $Re_{Jet} = 73$, was included for further clarification. From low-level velocity vectors adjacent to the orifice it is apparent that at lower strengths the jet does not follow the Coanda surface; it instead gets entrained into the shear layer. This is due to the low momentum of the jet combined with the local backward flow of the greater

recirculation zone behind the step. The jet exerts more influence locally as the strength is increased, but it takes until $Re_{steady} = 645$ for the jet to fully follow the Coanda surface in this view.

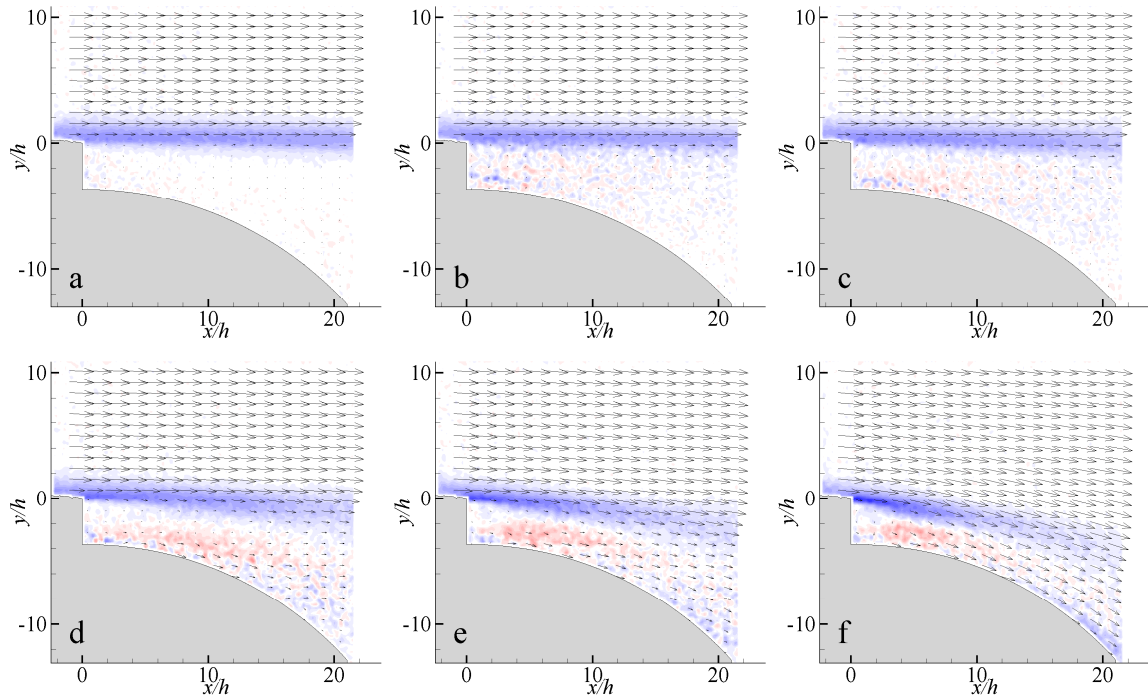
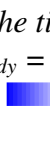


Figure 76. Magnified PIV images of the time-averaged flow field response to steady blowing while $U_\infty = 30$ m/s: (a) $Re_{steady} = 0$ (baseline), (b) 161, (c) 323, (d) 484, (e) 645, and (f) 904. Vorticity scale: -100,000  100,000 1/s. $y/h > 9$: Vector lengths indicate 30 m/s.

In the case of suction, shown in Figure 77, the jet again appears to simply supplement the existing condition at lower strengths. In this case the suction entrains fluid from the existing downstream recirculation zone rather than the upstream boundary layer. As the strength is increased the shear layer is first affected downstream of the actuator, being pulled down by the reverse flow accelerating toward the orifice. It takes a

great deal of jet strength, as in $Re_{steady} = 904$, for the suction to finally switch to entrainment of the upstream boundary layer, and when this switch occurs it appears abrupt as the flow into the orifice appears to never come from both areas. In fact, the complete reversal of flow along the Coanda surface downstream of the orifice between $645 < Re_{steady} < 904$ is a clear indicator of this change in the mechanism, and with the free stream now engaging the surface of the radius, the Coanda effect ensues. This observation supports the slower initial response and related high sensitivity indicated by the analysis as discussed earlier.

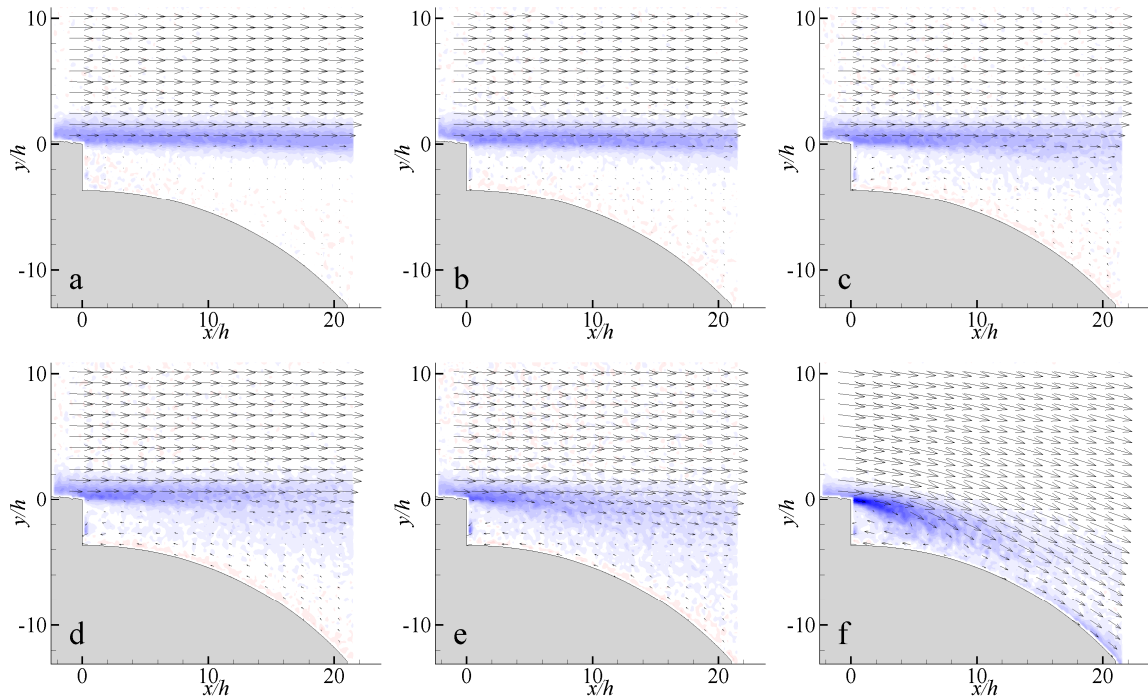



Figure 77. Magnified PIV images of the time-averaged flow field response to steady suction while $U_\infty = 30$ m/s: (a) $Re_{Steady} = 0$ (baseline), (b) 161, (c) 323, (d) 484, (e) 645, and (f) 904. Vorticity scale: $-100,000$  $100,000$ 1/s. $y/h > 9$: Vector lengths indicate 30 m/s.

The reasons behind the lack of effect for steady suction and blowing at low strengths are clear, but those behind the superior performance of the synthetic jet at low strengths are less obvious. Beginning first with further examination at high jet strength, key images from the last cycle ($4 < t/T_{Jet} < 5$) obtained in the prior high-resolution study of the transient response to actuation (in Section 5.7) are shown in Figure 78 ($Re_{jet} = 407$ and $U_\infty = 30$ m/s). While part of a transient record, for the purposes here the measurements in this magnified view can be considered equivalent to the phase-averaged behavior of the interaction domain during continuous actuation. Again recall that the blowing stroke occurs over the first half of the cycle, followed by the suction stroke.

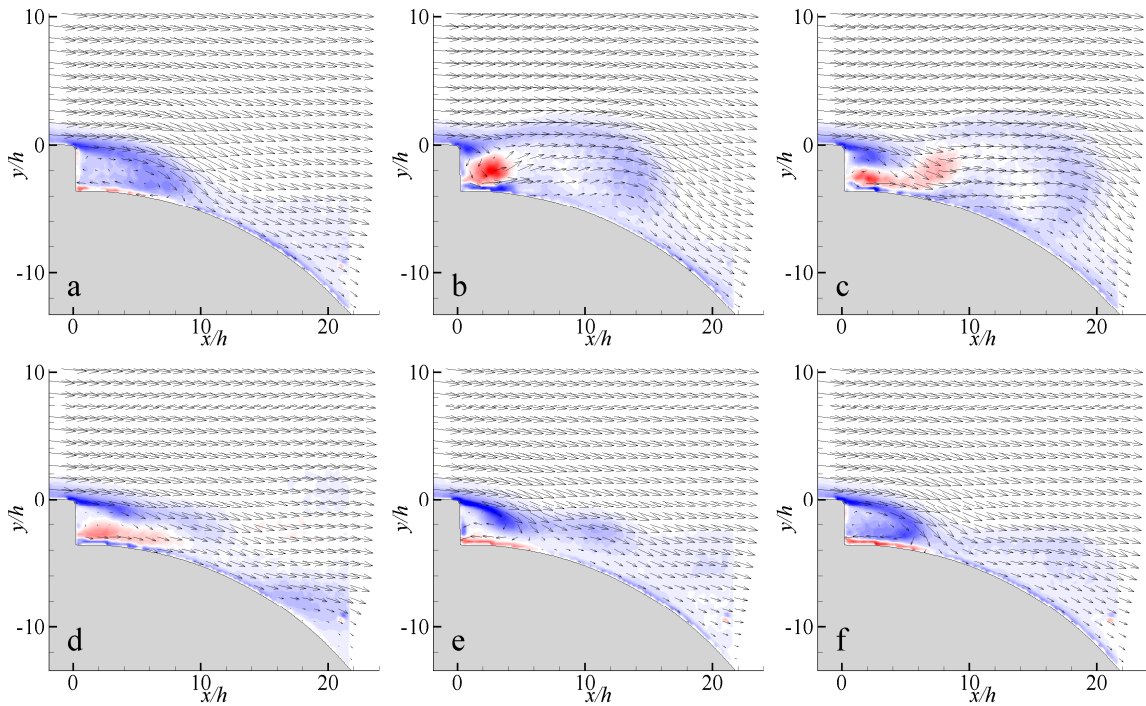



Figure 78. High-resolution PIV images of the phase-averaged transient flow response to the onset of actuation while $Re_{Jet} = 407$ and $U_\infty = 30$ m/s: (a) $t/T_{Jet} = 4.000$, (b) 4.250, (c) 4.350, (d) 4.500, (e) 4.7000, (f) 4.850. Vorticity scale: $-100,000$  $100,000$ 1/s. $y/h > 9$: Vector lengths indicate 30 m/s.

Starting at $t/T_{Jet} = 4.0$, the blowing stroke is about to begin but the present view shows the end result of the prior suction stroke. Much like steady suction at equivalent strength, the upstream boundary layer is entrained into the orifice, forming a small recirculation zone, while the free stream drops down and attaches to the Coanda surface, forming a small layer of vorticity along it. As the blowing stroke commences, the boundary layer vorticity gathered by the prior suction stroke is pushed away from the orifice, downstream. The actual vortex pair being ejected from the actuator (visible at $t/T_{Jet} = 4.250$) is far behind this and diffuses. However ahead of this vortex pair the tail end of the gathered vorticity is vectoring upward slightly as it is pushed from the orifice, which causes the structure to roll over itself head first as it moves downstream. At the same time, in the area preceding this vorticity (downstream) a noticeable deficit in velocity occurs near the surface, combined with a simultaneous increasingly downward flow angle in the same area. Directly under the vorticity, the velocity near the surface drops to nearly zero. However the ejected jet follows behind this and entrains free stream flow along with it to fill the void along the surface as fast as it is created. At the end of the blowing stroke ($t/T_{Jet} = 4.5$) the flow appears almost identical to that of steady blowing, with one important difference. In the steady blowing case the shear layer formed by the upstream boundary layer remains relatively coherent across the same field of view (cf. Figure 72), whereas with the synthetic jet the flow is clearly segmented, due to the prior suction stroke which had collected the upstream boundary layer vorticity. As the next suction stroke begins, some of the vorticity now leading off the orifice edge escapes and continues downstream, but diffuses rapidly. However behind this the flow

along the radius strengthens as the high-momentum free stream fluid is again pulled down to the surface while the suction entrains the boundary layer.

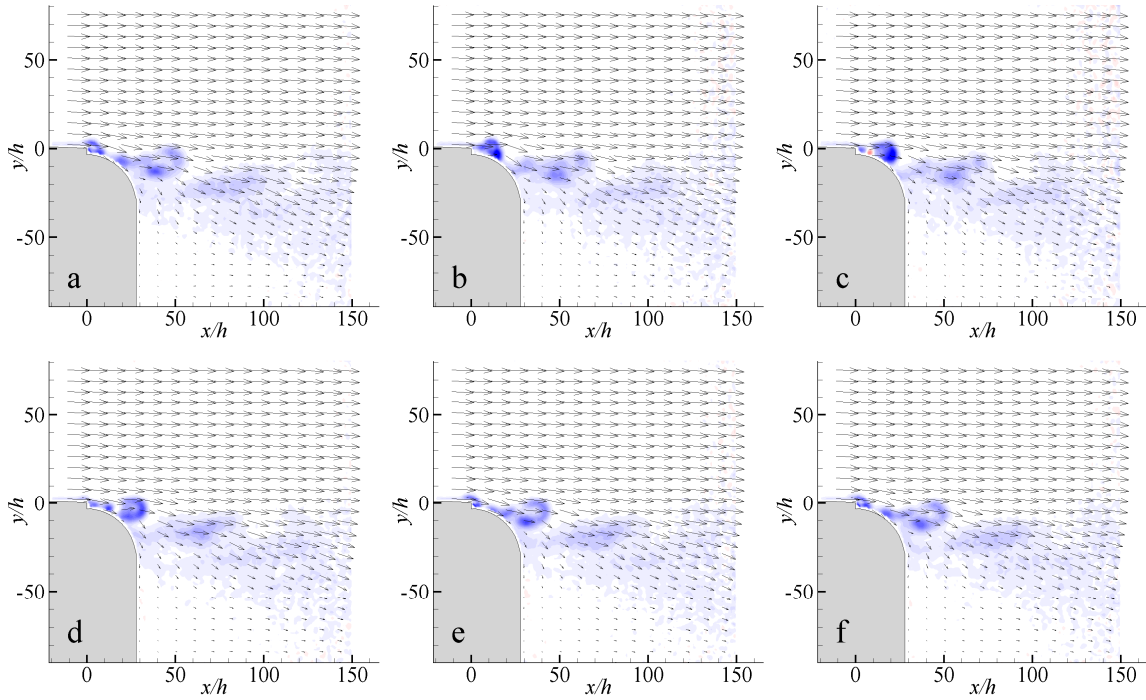



Figure 79. PIV images of the phase-averaged flow response to continuous synthetic jet actuation while $Re_{Jet} = 407$ and $U_\infty = 30$ m/s: (a) $\phi = 0^\circ$, (b) 90° , (c) 144° , (d) 216° , (e) 288° , (f) 342° . Vorticity scale: $-15,000$  $15,000$ 1/s. $y/h > 50$: Vector lengths indicate 30 m/s.

In a larger view of continuous actuation, again phase averaged over one cycle at the same settings, the downstream behavior of the vortex ejected by the blowing stroke becomes apparent. As witnessed earlier, the deficit in velocity and simultaneous increase in downward flow angle which precede the vorticity continue throughout the field as shown in Figure 79. The structure effectively rolls over itself by half of a revolution and diffuses to triple or more of its original size as it moves downstream in this view. The

vectors in the region through which the vorticity pass undergo substantial changes in angle and magnitude, with many changing in speed by a factor of two and varying in angle by sixty degrees, however retaining a mean downward angle. In the region below this the magnitude and angle of the vectored flow are far less variable. The “disposal” of the gathered upstream vorticity into discrete structures associated with each blowing stroke appears central to the flow turning mechanism. The vorticity concentration induces a downward twist in the flow which appears to aid in flow vectoring, and the flow appears to locally accelerate once the vorticity concentration is advected, further aiding in bringing flow into the wake.

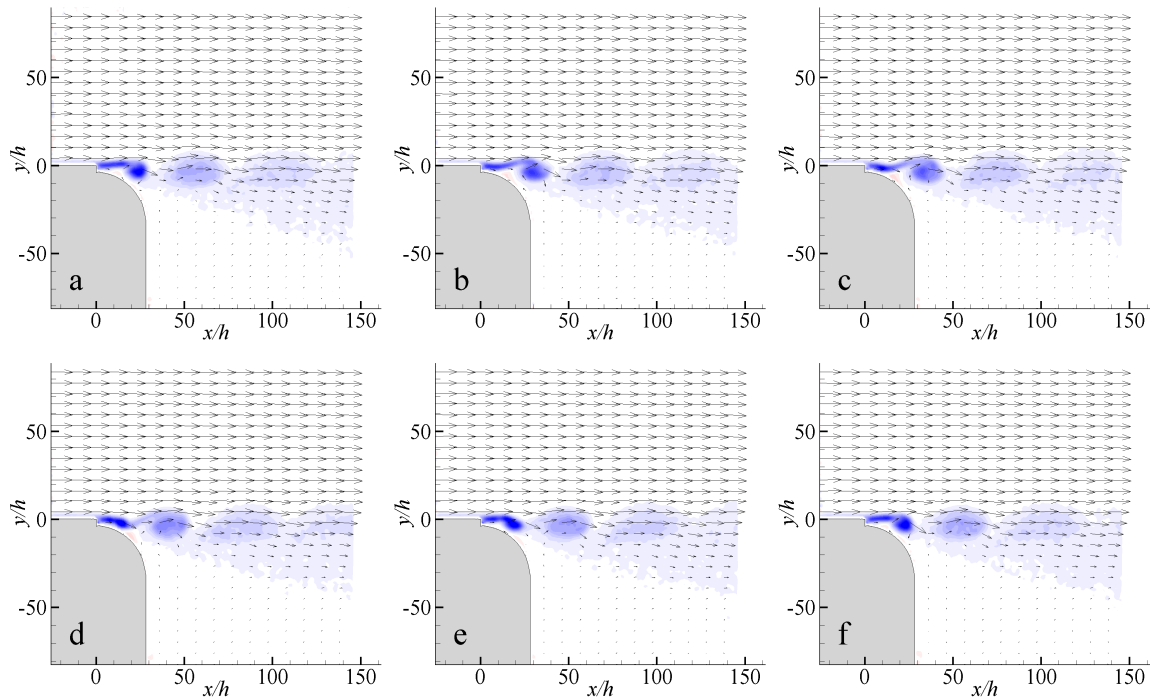



Figure 80. PIV images of the phase-averaged flow response to continuous synthetic jet actuation while $Re_{Jet} = 73$ and $U_\infty = 30$ m/s: (a) $\phi = 0^\circ$, (b) 90° , (c) 144° , (d) 216° , (e) 288° , (f) 342° . Vorticity scale: -20,000  20,000 $1/s$. $y/h > 50$: Vector lengths indicate 30 m/s.

An examination of similar data at a much lower jet strength of $Re_{Jet} = 73$, shown in Figure 80, indicate the same behavior, even though the Coanda effect is not present. The discrete vortices cause downward ripples in the flow which precede them, which produce a time-averaged downward flow angle locally. Analysis shown in Figure 81 further supports this observation where despite the difference in shear layer width and the flux vector angle, a coherent temporal variation in flux vector angle is apparent for both, with even greater fluctuation at $Re_{Jet} = 73$ and a mean sustained flux vector angle of about -6 degrees at the plotted streamwise position of $x/h = 100$. Whereas steady blowing and suction at similar low strengths simply supplement the baseline condition, the concentrated vorticity and momentum in these discrete structures are more capable of influencing the shear layer in a dynamic way which on average causes a slight vectoring effect. In this way, the synthetic jet is able to perform better at low strengths than a conventional steady jet.

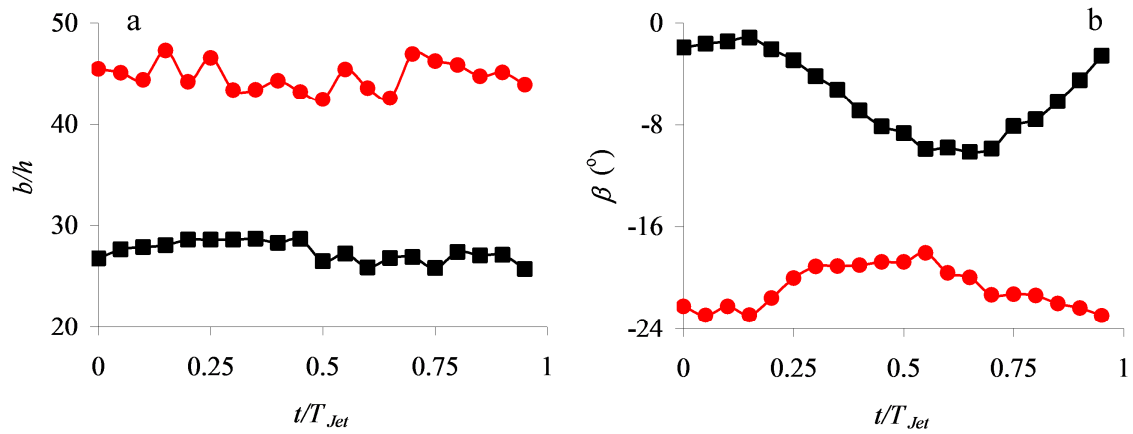


Figure 81. Analysis of PIV data shown in Figures 79 and 80 regarding the temporal variation of the flow response to continuous synthetic jet actuation while $U_\infty = 30$ m/s: Temporal variations of (a) the shear layer's cross-stream width and (b) the angle of the momentum flux vector, calculated between cross-stream elevations of 0.2 and $0.9 U_\infty$ at $x/h = 100$. $Re_{Jet} = \blacksquare$ 73, and \bullet 407

REFERENCES

- Amitay, M. and A. Glezer, "Aerodynamic Flow Control of a Thick Airfoil using Synthetic Jet Actuators", Proceedings of the 3rd ASME/JSME Joint Fluids Engineering Conference, San Francisco, California, 1999.
- Amitay, M. and A. Glezer, "Controlled Transients of Flow Reattachment over Stalled Airfoils", Int'l J. Heat and Fluid Flow **23**, pp. 690-699, 2002.
- Amitay, Michael, Barton L. Smith, and Ari Glezer, "Aerodynamic Flow Control Using Synthetic Jet Technology", AIAA Paper No. 98-0208, 1998.
- Amitay, M., D.R. Smith, V. Kibens, D.E. Parekh, and A. Glezer, "Aerodynamic Flow Control over an Unconventional Airfoil using Synthetic Jet Actuators", AIAA J. **39**, pp. 361-370, 2001.
- Amitay, M., V. Kibens, D.E. Parekh, and A. Glezer, "Flow Reattachment Dynamics over a Thick Airfoil Controlled by Synthetic Jet Actuators", AIAA Paper No. 99-1001, 1999.
- Betz, A., "History of Boundary Layer Control in Germany", *Boundary Layer and Flow Control I*, edited by Lachmann, G. V., Pergamon, London, pp. 1-20, 1961.
- Brown, F. N. M., Proceedings of the Sixth Midwestern Conference on Fluid Mechanics, University of Texas, pp. 331-49, 1959.
- Chang, R.C., F.B. Hsiao, and R.N. Shyu, "Forcing Level Effects of Internal Acoustic Excitation on the Improvement of Airfoil Performance", J. Aircraft **29**, pp. 823-829, 1992.
- Cheney, Ward, and David Kincaid, *Numerical Mathematics and Computing*, Brooks / Cole Publishing, Pacific Grove, CA, 1994.
- Chun, K.B., and H.J. Sung, "Control of Turbulent Separated Flow over a Backward-facing Step by Local Forcing", Exp. in Fluids **21**, pp. 417-426, 1996.
- Coanda, H., "Device for Deflecting a Stream of Elastic Fluid Projected Into an Elastic Fluid", U.S. Patent 2,052,869, September 1, 1936.
- Collins, Frank G., and James Zelenevitz, "Influence of Sound upon Separated Flow over Wings", AIAA J. **13**, pp. 408-410, 1975.
- Eaton, J. K., and J. P. Johnston, "A review of research on subsonic turbulent flow reattachment", AIAA J. **19**, pp. 1093-1100, 1981.

- Englar, Robert J., “Advanced Aerodynamic Devices to Improve the Performance, Economics, Handling, and Safety of Heavy Vehicles”, SAE Paper 2001-01-2072, 2001.
- Englar, Robert J., “Circulation Control Pneumatic Aerodynamics: Blown Force and Moment Augmentation and Modification; Past, Present, & Future”, AIAA Paper No. 2000-2541, 2000.
- Englar, Robert J. and Gregory S. Jones, “Advances in Pneumatic-Controlled High-Lift Systems Through Pulsed Blowing”, AIAA Paper No. 2003-3411, 2003.
- Erk, P.P., “Separation Control on a Post-stall Airfoil using Acoustically Generated Perturbations”, PhD Thesis, Tech. Univ. Berlin, Germany, 1997.
- Freund, J.B., and M.G. Mungal, “Drag and Wake Modification of Axisymmetric Bluff Bodies Using Coanda Blowing”, J. Aircraft **31**, pp. 572-578, 1994.
- Fric, T.F, and A. Roshko, “Vortical structure in the wake of a transverse jet”, J. Fluid Mechanics **279**, pp. 1-47, 1994.
- Geropp D., and H.-J. Odenthal, “Drag Reduction of Motor Vehicles by Active Flow Control using the Coanda Effect”, Exp. In Fluids **28**, pp. 74-85, 2000.
- Honohan, Andrew M, Michael Amitay, and Ari Glezer, “Aerodynamic Control Using Synthetic Jets”, AIAA Paper No. 2000-2401, 2000.
- Honohan, Andrew, “The Interaction Of Synthetic Jets With Cross Flow And The Modification Of Aerodynamic Surfaces”, Ph.D. Thesis, Georgia Tech, April 2003.
- Howard, Floyd G., and Wesley L. Goodman, “Axisymmetric Bluff-Body Drag Reduction Through Geometrical Modification”, J. Aircraft **22**, pp. 516-522, 1985.
- Hsiao, F.B., C.F. Liu, and J.Y. Shyu, “Control of Wall-separated Flow by Internal Acoustic Excitation”, AIAA J. **28**, pp. 1440-46, 1990.
- Kim, S.W., and T.J. Benson, “Fluid Flow of a Row of Jets in Crossflow – A Numerical Study”, AIAA J. **31**, pp. 806-811, 1993.
- Koenig, Keith, and Anatol Rosko, “An experimental study of geometrical effects on the drag and flow field of two bluff bodies separated by a gap”, J. Fluid Mech. **156**, pp. 167-204, 1985.
- Koopman, G. H., “The Vortex Wakes of Vibrating Cylinders at Low Reynolds Numbers”, J. Fluid Mechanics **28**, pp. 501-512, 1967.
- Kuchemann, D, *The Aerodynamic Design of Aircraft*, Pergamon Press, New York, 1978.
- Lachmann, C., “Experiments with Slotted Wings”, NACA TN-71, 1921.

- McCoy, Robert L., *Modern Exterior Ballistics: The Launch and Flight Dynamics of Symmetric Projectiles*, Schiffer Publishing Ltd, Atglen PA, 1999.
- Newman, B.G., “The Deflexion of Plane Jets by Adjacent Boundaries- Coanda Effect”, *Boundary Layer and Flow Control I*, edited by Lachmann, G. V., Pergamon, London, pp. 232-264, 1961.
- Prandtl, L., “Motion of fluids with very little viscosity”, NACA TM-452, 1928, English translation of “Über Flüssigkeitsbewegung bei sehr kleiner Reibung”, *Vehr. III. Intern. Math. Kongr., Heidelberg, 1904*.
- Raffel, Markus, Christian E. Willert, and Jurgen Kompenhans, *Particle Image Velocimetry: A Practical Guide*, Springer-Verlag, Berlin, 1998.
- Riesenthal, P.H, H.M. Nagib, and D.J. Koga, “Control of Separated Flows using Forced Unsteadiness”, AIAA Paper No. 85-0556, 1985.
- Roos, Frederick W., and Jerome T. Kegelman, “Control of Coherent Structures in Reattaching Laminar and Turbulent Shear Layers”, *AIAA J.* **24**, pp. 1956-63, 1986.
- Roshko, A., “On the Drag and Shedding Frequency of Two-Dimensional Bluff Bodies”, NACA Technical Note 3169, 1954.
- Seifert, A., Bachar, T., Koss, D., Shepshelovich, M. and I. Wygnanski, “Oscillatory blowing: A tool to delay boundary-layer separation”, *AIAA J.* **31**, pp. 2052-2060, 1993.
- Seifert A., and L.G. Pack, “Oscillatory control of separation at high Reynolds numbers”, *AIAA J.* **37**, pp. 1062-1071, 1999.
- Sigurdson, L.W., “The structure and control of a turbulent reattaching flow”, *J. Fluid Mech.* **298**, pp. 139-165, 1995.
- Smith, Barton L., and Ari Glezer, “Vectoring and Small-Scale Motions Effected in Free Shear Flows Using Synthetic Jet Actuators”, AIAA Paper No. 97-0213, 1997.
- Smith, Barton L., and Ari Glezer, “The formation and evolution of synthetic jets”, *Physics of Fluids* **10**, pp. 2281-97, 1998.
- Smith, B. L., and A. Glezer, “Jet vectoring using synthetic jets”, *J. Fluid Mech.* **458**, pp. 1-34, 2002.
- Smith, D.R., M. Amitay, V. Kibens, D.E. Parekh, and A. Glezer, “Modification of Lifting Body Aerodynamics using Synthetic Jet Actuators”, AIAA Paper No. 98-0209, 1998.
- Stueper, T., “Flight experiences and tests on two airplanes with suction slots”, NACA Technical Memorandum 1232, 1943.

Vukasinovic, Bojan, and Ari Glezer, "Transitory Fluidic Control of Turbulent Shear Flows", AIAA Paper No. 2006-3227, 2006.

Vukasinovic, Bojan, Davidson G. Lucas, and Ari Glezer, "Direct Manipulation of Small-Scale Motions in a Plane Shear Layer", AIAA Paper No. 2004-2617, 2004.

Weickgenannt, Ansgar, and Peter A. Monkewitz, "Control of vortex shedding in an axisymmetric bluff body wake", *Eur. J. Mech. B – Fluids* **19**, pp. 789-812, 2000.

Williams, David R., Mukund Acharya, John Bernhardt, and Pan-Mei Yang, "The Mechanism of Flow Control on a Cylinder with the Unsteady Bleed Technique", AIAA Paper No. 91-0039, 1991.

VITA

CHRISTOPHER S RINEHART

Chris Rinehart was born in York, Pennsylvania on February 27, 1974 to Paul and Carolyn Rinehart. He attended public schools in Dallastown, Pennsylvania and graduated in 1992 as valedictorian from the York Vocational-Technical High School with a background in electronics. His college career began with two and a half years of attendance at York College, where he graduated in 1994 with Associate's Degrees in Math, Physics, Engineering, and Liberal Arts. He completed his Bachelor's program at Johns Hopkins University in Baltimore, Maryland, where he graduated in 1997 with degrees in Biomedical Engineering and Engineering Mechanics. Immediately upon graduation Chris moved to Atlanta, Georgia and began working with Professor Ari Glezer in the Fluid Mechanics Research Laboratory at Georgia Tech, contributing most significantly to the SCORPION project which went from concept to flight test in only a few short years. Chris has a great interest in cars, including restoration and performance enhancements, which served to enrich his life and expand his engineering and business competency while also contributing to his delinquency. In a bid to preemptively escape graduate school, Chris took a job in the oilfield services industry in Sugar Land, Texas in 2008, where he continued to expand his life with a newborn daughter while completing his thesis. Chris presently enjoys the good life with his wife, daughter, three cats, a Ford GT supercar, and a few too many car parts.